



HAL
open science

Stability of the two-phase displacement in porous media studied by MRI techniques

Jamal Fannir

► **To cite this version:**

Jamal Fannir. Stability of the two-phase displacement in porous media studied by MRI techniques. Fluids mechanics [physics.class-ph]. Université de Lorraine, 2019. English. NNT : 2019LORR0330 . tel-02880651

HAL Id: tel-02880651

<https://hal.univ-lorraine.fr/tel-02880651>

Submitted on 25 Jun 2020

HAL is a multi-disciplinary open access archive for the deposit and dissemination of scientific research documents, whether they are published or not. The documents may come from teaching and research institutions in France or abroad, or from public or private research centers.

L'archive ouverte pluridisciplinaire **HAL**, est destinée au dépôt et à la diffusion de documents scientifiques de niveau recherche, publiés ou non, émanant des établissements d'enseignement et de recherche français ou étrangers, des laboratoires publics ou privés.



AVERTISSEMENT

Ce document est le fruit d'un long travail approuvé par le jury de soutenance et mis à disposition de l'ensemble de la communauté universitaire élargie.

Il est soumis à la propriété intellectuelle de l'auteur. Ceci implique une obligation de citation et de référencement lors de l'utilisation de ce document.

D'autre part, toute contrefaçon, plagiat, reproduction illicite encourt une poursuite pénale.

Contact : ddoc-theses-contact@univ-lorraine.fr

LIENS

Code de la Propriété Intellectuelle. articles L 122. 4

Code de la Propriété Intellectuelle. articles L 335.2- L 335.10

http://www.cfcopies.com/V2/leg/leg_droi.php

<http://www.culture.gouv.fr/culture/infos-pratiques/droits/protection.htm>

Mémoire en vue de l'obtention du grade de
Docteur de L'Université de Lorraine
Spécialité : Mécanique et Energétique
Ecole doctorale : SIMPPE
Présenté par
Jamal FANNIR

Stability of the two-phase displacement in porous media studied by MRI techniques

Soutenance prévue le 16 décembre 2019 devant le jury :

| | | |
|---------------|---|--|
| Rapporteurs : | Daniel BROSETA Marc FLEURY | Professeur, Université de Pau et des Pays de l'Adour Ingénieur de Recherche (PhD, HDR), IFP Energies Nouvelles, Rueil-Malmaison |
| Examineurs : | Marie-Odile SIMONNOT Henri BERTIN Irina PANFILOVA (Directeur de thèse) | Professeur, Université de Lorraine Directeur de Recherches CNRS, Université de Bordeaux Maître de Conférence HDR, Université de Lorraine |
| Invités : | Sébastien LECLERC (Co-directeur de thèse) Didier STEMMELEN (Co-encadrant de thèse) Benjamin NICOT | Ingénieur de Recherches, Université de Lorraine Chargé de Recherches CNRS, Université de Lorraine Spécialiste de l'évaluation de la formation au laboratoire de Pétrophysique du CSTJF, TOTAL |

Acknowledgments

Firstly, It is difficult to overstate my gratitude to my thesis director, Professor Irina Panfilova, to my co-director, Mr. Sébastien Leclerc, Lemta research engineer, and my co-supervisor, Mr. Didier Stemmelen, CNRS researcher, for the continuous support of my PhD study and related research during the last three years. They have been tremendous mentors for me throughout my thesis work, they provided encouragement, sound advice, good teaching techniques and excellent collaborators. I would like to thank them very much, for their patience, motivation, and immense knowledge.

I would like to express my gratitude to Professor Marie-Odile Simonnot, Lorraine university, Professor Daniel Broseta, Pau university, Mr. Marc Fleury, IFP research engineer, and Mr. Henri Bertin, CNRS research director, for being integral members of my thesis committee, and for their insightful comments and encouragement, I thank them all for bringing their expertise to my thesis work.

I would like to express my sincere thanks to TOTAL company and LEMTA laboratory for financially supported my PhD study.

I would like to thank the mechanical design team in LEMTA and in particular Franck Demeurie and Jeremy Bianchin, for their involvement of designing and the preparing the experiments setup, and also, I would like to thank the IT engineer, Ludovic Buhler for his help in solving the computer issues.

I also would like to express my thanks to the secretaries of the laboratory, especially Dalida, Valerie and Irene. Thank you for your invaluable help on the Logistic plans, and your guidance for administrative documents preparations.

Many thanks to my colleagues in the office: Juan D, Ahmad, Thomas L, Arthur. Our office was an international place where we had an excellent environment to exchange our ideas and helping each other, thank you for sharing your stories and the discussions we had, thank you for the coffee breaks that we had together.

Finally, I would like to thank my parents, all my family and friends for enduring and having undergone this long journey with me, providing support at all times.

A mes parents, à toute ma famille

Table of contents

| | |
|---|-----------|
| Introduction générale (Version Française)..... | 12 |
| General Introduction (English Version) | 18 |
| 1. CONTEXT..... | 22 |
| 1.1 Introduction..... | 24 |
| 1.2 Importance of two phase flow in the oil industry..... | 24 |
| 1.3 Applications of MRI to porous media..... | 26 |
| 1.4 MRI comparison to other visualisation techniques..... | 29 |
| 1.5 Conclusions | 33 |
| 2. TWO-PHASE FLOW IN POROUS MEDIA..... | 35 |
| 2.1 Introduction..... | 37 |
| 2.2 Basic elements | 37 |
| 2.2.1 Porous medium..... | 37 |
| 2.2.2 Fluid viscosity..... | 38 |
| 2.2.3 Wettability..... | 39 |
| 2.2.4 Interfacial tension | 41 |
| 2.3 Flow equations in permeable media..... | 42 |
| 2.3.1 Capillary pressure..... | 42 |
| 2.3.2 Leverett J-Function..... | 43 |
| 2.3.3 Governing equations for two-phase displacement | 44 |
| 2.3.4 The competition between forces | 46 |
| 2.4 Conclusions..... | 47 |
| 3. PRINCIPLES OF MAGNETIC RESONANCE IMAGING (MRI)..... | 49 |
| 3.1 Introduction and brief history | 51 |
| 3.2 Nuclear magnetic moment | 51 |
| 3.3 Magnetic Resonance Phenomenon | 52 |
| 3.4 Acquisition of NMR signal | 55 |
| 3.4.1 Longitudinal relaxation time T1..... | 55 |
| 3.4.2 Transverse relaxation time T2..... | 56 |
| 3.4.3 Spin-Echo sequence | 57 |
| 3.5 NMR signal recovery and images | 59 |
| 3.6 Conclusions..... | 61 |

| | | |
|---------|--|-----|
| 4. | EXPERIMENTAL SETUP, INSTRUMENTATION AND METHODS..... | 64 |
| 4.1 | Introduction..... | 66 |
| 4.2 | Experiments | 66 |
| 4.2.1 | Experimental system | 66 |
| 4.2.2 | MRI Resolution and field of view | 67 |
| 4.3 | Sample material | 68 |
| 4.3.1 | Porous medium..... | 68 |
| 4.3.2 | Fluids | 70 |
| 4.4 | Experimental process | 70 |
| 4.5 | Imaging protocol and methods..... | 72 |
| 4.5.1 | MSME protocol | 72 |
| 4.5.2 | Imaging methods..... | 74 |
| 4.5.2.1 | Selective method..... | 74 |
| 4.5.2.2 | Nonselective method | 76 |
| 4.6 | Conclusion | 77 |
| 5. | EXPERIMENTAL RESULTS AND DISCUSSIONS | 75 |
| 5.1 | Introduction..... | 81 |
| 5.2 | Experiments performed..... | 81 |
| 5.2.1 | Experiment with a packed glass-beads model, selective method | 81 |
| 5.2.2 | Experiment with a packed polystyrene-beads model | 83 |
| 5.2.3 | Experiments with packed sand column | 98 |
| 5.3 | Relative phase permeability calculation..... | 104 |
| 5.4 | Discussion | 109 |
| 5.4.1 | Dimensionless groups | 110 |
| 5.4.2 | Displacement mechanism and the wettability effect | 112 |
| 5.4.3 | Additional observations | 114 |
| 5.5 | Conclusions | 117 |
| 6. | NUMERICAL SIMULATION AND COMPARISON WITH EXPERIMENTAL RESULTS... | 120 |
| 6.1 | Introduction..... | 122 |
| 6.2 | Numerical modelling | 122 |
| 6.2.1 | Case 1 classical model, viscous force effect..... | 126 |
| 6.2.2 | Case 2 gravity and viscous forces effect..... | 127 |
| 6.2.3 | Case 3 gravity, capillary and viscous forces effect..... | 128 |
| 6.3 | Comparison of the influence of three main forces | 129 |

| | | |
|------|---|-----|
| 6.4 | Comparison of experimental results with the numerical model | 132 |
| 6.5 | Conclusions | 134 |
| 7. | General conclusions and perspectives | 136 |
| | CONCLUSIONS ET PERSPECTIVES (VERSION FRANÇAISE) | 138 |
| | CONCLUSIONS AND PERSPECTIVES (ENGLISH VERSION) | 143 |
| | BIBLIOGRAPHY | 147 |
| | ANNEXES | 155 |
| I. | Details of the experimental installation | 157 |
| II. | Sample preparation | 160 |
| III. | Determination of porous media porosity | 162 |
| IV. | NMR relaxation time measurements T2 (CPMG): | 162 |
| V. | MRI Experimental results for some experiments: | 171 |
| VI. | PTX2000 data sheet | 178 |

Nomenclature

| <i>Symbols</i> | <i>Descriptions</i> | <i>Units</i> |
|----------------|--|------------------------|
| A | Area | m^2 |
| A_s | Amplitude of the MR signal | arbitrary units (a.u.) |
| AOI | Area of interest | [-] |
| B_0 | Bond number | [-] |
| B_0 | Static magnetic field | T |
| B_1 | Radio-frequency magnetic field | T |
| C | Kozeny-Carman constant | [-] |
| Ca | Capillary number | [-] |
| CDC | Capillary desaturation curves | [-] |
| D | Average pore size | Mm |
| d_p | Particle diameter | Mm |
| F | Resonance frequency | Hz |
| FOV | Field of view | Cm |
| G | Gravitational constant | $m.s^{-2}$ |
| GSS | Slice selection gradient | $T.m^{-1}$ |
| H | Capillary pressure head | M |
| 1H | Number of protons | [-] |
| I | Observed signal intensity | [-] |
| I_0 | Intrinsic signal intensity | [-] |
| I_{ref} | Reference signal intensity | [-] |
| K | Intrinsic permeability | m^2 |
| Kr | Relative permeability | [-] |
| M_0 | Macroscopic magnetization at equilibrium | $A.m^{-1}$ |
| M_{xy} | Transversal macroscopic magnetization | $A.m^{-1}$ |
| M_z | Longitudinal macroscopic magnetization | $A.m^{-1}$ |
| M_{wo} | Mobility ratio | [-] |
| MRI | Magnetic resonance imaging | [-] |
| NMR | Nuclear magnetic resonance | [-] |
| P_c | Capillary pressure | Pa |
| P_o | Oil phase pressure | Pa |
| P_w | Water phase pressure | Pa |
| PV | Pore volume | Ml |
| Q_{inj} | Injection rate | $mL.min^{-1}$ |
| R | Tube radius | Mm |
| RF | Radio frequency | MHz |
| S_o | Saturation of oil phase | % |
| S_{or} | Residual oil saturation | % |
| S_w | Saturation of water phase | % |

| | | |
|--------------|--|-------------------------------------|
| SM | <i>Selective method</i> | $[-]$ |
| NSM | <i>Non-selective method</i> | $[-]$ |
| t | <i>Time following the RF pulse</i> | s |
| TE | <i>Echo Time</i> | s |
| TR | <i>Repetition time</i> | s |
| $T1$ | <i>Longitudinal relaxation time</i> | s |
| $T2$ | <i>Transverse relaxation time</i> | s |
| v | <i>Darcy velocity of injected phase</i> | $m.s^{-1}$ |
| φ | <i>Sample porosity</i> | $\%$ |
| ρ_o | <i>Density of oil phase</i> | $kg.m^{-3}$ |
| ρ_w | <i>Density of wetting-phase</i> | $kg.m^{-3}$ |
| $\Delta\rho$ | <i>Density difference</i> | $kg.m^{-3}$ |
| μ_o | <i>Oil viscosity</i> | cP |
| μ_w | <i>Wetting-phase viscosity</i> | cP |
| μ_i | <i>Nuclear magnetic moment</i> | $A.m^2$ |
| σ | <i>Interfacial tension</i> | $N.m^{-1}$ |
| θ | <i>Contact angle</i> | <i>Degree ($^\circ$)</i> |
| λ | <i>Fluid mobility</i> | $m^2.cP^{-1}$ |
| γ | <i>Gyromagnetic ratio</i> | $rad.s^{-1}.T^{-1}$ |
| τ | <i>Shear stress</i> | $N.m^{-2}$ |
| ω_o | <i>Angular velocity of Larmor precession</i> | $rad.s^{-1}$ |
| η_c | <i>Specific concentration in meniscus</i> | $[-]$ |

Introduction générale (Version Française)

L'écoulement de deux phases immiscibles dans un milieu poreux est un sujet d'attention très important et largement applicable dans l'industrie du pétrole, notamment pour l'estimation des réserves de pétrole récupérables, ou encore l'optimisation des techniques de récupération, mais aussi dans le secteur de l'industrie chimique (réacteurs catalytiques, séparation et extraction) ou dans le domaine de l'hydrogéologie (pollution des aquifères par les NAPL). Ceci explique l'importance des études visant à améliorer la description des écoulements multiphasiques en milieu poreux. En effet, l'écoulement simultané de deux fluides non miscibles (eau-huile) dans un milieu poreux n'est pas toujours bien décrit par la loi de Darcy généralisée, qui ne prend en compte que la saturation en eau (et huile) comme variable descriptive. Ceci a un impact important sur la description de la stabilité de l'écoulement de deux phases sous l'effet simultané des forces de gravité, de frottement visqueux et de tension superficielle.

Pour l'étude de l'écoulement diphasique dans un milieu poreux, plusieurs méthodes d'imagerie ont été appliquées, notamment la tomographie par rayons X ou tomomodensitométrie (TDM), Akin et al. ; Larachi et al. et Pak et al. [1,2,3], la tomographie par synchrotron, D. Bernard [4] et l'imagerie par résonance magnétique (IRM), Chen et al. ; Zhao et al. ; Mitchell et al. et M. Li [5,6,7,8,9]. Parmi ces méthodes, seule l'IRM est capable de visualiser la structure interne d'un système en trois dimensions avec une résolution spatiale des espèces présentes. En outre, l'IRM permet également des mesures in situ de la vitesse d'écoulement, de la saturation et de la diffusion-dispersion de l'écoulement de fluide dans le milieu poreux. Une autre opportunité de l'IRM est qu'elle peut être utilisée pour sonder à la fois les propriétés microscopiques à l'échelle des pores mais aussi macroscopiques à l'échelle du volume élémentaire représentatif.

Le développement rapide de nouvelles technologies quantitatives d'imagerie par résonance magnétique a ouvert de nouvelles perspectives avec des résultats intéressants pour les mesures de vitesse d'écoulement dans des milieux poreux. Johns et Gladden [10] ont eu recours à la technique d'IRM pour visualiser la dissolution, par une phase aqueuse mobile, de ganglions d'octanol piégés dans l'espace des pores d'un lit de billes de verre tassées au hasard. Ils ont également acquis des images en trois dimensions et ont été capables de distinguer les phases solide, hydrocarbure et aqueuse. Enfin, ils ont obtenu des cartes de vitesse de la phase aqueuse mobile. Ersland et al. [11] ont utilisé les techniques d'IRM pour étudier l'impact de fractures dans le milieu poreux sur la récupération d'huile. Ils ont obtenu des images spatiales à haute résolution spatiale du flux eau-huile dans une fracture de 1 mm. En outre, dans un travail récent du laboratoire LEMTA, l'IRM a été utilisée pour étudier l'écoulement d'un fluide dans un milieu poreux granulaire [12]. Les auteurs ont montré la possibilité de visualiser le champ de vitesse dans un milieu poreux et de mesurer avec précision les vitesses interstitielles et moyennes dans des lits à garnissage.

La présente étude a pour objet l'étude du déplacement de deux fluides non miscibles dans un milieu poreux. Nous avons retenu comme forces mises en jeu dans le déplacement des deux liquides : les forces capillaires, visqueuses et gravitationnelles. Nous nous sommes concentrés plus particulièrement sur les propriétés de mouillabilité des fluides avec les surfaces solides car il s'agit d'un facteur important pour la récupération secondaire des hydrocarbures. Dans ce travail, l'IRM a été utilisée pour examiner expérimentalement le flux d'eau et d'huile à travers un modèle poreux vertical.

En utilisant la technique IRM, nous étudions également la dynamique du front de déplacement, sa déformation et le piégeage au cours du processus d'écoulement diphasique. Lors du déplacement des phases dans le milieu poreux différentes structures dans la distribution des phases apparaissent. Pour une même saturation, l'occupation des fluides peut prendre différentes formes. Ces formes peuvent être décrites par la saturation S de la phase injectée et un paramètre supplémentaire, responsable du type de forme. Il est insuffisant de n'avoir que la surface spécifique de distribution de phase dans l'espace comme paramètre additionnel, ainsi que le proposent plusieurs auteurs, car différentes formes peuvent avoir une étendue de la surface de contact du même ordre de grandeur. Nous recommandons d'utiliser deux paramètres de forme supplémentaires : l'un pour caractériser l'interface spécifique entre les phases, et l'autre pour évaluer le degré de connectivité entre les phases.

Nous utiliserons dans nos travaux l'imagerie par résonance magnétique (IRM), technique innovante, disponible au LEMTA, et relativement peu utilisée dans le contexte des écoulements diphasiques en milieu poreux. L'expérimentation consistera à suivre par IRM le déplacement de deux liquides non miscibles (eau-huile) au sein d'un milieu poreux. Le support poreux consistera en un tube de verre ou de PVC rempli de billes sphériques en polystyrène (mono-disperses) ou de grains de sable d'un peu moins de 1 mm de diamètre.

Une séquence IRM d'écho de spin sera mise en œuvre pour déterminer la saturation et la vitesse du fluide sur la longueur de l'échantillon. Parallèlement à cela, des méthodes de relaxation RMN seront utilisées pour obtenir des informations sur la distribution de taille des pores dans les échantillons.

Dans le même temps, les simulations numériques seront comparées aux études expérimentales. Pour la modélisation des écoulements diphasiques à l'échelle macroscopique, nous utiliserons un code de simulation développé sous Comsol Multiphysics. Les résultats de l'expérimentation basés sur les distributions stochastiques de phase résiduelle piégée dans le milieu poreux nous permettront d'obtenir la cinétique du processus de piégeage.

L'évaluation de la saturation S de la phase injectée, et aussi de celle connectée et de celle déconnectée (piégée), nous permettront de compléter le modèle phénoménologique de ménisques proposé par Panfilova et Panfilov [13],

Les approches IRM suivantes seront utilisées :

- L'ajustement des protocoles IRM adaptés aux phases eau et huile qui coexistent dans les milieux poreux.
- L'utilisation principalement de la cartographie du temps de relaxation T2 pour étudier les fluides coexistants dans les milieux poreux.
- L'usage de l'intensité du signal pour observer le déplacement des fluides dans les milieux poreux et pour estimer les saturations des fluides.
- L'obtention d'images verticales le long de l'axe de l'échantillon, combinées à des sections horizontales.

Dans ce manuscrit, les chapitres sont classés de la manière suivante :

Chapitre 1 : dans ce chapitre, nous montrons d'abord l'importance des écoulements diphasiques dans les milieux poreux. Nous insistons plus particulièrement sur le domaine pétrolier et la récupération du pétrole dans les roches-réservoirs. Nous rappelons notamment les techniques classiques de récupération du pétrole. Nous présentons ensuite, de façon très générale, la méthode d'imagerie par résonance magnétique nucléaire (IRM) en donnant au passage quelques applications de l'utilisation de l'IRM pour investiguer les milieux poreux. Nous soulignons aussi les avantages et inconvénients de la technique d'IRM. Nous rappelons les principales méthodes d'imagerie non invasives et faisons une revue des travaux publiés. Cela nous permet de comparer les différentes méthodes de tomographie avec les techniques d'IRM. L'intérêt de l'utilisation de l'IRM est finalement mis en évidence pour les problèmes d'écoulements diphasiques en milieu poreux.

Chapitre 2 : notre travail comprend deux aspects, les déplacements de fluides dans les milieux poreux et l'utilisation de la technique d'imagerie non-invasive par IRM pour suivre ces déplacements. Ce travail peut donc intéresser à la fois les chercheurs travaillant dans le domaine du transport en milieu poreux, mais aussi ceux qui s'intéressent au développement et à l'utilisation des techniques d'IRM. Les principes de ces deux domaines doivent donc être précisés.

Dans ce chapitre, nous présentons les éléments de base des milieux poreux. Nous abordons les principaux phénomènes à prendre en compte dans le déplacement de deux fluides non-miscibles dans un milieu poreux : la viscosité des fluides, la mouillabilité des surfaces solides et la tension superficielle des fluides. L'approche théorique pour la modélisation des écoulements est basée sur le modèle de Buckley-Leverett décrivant le déplacement simultané de deux fluides non-miscibles. Quelques éléments sont donnés quant à la théorie de la capillarité vectorielle et ses conséquences sur l'écriture du modèle de Buckley-Leverett. Finalement les nombres adimensionnels, pertinents pour la

description du problème, sont introduits, à savoir le nombre de Bond (Bo) ainsi que le nombre capillaire (Ca).

Chapitre 3 : Ce chapitre présente, dans ces grandes lignes, les principes de l'imagerie par résonance magnétique (IRM). On abordera successivement le phénomène de résonance magnétique nucléaire (RMN), la définition des temps de relaxation RMN, T1 et T2, et leur mesure. On présentera aussi la méthode d'acquisition du signal RMN et de construction des images par IRM par utilisation de gradients de champ magnétique suivant les directions de l'espace. On précisera aussi la notion de séquence IRM, c'est-à-dire l'ajustement au cours du temps des différentes impulsions tantôt radio-fréquences (excitation des spins), tantôt de gradient de champ magnétique (marquage spatial).

Chapitre 4 : dans cette partie, nous décrirons notre configuration expérimentale, l'instrumentation IRM utilisée, les échantillons et leur mode de préparation. Nous expliquerons ensuite le protocole expérimental qui amène à effectuer un déplacement de l'huile saturant initialement le milieu poreux à partir d'une injection contrôlée d'eau par le bas de l'échantillon. Nous donnerons les techniques d'imagerie utilisées durant la thèse : la méthode sélective, basée sur une différenciation des deux fluides à partir de leur fréquence de résonance (déplacement chimique) et la méthode non-sélective, basée sur l'utilisation d'ions Mn^{2+} comme agent de contraste, permettant *in-fine* d'éteindre le signal de l'eau, mais pas celui de l'huile.

Chapitre 5 : la partie expérimentale est celle la plus importante de ce travail et la majeure partie du temps de la thèse y a été consacrée. Les expériences concerneront principalement deux séries d'échantillons (empilement de billes en polystyrène, colonne de sable compacté) qui diffèrent essentiellement par leurs propriétés de mouillage. Ces échantillons seront préalablement saturés d'huile puis soumis à une injection d'eau par le bas à débit constant.

Le suivi du déplacement des fluides dans les échantillons sera réalisé à l'aide de la technique IRM. Nous ferons varier le débit d'injection d'un essai à l'autre dans une gamme admissible pour la mesure par IRM (0.06 à 0.16 ml/min). Pour chaque échantillon, plusieurs images seront prises suivant une section d'orientation verticale et aussi suivant plusieurs coupes axiales horizontales. Cette stratégie permet d'avoir une connaissance presque complète de la répartition des fluides dans le milieu poreux en conservant des temps d'acquisition relativement courts (quelques minutes). Les principaux résultats de ces différentes expériences concerneront l'évaluation de la saturation en huile, la saturation finale en huile résiduelle et l'observation locale du déplacement huile-eau à l'intérieur du milieu poreux. Les expériences seront répétées plusieurs fois pour vérifier la reproductibilité et confirmer les résultats. Nous tenterons également d'évaluer les courbes de perméabilités relatives en fonction de la saturation, à partir des résultats d'IRM.

A la fin de ce chapitre, nous présenterons une synthèse des résultats qui s'appuiera sur une comparaison des différents cas étudiés (type d'échantillon, débit d'injection). Nous ferons en particulier une analyse des mécanismes de déplacement au niveau du front eau-huile prenant en compte les effets de digitation, de mouillage et d'hétérogénéité du milieu. Nos résultats seront replacés sur des diagrammes proposés dans la littérature (Lake [91], Lenormand [93]).

Chapitre 6 : dans cette partie du document, un modèle général d'écoulement diphasique en milieu poreux sera présenté. La méthode de simulation de l'écoulement diphasique (eau-huile) vertical en milieu poreux à l'aide du logiciel COMSOL sera décrite. Les équations constitutives introduites au chapitre 2 seront utilisées et l'effet des différentes forces en présence sera examiné.

La situation envisagée pour la simulation est celle d'une colonne remplie de sable compacté, initialement saturé d'huile, où l'eau est injectée vers le haut à débit constant. Pour le sable, l'eau est le fluide mouillant et l'huile représente le fluide non-mouillant. Les propriétés des fluides sont essentiellement tirées de la littérature, quant aux propriétés du milieu poreux, elles sont en partie obtenues à partir des essais IRM sur le sable tassé, ou encore par des caractérisations complémentaires (voir annexe).

Le modèle proposé est 1D et profite de la géométrie axisymétrique des expériences. Les simulations numériques de difficulté croissante seront réalisées pour tester l'effet respectif des forces de viscosité, de gravité et de capillarité :

- Cas 1 : avec uniquement l'effet de viscosité,
- Cas 2 : avec forces de viscosité et de gravité,
- Cas 3 : avec forces de viscosité, de gravité et de capillarité.

Le modèle de capillarité vectorielle sera également testé en prenant soin de déterminer, à partir des essais expérimentaux, le paramètre η_c de concentration de ménisques.

Finalement, la simulation numérique sera confrontée à des résultats d'expériences obtenues par IRM sur le sable compacté. La comparaison s'appuiera uniquement sur le profil de saturation moyen (valeur moyenne suivant une coupe horizontale) dans la direction verticale. Le but est d'obtenir une validation qualitative des différents modèles de simulation.

Enfin, chapitre 7 : ce chapitre présente les conclusions générales, les recommandations et la voie à suivre.

General introduction (English Version)

Two-phase flow of immiscible fluids in porous media is a very important research subject, widely applicable in the petroleum industry (such as estimation of recoverable oil reserve, optimization of the recovery techniques...), but also in the sector of chemical industry (catalytic reactors, separation and extraction) or in the hydrogeology domain (pollution of aquifers by NAPL). This explains the importance of the studies aimed at improving the description of multi-phase flow in porous media. Indeed, the simultaneous flow of two immiscible fluids (water-oil) in porous media is not always well described by the generalized Darcy's law, which only takes into account water (or oil) saturation as additional descriptive variable. This has a significant impact on the description of the two-phase flow stability under the simultaneous effect of gravity, viscous friction and surface tension forces.

For the study of two-phase flow in porous media, several imaging methods have been applied including X-ray, computed tomography scanners (CT), Akin et al.; Larachi et al. and Pak et al. [1,2,3] synchrotron imputed micro-tomography, Bernard [4] and magnetic resonance imaging (MRI) techniques, Chen et al.; Zhao et al., Mitchell et al. and M. Li [5,6,7,8,9]. Among these methods, only MRI is able to visualize the internal structure of a three dimensional system with a spatial resolution of the species present. Furthermore, MRI also allows in-situ measurements of flow velocity, saturation and diffusion-dispersion of the fluid flow within the porous medium. Another opportunity of the MRI is that it can be used to probe both microscopic properties at the pore scale and also macroscopic ones at the scale of the representative elementary volume.

The rapid development of new quantitative magnetic resonance imaging technologies led to new opportunities with interesting results for measurements of fluid flow in porous media. For example, Johns and Gladden [10] have used MRI technique to visualize the dissolution by a mobile aqueous phase, of entrapped ganglia of octanol within the pore space of a randomly packed bed of glass beads. They also acquired three dimensional images and were able to distinguish the solid, hydrocarbon and aqueous phases. Finally, they also obtained velocity maps of the mobile aqueous phase. Ersland et al. [11] used the MRI techniques to study how the oil recovery is affected by fractures. They have obtained high spatial resolution images of the water-oil flow inside a fracture of 1 mm. Furthermore, in a recent work by the LEMTA laboratory, MRI was used to study the flow of a fluid in a granular porous medium [12]. The authors have shown the possibility of visualizing the velocity field in porous medium and accurately measuring interstitial and averaged velocities in packed beds.

The purpose of the present study is the investigation of the immiscible fluid displacement in porous media. We have retained as forces involved in the displacement of the two liquids: the capillary, viscous and gravitational forces. In particular, we focus on the wettability properties of the fluids with solid surfaces as this is an important factor for secondary recovery of hydrocarbons. In this work, MRI was used to experimentally examine the flow of water and oil through a vertical porous model.

Using MRI technique, we also study the dynamics of the displacement front, its deformation and the phase trapping during the two-phase flow process. Displacement in porous media is characterized by the formation of different structures of the phase distribution in porous space. For the same saturation value, the occupation of the fluids can take different forms. These various shapes can be described by the saturation S of the displacing phase and an

additional parameter, responsible for the type of the shape. It is insufficient to have only the specific surface of phase distribution in space, as proposed by several authors, because different shapes can have a contact surface area of the same order of magnitude. We recommend using two additional parameters of shape: one to characterize the specific interface between the phases, and the other to evaluate the degree of connectivity between the phases.

In our work, we will use magnetic resonance imaging (MRI), an innovative experimental technique available at LEMTA, and relatively little used in the context of two-phase flows in porous media. The experiments will consist in following MRI the displacement of two immiscible liquids (water-oil) within a porous medium. The porous samples consist of a glass or PVC tube filled with randomly packed spherical polystyrene beads (monodisperse) or packed sand grains less than 1 mm in diameter. A spin echo MRI sequence is used to determine the saturation and velocity of the fluid over the length of the sample, and provides information about the pore size distribution and pore occupancy in the sample.

At the same time, numerical simulations will be compared with the experimental studies. For the modelling of two-phase flow at macro scale, we will use a simulation software code based on Comsol Multiphysics. The experimental results based on the stochastic distributions of residual phase trapped in the porous medium will allow us to obtain the kinetics of trapping process.

The saturation of the displacing phase, the connected displaced phase and disconnected trapped phase, will allow us to complete the phenomenological menisci model proposed by Panfilova and Panfilov [13].

The following MRI approaches will be used:

- Adjustments of MRI protocols suitable for water/oil displacement in porous media.
- Mainly, using T2 relaxation time mapping to investigate coexisting fluids in porous media.
- Using signal intensity to observe the movement of fluids in porous media and to estimate fluid saturations.
- Obtaining vertical images along the axis of the sample combined with horizontal sections.

In this manuscript, the chapters are ordered as follows:

Chapter 1: In this chapter, we first show the importance of two-phase flow in porous media. We then present the main non-invasive imaging methods and review the most important published works. The different tomography methods are compared with MRI techniques.

Chapter 2: Our work includes two aspects, the movement of immiscible fluids in porous media and the use of non-invasive MRI imaging to track these movements. This work may therefore be interesting for researchers working in the field of transport in porous media, but also to those interested in the development and use of MRI techniques. That is why the principles of these two domains should be recalled. In this chapter, we present the basic elements of porous media, including the governing equations of two-phase displacement based on Buckley-Leverett approach.

Chapter 3: It outlines the principles of magnetic resonance imaging (MRI). We will successively address the phenomenon of magnetic resonance, the definition of NMR relaxation times and their measurement. We will also discuss the acquisition of the MRI signal and the way of building images.

Chapter 4: In this part, we will describe our experimental setup, the MRI instrumentation used, the sample material and how it is prepared. We will then explain the experimental process and the MRI imaging protocol, including the methods used in this thesis: the selective method based on chemical shift phenomenon and the non-selective method based on the use of Mn^{2+} ions as a contrast agent.

Chapter 5: The experiments effort is the most important part of this work and most of the thesis time was devoted to it. Two sets of samples were prepared according to their wetting properties. They were then saturated with oil and subjected to an injection of water at different flow rates. The studies and investigation were performed using the MRI technique. For each sample, several images were taken according to a section of vertical orientation and also in horizontal axial slices. The main results of these different experiments concern the evaluation of the oil saturation, the final saturation of residual oil and the local observation of the oil-water displacement inside the porous medium. The series of tests were also repeated several times to confirm the results. At the end of this chapter we present a summary of the results based on a comparison of the different cases studied. In particular, we make an analysis of displacement mechanisms, especially at the water-oil front, taking into account the effects of fingering, wetting and heterogeneity of the samples.

Chapter 6: In this part of the document, a general model of the two-phase fluid flow in porous medium is presented. The method for simulating immiscible two-phase flow (water-oil) in a vertical porous medium is also described using COMSOL software. The governing equations introduced in chapter 2 have been used, and the effect of the different forces involved was examined. The experimental data will be compared with the results of the simulation model.

Finally, chapter 7: This chapter presents the general conclusions, recommendations and way forward.

1. Context

| | | |
|-----|---|----|
| 1. | CONTEXT..... | 22 |
| 1.1 | Introduction..... | 24 |
| 1.2 | Importance of two phase flow in the oil industry | 24 |
| 1.3 | Applications of MRI to porous media | 26 |
| 1.4 | MRI comparison to other visualisation techniques | 29 |
| 1.5 | Conclusions..... | 33 |

1.1 Introduction

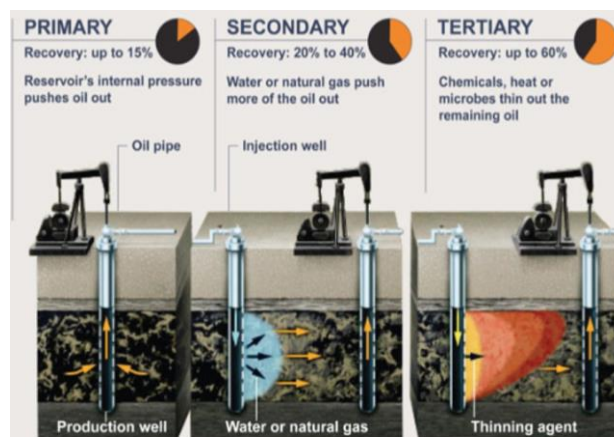
The two-phase simultaneously flow in porous media affects several subsurface processes such as crude oil recovery and NAPL contamination of groundwater. These processes are indirect measurements in most cases, because the permeable media and process occurring inside them, are not amenable to direct observation. And these indirect observations could lead to different results and different interpretations. Many experiments have been conducted in the past based on the results obtained at the boundary of these experiments (input and output), or on a limited direct observation, without a complete real information about the process within the permeable media. Thus, there is a need for methods to permit direct observation or imaging of the properties of porous media and the processes in which they occur. In order to get a consolidated information and complete displacement phenomena understanding, new experiments should be conducted and updated using direct visualisation of recent devices and methods such as MRI.

1.2 Importance of two phase flow in the oil industry

Extraction and recovery of crude oil from oil reservoirs is run through two or three of production stages. These stages can be classified as following:

- Primary recovery: it is the natural drive mechanism; the recovery ration is from 5 % to 15 % [14, 15] of original oil in place, produced mainly by the depletion of reservoir own energy, such as water or gas drives or gravity drainage. Producer wells drilled into the target reservoir.
- Secondary recovery: in this stage another 15 % to 25 % [14] of oil produced mainly by water injection/flooding process (water and oil displacement in rock), there are a lot of projects around the world use water flooding system, in some cases this method used from the first stage. This system includes producer and injection well drilled to the reservoir.
- The tertiary recovery: it is known as enhanced oil recovery (EOR), additional 5 % to 15 % of oil could be extracted from oil reservoirs by applying these techniques.

Up to date the limitation of two-phase flow understanding has great impacting on the oil recovery methods. So far, the maximum oil can be produced from the oil reservoir is in range between 30 % to 60 %. In most cases 40 % to 50 % of original oil in place is not produced. Figure 1.1 indicates the range of recovery factors for conventional oil reservoirs at different stages of production.



Ref. <https://petgeo.weebly.com/thereservoir.html>

Figure 1.1. Production of conventional oil reservoirs, recovery factor for each process.

Oil recovery efficiency depends on the understanding of the fluids displacement in the microscopic and macroscopic levels. Mostly, the displacement efficiency at the microscopic level depends on the fluid and rock properties such as material wettability, interfacial tension, capillarity, and fluids relative permeability within permeable media. Any change in fluid displaced viscosity (here oil), capillary pressure or interfacial tension could have a positive impact on the microscopic displacement efficiency [15]. These controlled forces can be described by capillary and Bond numbers (see section 2.3.4). The equations of conservation of moment, mass and energy are used to describe the microscopic approach. Some parameters in these equations could be investigated using lab experimental work.

The macroscopic displacement efficiency can be defined as the measure of the extent to which the displacing fluid is in contact with the oil-bearing parts of the reservoir. It is highly impacted by the fluid mobility ratio (here water and oil), and also impacted by porous media geometry and heterogeneities [15].

Mobility ratio (M_{wo}) is the ratio of the mobility of the displacing fluid (water) behind the front to the mobility of the displaced fluid (oil) ahead of the front (Eq. 1.1):

$$M_{wo} = \frac{\lambda_w}{\lambda_o} = \frac{k_{rw}/\mu_w}{k_{ro}/\mu_o} \quad (1.1)$$

where M_{wo} is the mobility ratio, k_r is the relative permeability, μ is the viscosity; λ is the mobility, and w,o is the subscripts denoting oil and water, respectively. Figure 1.2 below is the schematic diagram of oil-water mobility.

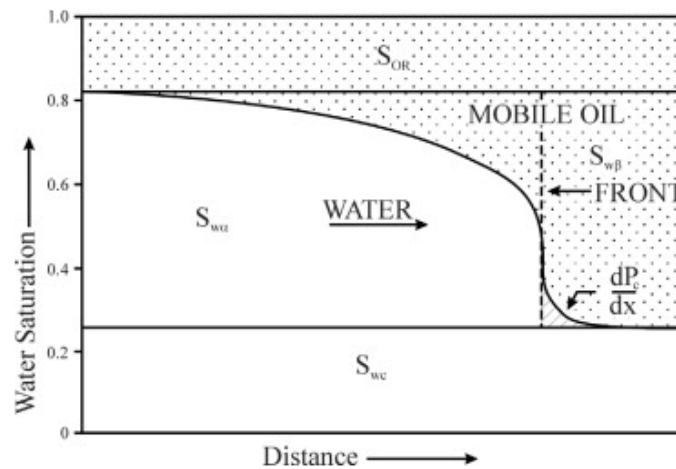


Figure 1.2. Schematic diagram of fluids mobility [16].

The displacement stability is function in the mobility ration [15]:

- If mobility ratio (M_{wo}) $\leq 1 \Rightarrow$ favourable.
- If mobility ratio (M_{wo}) $> 1 \Rightarrow$ unfavourable.

Figure 1.3 shows the expected displacement fronts during water-flooding for different mobility ratios and pore volumes injected until breakthrough [17].

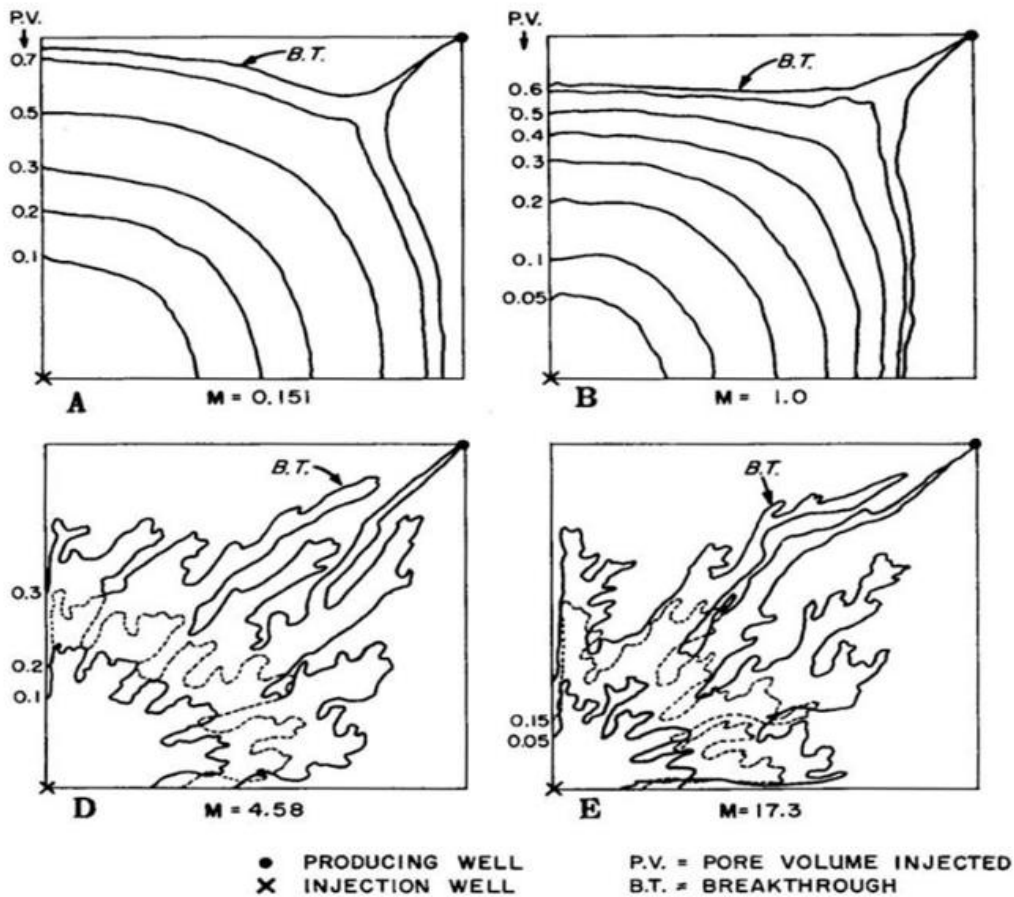


Figure 1.3. Displacement fronts during water-flooding for different mobility ratios and pore volumes injected until breakthrough [17].

1.3 Applications of MRI to porous media

Magnetic Resonance Imaging (MRI) can be utilized to obtain images of liquid phases in different porous materials. In the recent years several examples have started to be explored and display the potential interest of more detailed studies. Furthermore, In-situ imaging of fluids in materials such as cement, concrete, or of water and oil in reservoir rocks should in fact have clear practical interest and help to better understand the behaviour of fluids in porous media. MRI is relied on nuclear spin, which is an essential property of elementary particles. The MRI principles and theory are explained in chapter 3.

The components of MRI system including [18, 19]:

1. Primary magnet: The biggest and most important component of MRI system. Field refers to the strength of the static permanent field for example at 0.3 to 1.5 T in medicine. In scientific applications in higher, in our example is 14 T (LEMMA).
2. Gradient magnet: generate secondary magnetic fields over the primary field. They are located within the bore of the primary magnet and arranged in opposition to each other to produce positive and negative poles. The arrangement of these gradient coils gives MRI the capacity to image directionally along the Z, X and Y-axis.
3. Shim coil: it is the process of adjusting the magnetic field to make it more uniform. The homogeneous magnet is one of the requirements to achieve good imaging.

4. The Radio Frequency or RF coils: they are used for transmitting the radio frequency or RF pulse and receiving signals in MRI. They come in many designs altered to best suit each material part and all aiming to improve signal-to-noise ratios to produce the best possible diagnostic images.
5. The computer system receives the RF signal and performs an analog-to-digital conversion. The digital signal representing the imaged material part which is stored in the temporary image space or k-space. The k-space stores digitized NMR signals during data acquisition. The digital signal is then sent to an image processor where a mathematical formula called Fourier Transformation is applied as the image of the MRI scan is displayed on a monitor.

Figure 1.4 is the schematic diagram of MRI machine components.

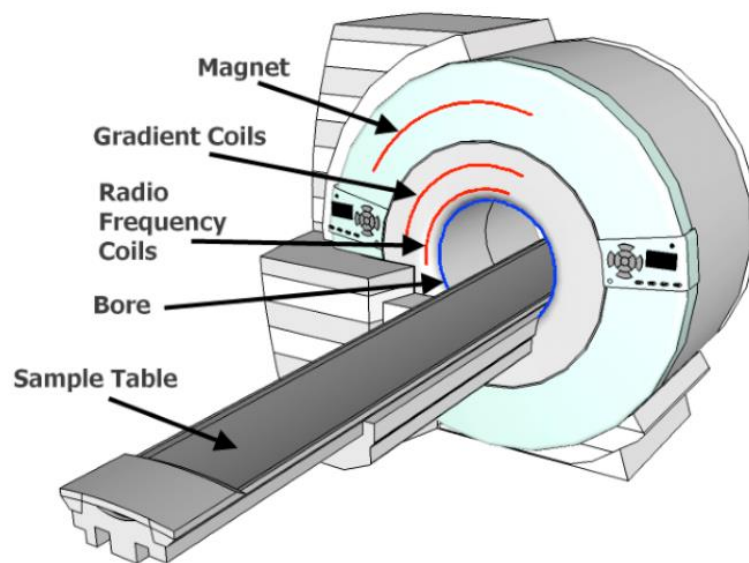


Figure 1.4. Schematic diagram of an MRI machine [20].

Magnetic resonance imaging has been used in porous media researches to characterize the main properties like grain size and porosity, to determine fluid distribution and saturation, to define water and oil flow patterns, front displacement and fluid velocities. The maximum MR imaging resolution of sample is on order of mm's (a few of tens of microns). This MRI resolution depends on the MRI device specifications, sample size and sample characteristics. In the following sections there are some examples given about MRI application in porous media.

Figure 1.5 shows A Typical MRI image of octanol ganglia entrapped within the water-saturated packing of glass beads as per presented by Johns et al. [10].

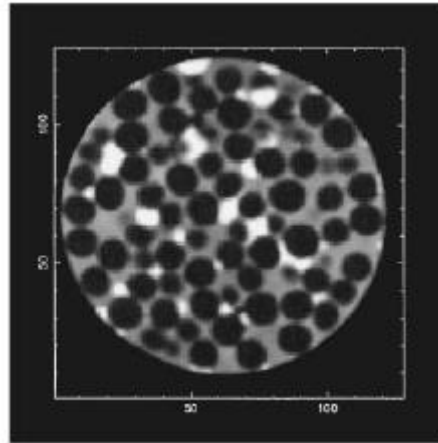


Figure 1.5. Typical MRI image of octanol ganglia entrapped within the water-saturated packing of glass beads [10].

The main MRI applications in porous media are:

Porous Media Characterization: Pore size distribution and grain size distribution all have been studied using NMR or MRI techniques, such as: characterization of structural inhomogeneities in porous media [21]; determining the pore sizes by using an internal magnetic field [22]; determining multiple length scales in rocks [23].

NMR studies of adsorbates that specifically give information on the pore space, and the technique of relaxation time measurements that have been widely used to characterize porous solids. Moreover, the pulsed field gradient methods can be used to probe the local structure of the pore space and to characterize transport within it. Such as: Characterization Visualizing the internal physical characteristics of carbonate sediments with magnetic resonance imaging and petrography [24].

NMR technique can be applied to measure the pore size distribution in partially saturated porous media, for example: the internal magnetic field distribution, and single exponential magnetic resonance free induction decay, in rocks [25]. New method was presented to directly characterize the averaged pore size of a porous sample with a narrow pore size distribution that based on the parallel plates pore model and the T2-T2 correlation sequence, such as a new research in 2019 about the characterization of porous media by T2-T2 correlation beyond fast diffusion limit by Zhou Yu et al. [26].

Fluid Distribution and flow: MRI technique has been applied to measure the fluid distribution, saturations and observation of multi-phase flow in porous media, for example, studying of the dissolution kinetics of octanol in porous media [10]; numerical simulation of water flow in three-dimensional heterogeneous porous media observed in a magnetic resonance imaging experiment [27]; two phase flow experiment of CO₂ and water [28].

In some cases, and conditions, MRI able to probe monophasic flow velocity within the inter-particle space of a packed bed, such as: three-dimensional velocity measurement of complex interstitial flows through water-saturated porous media by the tagging method [29]; NMR imaging of water flow in packed beds [12]; Pore structure and liquid flow velocity distribution in water-saturated porous media [30].

MRI has its capacity to give unprecedented quantitative information about fluid-phase distributions in porous media, Teng et al. (2017) are able to Study density-driven convection in porous media [31].

In recent researches (2019), a method for under-sampling and compressed sensing of 3D spatially resolved propagators is presented and demonstrated for flow in a packed bed and a heterogeneous carbonate rock [32].

The advantages and disadvantages of MRI can be summarized in the following points:

- MRI image analysis would have the advantage of determining the pore distribution and network structure to characterize the interstitial flow through the porous media.
- In porous media from pore to continuum scale the MRI can immediately image 1D to 3D processes that occur. The MRI signal is created directly from solid or fluid phase, which is different from other imaging techniques. To recognize different chemical species of interest the external magnetic field and gradient can be manipulated in a diversity way.
- In terms of spatial and temporal resolution, MRI has the characteristic of flexibility. When higher spatial resolution is needed 3D volumetric imaging can be utilized to obtain up to ten micron of resolution, and fast imaging pulse sequences such as slice by slice imaging in 2D that is obtainable to capture transient effects on the time scale of seconds.
- There are a number of MRI disadvantage, first the researchers need to use porous media materials with low levels of ferromagnetic materials because MRI signal attenuated by these ferromagnetic materials like glass beads, silica gel, quartz sand, or limestone, and by paramagnetic species when present in enough quantities.
- Second, the spatial and temporal resolutions of MRI are restricted to the magnetic field and gradient strength; a stronger gradient is wanted for faster imaging or higher spatial resolution.
- Third, the image resolution is balanced with sample size (because the MRI probe must image all the object, and size of voxels must be sufficiently large to have enough signal), which means the accurate resolution is gained with smallest samples.
- Forth, MRI needs a magnetic resonance device, which is very expensive and difficult to operate and maintain.

1.4 MRI comparison to other visualisation techniques

In this section we present a comparison between MRI and the main experimental techniques which have been used to visualise the fluids distributions inside porous media. We present the basic principles of these methods, compare its advantages and drawbacks, and we give several examples of its applications performed in some recent and old researches.

Optical Imaging: They are many techniques of using optical methods to image fluid flow in porous media, and the most common used methods is the visible light which is used to image processes that are visible to aided or unaided eye. Most optical imaging application use cameras (CCD) to digitally record incident light, in some cases the microscopes must be used in combination with cameras for better image resolution (Fig. 1.6), for instance to visualize the flow path in pore-scale.

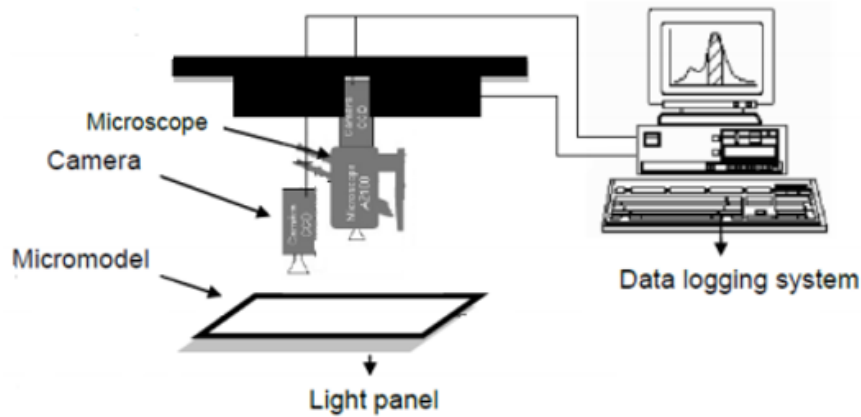


Figure 1.6. Schematic diagram of an optical imaging system [33].

Optical imaging has been employed to measure fluid distribution, saturations, velocities, and also to study fluid flow in 2D cells filled for example with glass beads or sands. Different models of optical imaging applications including recent researches such as: studying immiscible fluid displacement in glass bead packing [34]; glass bead micromodel study of solute transport [35]; investigation of two-phase flow in a micro-pillar microfluidic device [36]; use of micromodels to study multiphase flow in porous media [37], Figure 1.7 shows the CCD image of dissolution of toluene blobs in the micromodel [33]. This technique of imaging has also been used in 2D model networks to test and quantify the average velocity and transport parameters of tracer plumes in saturated porous media [38].

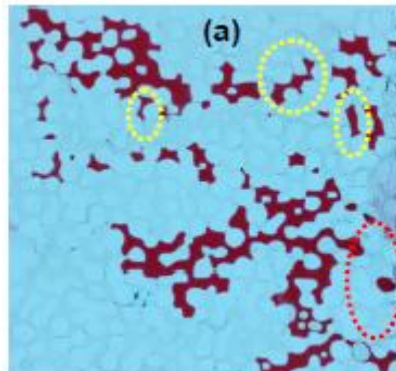


Figure 1.7. CCD Image of dissolution of toluene blobs in the micromodel [33].

The advantages of direct optical imaging methods are inexpensive, high spatial resolution, and real time imaging with low acquisition time and highly sensitive. Beginning with direct imaging with a CCD camera and moving to microscopic techniques, the cost of tools the image resolution and the cost of tools increases. In addition, the higher the imaging resolution, the lower is the field of view.

Microscopic resolution is approximately $0.5 \mu\text{m}$, while the resolution using a digital camera and a macro objective is on the order of $10 \mu\text{m}$. The field of sight is usually 100 to 1000 times bigger than the image resolution. The resolution of optical imaging is restricted by the wavelength of light, the required field of sight, and the pixel density of the digital camera, except the fluorescent particles that can project an image much bigger than their real size because of light diffraction (i.e., outshining) [39].

The main disadvantage of optical imaging is that sample porous media, or very simple representations of heterogeneity are usually utilized. Moreover, optical methods are restricted to translucent media too, which are an obvious exception in natural environments. Quantification of processes requires a calibration of the fluorescence signal, which is second challenge. Set of factors can cause variations in light intensity such as a nonuniform light source, dirt on flow cell substrates, variable packing density in a flow cell, imperfections or background light, and photo-bleaching. Great care must be taken to remove or correct these problems. Comparison with other visualization techniques, optics can then be used to study a very restricted types of porous media.

X-ray tomography or Microtomography (XMT): It is a non-invasive and non-destructive imaging technique has expended rapidly in the recent years. The method is form on mapping the spatially-distributed differential absorption of an X-ray beam as it passes through the sample. The amount of absorption relies on sample structure and capacity of the X-ray. More X-rays can be absorbed with the materials of high atomic mass, (e.g. rock vs. water) will reduce the X-rays to different degrees. This lets one material to be distinguished from another material. The energy of the beam can be tuned to image specific elements, as a result reinforcing resolution. The X-ray beam is highly collimated, which moreover enhances resolution. Absorption-based microtomography is the most widely used method for subsurface science. Other synchrotron X-ray tomography methods have been employed, such as tomographic X-ray fluorescence [40].

The transmitted X-rays are transformed to visible light with a single-crystal scintillator, and brought down onto a surface. A photograph of the image on the surface is then taken with a high-resolution CCD camera. This image exemplifies a 2D depth-integrated grayscale map of the linear attenuation of the X-ray beam as it transited through the sample.

Figure 1.8 shows the schematic diagram of X-ray scanning device.

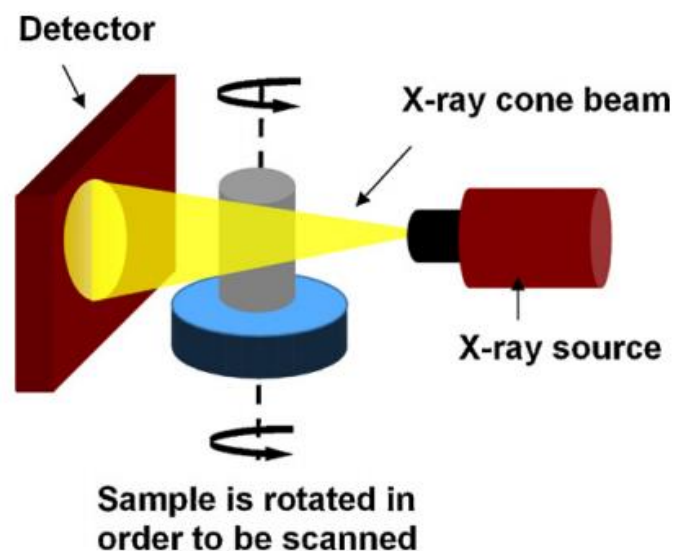


Figure 1.8. Schematic diagram of X-ray scanning device [42].

X-ray computed tomography (CT), has been used to visualize oil, water and gas internal natural rocks, and measure residual saturations from X-ray attenuation [43]. It has been used for more than twenty years in subsurface science fields. It has seen noteworthy use to describe porous-media structure and fluid-displacement processes. Standard X-ray CT has also been applied in the environmental field, for instance, to investigate the infiltration and subsequent immobilization of NAPL in saturated heterogeneous media [44].

Associated resolutions range from 100's to 1000's of μm . In general, the X-ray computed tomography method is restricted to producing measurements of fluid saturation and describing porous-media structure and fluid distributions at the macroscopic scale. It is possible to represent individual fluid bodies and to measure fluid-fluid interfacial areas in natural porous media, with resolutions ranging from 1 to 10 μm using synchrotron X-ray microtomography, this resolution permits the method to be used for quantitative characterization of the pore network and fluid distributions for many natural materials, which is mostly the greatest resolution among the imaging methods that are applied to 3D systems [39].

The initial application of X-ray computed tomography in porous media was focused on pore characterization, such as: porosity imaging in porous media using synchrotron tomographic techniques [40]. But it has been also used to test fluid flow under immiscible-displacement, there are several studies including recent researches: visualization of three phases in porous media using micro computed tomography [45]; study on mechanism of two-phase flow in porous media using micro focused X-ray CT [46].

Figure 1.9: Example of CT image for the dry core, the solid is denoted by white and the pore space by black.

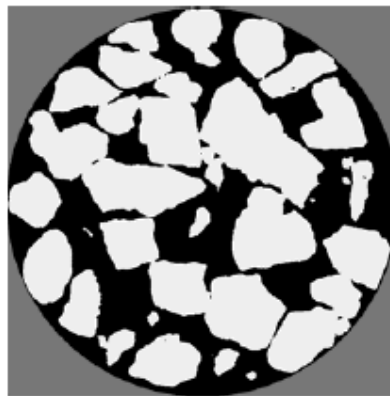


Figure 1.9. Typical CT scan image, where the solid is denoted by white and the pore space by black [43].

The drawbacks of the X-ray method compared to MRI come from the contrast source of the technique: X-rays are sensitive to atomic mass differences only, whereas MRI is sensitive to physico-chemical properties of fluids (especially the mobility of the molecules between them). The other main difference is the choice of the orientation in a 2D plane image: MRI can be obtained directly using a selection gradient (orientable in any direction), while X-ray has two steps, first the total information is collected on the total volume and later they are analysed to get the desired direction [47].

1.5 Conclusions

Understating of two-phase flow in porous media is very important for many engineering systems such as petroleum industry. More than 40-50% of oil in place in most reservoirs are not produced yet. This economic amount needs more investigation and experimental work using new powerful visualisation systems and methods.

Non-invasive imaging methods including MRI have a unique technology for visualizing and imaging different fluid flow in porous media. They provide valuable insights about the architecture of the porous structure and a variety of fluid movement process. MRI is one of the best methods compared to with others to be used in experimental stages, and in addition to high spatial resolutions.

For spatial resolution, many experiments have been conducted using packing beds with a grain diameter of several millimetres. In order to study the displacement parameters, taking into account in particular the capillarity effects that are organized at the pore scale, the porous media should be more representative of the reality of rocks. Therefore, we have use beads of around 0.4 mm and sands of around 0.13 mm in our research.

2. Two-phase flow in porous media

| | | |
|-------|---|----|
| 2. | TWO-PHASE FLOW IN POROUS MEDIA..... | 35 |
| 2.1 | Introduction..... | 37 |
| 2.2 | Basic elements..... | 37 |
| 2.2.1 | Porous medium..... | 37 |
| 2.2.2 | Fluid viscosity..... | 38 |
| 2.2.3 | Wettability..... | 39 |
| 2.2.4 | Interfacial tension..... | 41 |
| 2.3 | Flow equations in permeable media..... | 42 |
| 2.3.1 | Capillary pressure..... | 42 |
| 2.3.2 | Leverett J-Function..... | 43 |
| 2.3.3 | Governing equations for two-phase displacement..... | 44 |
| 2.3.4 | The competition between forces..... | 46 |
| 2.4 | Conclusions..... | 47 |

2.1 Introduction

The objective of the present thesis is to characterize a displacement process in porous space. Therefore, it is important to mention some notions concerning porous media, fluid properties and general flow equations. For example, the oil reservoirs systems are an example of a porous medium, and it is very important to the petroleum engineers to understand the fluid flow and recovery process in this structure, in order to enhance the hydrocarbon recoverable methods and increase the company profits.

2.2 Basic elements

This section is a brief introduction to the basic concepts of the porous medium, and the important elements of fluid properties are presented. Typically, porous media consists of solids and fluids, two or three phases, which are competing with each other to occupy more space. However, the heart of our study is interested in two-phase flow of water and oil (wetting and non-wetting) without taking in consideration the presence of gas/air phase.

2.2.1 Porous medium

A porous medium is a solid material interspersed with void spaces (pores) of different sizes filled with a fluid such as water, oil, air etc. Many natural substances such as: sandstone, limestone, bones, wood and man-made material such as cements can be considered as porous medium. The porosity φ is the main characteristic property of porous medium, and it is the ratio of pore space to the total volume of sample, and reflects the fluids storage capacity:

$$\varphi = \frac{\text{Volume of pore space}}{\text{Total sample volume}} = \frac{V_{pores}}{V_{pores} + V_{matrix}} \quad (2.1)$$

where V_{pores} is the volume of void space and V_{matrix} is the volume of solid matrix.

The other most important property of the porous media is the permeability K , it describes the capacity and ability of the porous media to transmit fluids. The permeability It can be derived from the medium porosity, solid matrix and pore size distribution. But, such indirect measurement can be complicated with a range of uncertainty.

The total porosity is the total void space of the medium, and the effective porosity is the void space that contributes to the flow of fluids. Usually, both types of porosity can be determined in laboratory and used for fluid flow calculations [48]. Oil reservoir porosities are in the range of 5 % to 40 % in sandstones and from 5 % to 25 % in carbonates [49, 50, 51].

The porous media is considered in two different length scales:

- First, the pore scale (or microscopic scale) taking in account the average radius of the pore and grain size. Study of two-phase flow in this scale length is not easy task due to

the effect of different forces such as capillarity, gravity, viscosity and wettability of the two phases. In our case it is the pore size of the sample.

- The second length scale is Darcy scale (or macroscopic scale), taking in account the average parameters of porous media such as saturation, porosity and permeability. Figure 2.1 shows porous media different scales.

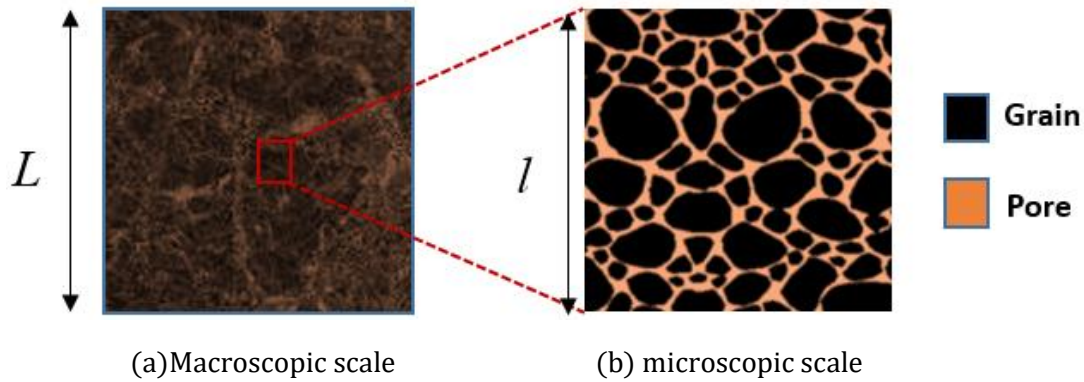


Figure 2.1. Scale of porous media.

In this thesis we study two-phase flow water/oil in a sample of porous media of different wettabilities of material.

2.2.2 Fluid viscosity

Since the fluid viscosity is widely introduced in literature, only a brief quantitative description will be mentioned in this section. Viscosity is a fluid property that is very important for fluid flow through pipes or porous media, and it could be define as a measure of fluid's resistance to flow. For example, the water is easier to pass through a tube than the oil, because water has less viscosity. Fluid viscosity can be abstracted by quantifying the forces of frictional that appear between adjacent fluid layers that are in relative motion. Although this phenomenon becomes more complicated when it comes to the fluid flow in porous media, it is an essential parameter that controls the two-phase flow in porous media.

Consider a fluid trapped between two large parallel plates separated by a fluid layer (Fig. 2.2). The bottom one is fixed and the upper plate moves in parallel at a constant velocity U . If the top plate velocity is low (laminar flow case), then the fluid moves in parallel layers with different speeds. In many fluids, the fluid velocity varies from zero on the bottom plate to U at the top. The force F applied to the top plate is proportional to the velocity U , and the area A of the plates.

$$F = \mu A \frac{U}{y} \quad (2.2)$$

where μ is fluid dynamic viscosity in Pa. s, and A is the area of the plate. The term U/y is called shear deformation rate (shear velocity). Term F/A is called shear stress τ and it is proportional to the velocity gradient [52].

$$\tau = \frac{F}{A} \propto \frac{dU}{dy} \quad (2.3)$$

$$\tau = \mu \frac{dU}{dy} \quad (2.4)$$

The kinematic viscosity is also defined as:

$$\nu = \frac{\mu}{\rho} \quad (2.5)$$

where ρ is the density of fluid.

The case mentioned above corresponds to the calculation formula of the shear stress for Newtonian fluids, and many common fluids are Newtonian. The situation is more complicated if the fluid is non-Newtonian.

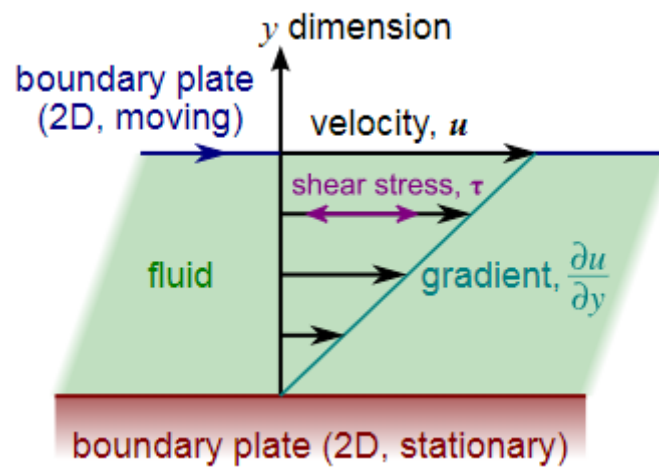


Figure 2.2. Behaviour of a fluid placed between two parallel plates, when a force F is applied on the upper plate, it will move continuously with a velocity u . The bottom plate is fixed. The arrows indicate the linear velocity gradient in the Y-direction [53].

In a two phase flow system, the viscosity of the fluids is customary to define the mobility ratio M :

$$M = \frac{\mu_{nw}}{\mu_w} \quad (2.6)$$

where μ_{nw} and μ_w describe the viscosities of non-wetting and wetting fluid respectively. The concept of wettability will be discussed in in the next section.

2.2.3 Wettability

Wettability is the ability of a fluid to spread on the surface of the solid or to stick on it in the presence of another immiscible fluid. Wettability plays an important role in the flow displacement process. When the liquid droplet is in contact with a solid surface, it can take different shapes, according to the contact properties between fluids and the solid surface. The contact angle (wetting angle) is a quantitative measure of the surface wettability. This is the angle that a liquid interface makes with a solid surface.

Therefore, the wetting description term is based on this contact angle θ :

$$0^\circ < \theta < 90^\circ \Rightarrow \text{wetting}$$

$$90^\circ < \theta < 180^\circ \Rightarrow \text{non-wetting}$$

Idealized examples of contact angle are presented as following:

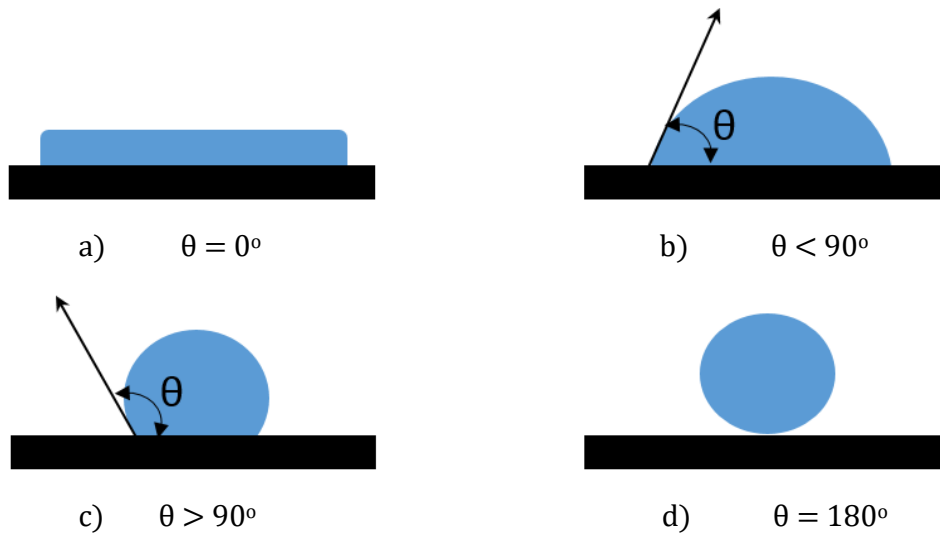


Figure 2.3. Degree of wettability based on the contact angle between a smooth solid surface (black colour) and a liquid (blue colour): a) spreading or complete-wetting, b) good wetting, c) incomplete or low wetting and d) no-wetting.

According to figure 2.3, the liquid has a high wettability if the contact angle less than 90° , and a low wettability if the contact angle greater than 90° .

Table 2.1 provides more detailed information on contact angles for different wettabilities.

| Wettability preference | Contact angle, degree |
|------------------------|-----------------------|
| Strongly water wet | 0 - 30 |
| Moderately Water-wet | 30 - 75 |
| Neutrally Wet | 75 - 105 |
| Moderately Oil-wet | 105 - 150 |
| Strongly oil-wet | 150 - 180 |

Table 2.1. Illustrates detailed wettability preference expressed by contact angle [54].

When two fluids are presented in the pore space, one of them is preferentially attracted by the surface of the solid skeleton. It is called the wetting fluid (or phase), while the other phase is called non-wetting fluid. Moreover, if water has a high affinity to the solid surface the solid is hydrophilic ($\theta < 90^\circ$), otherwise the solid is hydrophobic ($\theta > 90^\circ$). In our research we investigate both wettability systems. But we pay more attention to hydrophilic system, as it is more widespread in nature. In the following the term wetting phase will be used as a synonym for water and the term non-wetting phase—as a synonym for oil.

Wetting properties have an important impact on the recovery factor during two-phase flow displacement in porous media. And any changing in these properties could alter the displacement process (Fig. 2.4).

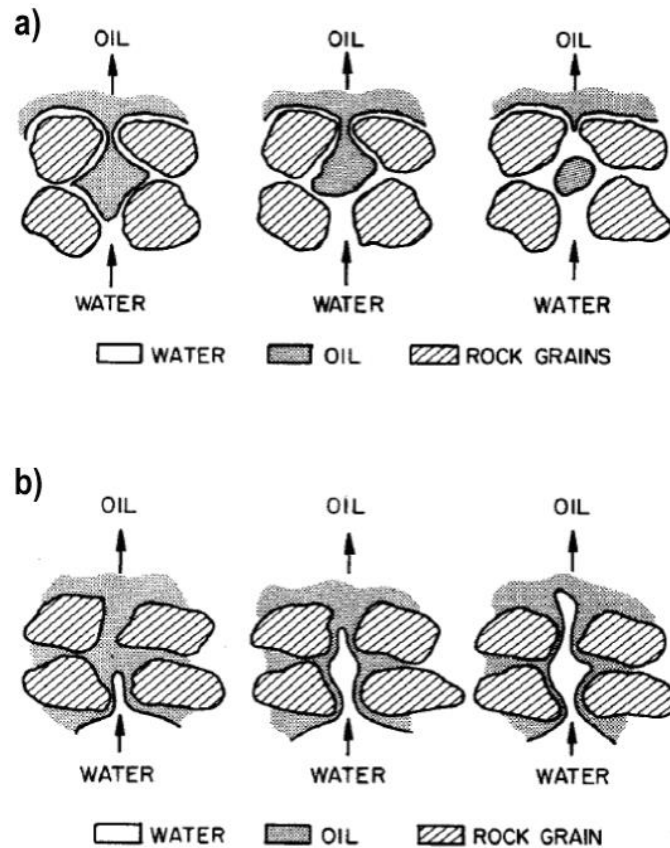
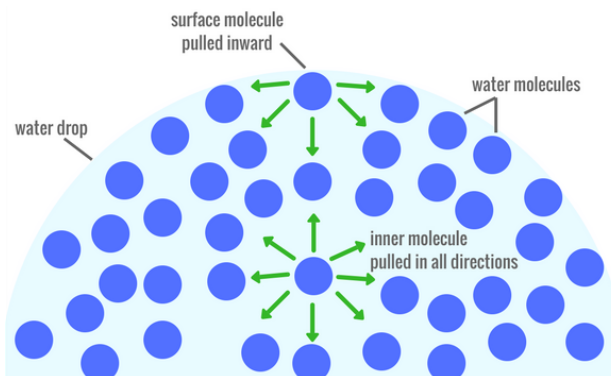


Figure 2.4. Water displacing oil in porous media; (a) water-wet system (hydrophilic), and (b) oil-wet system (hydrophobic) [55].

2.2.4 Interfacial tension

When two immiscible liquids come into contact with each other, the molecules of the two phases undergo unbalanced attraction forces. This imbalance creates interfacial tensions. It will be noted that the surface tension is the property of the liquid in contact with gaseous phase, usually air.

The interfacial surface tension is measured in force per unit length (mN/m), and noted by the character σ . The interfacial tension occurs due to the imbalance of the molecular attraction forces experienced by the molecules on the surface. Figure 2.5 shows an example of interfacial tension in water droplet.



Ref: <https://yellow-scope.com>

Figure 2.5. Interfacial tension in water droplet.

Therefore, interfacial tension is a crucial parameter in the fluid displacements process, and the evaluation of solid wettability can be made through measurements of interfacial tension. In case of two fluids and solid, tension acts at the interfaces of liquids and solid surfaces.

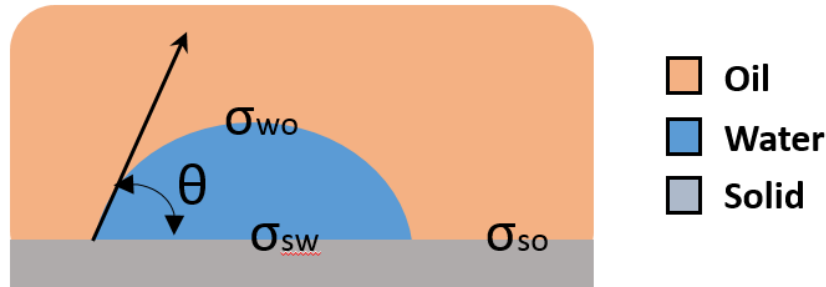


Figure 2.6. Contact angle between water and oil formed on a water-wet solid surface.

From figure 2.6,

$$\cos \theta = \frac{\sigma_{so} - \sigma_{sw}}{\sigma_{wo}} \quad (2.7)$$

where, σ_{wo} is the interfacial tension between water & oil, σ_{sw} the interfacial tension between solid and water, and σ_{so} the interfacial tension between solid and oil.

At standard conditions, the interfacial tension between water and air is [0.073 N/m] and between oil and water about [0.03 N/m]. In our study the interfacial tension between water and PTX2000 fuel (oil phase) is [0.05 N/m] [56].

2.3 Flow equations in permeable media

In this section we present the essential equations that govern fluid flow in permeable media. Starting by introducing the capillary pressure saturation relationship, and then we introduce the classical approach of Buckley-Leverett theory, where two fluids are considered as immiscible.

2.3.1 Capillary pressure

Capillary pressure is the pressure difference existing across the interface separating two immiscible fluids. If the wettability of the system is known, then the capillary pressure will always be positive if it is defined as the difference between the pressures in the non-wetting (oil) and wetting (water) phases.

$$\Delta p = p_c = p_o - p_w = \frac{2 \cdot \sigma_{ow} \cdot \cos \theta_{ow}}{r_c} \quad (2.8)$$

Where r_c is the tube radius. If we have a capillary tube or a rock sample that contains 100% saturation of non-wetting fluid (oil) and we introduce a wetting fluid (water) to the inlet, the capillary pressure will draw the wetting fluid into the tube or the pores of the rock spontaneously. If the pathway is down or horizontal this process can continue as long as there is more tube or rock for the wetting fluid to fill. If the pathway is upward or vertical, the process will continue until the capillary force pulling the fluid into the tube or rock pores is balanced by the gravitational force acting on the suspended column of fluid. The two

expressions for capillary pressure in a tube, one in terms of height of a fluid column and the other in terms of the radius of the capillary tube can be combined to give an expression for the height of a fluid column in terms of the radius of the tube as follows:

$$h \cdot \rho \cdot g = \frac{2 \cdot \sigma \cdot \cos \theta}{r} \quad (2.9)$$

Therefore, for an oil-water system,

$$h_w = \frac{2\sigma_{ow} \cos \theta}{r(\rho_w - \rho_o)g} \quad (2.10)$$

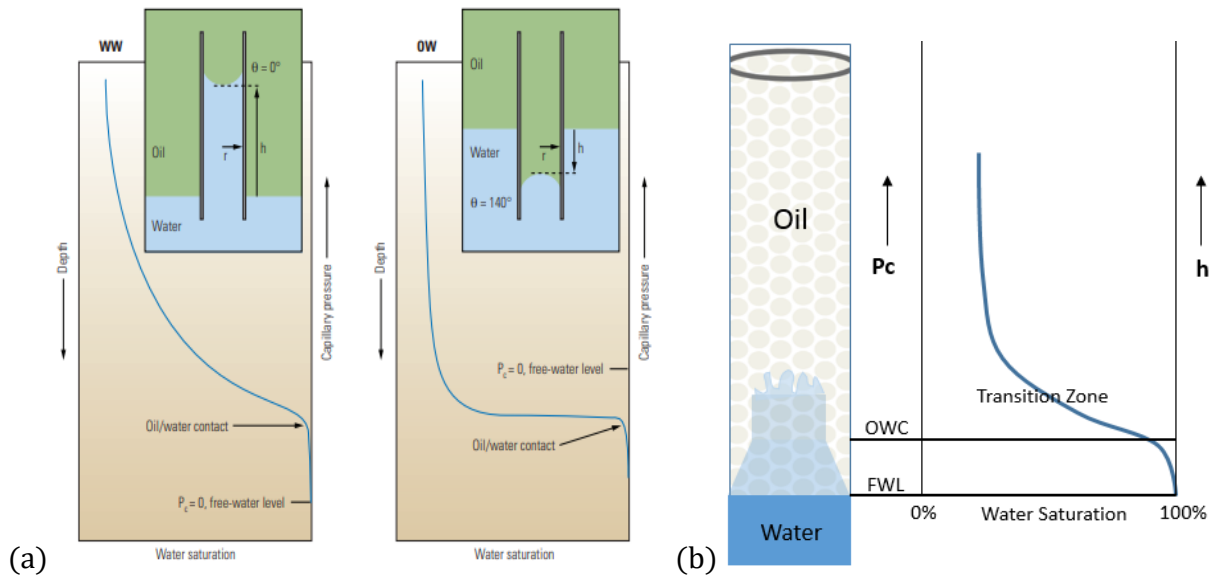


Figure 2.7. (a) capillary pressure curve in water wet (ww) and (ow) systems [57]; (b) expected fluid distribution in packed beads sample based on the capillary pressure curve.

2.3.2 Leverett J-Function

Capillary pressure data are obtained on small core samples that represent an extremely small part of the reservoir and, therefore, it is necessary to combine all capillary data to classify a particular reservoir. The fact that the capillary pressure-saturation curves of nearly all naturally porous materials have many features in common has led to attempts to devise some general equation describing all such curves. Leverett (1941) approached the problem from the standpoint of dimensional analysis [58].

Realizing that capillary pressure should depend on the porosity, interfacial tension, and mean pore radius, Leverett defined the dimensionless function of saturation, which he called the J-function, as:

$$J(S_w) = \frac{P_c}{\sigma \cos \theta} \cdot \sqrt{(K/\phi)} \quad (22.11)$$

where, K is the permeability, σ is the interfacial tension (dynes/cm), ϕ is the porosity.

In doing so, Leverett interpreted, the ratio of permeability, K , to porosity, φ , as being proportional to the square of a mean pore radius. The J-function was originally proposed as a means of converting all capillary pressure data to a universal curve. There are significant differences in correlation of the J-function with water saturation from formation to formation, so that no universal curve can be obtained. For the same formation, however, this dimensionless capillary-pressure function serves quite well in many cases to remove discrepancies in the P_c versus S_w curves and reduce them to a common curve. The J-function of Leverett was obtained from the experimental studies and seems to be universal for the unconsolidated rocks.

2.3.3 Governing equations for two-phase displacement

The governing equations for the two-phase flow in porous media are obtained by applying the theory of mass conservation to the Darcy-scale representative elementary volume (R.E.V.), as provided by Szymkiewicz in the following equations [59].

The mass balance equation for two phases becomes:

$$\frac{\partial}{\partial t}(\rho_i \cdot S_i \cdot \varphi) + \nabla(\rho_i \cdot V_i) = 0 \quad (2.12)$$

where i is the index of phase, namely $i = o, w$; ρ is the density; S is the saturation; φ is the porosity; V is the Darcy velocity. The velocity of each fluid phase with respect to the solid phase is given by the Darcy formula:

$$\begin{cases} V_w = -\frac{K k_w}{\mu_w} \text{grad}(p_w + \rho_w g z) \\ V_o = -\frac{K k_o}{\mu_o} \text{grad}(p_o + \rho_o g z) \end{cases} \quad (2.13)$$

where μ is the dynamic viscosity; P is the pressure; K is the intrinsic permeability of porous medium; k_r is the relative permeability; g is the gravitational acceleration; z corresponds to the vertical coordinate.

Substituting Darcy equation into the mass balance equation for both phases results in the following system of two combined partial differential equations:

$$\frac{\partial}{\partial t}(\rho_w S_w \varphi) - \nabla \left[\frac{\rho_w K k_{rw}}{\mu_w} (\nabla p_w - \rho_w g) \right] = 0 \quad (2.14)$$

$$\frac{\partial}{\partial t}(\rho_o S_o \varphi) - \nabla \left[\frac{\rho_o K k_{ro}}{\mu_o} (\nabla p_o - \rho_o g) \right] = 0 \quad (2.15)$$

The oil saturation is uniquely defined by the water saturation (or vice versa):

$$S_w + S_o = 1 \quad (2.16)$$

The water saturation is a function of the capillary pressure. The capillary pressure P_c at any point of the porous medium denotes the difference between the P_o and P_w (Eq. 2.8).

There are many possibilities to select the primary unknown variables. It is possible to choose the fluid pressures, P_o and P_w , and compute the P_c and the fluid saturations. However, such a formulation cannot be used in the numerical solution if the oil phase disappears completely from the pore space. Therefore, it is better to choose one of the fluid pressures and one of the saturations as the primary unknowns, e.g. Since this study focuses on water flooding, the water saturation S_w and water pressure P_w are chosen as the primary variables.

Then the equations (2.14) & (2.15) can be rewritten in order to display the dependency of each term on the primary variable chosen.

$$\frac{\partial}{\partial t} (\rho_w(p_w) S_w \varphi) - \nabla \left[\frac{\rho_w(p_w) K k_{rw}(S_w)}{\mu_w} (\nabla p_w - \rho_w(p_w) g) \right] = 0 \quad (2.17)$$

$$\begin{aligned} & \frac{\partial}{\partial t} (\rho_o(p_w, S_w) (1 - S_w) \varphi) \\ & - \nabla \left[\frac{\rho_o(p_w, S_w) K k_{ro}(S_w)}{\mu_w} (\nabla p_w + \nabla p_c(S_w) - \rho_o(p_w, S_w) g) \right] = 0 \end{aligned} \quad (2.18)$$

If the compressibility of porous media and the fluid are neglected (no variation of fluid density), this hypothesis can be accepted in our case for the displacement process of oil by water at the ambient conditions, then the governing equations can be simplified as following:

$$\varphi \frac{\partial S_w}{\partial t} - \nabla v_w = 0 \quad (2.19)$$

$$-\varphi \frac{\partial S_w}{\partial t} - \nabla v_o = 0 \quad (2.20)$$

Then, the above equations can be transformed into the fractional flow equation:

$$\nabla (v_w + v_o) = \nabla v_t = 0 \quad (2.21)$$

where v_t is the total fluid velocity.

By using water and oil velocities, fractional flow function can be expressed as:

$$F(S) = \frac{V_w}{V_{tot}} = \frac{v_w}{v_o + v_w} \quad (2.22)$$

$$V_w = V_{tot} * F(S) \quad (2.23)$$

$$\lambda_i = \frac{K k_{ri}(S_i)}{\mu_i}, i = w, o \quad (2.24)$$

The function $F(S)$ defines a fraction of the displacing phase flux in the total flux neglecting the gravity and the capillary forces; λ_i is the i -phase mobility.

The power-type relationships between the normalized saturation and the relative permeability are defined as:

$$\begin{cases} S \leq S_{wr} : 0, & S > S_{wr} : k_{rw}(S) = \left(\frac{S - S_{wr}}{1 - S_{wr}}\right)^2 \\ S \leq S_{ro} : k_{ro}(S) = \left(\frac{1 - S - S_{or}}{1 - S_{or}}\right)^2, & S > S_{or} : 0 \end{cases} \quad (2.25)$$

where k_{rw} and k_{ro} are the relative permeability for two phases water & oil respectively.

From equation 2.8, P_o can be found as:

$$P_o = P_w + P_c \quad (2.26)$$

Inserting Eq. (2.26) into Eq. (2.13) we can add capillary pressure to the mathematical formulation. The capillary pressure between two phases varies due to fluid saturation and by using differential simplification it can be added to the equations as the function of saturation.

By simplifying all these mathematical formulations, the following equation for water saturation can be written as:

$$\varphi \frac{\partial S_w}{\partial t} - \nabla(F(S)V_{tot} - F(S)\lambda_o g(\rho_w - \rho_o) - F(S)\lambda_o \frac{dP_c}{dS} \frac{dS}{dz}) = 0 \quad (2.27)$$

Eq. (2.27) has the form of an advection–diffusion equation. The first two terms in brackets reflects the advection flow. The first term corresponds to the viscous forces (in red), the second term is the gravity forces (in green). The third term (the diffusive transport) is related to the act of capillary forces (in blue).

In advance work of two-phase flow equation, the phenomenological model with vector nature of capillarity was proposed in Panfilova and Panfilov, [13]. To describe the phase distribution this model demands two specific parameters: the volume fraction of the mobile displacing phase in the area of interface between the phases (1), and the degree of connectivity between them (2). Basing on the experimental results and the properties of the internal structure of phase distributions in the model we propose closing relations for the vector model and compare it with the classical approach.

For the model with the vector nature of capillary forces the equation 2.27 takes form:

$$\varphi \frac{\partial S_w}{\partial t} + \nabla \left(F(S)V_{tot} - F(S)\lambda_o g(\rho_w - \rho_o) + F(S)\lambda_o \gamma \eta_c \frac{P_c}{l} \right) = 0 \quad (2.28)$$

where γ is the sign of the acting of the capillary forces, which depends on the wettability of the phases; η_c is the specific concentration in meniscus or volume fraction of mobile wetting phase in the area of interface; l is the characteristic pore size; \vec{e}_c is the unit vector of capillary force.

2.3.4 The competition between forces

Two-phase displacement in porous media is a complex process, and it is difficult to provide precise solutions based on the equations mentioned in section (2.2.3) alone. Hence, we try to identify the dominant forces that drive these processes. The most important dominated forces are the viscosity, capillarity, and gravity. In fluid dynamics theory, the following main dimensional groups are usually suggested to compute the relative magnitudes of the prevailing forces in water flooding processes:

(I) Capillary number (Ca) which is defined as the ratio of the viscous forces to the capillary forces at pore scale and it is expressed as [60]:

$$Ca = \frac{d^2 v \mu_w}{K \sigma \cos \theta} \quad (2.29)$$

where μ_w is the wetting-phase viscosity, v is Darcy velocity of the injected phase through porous medium (water injection rate divided by the cross-sectional area of the porous medium), K is the intrinsic permeability, σ is the interfacial tension between wetting and non-wetting phases, θ is the contact angle and d is the average pore size.

And (II) the Bond number (Bo) which is defined as the ratio of buoyancy forces to capillary forces:

$$Bo = \frac{\Delta \rho g d^2}{\sigma \cos \theta} \quad (2.30)$$

where $\Delta \rho$ is the difference of density between the two fluids and g is the gravity acceleration.

The pore size d can be calculated as the hydraulic diameter deduced from the average grain diameter d_p and the porosity φ :

$$d = \frac{2\varphi}{3(1-\varphi)} d_p \quad (2.31)$$

The capillary number is an important parameter to determine the stability of water displacement process. For low capillary number, less than $10E-5$, flow is dominated by capillary forces [61].

2.4 Conclusions

The principles of two-phase flow in porous media related to our project are presented in this chapter. The classical approach of Buckley-Leverett is mentioned, taking in consideration the three kinetic forces. The governing equations are formulated at Darcy scale, using the capillary pressure-saturation relationship and Darcy equation for multiphase flow. These equations will be used in our work to create the simulation model.

3. Principles of Magnetic Resonance Imaging (MRI)

| | | |
|-------|---|----|
| 3. | PRINCIPLES OF MAGNETIC RESONANCE IMAGING (MRI)..... | 49 |
| 3.1 | Introduction and brief history | 51 |
| 3.2 | Nuclear magnetic moment | 51 |
| 3.3 | Magnetic Resonance Phenomenon | 52 |
| 3.4 | Acquisition of NMR signal | 55 |
| 3.4.1 | Longitudinal relaxation time T1 | 55 |
| 3.4.2 | Transverse relaxation time T2 | 56 |
| 3.4.3 | Spin-Echo sequence | 57 |
| 3.5 | NMR signal recovery and images | 59 |
| 3.6 | Conclusions..... | 61 |

3.1 Introduction and brief history

Magnetic resonance imaging (MRI) is based on the principle of nuclear magnetic resonance (NMR) discovered in 1946 by Felix Bloch and Edward Mills Purcell [62, 63, 64], both shared the Nobel Prize in Physics in 1952 for their work on the phenomenon of spin precession in a homogeneous magnetic field. In 1950 it was discovered that there is a slight change in the atomic nucleus (Larmor frequencies) caused by the chemical bonding state of the atoms. This led to idea of using NMR to analyse and identify different materials, the beginning of NMR spectroscopy. In the same year, E.L. Hahn [65, 66] proposed a spin-echo method to overcome the local inhomogeneities of the magnetic field.

In 1956, H.C. Torrey [67] revised Bloch's equations by introducing a diffusion term, R.R Ernst [68] proposed to analyse the time signals generated by pulses techniques and he was awarded the Nobel Prize in chemistry for his contributions towards the development and use of Fourier transformer.

MRI was introduced to the scientific community in 1973, when P.C Lauterbur [69] (Nobel Prize in Medicine 2003) made the first NMR images of two capillary tubes filled with water. Mansfield was jointly awarded the Nobel Prize in Medicine for the development of fast imaging techniques (echo-planar), a crucial step in making MRI a practical tool for medicine [70, 71].

In this chapter we introduce the basic of NMR/MRI; the acquisition of the resonance signal, the measurement of the T1 and T2 relaxation times, the basic sequences of MRI, the signal detection and the steps leading to the formation of the MRI image.

3.2 Nuclear magnetic moment

In NMR, the nucleus of the atom gives the information. The protons and neutrons, which are the basic structure of the atomic nucleus, revolve around their own axes. This is called the spin. The protons behave like a magnetic rod because of their magnetic properties, and a magnetic field naturally occurs around them, this sphere generates a magnetic moment that is directed along the axis of rotation with an amplitude μ .

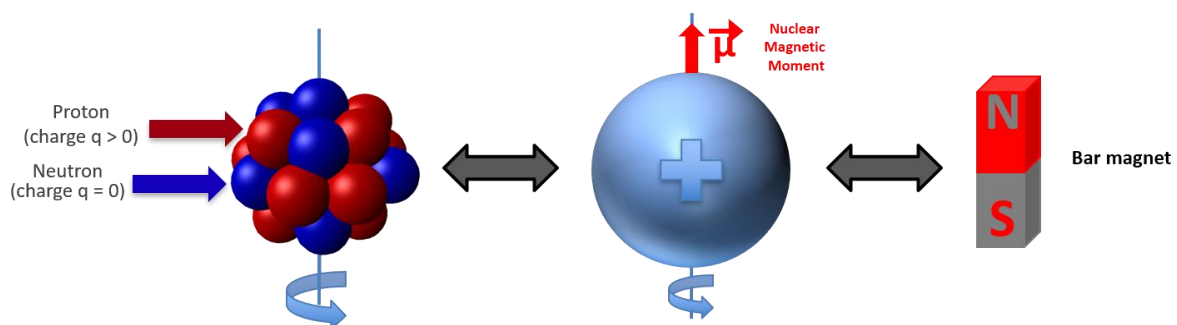


Figure 3.1. Equivalents of an atomic nucleus.

NMR can detect many nuclei as long as their spin is not null. As the hydrogen nucleus (proton) is the most sensitive and abundant, it is the most commonly used in the medical imaging domain. In the human body, 63% of the atoms are hydrogens mostly present in water and lipids. Therefore, in medical imaging, we detect mostly the protons in the cell fluids and the fat.

In the case of the study of the two-phase flow (i.e. water and oil), the nuclei of the hydrogen atoms of the H₂O molecules as well as those of the hydrogen atoms of the C-H bonds of the hydrocarbons will be observed [18].

3.3 Magnetic Resonance Phenomenon

The magnetic resonance phenomenon goes through three distinct stages:

- Polarization \Rightarrow under the effect of a static magnetic field.
- Resonance \Rightarrow disturbance using a radio-frequency field.
- Relaxation \Rightarrow return to balance condition.

Polarization [18, 72, 73]: Naturally, the protons are randomly arranged in the material to remove the influence of each other. For this reason, the vector sum of nuclear magnetic moments μ_i for this material is zero ($\sum \mu_i = 0$), figure 3.2.a. In this case, all spins are distributed on the same level of energy. Nuclear Magnetic Resonance (NMR) studies the response of atomic nuclei when subjected to an external magnetic field. Here, we apply the field along the z-axis. The protons magnetic moment is therefore oriented in the direction of the magnetic field vector (Fig. 3.2.b). Nuclear magnetic moment μ_z then takes the value of $+\mu/2$ or $-\mu/2$.

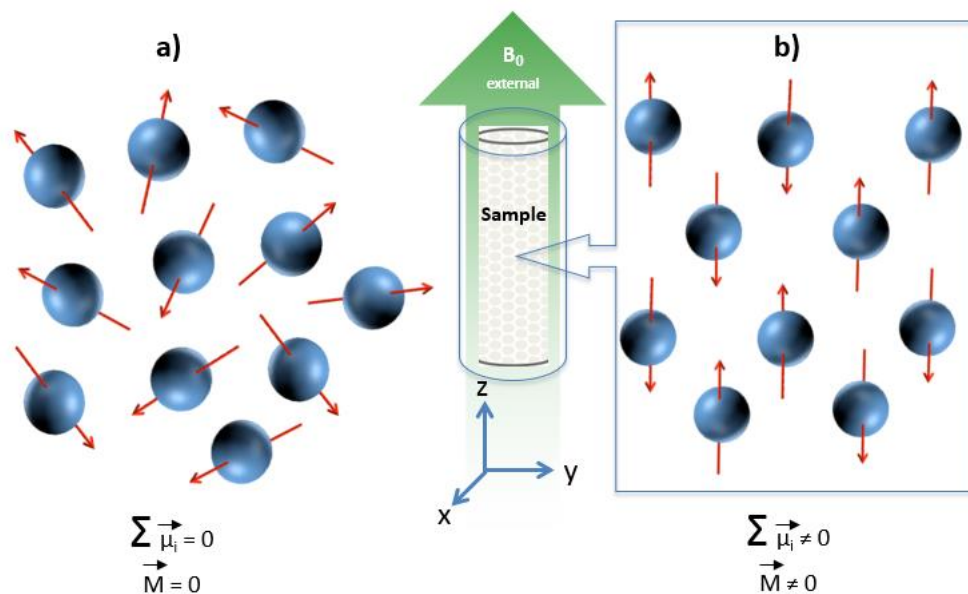


Figure 3.2. Equivalents of an atomic nucleus.

These two possible orientations involve two possible states of energy for the particles. A state called "parallel" when the particles are oriented in the positive direction of B_0 ; the interaction with the latter is then "stabilizing". A so-called "anti-parallel" state when the particles are oriented in the negative direction of B_0 ; the interaction with the latter is then "destabilizing". The distribution of the particles according to the two energy states is governed both by the effect of the interaction with B_0 and by the thermal agitation which causes the particles to vibrate.

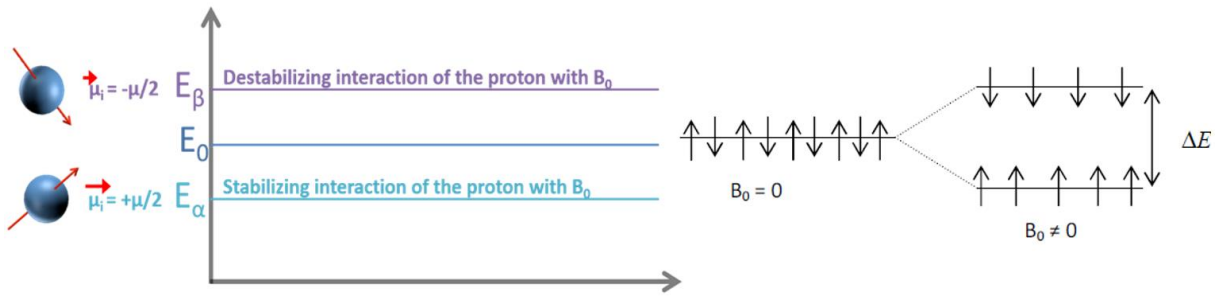


Figure 3.3. Splitting of the spin energy levels due to the application of the static magnetic field B_0 .

These two situations correspond to two different levels of energy (Fig. 3.3) whose difference is worth:

$$\Delta E = h \nu_0 \quad (3.1)$$

$$\nu_0 = \frac{\gamma B_0}{2\pi} \quad (3.2)$$

where h is Planck 's constant and ν_0 is the natural frequency of the system at equilibrium, which is called the Larmor frequency.

By making the vector sum of the nuclear magnetic moments of these particles subjected to an external field, the resultant, called nuclear magnetization M is non-zero ($\sum \mu_i \neq 0$), and oriented according to B_0 . This resultant is proportional to the number of nuclei and is the physical quantity measured by NMR.

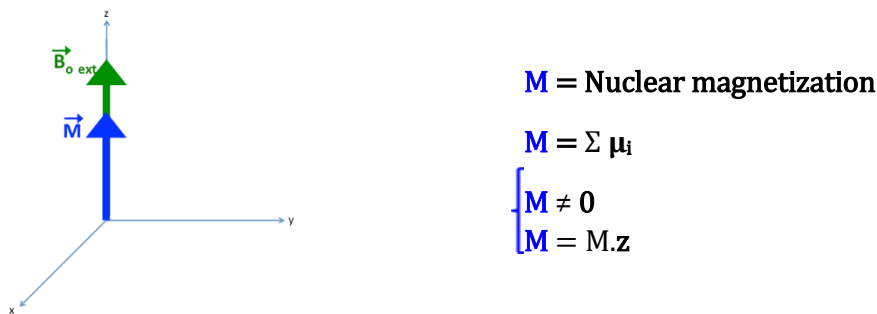


Figure 3.4. Nuclear magnetization, resulting from the vector sum of the magnetic moments.

Resonance [18, 72, 73]: In addition to being oriented in two possible ways, the spins leads to a precession motion of magnetization vector around the axis of B_0 at the speed ω_0 (Larmor frequency) when exposed to this external magnetic field.

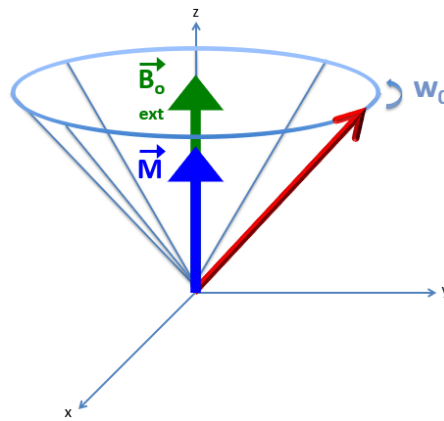


Figure 3.5. Precession movement subjected to an external magnetic field.

Larmor frequency ω_0 (Resonance frequency) is function in B_0 and the gyromagnetic ratio.

$$\omega = \gamma B_0 \quad (3.3)$$

where γ is the gyromagnetic ratio of the nucleus between the magnetic moment & the angular moment, ^1H it is defined as 42.58 MHz/T for ^1H .

However, when M is in the direction of B_0 , it cannot be measured. It is therefore necessary to switch M on the plane perpendicular to B_0 , here the plane XY .

To this effect, we apply a radiofrequency field B_1 in the XY plane (with $B_1 \approx 10^{-3} B_0$). A B_1 pulse flips the spins out of B_0 until M belongs to the XY plane.

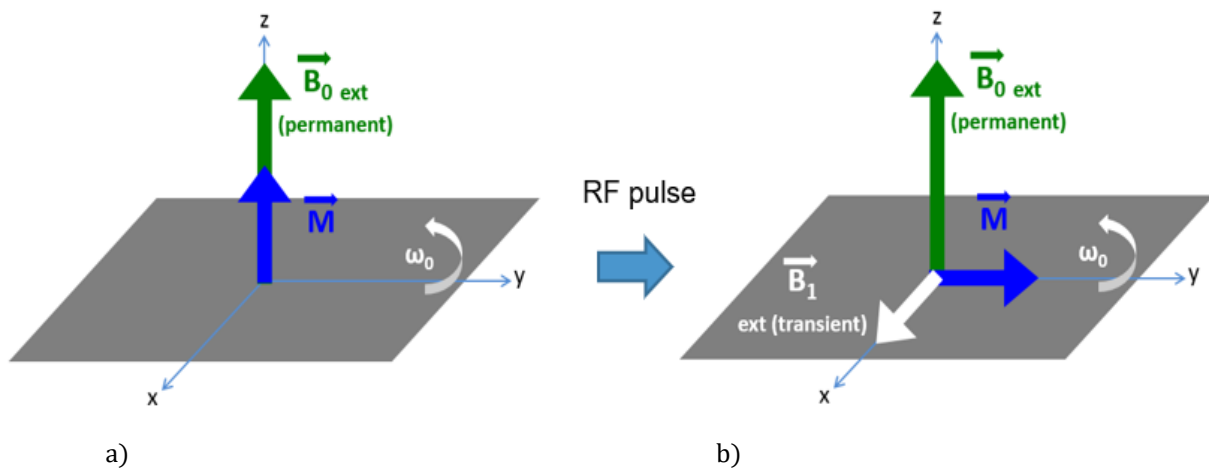


Figure 3.6. (a) Coupling B_0 and B_1 fields to achieve magnetic resonance, (b) Final position of M after a precession around the axis of magnetic field composition B_0 and B_1 .

Relaxation, Relaxation [18, 72, 73]: Once the vector M belongs to the plane XY , B_1 can be stopped to make room for the relaxation phenomenon.

Due to its permanent interaction with the external magnetic field B_0 , M returns back to its equilibrium state parallel to it. It is at this point that signal is measured, when M is initially on the XY plane and gradually returns to its initial position with a precession motion due to the interaction with B_0 .

The relaxation phenomena are governed by the Bloch equations:

$$\frac{dM_{x,y}}{dt} = \gamma(\vec{M} \wedge \vec{B})_{x,y} - \frac{M_{x,y}}{T_2} \quad (3.4)$$

$$\frac{dM_z}{dt} = \gamma(\vec{M} \wedge \vec{B})_z - \frac{(M_0 - M_z)}{T_1} \quad (3.5)$$

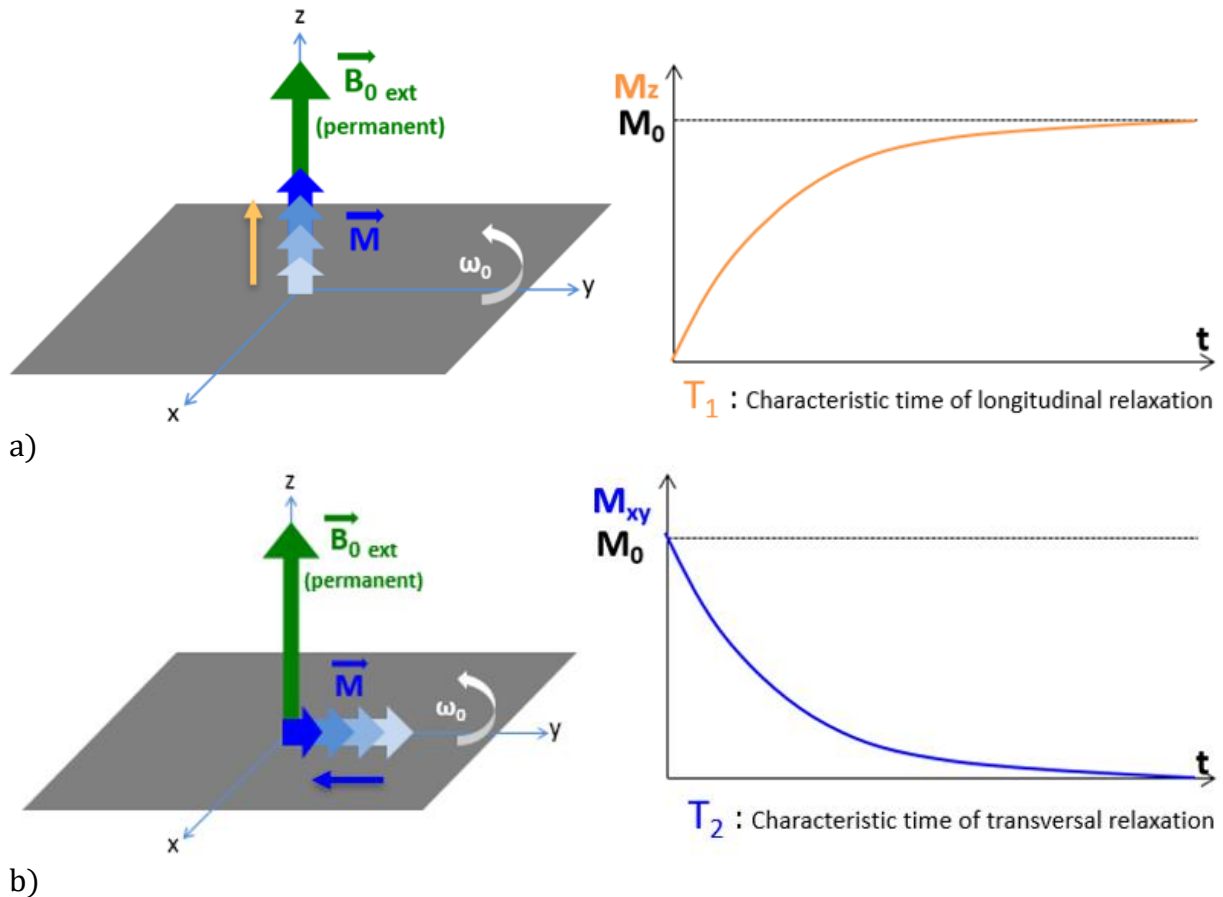


Figure 3.7. Evolution of the longitudinal (a) and transverse (b) components during the return to equilibrium of M on B0 (nuclear magnetic relaxation).

M_z and M_{xy} behave like first-order systems where we can read the characteristic times T_1 and T_2 for which the signal, respectively, is reconstructed on the axis of B_0 and is destroyed on the XY plane.

3.4 Acquisition of NMR signal

As mentioned above, two relaxation times can be measured known as T_1 and T_2 . Both times measure the spontaneous energy transfer by an excited proton, but they differ in the final deposition of the energy.

3.4.1 Longitudinal relaxation time T_1

It is the time required for the z component of M to return to 63% of its original value following an excitation pulse. It is also known as the spin-lattice-relaxation time or longitudinal

relaxation time. This return of magnetization follows an exponential growth process, with T1 being the time constant describing the rate of growth:

$$M_z(t) = M_0 \left(1 - e^{\left(-\frac{t}{T_1}\right)} \right) \quad (3.6)$$

where t is time following the RF pulse, M_0 is the net magnetization, the orientation of M_0 will be in the same direction as B_0 . After three T1 time periods, M_z will have returned to 95% of its value prior to the excitation pulse, M_0 . The term spin lattice refers to the fact that the excited proton (spin) transfers its energy to its surroundings (lattice) rather than to another spin. The energy no longer contributes to spin excitation [18].

3.4.2 Transverse relaxation time T2

It is the time required for the transverse component of M to decay to 37% of its initial value via irreversible processes. It is also known as the spin-spin relaxation time or transverse relaxation time. Recall from previous that M_0 is oriented only along the z (B_0) axis at equilibrium and that no portion of M_0 is in the XY plane. The coherence is entirely longitudinal. Absorption of energy from a 90° RF pulse, causes M_0 to rotate entirely into the XY plane, so that the coherence is in the transverse plane at the end of the pulse. As time elapses, this coherence disappears, while at the same time the protons release their energy and reorient themselves along B_0 . This disappearing coherence produces the FID (Free Induction Decay). As this coherence disappears, the value of M in the XY plane decreases toward 0. T2 or T2* relaxation is the process by which this transverse magnetization is lost [18].

$$M_{XY}(t) = M_{XY \max} \left(e^{\left(-\frac{t}{T_2}\right)} \right) \quad (3.7)$$

The frequency of precession is not perfectly homogeneous because of inhomogeneities of the field which leads to a loss of signal. This loss of signal is characterized by a T2* time, lower than T2, due to the loss of phase coherence between the different magnetizations during the precession. This signal decreases exponentially in T2* and not in T2 (Fig. 3.8). If the field was perfectly homogeneous, the shape of the signal would be an exponential decay in T2. The T2 exponential curve given by formula (3.6).

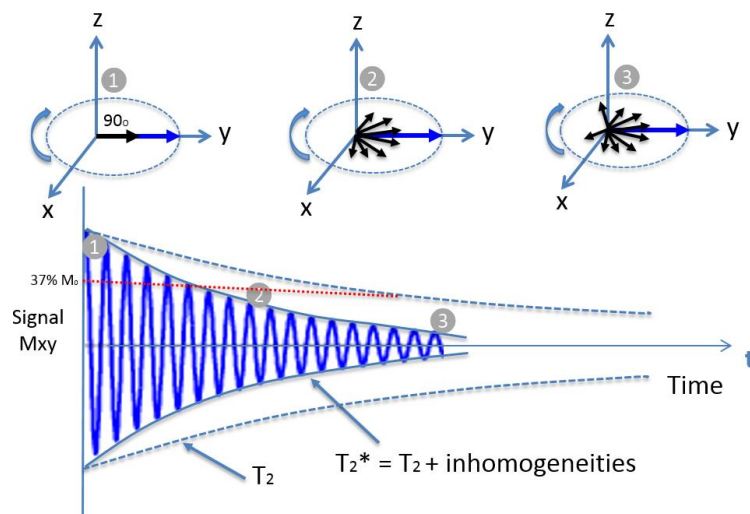


Figure 3.8. This diagram showing the process of transverse relaxation after a 90° RF pulse is applied at equilibrium.

Throughout the relaxation period, the magnetic moment from spins produces an alternating current in the coil that is recorded as the MR signals. In order to recover these signals, it is more common to work with a pair of RF pulses (90° and 180°) called Spin-Echo sequence.

3.4.3 Spin-Echo sequence

The basic of MRI Spin-Echo sequence has two selective pulses, a 90° pulse is first applied for excitation, the spins flip from Z direction into XY plane, the application of a 90° RF pulse in the presence of a slice selection gradient (GSS) makes it possible to select a section. Then a 180° selective RF pulse is applied after a time $TE/2$, initiating the precession to be reversed and to be in phase after another time $TE/2$, yielding an echo [72].

The Spin-Echo sequence can be summarized as:

$t = 0$, RF 90° pulse \Rightarrow wait $TE/2 \Rightarrow$ RF 180° pulse \Rightarrow wait $TE/2 \Rightarrow$ measure MR signal

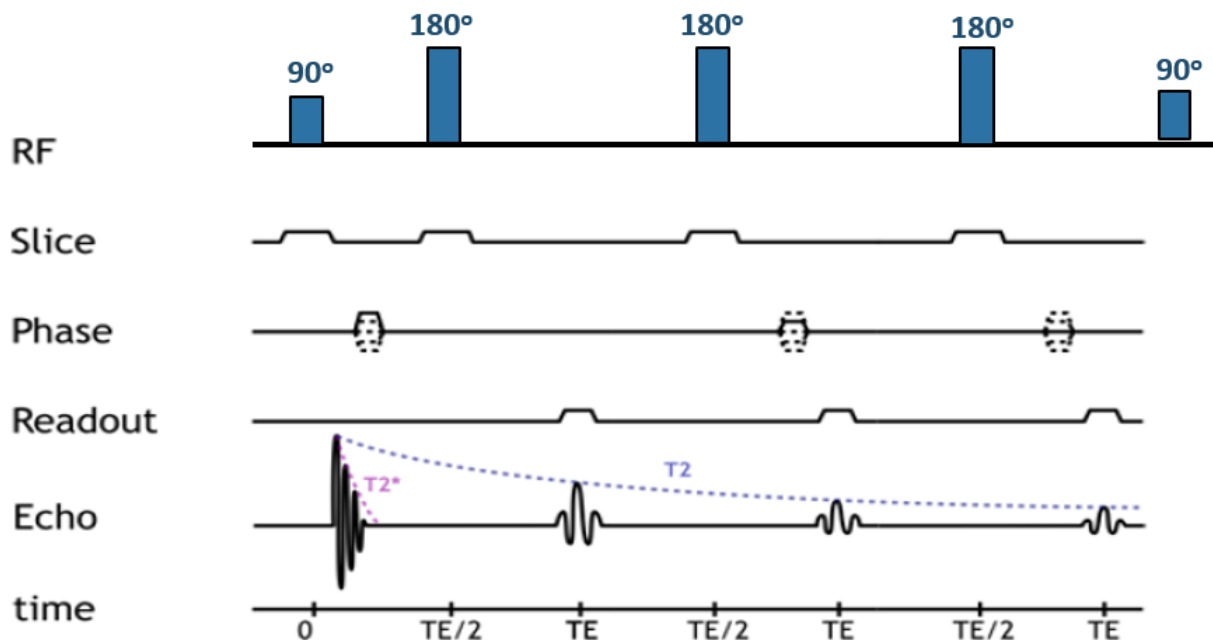


Figure 3.9. Timing diagram for the spin echo sequence [74].

This sequence is defined by two parameters:

- **Echo time (TE)**, which refers to time between the application of radiofrequency excitation pulse and the peak of the signal induced in the coil.
- **Repetition time (TR)**, which is the time from the application of an excitation pulse to the application of the next pulse (representing the time separating two RF pulses of 90°). It determines how much longitudinal magnetization recovers between each pulse.

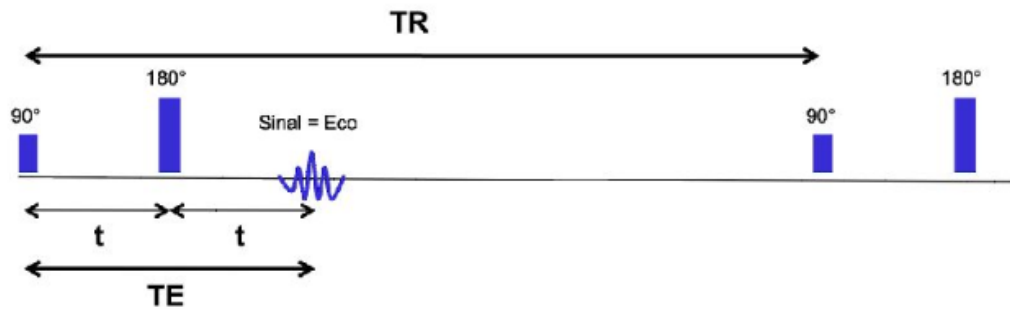


Figure 3.10. Echo sequence, definition of TE and TR [75].

The RF pulses (90 ° and 180 °) must be applied as many times as there are lines in the image matrix.

And the amplitude of the MR signal (A_S) can be expressed as per Liang [76]:

$$A_S = M_0 \left(1 - 2e^{-(TR - \frac{TE}{2})/T_1} + e^{-TR/T_1} \right) e^{-TE/T_2} \quad (3.8)$$

where M_0 is the spin density. The MR imaging contrast depends of the spin density, T1 and T2.

The Spin-Echo sequence allows us to obtain weighted images T1 and T2/T2*, by playing on the respective values of the repetition times TR and the echo times TE. The contrast in T1 or T2/T2* among phases can be used to distinguish one phase over another. For example, we can obtain T1-weighted image by using a short TE and an appropriate TR and vice versa for T2-weighted image.

The acquisition time is very important during MRI, particularly if the sample has some dynamic process in progress, such as two-phase flow. This acquisition time is a function of TE, TR and the distinct phase gradients number.

In our study, two types of fluids have been used (water and oil), both fluids signal intensity are visible in the spectrum with a slight change in resonance frequency between the two phases called chemical shift. This leads to a superimposition of the signal of both phases, with bad imaging results. Therefore, MSME protocol with a chemical shift selective excitation pulses could be used to identify the signals of oil and water separately. For example, to suppress the signal from water, a selective spectral pulse nutates the water magnetization to the transverse plane, leaving the magnetization of oil unperturbed along the longitudinal axis. The water signals are dephased by applying one or more spoiler gradient pulses (Fig. 3.11). The spoiler gradient pulses have no effect on water signal [77]. The same sequence can also be used to suppress oil signals.

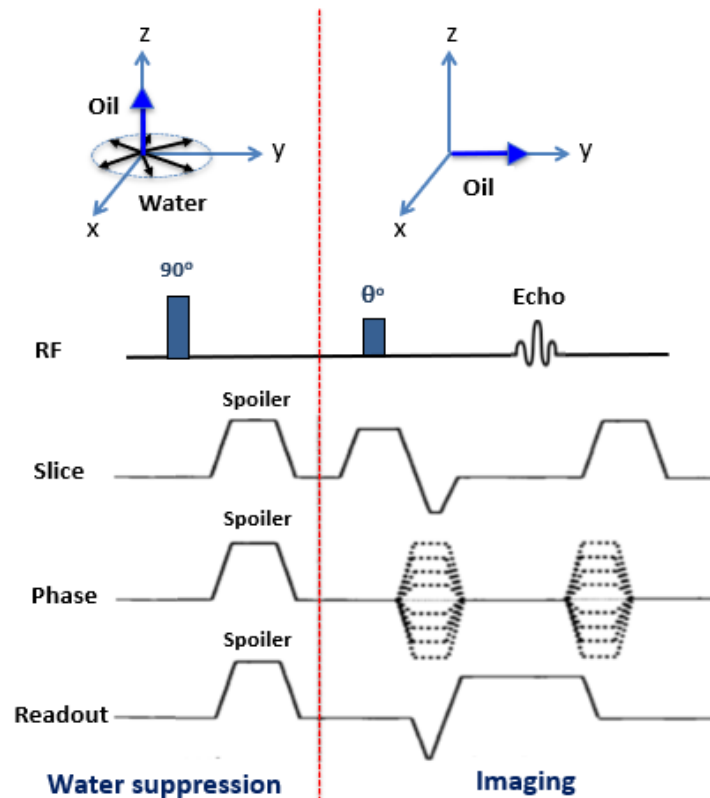


Figure 3.11. Sequence of using a spectrally selective pulse to suppress water signals [77].

3.5 NMR signal recovery and images

To obtain an MR image, magnetic field gradients are applied in X, Y, and Z directions. For instance, a slice selection in a sample is achieved by applying a one-dimensional magnetic field gradient on Z-axis, during the period that RF pulse is applied (Fig. 3.9.). Therefore, only the magnetization of the spins belong to the selected slice will be tilted, and the conversely the spins outside the slice will be neglected. The placement of a volume-element (voxel) in a slice is encoded with a phase Y-axis and a frequency gradient in the X-axis direction. The resolution of obtained image relies mostly on the strength of the gradients: if the gradients are higher the resolution will be better.

- **Fourier plane (k space):**

The recovered signal is recorded in a frequency space called k-space or Fourier plane. The filling of this space is carried out following the application of gradients in X, Y, and Z directions. A classic spin echo sequence fills the k-space line by line as follows [78]:

1. Beginning of the sequence, 90° RF excitation + gradient of slice selection: position at the centre of the Fourier plane.
2. Intense negative phase gradient: downward movement of the Fourier plane.
3. Positive frequency gradient: move to the right of the plane.
4. RF wave of 180° + gradient of slice selection: symmetry with respect to the centre of the plane, position in top on the left.
5. Positive Frequency Gradient + echo recovery of the signal: move and fill to the right in the Fourier plane.

- The sequence is then repeated, until the total filling of the Fourier plane, with phase gradients of increasing intensity. The K space is filled from bottom to top, line by line. It should be noted that the centre points of the Fourier space encode the low frequencies (contrast of the image) while the peripheral points encode the high frequencies (details of the image).

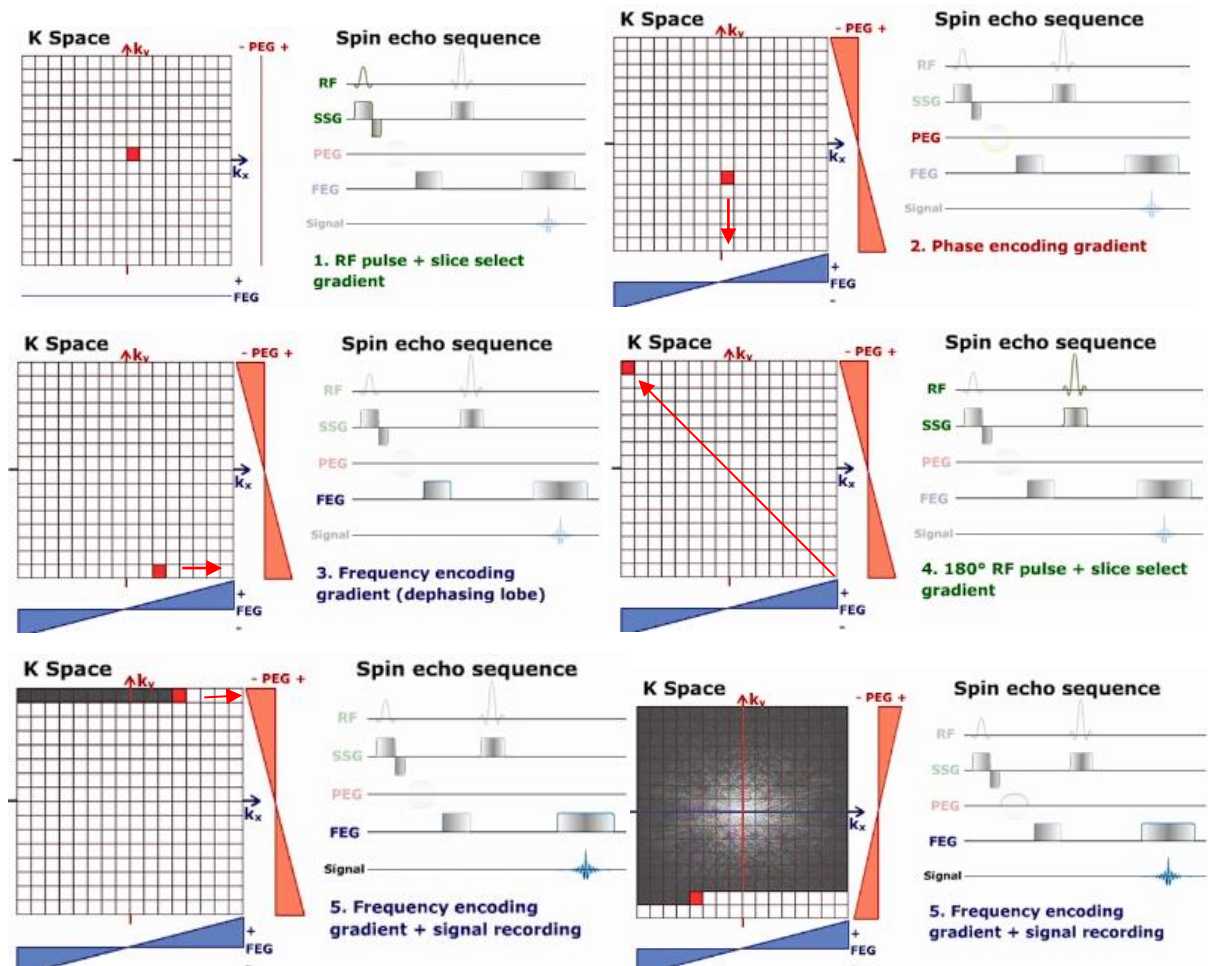


Figure 3.12. Navigation in the Fourier plane [78].

- The Fourier transform:**

In reality, the NMR signals recovered during the experiments is more complex. In fact, it consists of a large number of different frequencies to be able to differentiate spatially the observation zone. These frequencies, detected simultaneously, are proportional to the magnetic field B_0 modulated by the application of a gradient. It is essential to separate these frequencies in order to determine their respective intensities. This is the goal of the Fourier transformation. This mathematical operation transforms the NMR signal in a spectrum where each frequency is represented by a peak [18].

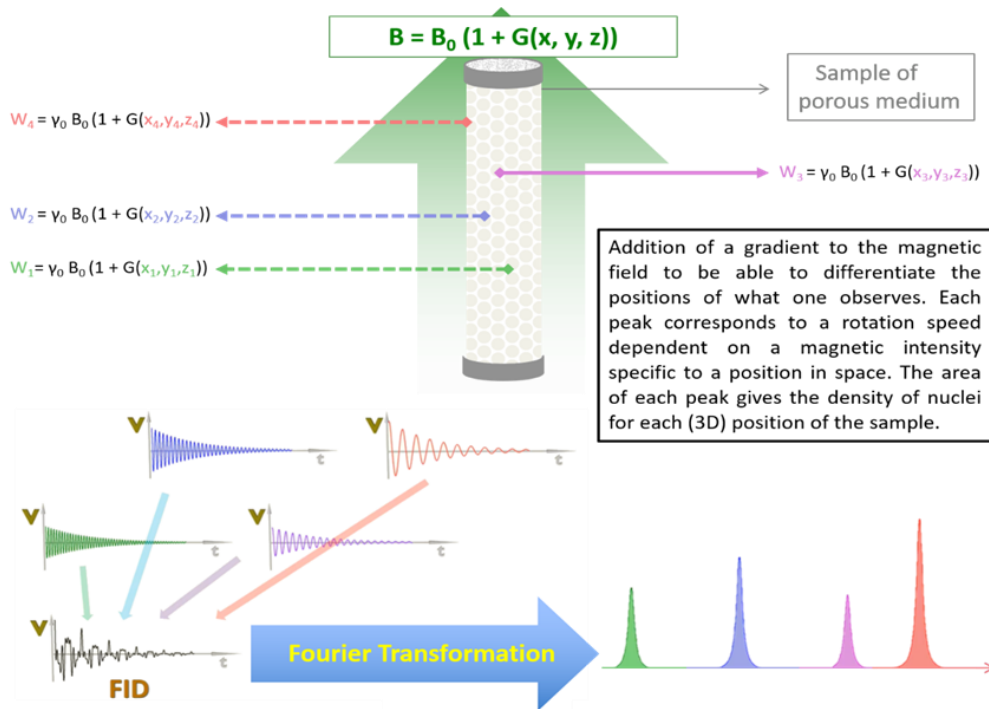


Figure 3.13. Addition of a gradient to the magnetic field to observe several zones in the sample space and this for a single acquisition.

3.6 Conclusions

MRI is an attractive and non-destructive technique that is based on the principle of NMR. This involves observing the magnetic resonance signal of hydrogen nuclei subjected to a static magnetic field and excitation by an RF wave. The superposition of a magnetic field gradient allows the spatial encoding of the information according to the position of the spins in space. The application of the magnetic field gradients along the three directions makes it possible to produce a three-dimensional image.

The intensity of the signal in a pixel (or voxel) of the image corresponds to the average of the intensities of the signals which come from the spins of the hydrogen nuclei in the liquid phase. This signal is a function of the density of spins modulated by their relaxation times.

The solid particles do not return a signal, which gives this method a specificity compared to other methods making it possible to use non-transparent materials.

However, it is limited by the use of materials: it is not possible to use ferromagnetic materials, and paramagnetic ones have an effect on the relaxation times and consequently on the NMR signal. Nevertheless, this property can be used to increase or decrease the signal in order to add a specific contrast.

Nuclear magnetic resonance (NMR) through its application (MRI) is able to provide unique information about fluid distributions, saturations, flow displacement within porous media by sequences sensitive to the nuclear spin density. Immiscible fluids distributions (i.e. water and oil) could be visualized using selective excitation of each fluid based on either different magnetically susceptible nuclei or on the distinction in T1 or T2.

High resolution MRI could be obtained in a short period of time using specific sequences. This type of sequence is a good method in dynamic conditions such as two or multi-phase flow, where the time is important.

4. Experimental setup, instrumentation and methods

| | | |
|---------|--|----|
| 4. | EXPERIMENTAL SETUP, INSTRUMENTATION AND METHODS..... | 64 |
| 4.1 | Introduction..... | 66 |
| 4.2 | Experiments | 66 |
| 4.2.1 | Experimental system | 66 |
| 4.2.2 | MRI Resolution and field of view | 67 |
| 4.3 | Sample material | 68 |
| 4.3.1 | Porous medium..... | 68 |
| 4.3.2 | Fluids | 70 |
| 4.4 | Experimental process | 70 |
| 4.5 | Imaging protocol and methods..... | 72 |
| 4.5.1 | MSME protocol | 72 |
| 4.5.2 | Imaging methods..... | 74 |
| 4.5.2.1 | Selective method..... | 74 |
| 4.5.2.2 | Nonselective method | 76 |
| 4.6 | Conclusion | 77 |

4.1 Introduction

As consistently when doing experimental work, much time is committed to instrumentation, experiment design, and verifying that the whole system is working properly. It is also the case here, and this part should be well prepared and supported in order to obtain useful results. indeed, the objective of this chapter is to give a description of the experiment setup and models used in this thesis. We will present the instrumentation used for imaging, the porous media construction and the sample preparation. The last part of this chapter concerns the imaging protocol, methods, and data treatment.

4.2 Experiments

4.2.1 Experimental system

The experimental setup used for this thesis consists of two parts: the first one is a high resolution of 600 MHz MRI spectrometer type Bruker III 600 wide bore (Fig. 4.1.a), equipped with a 14 T vertical magnet, shielded gradient coils providing a maximum gradient strength of 450 mT/m and a 40 mm diameter quadrature resonator.

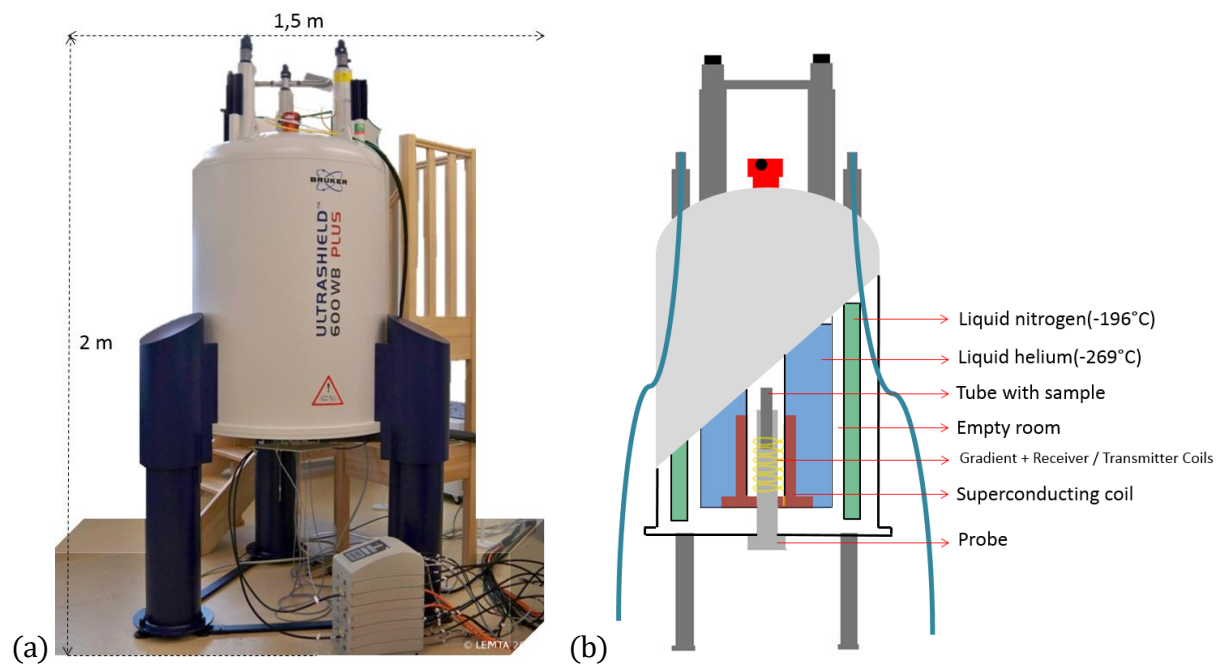


Figure 4.1. (a) MRI machine used during experiments, (b) Spectrometer diagram with its legend.

With this system we measure and visualize directly the two-phase flow in a vertical model of porous medium (packed beads or sands) under the ambient condition. The MRI technique allows for non-invasive measurements (2D or even 3D mapping) of the concentration of hydrogen nuclei ^1H in the liquid phase inside the porous media. These hydrogen nuclei can belong to molecules of water or other liquids. The ^1H species associated with water or hydrocarbon provide the phase distribution images, and it is also possible to distinguish the solid and liquid phases.

The second part is the porous medium column. A tube with 34 mm internal diameter and 14 cm in height was filled and compacted with sands or polystyrene beads. The beads are kept inside the tube by two porous filters and two caps. The materials used to design the setup have been carefully chosen in order to avoid any interferences with the experiment: we should not use ferromagnetic

materials inside or close to the magnet and conductive materials should be outside the resonator to avoid signal loss and images distortions.

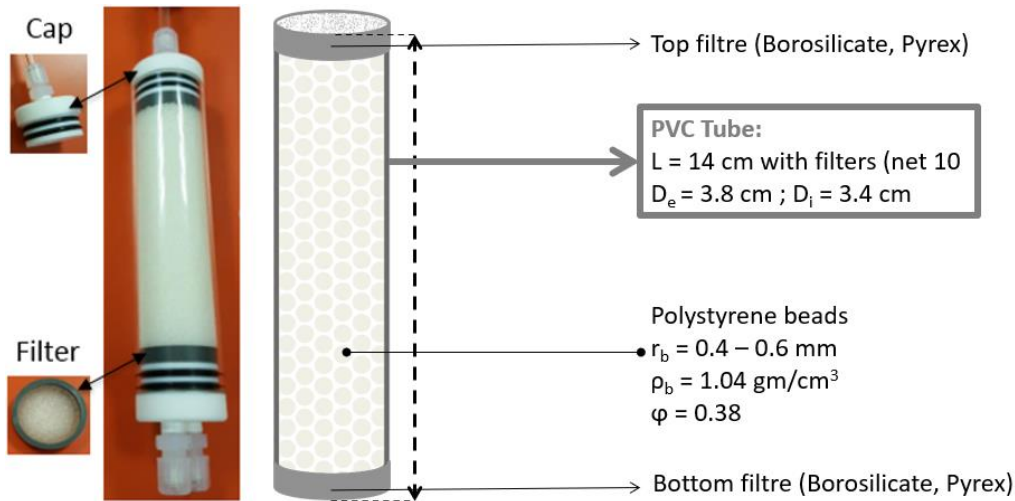


Figure 4.2. Schematic of polystyrene sample with beads.

A syringe pump is connected to the bottom of sample to inject the water upward at constant flow rate. This pump can inject at a very low rate with an accuracy of $\pm 0.5\%$, figure 4.7.

Signal is acquired and processed using the Bruker ParaVision software. Further processing is done with the Matlab software. The signal strength of the MRI intensity is proportional to the amount of target fluid in the sample.

4.2.2 MRI Resolution and field of view

The MRI signal is acquired in a volume resonator with a 4cm diameter and a comparable height. It means that we cannot detect signal outside this limited volume. Therefore, we have to carefully select the imaging area, also called field of view (FOV). As we are looking at a macroscopic phenomenon, we should image the biggest possible area. We decided to select a FOV of 5cm*5cm, a little bigger than the detection volume. This allows us to limit aliasing from signal outside the FOV. Furthermore, we choose to place the read direction in the flow direction as there is no aliasing in this direction due to the digital filtering (contrary to the phase direction).

We acquired a matrix of 256 pixels \times 256 pixels, which gives us a resolution of 0.19mm per pixel. It is possible to increase the size of the matrix, but the longer acquisition time leads to a decrease in signal due to T2* relaxation.

We had to design our study model according to the FOV constraints given above. To do so, our model was filled with glass beads of 3 mm diameter (Fig. 4.3.b), then installed inside a sample holder designed to fit in the imaging probe (Fig. 4.4). We acquired multiple images to precisely define the observation area in the sample. (Fig. 4.3.a).

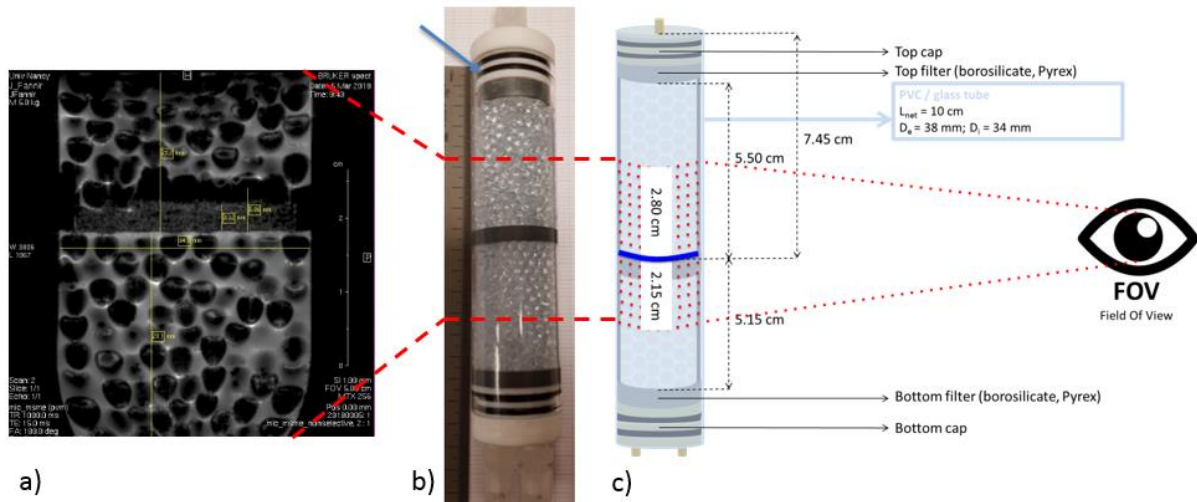


Figure 4.3. (a) image recovered from the MRI to find the sample observation area; (b) prepared sample with glass beads of 3mm diameter; (c) sample diagram with a mark placed at a known distance.

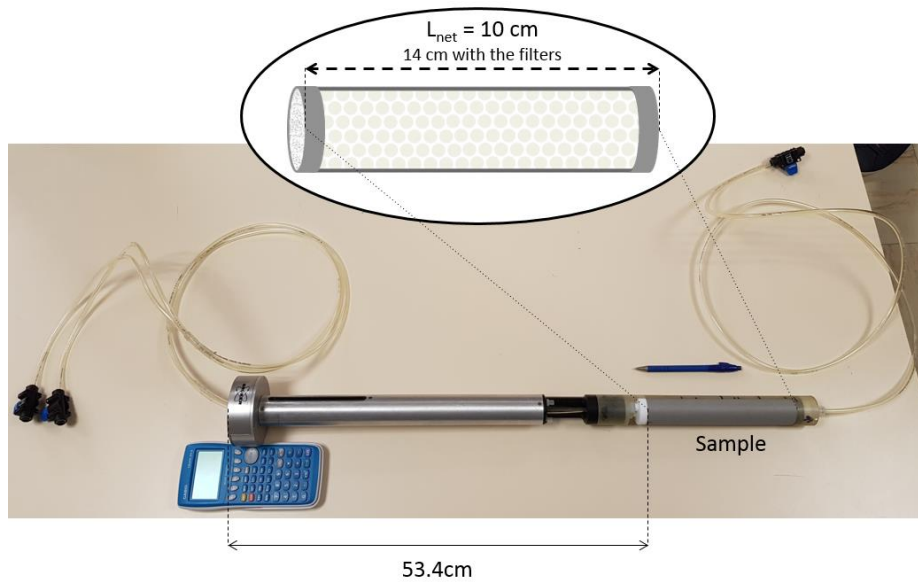


Figure 4.4. Sample holder containing porous media sample with injection / evacuation points.

4.3 Sample material

4.3.1 Porous medium

We have used two different types of materials for tubes and beads according to their wettability. The synthetic porous medium consisted of polystyrene beads or sands with average grain size of 0.5 mm and 0.13 mm respectively. The average estimated porosity measured by the gravimetric method was around 38%, and the intrinsic permeability was calculated using Kozeny-Carman equation for non-consolidated medium:

$$K = \frac{\varphi^3}{36C(1 - \varphi)^2} d_p^2 \quad (4.1)$$

where K is the sample intrinsic permeability, C is the Kozeny-Carman constant (in this study $C=5$), φ is the sample porosity, and d_p is the mean diameter of the grains.

The porous media characteristics for both materials are given in Table 4.1.

| Porous medium | Model tube material | Porosity (%) | MnCl ₂ (mole/l) | Permeability (m ²) | Model net length (cm) | Model internal diameter (cm) |
|-------------------|---------------------|--------------|----------------------------|--------------------------------|-----------------------|------------------------------|
| Polystyrene beads | Plastic | 38 | 0.01 | 2.9E-10 | 10 | 3.4 |
| Packed Sand | Glass | 39 | 0.02 | 1.5E-11 | 10 | 3.4 |

Table 4.1. The porous media characteristics for polystyrene beads and packed sand.

The samples of sand always have different grain sizes even though the grain size spectrum is relatively narrow. Indeed, it is important in our study to determine the average grain size and grain size distribution accurately as it will be used in our calculations and discussion. Therefore, the average grain size of the selected sand was evaluated from grain size populations (not directly from the mass fraction). Table 4.2 shows the sand particles size distribution as a function of mass. These data were obtained using different available sieves.

| Size of sieve (mm) | Average size of population (mm) | Mass (g) | Number of grains (supposed to be spherical) | Frequency % |
|--------------------|---------------------------------|----------|---|-------------|
| 0.025 | 0.040 | 0.11 | 188867 | 3.614 |
| 0.05 | 0.075 | 2.82 | 605232 | 11.581 |
| 0.1 | 0.130 | 82.63 | 3405372 | 65.159 |
| 0.16 | 0.205 | 92.75 | 974786 | 18.652 |
| 0.25 | 0.325 | 19.62 | 51749 | 0.990 |
| 0.4 | 0.450 | 0.16 | 206 | 0.004 |

Table 4.2. Sand particles size distribution versus mass and grain population.

Based on the above data, the average sand grain size estimated to be 0.13 mm using a log-normal function (Fig. 4.5). The value of the permeability shown in Table 4.1 was calculated from the Kozeny-Carman formula (Eq. 4.1) with the estimated average grain size.

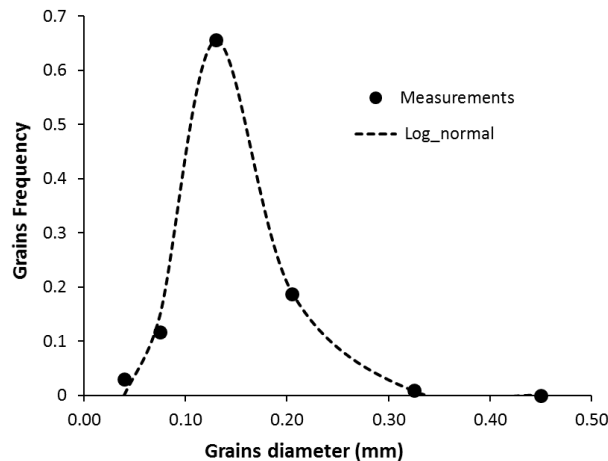


Figure 4.5. Sand Grain frequency vs grain size matching with Log-normal function.

The porosities in Table 4.1 were obtained from the dimensions of the model and the properties of the materials (Annex-III). Since the medium was filled uniformly, we suppose that the volume of porous medium observed in the FOV can be considered as an elementary representative volume (E.R.V.).

4.3.2 Fluids

In all experiments, two types of fluids have been used: a solution of water and $MnCl_2$ as displacing phase and PTX2000 fuel as oil phase. Different types of fluids have been investigated based on their physical properties and availability (octane, octanol, Soltrol, silicone oil & PTX-2000), in order to be used as an oil phase representative in the experimental stage (Fig. 4.6).

PTX-2000 (kerosene) was deemed a suitable one: it is a paraffinic oil consisting of a mixture of C11-C14, n-alkanes, and < 2% aromatics, it is stable under standard condition with neglected water solubility (see appendix). This fluid allows to approximate Oil behaviour in porous media, it has a viscosity of 2.96 mPa.S and a density of 810 kg/m³. Liquid sample of PTX2000 has been tested in Lemta laboratory to check its MRI compatibility in terms of signal and relaxation times with positive outcome.

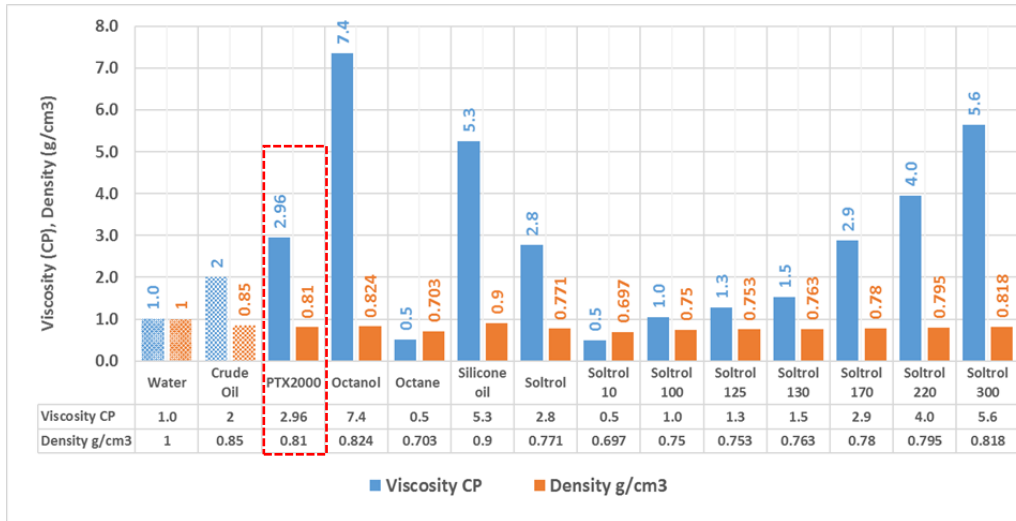


Figure 4.6. Viscosity & Density comparison for different type of fluids.

Physical properties of the two used fluids are given by the products data sheet and confirmed in our lab using standard measurements techniques (Table 4.3). The interfacial tension σ between oil and water was assumed to be 0.05 N/m according to [56].

| Oil density (kg/m ³) | Oil viscosity (cP) | Water density (kg/m ³) | Water viscosity (cP) | σ (N/m) |
|----------------------------------|--------------------|------------------------------------|----------------------|----------------|
| 800 | 2.96 | 1000 | 1 | 0.05 |

Table 4.3. Fluid properties (oil and water).

4.4 Experimental process

As a first step, the sample tube should be filled with oil. A vacuum pump was used to remove air in order to obtain fully saturated samples. At initial state, we installed a hydrostatic equilibrium of water-oil contact inside of the porous sample which was calculated with the levels of water and oil

in tanks (Fig. 4.7). In doing so the water-oil interface is homogeneously distributed near the bottom filter. The injection rate was controlled by the syringe pump. The water solution (distilled water with MnCl_2) was injected into the column from below with the objective to prevent the deformation of water-oil interface by the gravity. The volumetric injection flow rate was varied from 0.08 mL/min to 0.16 mL/min and the corresponding superficial velocity was calculated using the geometry and porosity of the model. For each experiment, the MR sequences were performed during more than 10 hours, a period corresponding to the injection of 3 and more pore volumes (PV) of water. See Annexe III for PV definition.

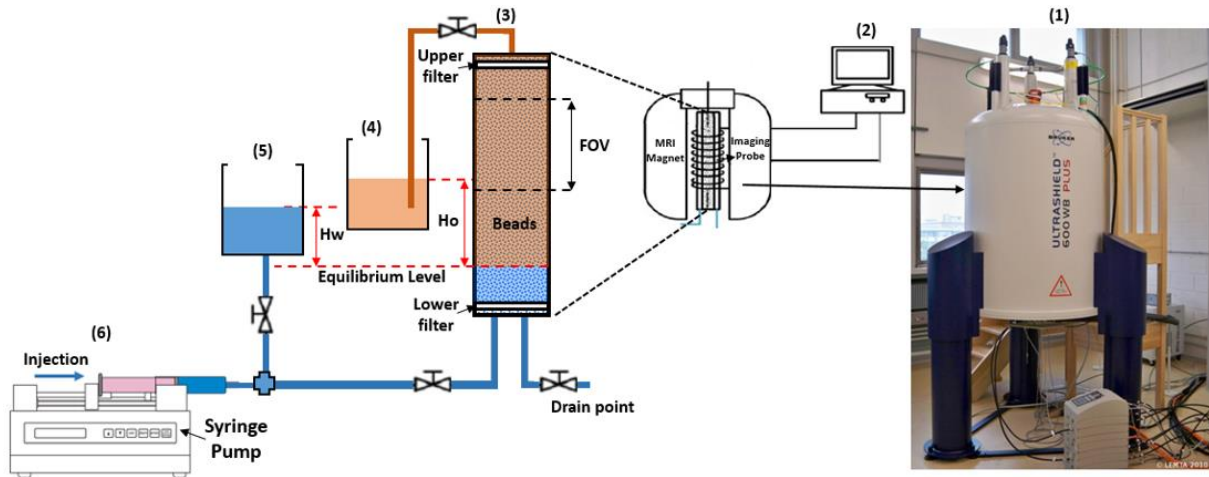


Figure 4.7. Experimental setup: (1) 600 MHz NMR system; (2) Computer for data process; (3) Porous media sample; (4) Oil tank; (5) Water tank; (6) Water injection pump.

Whenever a sample is placed inside the detection zone of MRI spectroscopy, it will affect the field homogeneity and distorted it. Before proceeding with images, every sample need to be shimmed. Moreover, it was very important to tune the imaging probe before acquiring each image (Fig. 4.8): because of the sensitivity of the probe, its tuning parameters are affected by the change of water /oil ratio during the experiment. If the probe is not correctly tuned, it leads to a decrease of the signal measured and reducing its accuracy. The probe adjustment stopped when the sweeping of oil was finished as no change was observed on the tuning parameters.

The accuracy of the measurements depends mainly on the signal-to-noise ratio (SNR) of the NMR intensity measurements obtained for each voxel in the image. This SNR itself depends on many factors such as size of the voxel, intensity of the magnetic field, nature of the porous medium, number of repetitions in the MRI sequence, etc. In our case, due to the use of a high field spectrometer (14T), it is of the order of a few percent.

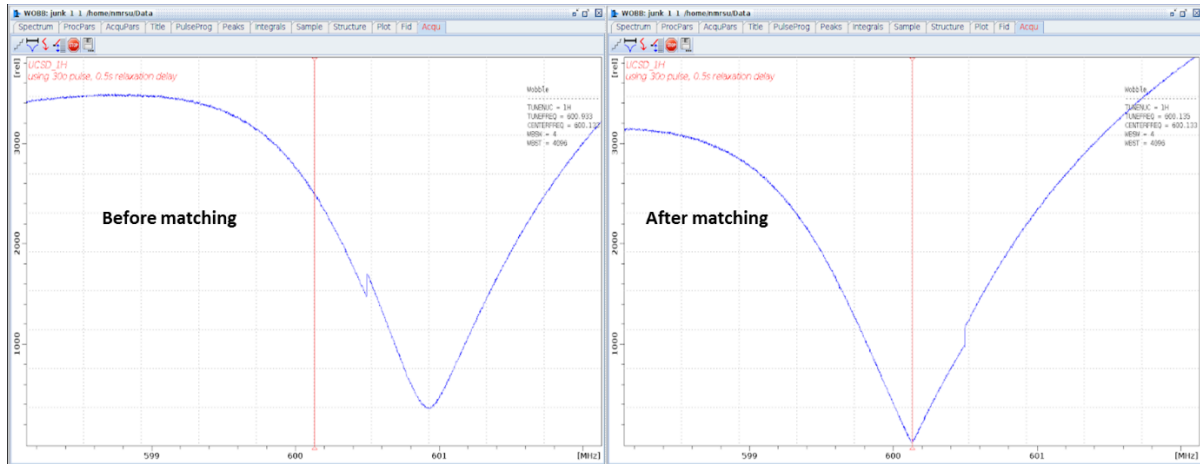


Figure 4.8. Wobble curve, before and after tuning & matching.

4.5 Imaging protocol and methods

The magnetic resonance imaging technique is an effective, non-invasive method for determining fluid saturation in porous media by detecting ^1H density. The imaging method used a classical multi-slice spin echo sequence. The MRI signal is explained in chapter 3 and can be described more as per S. Chen et al. and J. Yan et al. [5, 79]:

$$I(f, TE) = I_0(f) \left(1 - \exp\left(-\frac{TR}{T_1}\right) \right) \exp\left(-\frac{TE}{T_2}\right) \quad (4.2)$$

in which I is the observed intensity of the magnetic signal at resonance frequency f , I_0 is the intrinsic magnetic intensity, TE is the echo time, TR is the repetition time, T_1 is the longitudinal relaxation time and T_2 is the transverse relaxation time. The intrinsic magnetic intensity I_0 is in principle proportional to the number of protons ^1H . Taking $TR > 5T_1$ and $TE < T_2/5$, the observed magnetic intensity is close to the intrinsic one, i.e. $I(f, T_E) \approx I_0(f)$ which makes it possible to build an image in ^1H density almost independent of the relaxation times.

4.5.1 MSME protocol

The Multi Slice and Multi Echo MSME protocol has been selected to use in this study. It is based on the spin echo sequence (refer to chapter 3, section 3.4.3), with the possibility to select simultaneously different slices and to acquire consecutively several echoes. In our experiments, we acquired several slices but only one echo. The following settings are needed before recording a scan:

- Define the FOV and the pixel matrix size. This has an impact on the image resolution (see 4.2.2).
- Define the number of slices and the read direction. The FOV can be divided into several slices. The orientation of this slices can be along different directions: in either axial plane, coronal plane or sagittal plan. By changing the orientation of the magnetic field gradients in the imaging procedure, it is possible to obtain vertical sections along the axis of the sample or horizontal axial sections. Subsequently we realized over time one vertical section (acquisition time about 4 min) followed by 8 horizontal sections (Fig. 4.9) (acquisition time also about 4 min). The image resolution affects the required time to perform a complete scan, as we need to acquire more pixel in the phase direction: the acquisition time is

proportional to the number of pixels in this direction. High-resolution images (clear image) always take a longer time than the same image with lower resolution (blurry image).

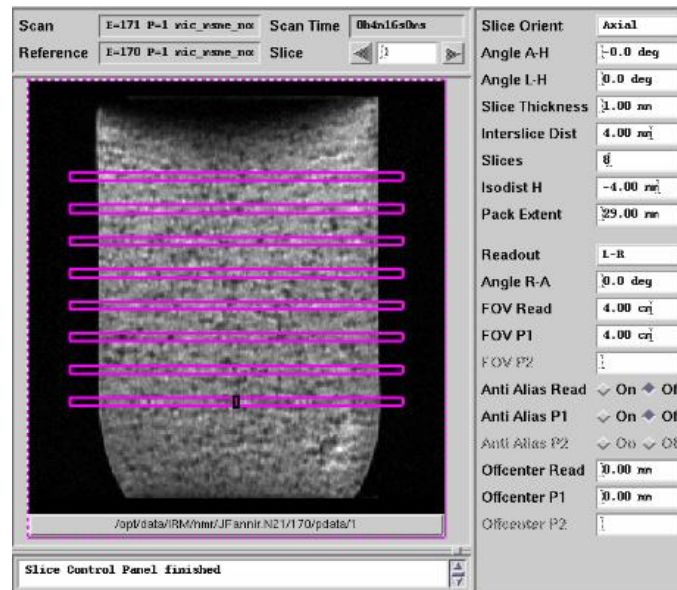


Figure 4.9. Eight horizontal sections locations for our sand sample (FOV is 5 cm)

- Define the echo time TE and repetition time TR (see chapter 3, section 3.4.3): TE value decides which relaxation time could be recorded. If the objective is to record the faster relaxation time, then this parameter should be kept as lower as possible. In the contrary, if we want to select only the spins with long relaxation time, TE should be increased.

In this study, the mapping was done with the following acquisition parameters:

- Echo time TE: 15 ms for polystyrene beads and 5 ms for sand experiments: as the oil relaxation time is shorter in the sand than in the polystyrene beads, it was necessary to decrease this value.
- Time of repetition TR: 1 s.
- Field of View FOV: $50 \times 50 \text{ mm}^2$.
- Imaging matrix: 256×256 pixels with a resolution of 0.19 mm for 1 pixel.
- One vertical slice of thickness: 1 mm.
- Eight horizontal sections along the sample's FOV.
- Voxel \rightarrow pixel with 1mm thickness.

The obtained images were satisfactory from the point of view of high spatial resolution, and it is clearly possible to visualize the oil trapping and the dynamic evolution of the two-phase flow (Fig. 4.10).

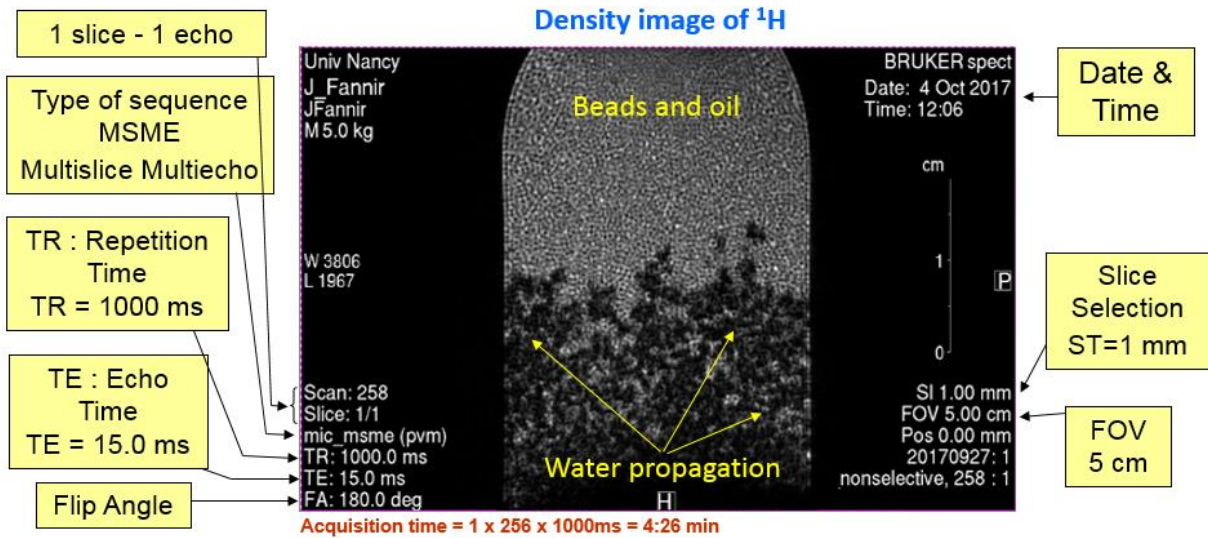


Figure 4.10. MRI vertical slice of a stack of polystyrene beads contained in a PVC tube and initially saturated with oil. The aqueous solution of $MnCl_2$ is injected from the bottom with a flow rate of 0.12 mL/min. Water saturated regions appear in black and those saturated with oil in grey.

MRI measures the signal intensity for each voxel. The oil saturation in the voxel is proportional to the signal intensity of this voxel.

From the MR intensity images, the oil saturation can be calculated as following:

$$S_o = I_i / I_{ref} \quad (4.3)$$

where S_o is the saturation of the oil phase, I_i is the dynamic MR signal intensity at time i , I_{ref} is the reference MR signal intensity (initial image at oil saturation of 100%).

4.5.2 Imaging methods

4.5.2.1 Selective method

Successive trials were performed with the objective to obtain high quality MRI images. The first method was called “selective method”. Due to the different molecular environment of the nuclei, there is a chemical shift between oil and water nuclei, i.e. a slight change in resonance frequency between the two nuclei. The shift in frequency between both phases in our case is 3.6 ppm, figure 4.11. This leads to a superimposition or a splitting of the signal of both phases, with bad imaging results at water oil interface (Fig. 4.12.b) The suppression of this chemical shift effect is usually achieved by using a chemical shift selective imaging method [8].

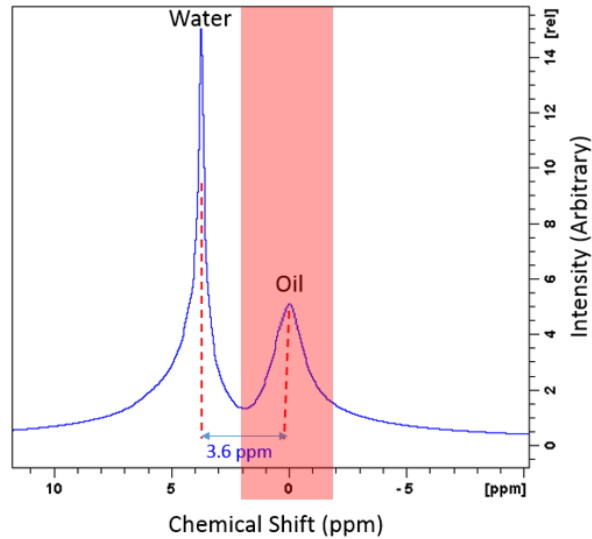


Figure 4.11. Both water and oil intensity are visible in the spectrum with a chemical shift of 3.6 ppm. The red part shows the bandwidth of the frequency selective pulses.

Therefore, MRI could be used to identify the signals of oil and water separately by using the MSME protocol with a chemical shift selective excitation pulses. This is done using low power pulses with an emission frequency and a bandwidth specific to each phase in the sample. The first results were satisfactory and we were able to observe the internal structure of the medium, figure 4.12.a).

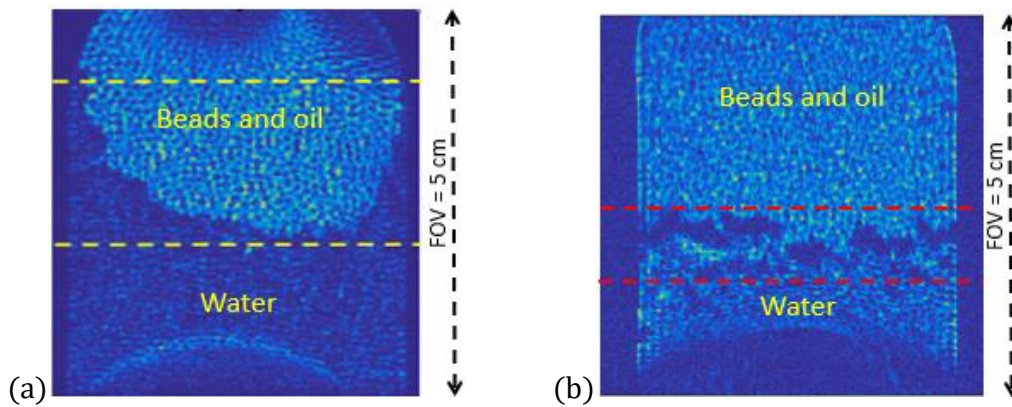


Figure 4.12. (a) MR image of selective method of water-oil displacement by using Glass tube and Borosilicate beads of 1mm diameter under pure water injection rate of 0.08 mL/min; (b) MR image of without selection phase, the chemical shift phenomenon is clear between red dashed lines.

There are two disadvantages of this method:

- The frequency selection is not perfect and there is an overlap of the signals coming from both compounds. This leads to a residual signal of the compound we want to eliminate. As a consequence, this leads to errors in the measurements of the water/oil ratio in the experiments.
- As the imaged volume is big in view of the magnet size, the field homogeneity is not perfect and there are strong variations of the resonance frequency in the sample. Therefore, when we apply frequency selective pulses, we also lose some signal coming

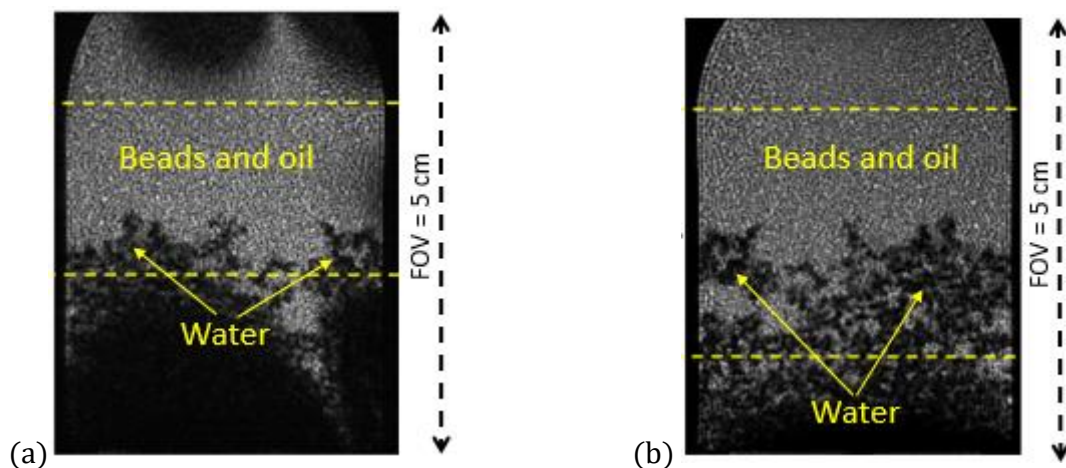
from the edges of the sample where the field homogeneity is not good enough (see 4.12.a).

4.5.2.2 Nonselective method

In spite of the fact that the polystyrene beads and the tube have a quasi-zero signal, the interface between oil and water was deformed by chemical shift artefacts. A number of methods were implemented to avoid this effect, namely non-selective imagery, modification of the intensity of the magnetic field gradient etc. Finally, the solution was in "the cancelling" of the water signal. Therefore, the MRI was mainly used to measure the oil signal intensity in each sample and to monitor the oil saturation change during the experimental test. We made sure that the NMR signal is only sensitive to oil. Indeed, both water and oil contain protons ^1H and produce NMR signals that are acquired in the same time. For biological applications of magnetic resonance, Bloembergen (1957) has found that the addition of Mn^{2+} affected the relaxation decay of the water phase [80]. Therefore, we added a strong paramagnetic contrast agent (Mn^{2+}) to reduce the relaxation times of the water. By taking an aqueous solution of MnCl_2 at 0.01 mol/l, the relaxation decay of the water phase could be greatly reduced: T_2 of water fell from 3 s to below 1 ms. In this way the signal of water disappeared so quickly that it was not possible to image it. However, MnCl_2 is not soluble in organic compounds, so there is no effect on the relaxation time of oil (~ 1 s). Therefore, the signal of oil was the only measured signal. Consequently, instead of using pure water as the injection phase, we used an aqueous solution of MnCl_2 with a very short T_2 time. For the imaging sequences, it is necessary to set the echo time TE between the transverse relaxation time T_2 of the aqueous solution and the oil (i.e. $T_{2w} \ll \text{TE} \ll T_{2o}$) and to take a relatively large repetition time ($\text{TR} \approx T_{1o}$). We called this method "nonselective method".

The non-selective method with MnCl_2 solution in water give clear images of beads and water-oil displacement for a FOV (field of view) of 5 cm (Fig. 4.13.b).

The results with this method were in good agreement with the selective technique (Fig. 4.13.c), more details will be presented in chapter 5. The obtained images were satisfactory from the point of view of high spatial resolution (0.19 mm for 1 pixel) and visualization of the dynamic evolution of the two-phase. Furthermore, we did not observe the signal losses at the edges of the images.



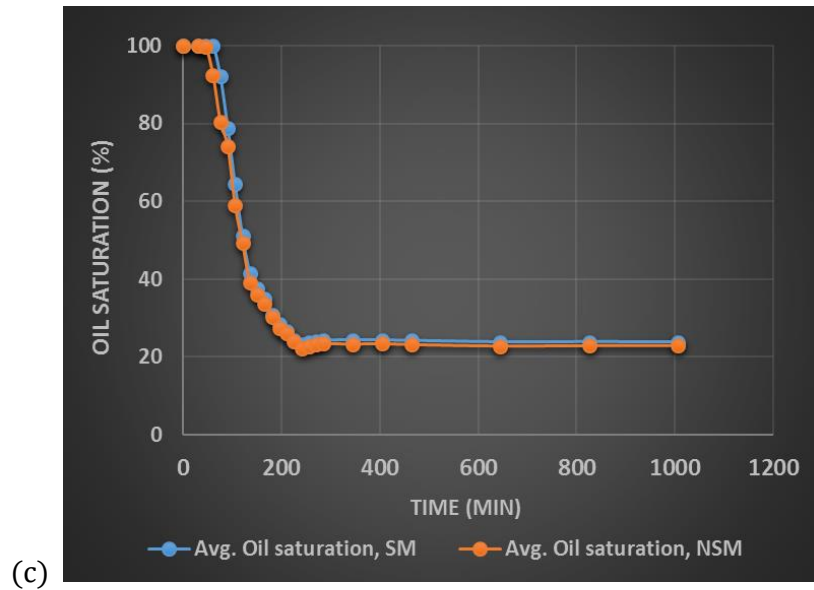


Figure 4.13. MRI image of polystyrene beads of 0.6mm stacked in PVC tube and saturated initially with oil after 3h45 of water injection with the rate of 0.12 mL/min (a) selective method; (b) nonselective method; (c) saturation profile of oil phase during displacement for selective and non-selective methods.

4.6 Conclusion

Two types of porous media are chosen for the experimental investigation using MRI technique, including water-wet and oil-wet materials. We carefully designed and tested our experimental setup to run the experiments plan. We choose an appropriate MRI imagery protocol based on the spin echo method and we used $MnCl_2$ to minimize water relaxation time (T_2), in order to avoid chemical shift effects.

In the following chapter, we will see different experiments results, using the MRI protocol and methods mentioned above.

5. Experimental results and discussions

| | | |
|-------|--|-----|
| 5.1 | Introduction..... | 81 |
| 5.2 | Experiments performed..... | 81 |
| 5.2.1 | Experiment with a packed glass-beads model, selective method | 81 |
| 5.2.2 | Experiment with a packed polystyrene-beads model | 83 |
| 5.2.3 | Experiments with packed sand column | 98 |
| 5.3 | Relative phase permeability calculation..... | 104 |
| 5.4 | Discussion..... | 109 |
| 5.4.1 | Dimensionless groups | 110 |
| 5.4.2 | Displacement mechanism and the wettability effect | 112 |
| 5.4.3 | Additional observations | 114 |
| 5.5 | Conclusions..... | 117 |

5.1 Introduction

The experimental protocol, methods and MRI instruments, were introduced in the previous chapters. In this chapter, we will present the experimental findings for this thesis.

5.2 Experiments performed

During this work, many experiments were performed, with the same instrumental setup and experimental conditions. At first, we performed experiments on test sample made with borosilicate beads of 1 mm diameter. Then two types of porous media (polystyrene of ~0.6 mm diameter and packed sand) were used in order to have a representative porous media with water-wet and oil-wet conditions.

Some supplementary data that were acquired and processed but not presented in this chapter, can be found in Annex A.

5.2.1 Experiment with a packed glass-beads model, selective method

The first try aimed to test our experimental setup, to capture the first images and to confirm the previous studied findings such as, Johns and Gladden [10]; L. Jianga et al. [28]. During this run we performed various manipulations to improve the imaging results, including the MRI probe adjustment, the injection rate setting and the subsequent parameters adaptation of the MRI sequences and the selection of slice positions. This was done using a glass tube (borosilicate tube, inner diameter of 34 mm and length of 11.5 cm) and borosilicate beads (diameter of 1 mm) and pure water was used as injection fluid, Table 5.1.

| | |
|--------------------|--|
| Porous | Glass Beads (Borosilicate) of 1 mm diameter |
| Tube | Glass Tube of 11.5 cm net length |
| Injection rate | 80 μ L/m |
| Estimated Porosity | 43% |
| Injected fluid | Pure water |
| Oil phase | PTX2000 |
| MRI Field of view | 5 cm |
| Matrix | 256 x 256 pixels |
| TR | 1 s |
| TE | 8.4ms |

Table 5.1. The experiment parameters of glass-beads model.

As mentioned before (section 4.5.2), there are chemical shifts effects when we try to image both liquids (oil and water) at the same time. In this try we used pure water as displacing fluid. The oil and water signals coexist and can be measured. Therefore, in order to visualize the two fluids in the motion, the selective imaging method was used. Vertical slice images were taken for each fluid (selection of the magnetic resonance of the liquid concerned) every 15 minutes until the end of the displacement process. Figure 5.1 shows the MRI images of oil phase.

During the MRI acquisition, the saturation of each fluid phase changes and as previously mentioned, this has an effect on the probe tuning. For this reason, tuning and matching of the probe have been adjusted throughout the acquisition of the MRI images.

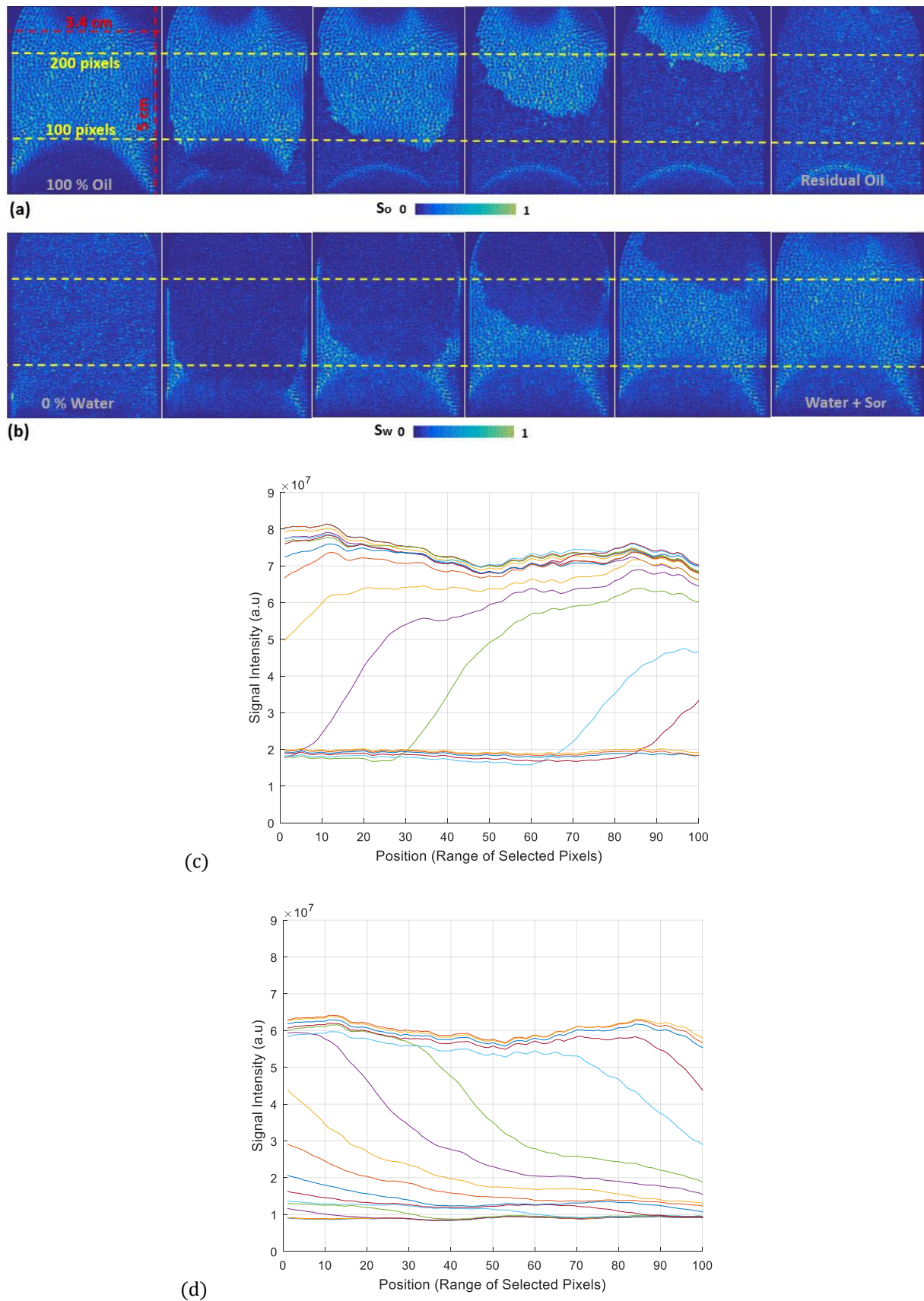


Figure 5.1. Vertical MR images of water-oil displacement by using glass tube and borosilicate beads of 1 mm diameter with pure water injection rate of 80 $\mu\text{L}/\text{min}$, (a) Oil phase & (b) Water phase, (c) MRI signals of oil phase during displacement, (d) MRI signals of water phase during displacement. The acquisition of MRI signal was made each 15 minutes and shown here from the first water appearance in FOV.

The figure above shows MRI images of oil displacement by water. Figure 5.1.a relates to the oil signal. This signal is maximum at the beginning of the displacement process (100% oil saturation). When the displacement of oil by water started, the signal of oil phase began to decrease until a weak signal for the residual oil. A quantity of signal from the water was also detected during the MR imaging of the oil phase, which had a negative impact on the images corresponding to the oil. Images of the water signal are also presented (Figure 5.1.b). The signal is weak (but not zero) at the beginning of the process. On the other hand, it is high at the end because of a relatively small amount of residual oil is present in the sample. The MRI images are therefore consistent with the expected visualization for the phenomenon of displacement of oil by water.

Glass beads are a water-wetting material, and the oil was almost completely displaced at the end of the flooding process. We injected an amount of water corresponding to three times of PV. Approximately 7% of residual oil was measured from the MRI signal, but this small amount of oil could not be verified by visual observation.

Note:

- MR Images were taken as a vertical slice of 1 mm thick. So, the oil saturation for each pixel of the image corresponds to the oil saturation averaged over each voxel, that is to say averaged over the thickness of the slice (1 mm).
- The raw images were processed using the MATLAB software to extract porosities.
- During phase measurement, a small signal corresponding to the presence of the other phase can be detected and produce a bias in the recorded signal.

However, as it can be seen in Figures 5.1 (a) and (b), there is a rapid filling of the space between the beads and the wall of the glass tube. This means that the flow of water is preferentially carried out near the walls, which does not correspond to the phenomenon that we wish to model.

This preference of water flow at the wall is due to the wettability of the solid surfaces with water (the glass being wetting with water). It is also due to the structured arrangement of the glass beads near the walls, causing relatively higher porosity and permeability. In order to remedy this problem, it is important to select a tube surrounding the sample composed of a less wetting material to avoid or reduce the tendency of the water to preferential flow near the wall of the tube.

5.2.2 Experiment with a packed polystyrene-beads model

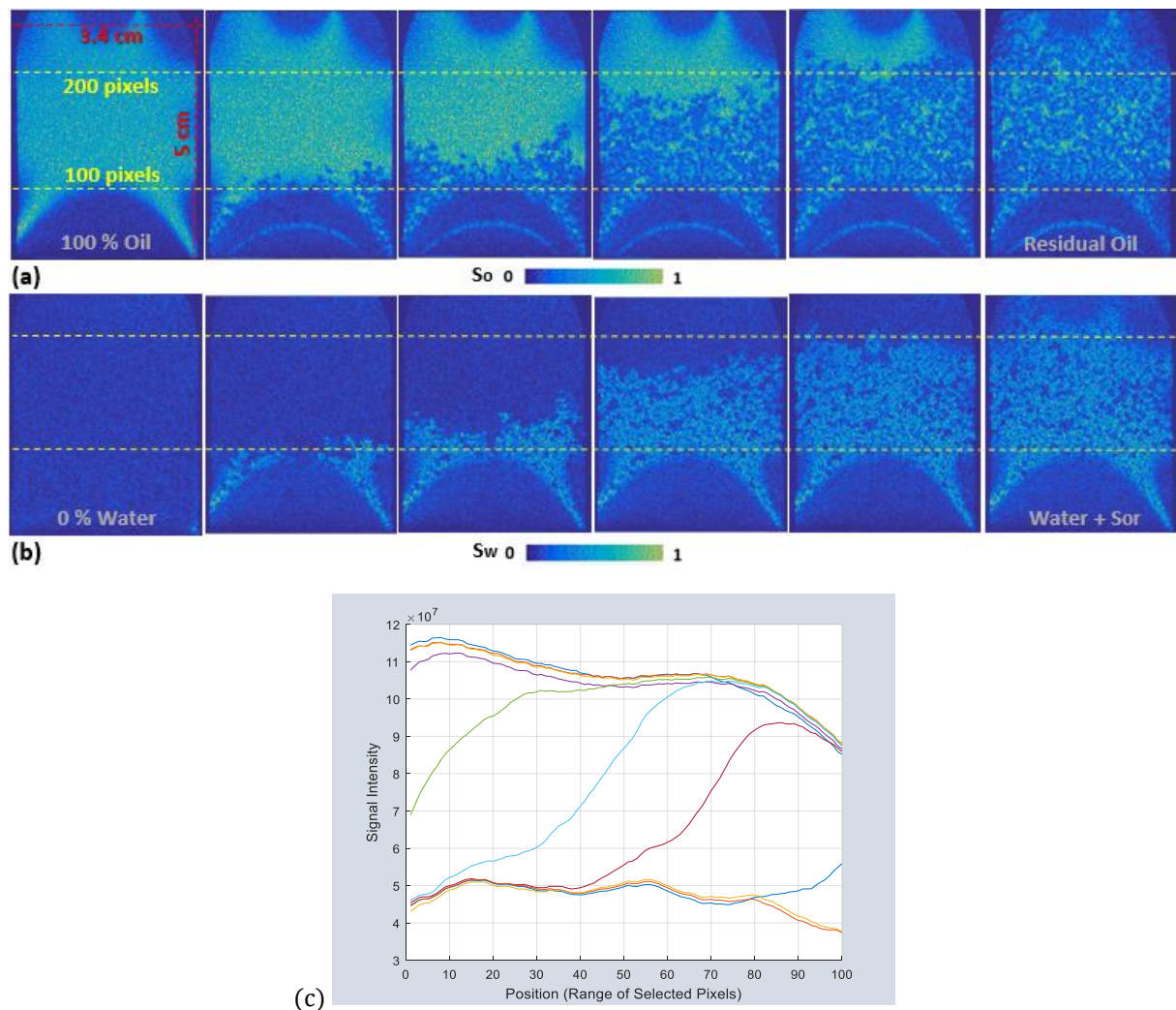
5.2.2.1 Packed polystyrene-beads model, selective method

The second try using the selective method was carried out with a plastic tube (PVC) of the same size and polystyrene beads with diameter of about 0.6 mm (Table 5.2). The preparation of the experiment with plastic tube and beads was done with the same protocol as in the previous experiments.

| | |
|--------------------|---------------------------------------|
| Porous | Polystyrene Beads of ~0.6 mm diameter |
| Tube | Plastic Tube of 10 cm net length |
| Injection rate | 80 $\mu\text{L}/\text{m}$ |
| Estimated Porosity | 38% |
| Injected fluid | Pure water |
| Oil phase | PTX2000 |
| MRI Field of view | 5 cm |
| Matrix | 256 x 256 pixels |
| TR | 1 s |
| TE | 8.4ms |

Table 5.2. The experiment parameters of polystyrene model, selective method (SM).

Figure 5.2 shows the MR images of oil phase displacement when the plastic tube and polystyrene beads were used. These MR images were taken for a period of 12 hours, equivalent to the injection of 2 times the pore volume (PV). The tuning and matching of the probe were adjusted before acquiring each of the images. The probe setting was stopped when the sweeping of oil was finished and no further changes were observed on the tuning parameters.



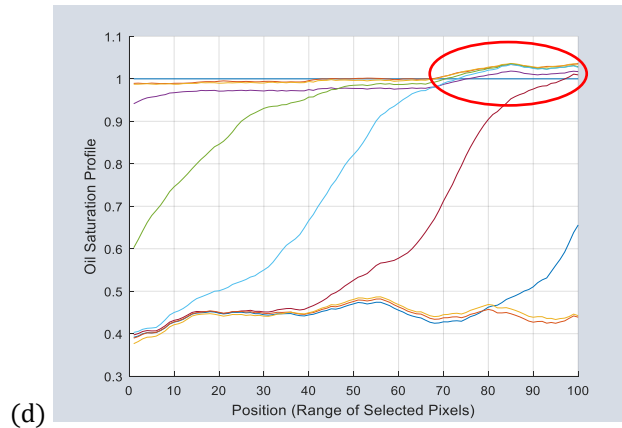


Figure 5.2. Vertical MR images of water-oil displacement by using plastic tube and polystyrene beads of 0.6 mm diameter with a pure water injection rate of 80 $\mu\text{L}/\text{min}$ (selective method), (a) Oil phase (b) Water phase, (c) MRI signals of oil phase during displacement, (d) Saturation profile of oil phase during displacement. The acquisition of MRI signal was made each 15 minutes and shown here from the first water appearance in FOV.

The advantage of this experimental setup is that by using plastic-bead pack, the recorded signals for oil and water were more stable compared to the stack of glass beads. This could be due to a better homogeneity of the sample compared to the glass beads, or cause by the presence of paramagnetic impurities on the surface of the borosilicate beads. But we believe it comes from the smaller difference in magnetic susceptibility between fluids and plastic beads than between fluids and glass beads, which leads to more uniform magnetic fields.

Since water is a non-wetting fluid for PVC tube and polystyrene beads (oil-wetting materials), both capillary and gravity forces play a stabilizing role for the upward vertical displacement. Despite this, the smaller size of polystyrene beads compared to glass beads causes instabilities and fingering ahead of the front. These fingerings were not seen clearly when the glass beads were used. The average residual oil saturation in the polystyrene model is around 45%, as measured by MRI.

For both beads material, the NMR signal of the water always has an impact on the selective signal of the oil even when the MR imaging selective protocol is used. This leads to a little higher oil saturation value than in reality. This bias effect is observed as soon as the water enters the sample observation area (light blue curve appears at the bottom of the oil images comparing with the reference image at 100 % of oil saturation). Therefore, it is important to think about correcting this effect in order to obtain the real values of oil saturation during the displacement process. In the next scenario we will address this issue with the appropriate solution obtained through the non-selective method.

5.2.2.2 Packed polystyrene-beads model, Methods comparison

In both previous tests, the spin density signal for water and oil was obtained separately for each liquid using the chemical shift selective imaging. In the next test, we will use the non-selective MR imaging protocol (NSM) to compare the results with the selective method (SM). To achieve that, it is necessary to reduce the relaxation time (T_2) of the aqueous-phase in order to capture only the oil signals. As mentioned in chapter 4, N. Bloembergen [80] found that the addition of Mn^{2+} strongly affected the relaxation decay of water (T_2 of water can be reduced to less than 1 ms depending on ions concentration). However, it has no effect on the relaxation time of oil (~ 1 s). Therefore, a concentration of 0.01 mol/L MnCl_2 was added to the

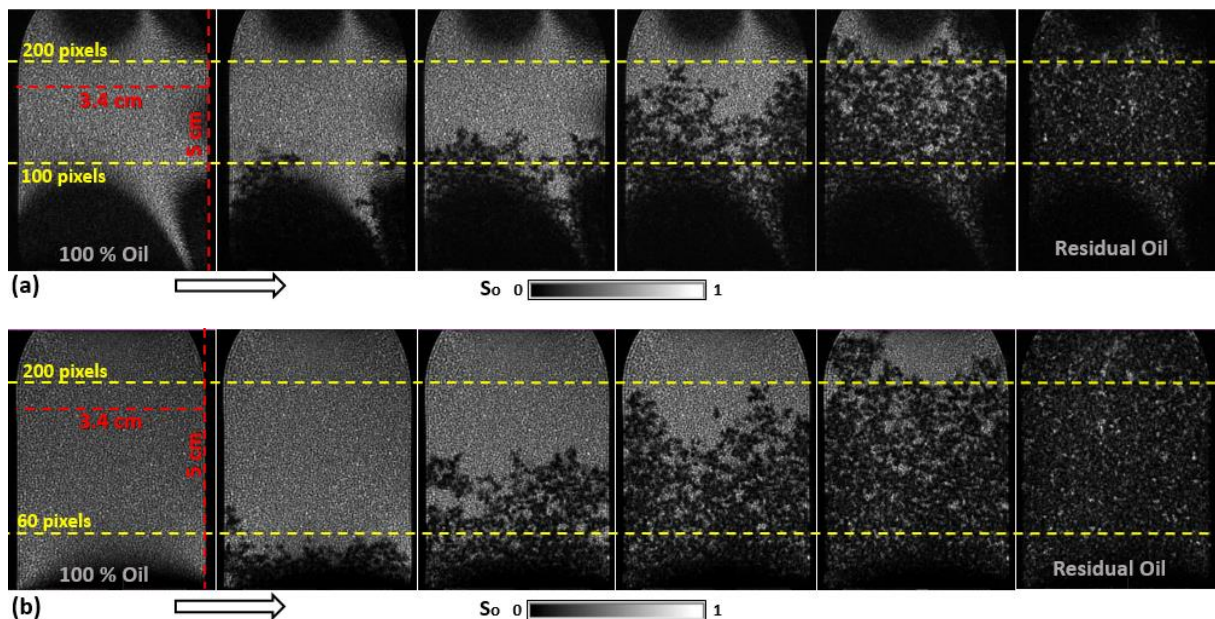
pure water to decrease its relaxation time and thereby enable the detection of only oil signal in the MR images. The sample preparation and material were similar to those of the previous scenario (polystyrene beads and plastic tube). The experiment is also performed at room temperature (24°C).

| | |
|--------------------|---|
| Porous | Polystyrene Beads of ~0.6 mm diameter |
| Tube | Plastic Tube of 11.5 cm net length |
| Injection rate | 80 $\mu\text{L}/\text{m}$ |
| Estimated Porosity | 38% |
| Injected fluid | Pure water + MnCl_2 (0.01 mol/L) |
| Oil phase | PTX2000 (kerosene) |
| MRI Field of view | 5 cm |
| Matrix | 256 x 256 pixels |
| TR | 1 s |
| TE | 15 ms |

Table 5.3. The experiment parameters of polystyrene model, non-selective method (NSM).

For the same experiment, two types of vertical images were captured at each step, the first image was taken using a non-selective method (NSM) followed by a second image with the selective method (SM). Figure 5.3 shows the MR Images of oil displacement for both methods, the selective method and the non-selective method respectively. The MR images were taken every 15 minutes for a total of 17 hours of the experiment. As in the previous scenarios, the saturation of fluids evolves within the porous medium. Therefore, the tuning and the matching of the probe must be adjusted for each image until the oil phase reaches the residual state.

Using manganese chloride (MnCl_2), the relaxation time of water was reduced from 2.35 s to 0.7 ms (water signal quenching), which allowed to capture stable MRI images of only the oily phase. In addition, by using the non-selective method (Fig. 5.3.b), we observed a decrease in the magnetic field non-homogeneity (dark deformed part in the images compared to the selective method, Figure 5.3.a).



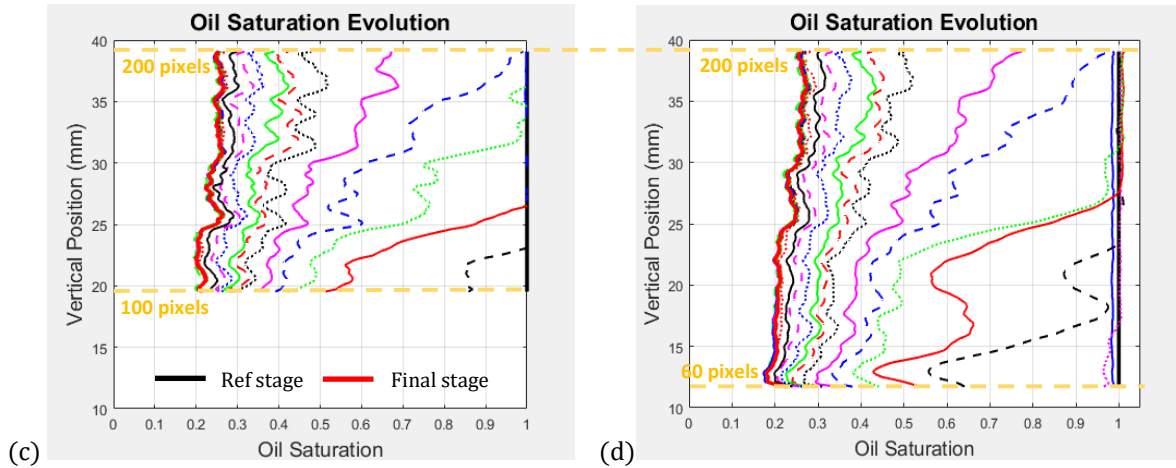


Figure 5.3. Vertical MR images of water-oil displacement using a plastic tube and polystyrene beads of 0.6 mm diameter with a water + MnCl_2 injection rate of $80 \mu\text{L}/\text{min}$; (a) Selective method (SM); (b) Non-selective method (NSM); (c) SM: oil saturation profile during displacement (signals analysis area from 100 to 200 pixels), (d) NSM: oil saturation profile during displacement (signals analysis area from 60 to 200 pixels). The acquisition of MRI signal was made each 15 minutes and shown here from the first water appearance in FOV.

Without any disturbance from water signals the clear NMR signals for the oil were acquired. The images using the selective method appear very distorted compared to those obtained by the non-selective method and this is due to the high effect of the NMR chemical shift, especially with a high MRI field.

Thanks to the high space resolution, the 0.6 mm polystyrene beads are clearly visible in the images, as well as the propagation of fluid flow within the pore space. We are also able to determine the oil saturation profile and the final saturation of residual oil by MRI. A reasonable oil saturation profile was achieved for both methods, the saturation of trapped oil was about 23% at the end of the displacement process, which is much lower than the previous experiment using the same porous media (43 %). Table 5.4 below shows the average oil saturation evolution for both cases during water-oil displacement process.

| Time (min) | Avg. Oil saturation, SM | Avg. Oil saturation, NSM |
|------------|-------------------------|--------------------------|
| 0 | 1.000 | 1.000 |
| 30 | 1.000 | 1.000 |
| 45 | 1.000 | 0.998 |
| 60 | 1.000 | 0.926 |
| 75 | 0.921 | 0.806 |
| 90 | 0.789 | 0.741 |
| 105 | 0.644 | 0.590 |
| 120 | 0.513 | 0.493 |
| 135 | 0.416 | 0.393 |
| 150 | 0.376 | 0.360 |
| 165 | 0.349 | 0.337 |
| 180 | 0.308 | 0.303 |
| 195 | 0.285 | 0.275 |
| 210 | 0.266 | 0.260 |
| 225 | 0.244 | 0.240 |
| 240 | 0.231 | 0.223 |
| 255 | 0.237 | 0.226 |
| 270 | 0.242 | 0.232 |
| 285 | 0.242 | 0.234 |
| 345 | 0.244 | 0.233 |
| 405 | 0.243 | 0.234 |
| 465 | 0.242 | 0.232 |
| 645 | 0.238 | 0.228 |
| 825 | 0.239 | 0.229 |
| 1005 | 0.238 | 0.229 |

Table 5.4. Average oil saturation comparison, obtained from MRI signals during displacement process, SM (signals analysis area from 100 to 200 pixels) and NSM (signals analysis area from 60 to 200 pixels).

From all our previous MRI results, we will consider the non-selective method (NSM) with the contribution of $MnCl_2$, as the best protocol to use in our future experimental scenarios and investigations, especially on the impact of injection rate. The oil saturation profile may also be affected by the material properties such as the wettability with the two fluids present or the structure of the porous sample, its porosity and its permeability in particular.

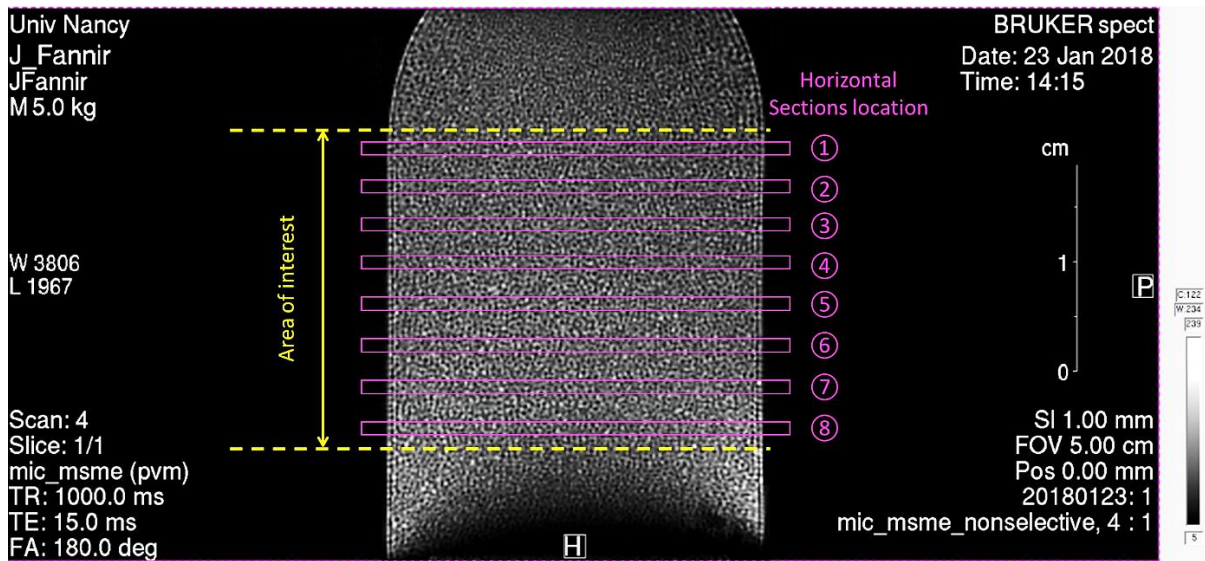
In the upcoming experimental scenarios, a vertical image completed by eight horizontal sections will be acquired along the sample at each attempt, in order to conduct an in-depth investigation from the collected data.

5.2.2.3 Packed polystyrene-beads model, non-selective method

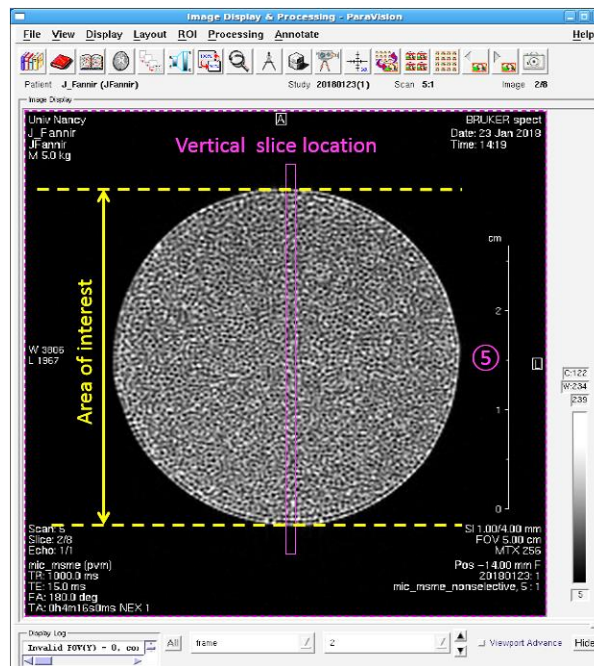
After several tests, the injection rate chosen for a better visualization of the phenomenon was fixed to 0.12 mL/min. For each porous model, data are recorded on the vertical and horizontal sections with a time interval of a 15 minutes and longer intervals when no more significant variations between two consecutives images is observed. We used a fairly long total recording time (about 15 hours) to reach a stage without variation of saturation from one image to another.

Figure 5.4.a illustrates a vertical slice of the reference image and shows in particular the location of the 8 horizontal sections. An example of a horizontal section is also shown below (Fig 5.4.b). The darker areas in the image (black colour) represent the zones of low intensity

of the NMR signal, and the brighter areas (grey colour) represents the zones of higher intensities of the signal (porous medium saturated with oil). With a spatial resolution of 0.19 mm for 1 pixel, the polystyrene beads 0.6 mm in diameter are clearly visible.



(a)



(b)

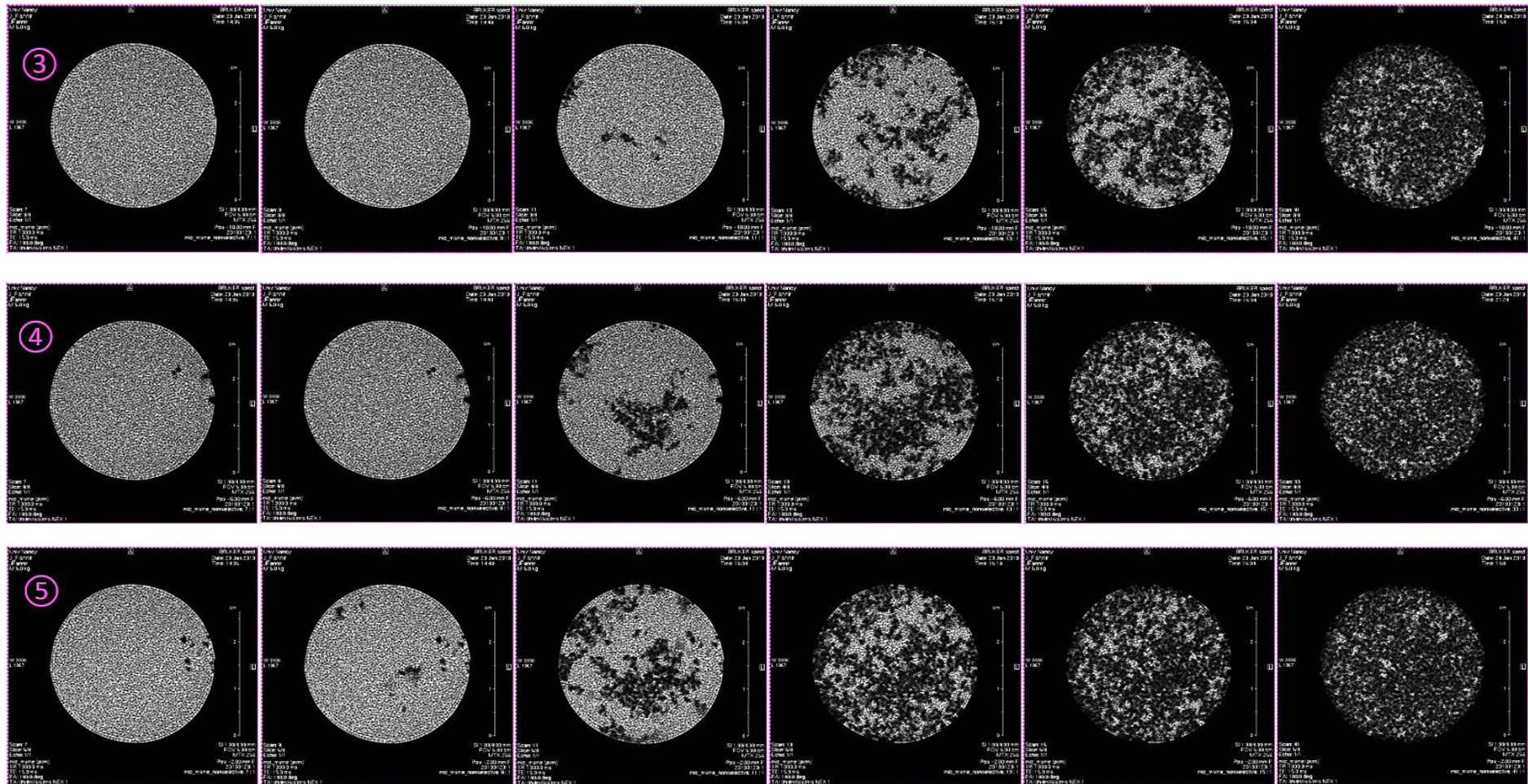
Figure 5.4. MRI reference Images (ParaVision display) of the polystyrene beads model with 100 % oil saturation; (a) Vertical image, indicates the position of the eight horizontal sections and the area of interest, (b) horizontal image (section 5), indicates as well the vertical slice location.

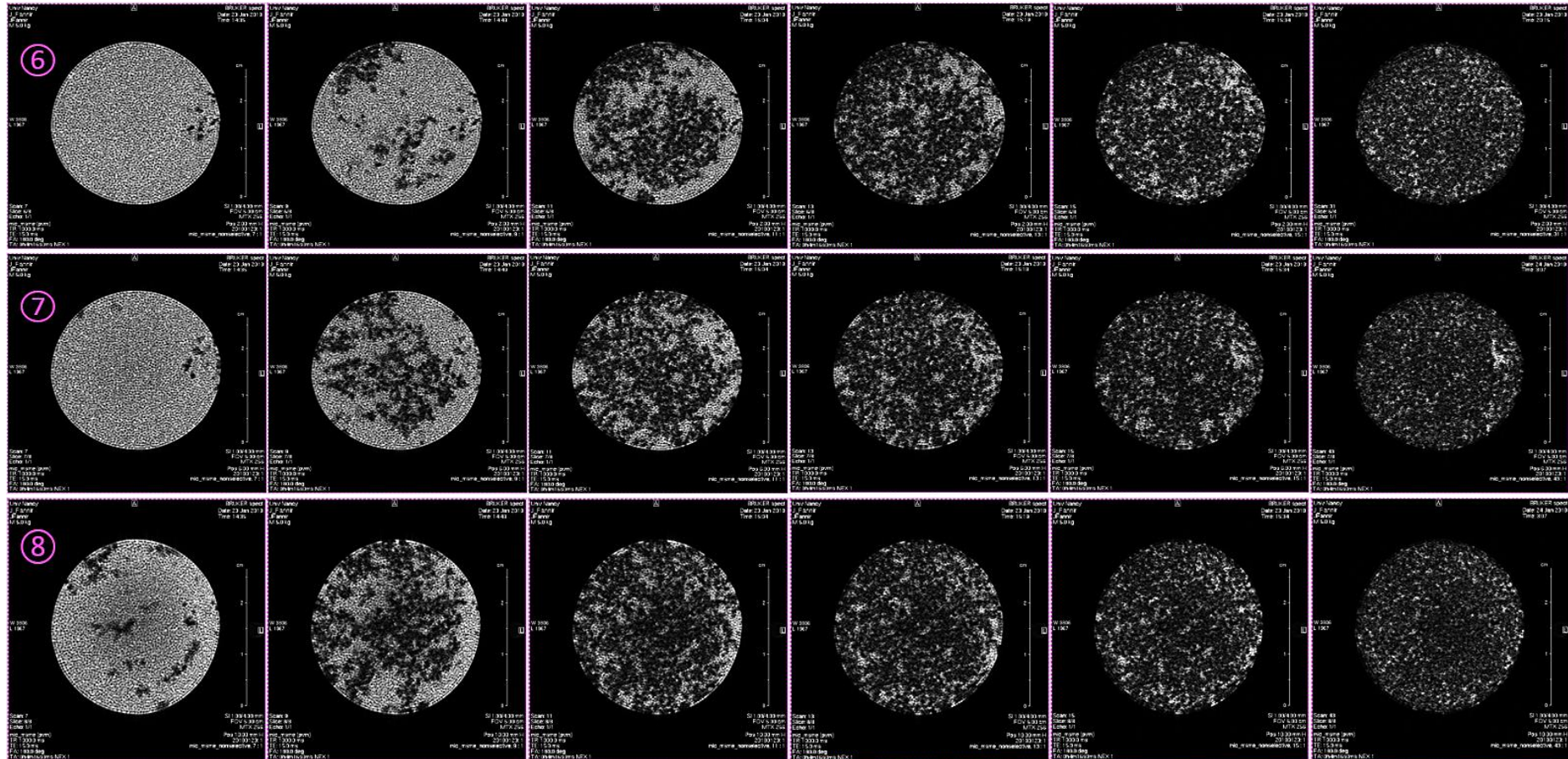
Figure 5.5 shows the consecutive images in the vertical and horizontal directions for the experiment on the polystyrene beads model with an injection flow rate of 0.12 mL/min. At the beginning of the acquisition, the porous medium being saturated with oil, the saturation is equal to (or close to) 1. Then, this saturation decreases progressively with time due to the sweep performed by the water injection, until the stabilization at a so-called residual saturation. For this test, water appears in the FOV around 3 hours after the start of the water injection. This delay in water intrusion varies from one test to another. It depends on the

injected flow rate and the water-oil contact position in respect of the bottom of the sample (before proceeding the injection of water).

Deformations of the edges of the image at the top and at the bottom for the vertical sections, clearly visible in Figure 5.5.a, correspond to the non-homogeneous detection regions of the MRI probe. A cropping of the image has therefore been performed in order to make observations only in undistorted areas of interest (the area between yellow dashed lines).

The vertical section makes it possible to obtain the information on the development of the phenomenon along a 1 mm thick slice in the centre of the sample. It is observed that during the fluid displacement the oil saturation is not uniformly distributed across the model. Therefore, it is necessary to take into consideration the data acquired from the horizontal sections as well.





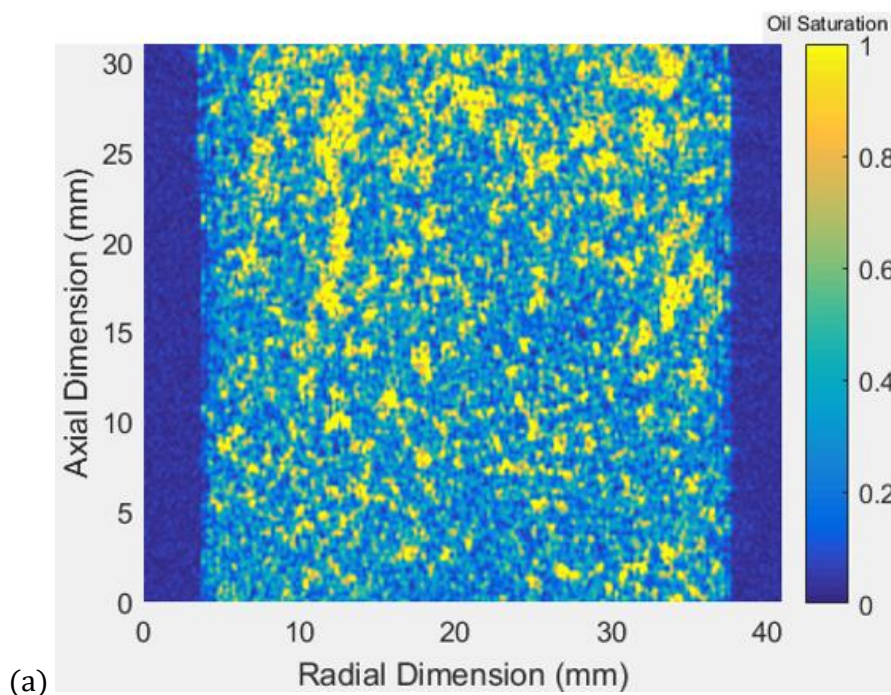
(b)

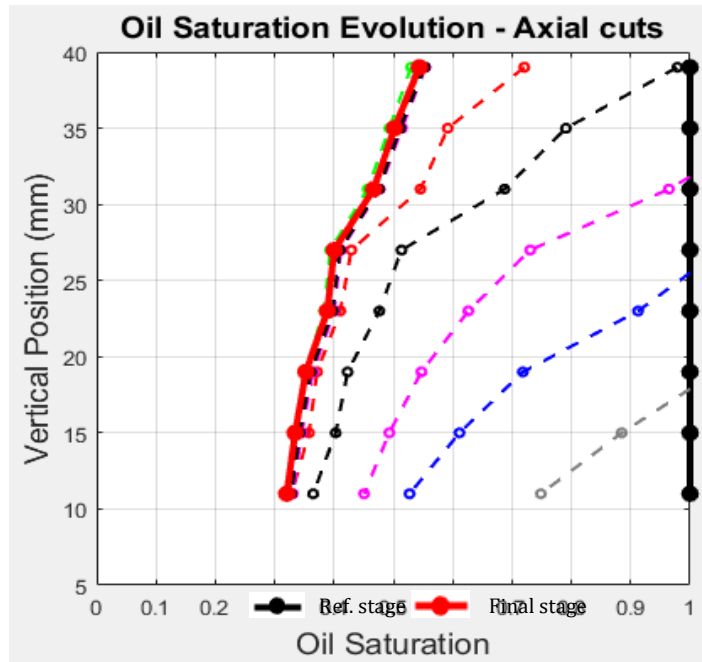
Figure 5.5. Consecutive MR images (ParaVision software) of water–oil displacement in the polystyrene beads model with an injection flow rate of 0.12 mL/min. The lighter areas correspond to those saturated with oil and the darker that gradually appear correspond to areas saturated with water. The acquisition of MRI signal was made each 15 minutes and shown here from the first water appearance in the FOV. The two dotted lines on the vertical images indicate the area of interest, where we can then perform the analysis and calculations. (a) Vertical cross-section. (b) The eight horizontal cross-sections.

The recorded data are then processed with the Matlab software in order to retrieve the images and perform the appropriate processing of these images. Digital processing under Matlab allows us to visualize the dynamics of the oil displacement, to highlight the impact of the different displacement criteria and to carry out a more detailed statistical analysis.

We observe that the displacement of the oil by water does not correspond to a piston-like flow, but generates fingers leading to a trapping of the oil during the two-phase flow. At the end of the displacement process, the total residual oil saturation, averaged through the sample volume, is equal to 38%.

Analysis of the last image (Fig. 5.6.a) of the series of previous vertical sections (Fig. 5.5.a), where the oil saturation was stabilized, shows an increasing distribution of the residual oil saturation as a function of the vertical position. The saturation is greater in the higher positions of the model (Fig. 5.6.b). The results show that the residual saturation varies globally between 0.32 in the lower section and 0.54 in the upper one. These differences are caused by the development of fingerings at the water-oil displacement front. We also note that the continuous field of low oil saturation, observed in figure 5.6.a in light blue colour, corresponds to an oil film left on the surface of the polystyrene beads. The variation of saturation of these zones depends on the thickness of these films and the interactions between oil, water and surface of the beads. Therefore, a distinction was made between these oil films and the oil occupying all the pores in the trapping area (yellow colour) due to the development of digitations.





(b)

Figure 5.6. (a) Residual oil saturation image in a vertical cross-section for the displacement process after the injection of 2.5 PV of water. (b) Time evolution of oil saturation profiles deduced from the 8 horizontal cross-sections, the acquisition of MRI signal was made each 15 minutes and shown here from the first water appearance in FOV.

For this test, the residual oil appears in two forms. The first corresponds to the large oil droplets grouped into small discontinuous formations, elongated in the direction of flow; the second is the oil films that cover the oil-wet polystyrene beads.

By studying the small areas on figure 5.6.a without big oil droplets the oil saturation less than 45% was observed. The statistical analysis of this experimental test (Fig. 5.7) shows that the oil saturation population less than 45% is equivalent to around two-third of total residual oil saturation, which was trapped in the form of thin films and small droplets due to hydrophobic behaviour of the bead surface.

The estimated oil saturation for large oil droplets (Fig. 5.6.a) is in the range from 45% to 100%. It represents approximately the last one-third of residual oil (Fig. 5.7). This amount of oil was trapped due to the development of digitations and the capillary effect.

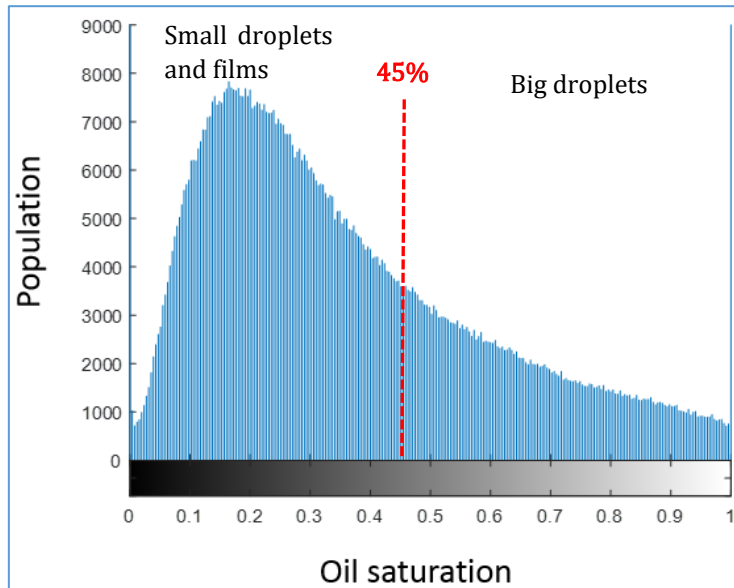
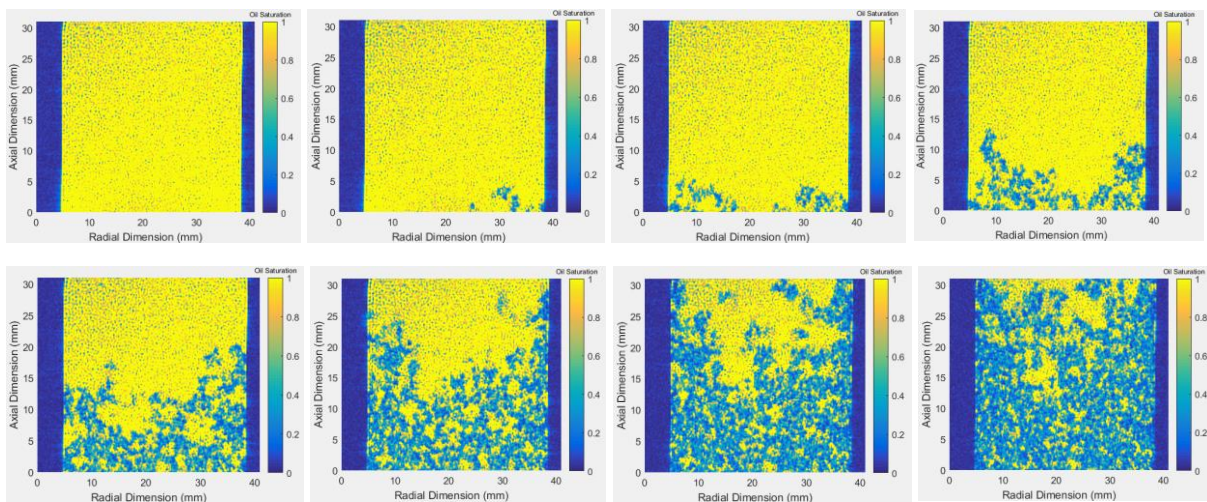


Figure 5.7. Histogram of residual oil distribution for the polystyrene beads model.

The lower and intermediate oil saturations on the histogram (Fig. 5.7) correspond to the film-form of fixed oil and the high saturations represent the droplets of oil trapped in the pores.

Because the development of the fingers depends on the time (or the distance covered by the water-oil front), the height of the porous sample has also been varied. The results for two sample models of various lengths with polystyrene packed beads were compared for the observation of the water-oil front displacement. A sample of 10 cm length was used previously and the observed results are presented in the paragraph 5.2.2.3. Subsequently, a longer sample of 16.5 cm in length (long tube model) was used to observe these phenomena at a more advanced stage of development (Fig. 5.8).



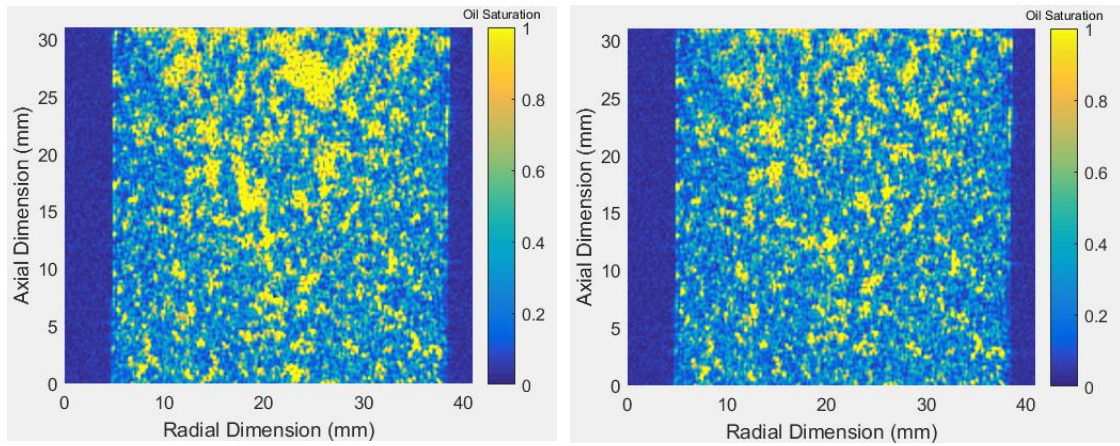


Figure 5.8. Visualization of the two-phase displacement in the long-tube model from the MR images of vertical sections. The oil is yellow and the water is light blue. The acquisition of MRI signal was made each 15 minutes and shown here from the first water appearance in FOV. The last image is the residual oil saturation image, where the oil saturation was stabilized.

The comparison of residual oil saturation for short and long models is shown on the following graph (Fig. 5.9). This comparison is according to the obtained MRI data of eight horizontal sections.

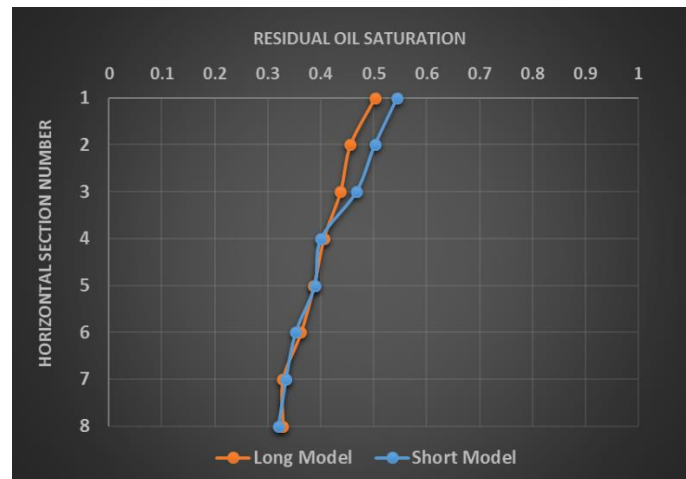


Figure 5.9. Average residual oil saturation comparison for short and long models, calculated as an average value for each horizontal section along the models.

It can be noted in this figure that the residual oil saturation varies overall between 0.32 and 0.54, with a difference of approximately 0.22 for the short model and between 0.33 and 0.5, with a difference of approximately 0.17 for the long model. This saturation increases gradually from the lowest section to the highest one, that is to say according to the direction of flow, and this increase can be seen for both models. However, the slope of the saturation curve has changed from section 3 in the case of the short model, while the long model has an almost constant slope. In addition, both models seem to record the same saturation values in the lower sections with a slight change in the last three sections.

For vertical slice data, the average residual oil saturation calculated for the short model is 0.356 vs. 0.354 for the long model. For the horizontal sections, the residual oil saturation averaged over the eight sections is equal to 0.32 in short model vs. 0.38 in long model. The

results confirm the same variation of final residual oil saturation with an increase in the residual saturation in the vertical direction due to the fingering phenomenon.

In the case of these experiments (polystyrene model), the porous medium is hydrophobic and therefore wetting with oil. In other words, the polystyrene-water surface tension is higher than the polystyrene-oil one, so that the polystyrene beads will prefer contact with the oil rather than with water. In such a configuration, the capillary forces are opposed to the flow and thus contribute to the stabilization of the oil-water displacement front. The appearance of fingerings then shows that the capillarity forces are not globally sufficient to ensure a stable moving front. Indeed, in order to have an effect of the capillary forces it is necessary that the pore size is sufficiently small. Also, due to the oil wettability of the porous medium, the flow of water is at the centre of the pores (Fig. 2.4 in chapter 2), so that the unmoved oil film remains on the surface of the grains, resulting in higher residual oil saturation (S_{or}).

In addition, we considered that the effects of capillarity and gravity forces on the development of digitations are negligible or not very significant in this type of porous media. The trapping of the oil would result from a macroscopic entrapment resulting from a high permeability of the medium. The permeability calculated using Kozeny-Corman equation (Eq. 4.1) gives $2.9E-10 \text{ m}^2$. In order to mitigate its effects, a smaller or finer grain size should be used. It would be advisable to use a hydrophilic porous medium rather than a hydrophobic one so as to analyze the inverse effect of the capillary forces on the development of fingerings. This has been taken into account for the next scenario, in which the experiments will be carried out on a fine sand. The development of a detailed experimental protocol will facilitate the realization of experiments and will make it possible to obtain data under the same study conditions in order to allow comparisons.

5.2.3 Experiments with packed sand column

The experiments on polystyrene and borosilicate beads have shown the internal structure of the porous model and the saturation distribution of phases in space and time. It was even possible to see beads of 0.6 mm diameter with the spatial resolution of MRI tool with 0.19 mm for 1 pixel. Unfortunately, this size of grains does not allow for the capillary forces to be important because of the large pore diameter. To study the simultaneous effect of the viscous, capillary and gravity forces, we have to reduce the grains size and also use some particle-size distribution. For this purpose, we used silica sand, and the experiments were performed at different injection rates (0.08, 0.12 and 0.16 mL/min).

Table 5.5 shows the main parameters of the experimental study with the packed sand model. The concentration of the manganese chloride was increased two times due to a slight adsorption effect of Mn^{2+} ions by sand. After carrying out some number of experiments, we have determined the concentration of manganese chloride (0.02 mole/L), which is enough to obtain the oil signal without interference from the water signal.

| | |
|--------------------|--|
| Porous | Packed sand of particle size $\sim 0.13 \text{ mm}$ diameter |
| Tube | Plastic tube of 10 cm net length |
| Injection rate | 0.06 mL/min |
| Estimated porosity | 39% |
| Permeability | $1.5E-11 \text{ m}^2$ |

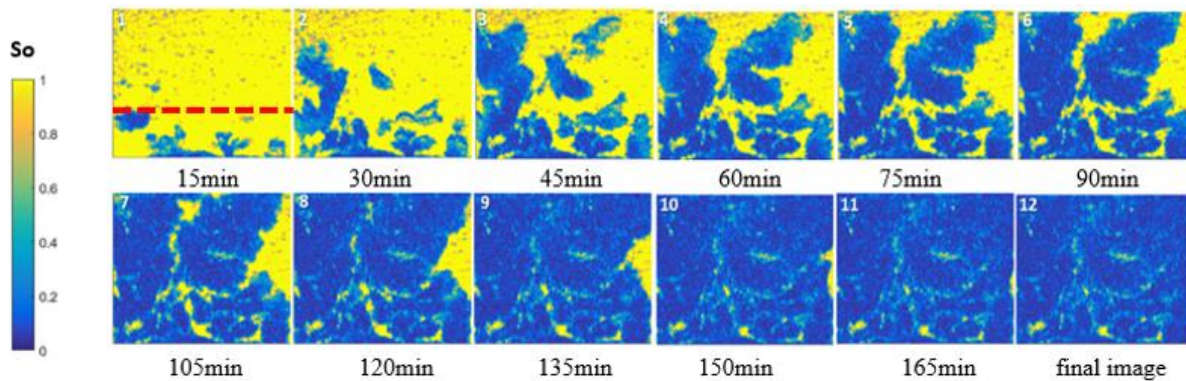
| | |
|-------------------------|--|
| Injected fluid | Pure water + MnCl ₂ (C = 0.02 mole/l) |
| Oil phase (kerosene) | PTX2000 $\rho = 800 \text{ kg/m}^3$, $\mu = 2.96 \text{ mPa s}$ at 20°C |
| MRI Field of view | 5 cm (256 x 256 pixels) |
| TR (time of repetition) | 1 s |
| TE (time of echo) | 5 ms |

Table 5.5. The experiment parameters of packed sand model, non-selective method (NSM).

Reference images of the sand model were acquired before starting the experiments in order to verify its compatibility with our imaging protocols. As the impact of the sand on the signal and especially on the relaxation times of oil was not observed, the sand model was supposed acceptable. The sand was packed using a vibrating table and then lightly compacted by hand. An estimation of the porosity was done in Annex III. The permeability of the sand model was calculated from the porosity and the particle size with Kozeny-Carman question, Table 4.1.

The oil extraction by water flooding in the packed sand model was performed with the same range of injection rates as in the polystyrene bead model, i.e. 0.08, 0.12 and 0.16 mL/min. The experiments were repeated several times for each rate to check reproducibility.

A series of twelve consecutive images with an interval of 15 minutes is shown in figure 5.10 from the first appearance of water in FOV (i.e. 1h50 after the start of water injection). The shape and the growth of fingers can be clearly observed in these pictures. The first fingers appear in the local micro imperfections of the sand model. Then, they slowly grow in space with help of the capillary forces. The next breakthrough of the fingering happens only when the water saturation on the front reaches a sufficient value. New fingers then appear and start to grow. An alternation between the capillary penetration and the appearance of a new viscous finger was observed. The time between these alternations depends on the injection rate and the model permeability.



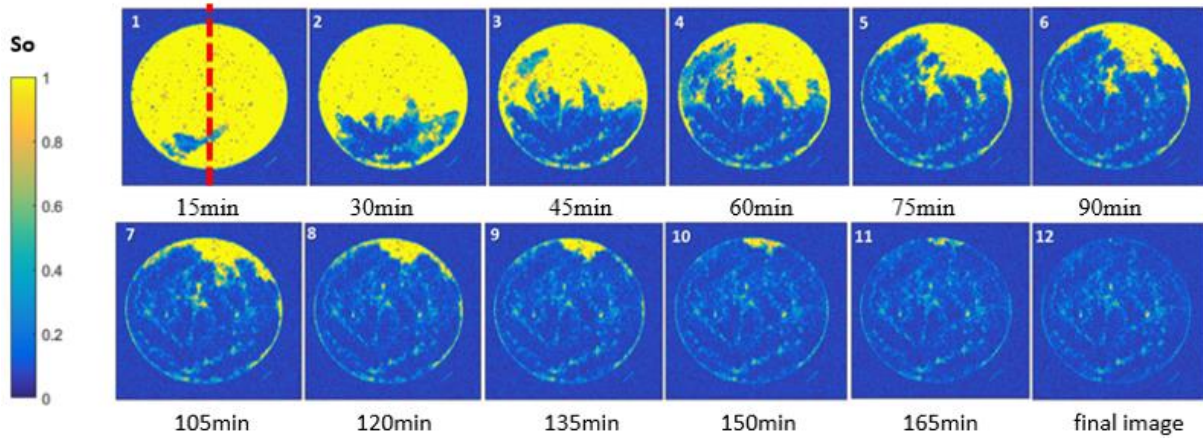


Figure 5.10. Consecutive MR images of the water–oil displacement in the packed sand model with an injection flow rate of 0.12 mL/min. The oil is yellow and the water is blue. The time interval between each image is equal to 15 minutes from the first water appearance in the FOV. The dotted line on the first vertical section indicates the position of the horizontal sections (and vice-versa for the horizontal section below).

The vertical and horizontal cross-sections from Figure 5.10 show that the loss of connectivity of the oil phase between the water fingers leads to an entrapment of the oil. For this experiment the final residual oil saturation after injection of 3 pore volumes of water is equal to 11 %.

To better understand the mechanism of the pulsating movements observed under slow injection conditions, a series of pictures is given in Figure 5.12.

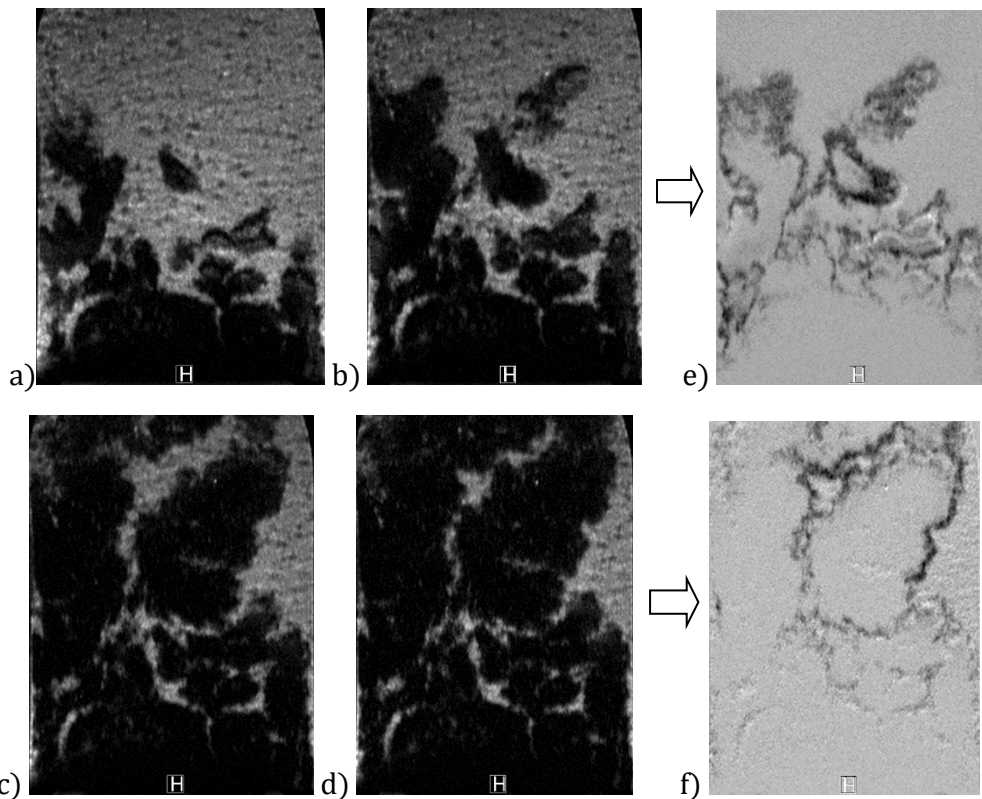
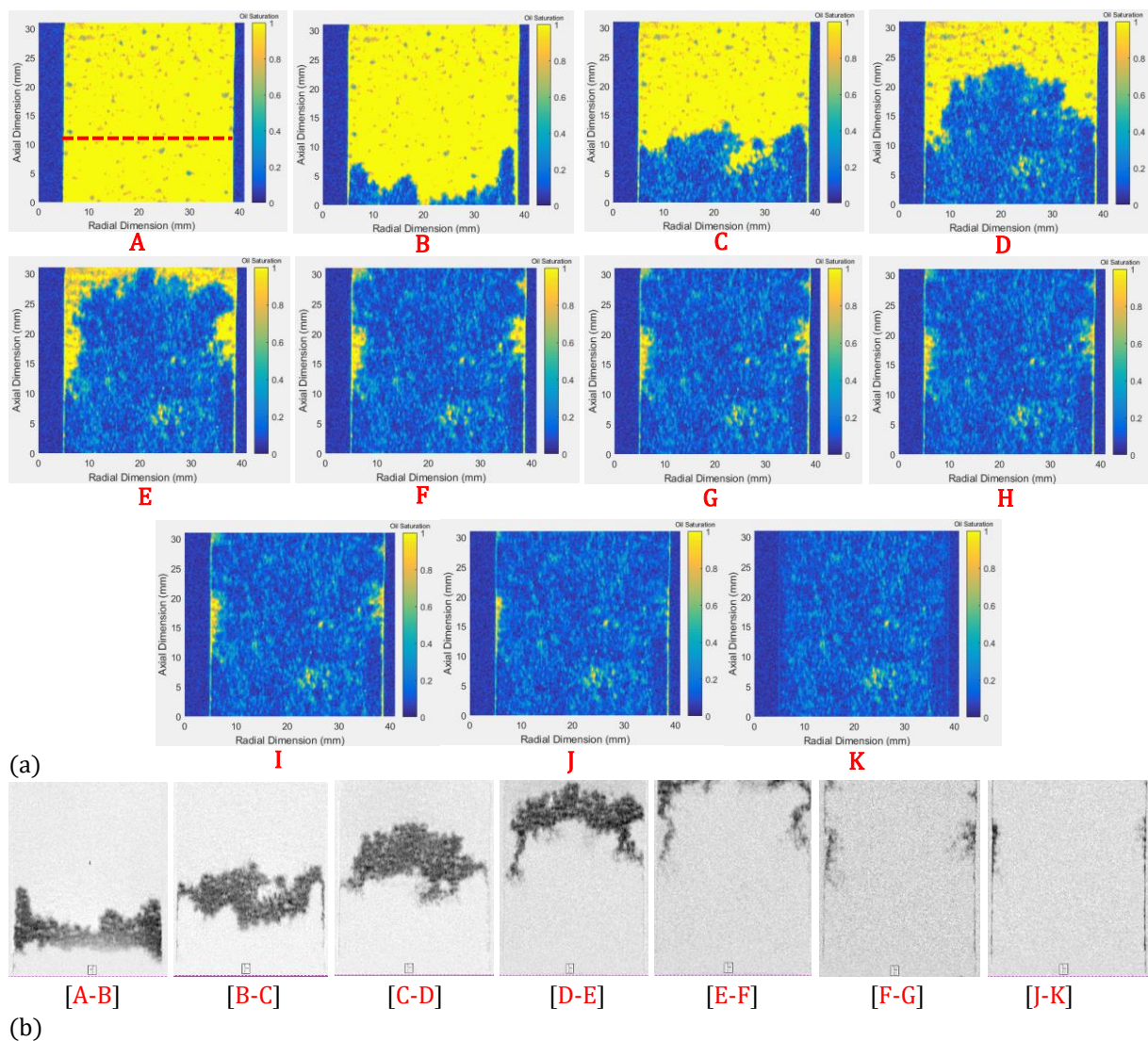


Figure 5.11. Oil-water displacement in the sand model, $Q_{inj} = 0.12$ mL/min: (a, b, c, d) consecutive images of fingers growth with an interval of 15 minutes; (e): difference between images (a) and (b). (f): difference between images (c) and (d). These two image differences show the local area where the displacement occurs.

The difference between the signals of two consecutive images highlights the movement of the two phases. Figure 5.11 (e) corresponds to the difference of signal for images (a) and (b). Here, the intensity of the grey colour indicates the part of the front where the changes in the saturation occur. Unlike stacked beads, the saturation variations for the sand model occur on the perimeter of the larger fingers caused by capillary displacement. The areas filled in grey (Fig. 5.11.e) correspond to the emergence of a new finger caused by the viscous force. For this experiment the average flow velocity is of the order of $1.0E-5$ m/s (estimated from injection rate which takes into account the volume of residual oil). From Figure 5.11(f), the averaged front diffusion velocity in any direction was estimated as $1.0E-6$ m/s. It means that the axial redistribution of water is slower than the average flow velocity in vertical direction.

The water injection experiments on sand were acquired with different flow rates. The observed process was similar, with the difference in the size of the fingers and the time of alternation of the capillary penetration (Fig.5.12).



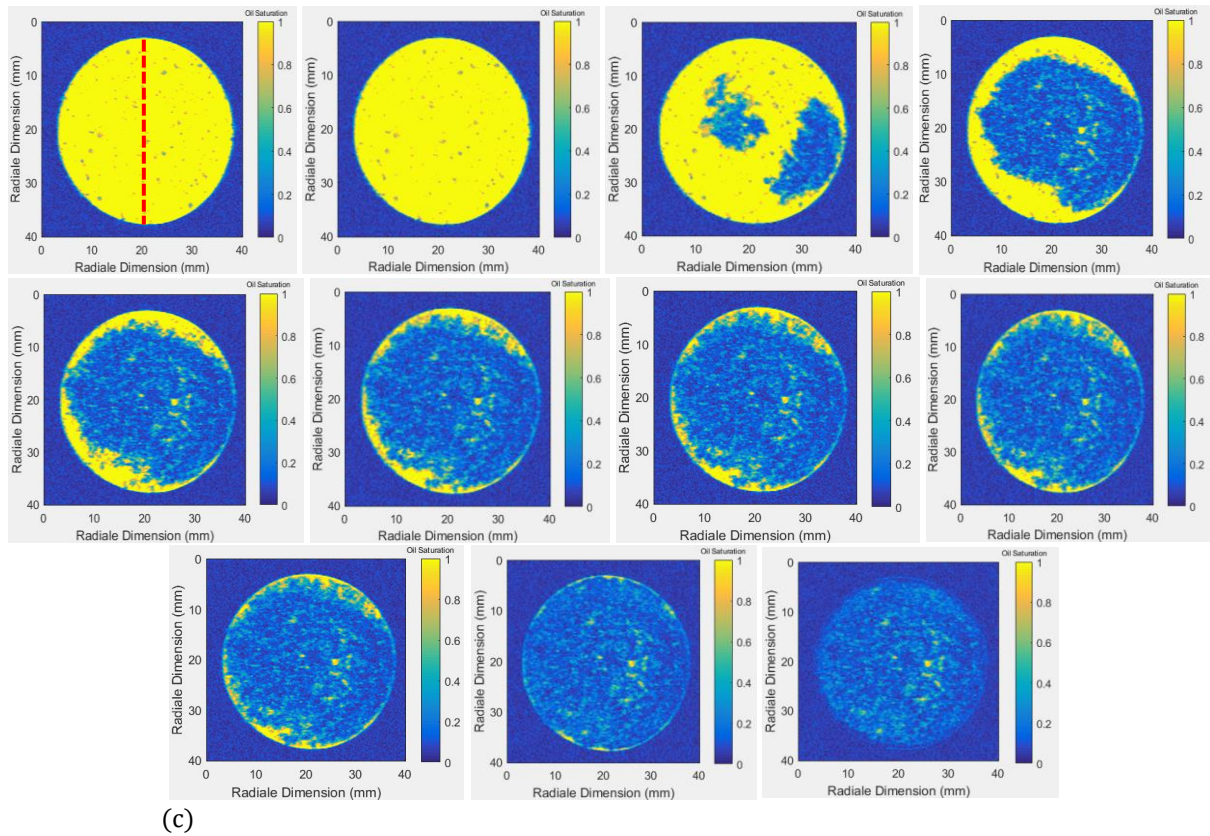
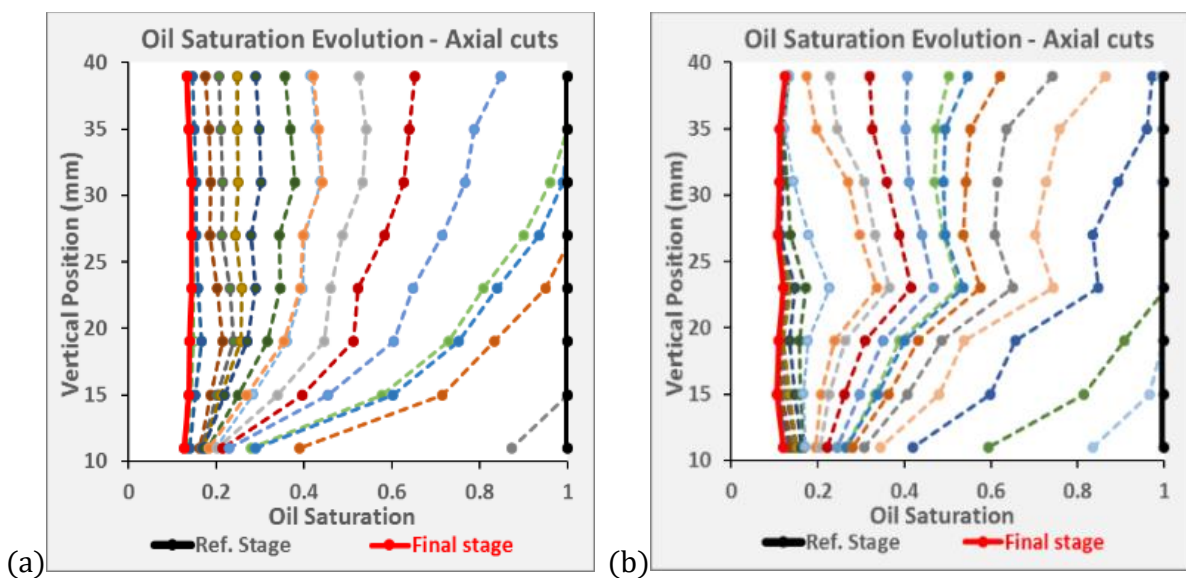


Figure 5.12. (a) & (c): Consecutive MR images of the water–oil displacement in packed sand model with a high injection flow rate of 0.16 mL/min. The oil is yellow and the water is blue. (ParaVision images are detailed in Appendix). The time interval between each image is equal to 15 minutes from the first water appearance in the FOV. The dotted line on the first vertical section indicates the position of the horizontal cross-sections (and vice-versa for the horizontal cross-section below). (b) The difference between vertical images to show the local area where the displacement occurs.

Saturation profiles along the vertical axis were reconstructed from images for each acquisition step for different rates: low rate of 0.08 mL/min, medium rate of 0.12 mL/min and a high flow rate of 0.16 mL/min.



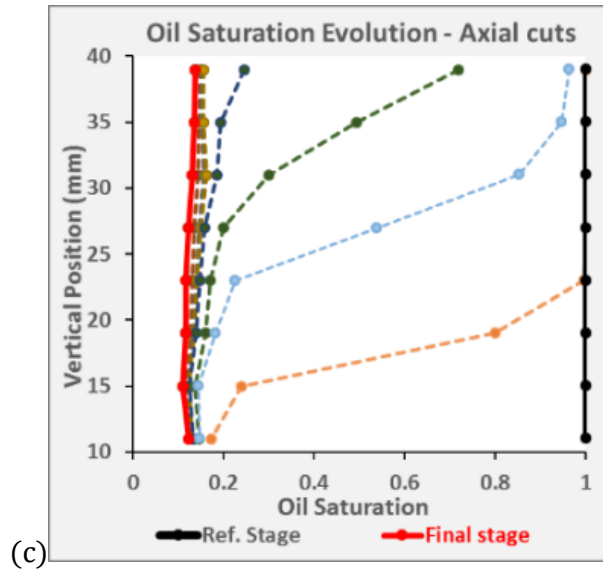


Figure 5.13. Oil saturation distribution in the packed sand model at different injection flow rates: (a) 0.08 mL/min, (b) 0.12 mL/min and (c) 0.16 mL/min. The acquisition of MRI signal was made each 15 minutes and shown here from the first water appearance in FOV.

Figure 5.13 shows the saturation profiles of oil phase recorded at regular intervals (15 minutes) during the experiments at three different flow rates. At lower injection rate (Fig. 5.13.a), the average saturation in vertical direction increases more monotonously comparing with higher injection rate (Fig. 5.13.b). When the injection rate increases twice (Fig. 5.13.c), the displacement is quite stable and seems to be piston like.

Table 5.6 summarizes the average residual oil saturation for each case. Remaining oil saturation is much lower for the packed sand model than for the polystyrene beads model due to the wettability effect (water-wet). Each experiment was repeated to confirm the obtained results. The oil saturation results ranged from around 10 % to 14 % at three different injection rates. The residual oil saturations for the various injection flow rate are of the same magnitude with a slight increase for the cases of slow displacement.

| Q_{inj} (mL/min) | 0.08 | 0.12 | 0.16 |
|---------------------|--------|--------|--------|
| S_{or} (series 1) | 13.8 % | 11.3 % | 11.8 % |
| S_{or} (series 2) | 13.9 % | 9.7 % | 12.3 % |

Table 5.6. Residual oil saturation at different injection rates for the packed sand model.

Figure 5.14 shows the histogram of the residual oil saturation for the sand model. The maximum values observed for the oil saturation at the final stage is around 0.6, which is different from the polystyrene model (Fig. 5.8) where the range can reach 1, due to the rest of big droplets of trapped oil.

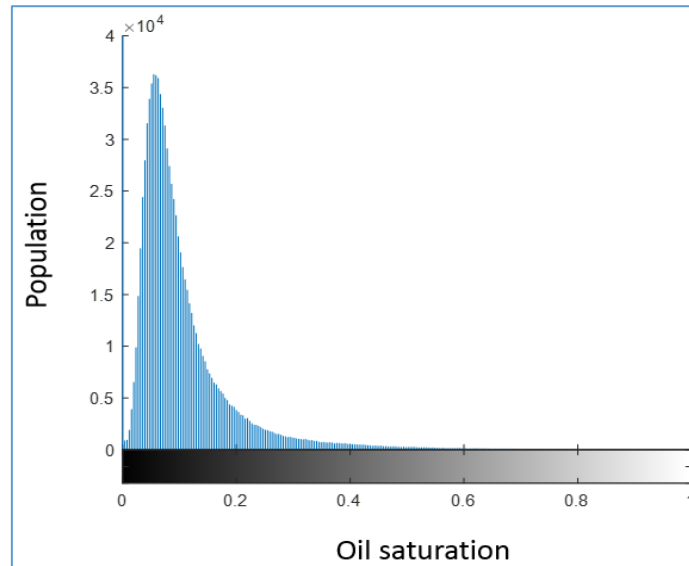


Figure 5.14 Histogram of residual oil distribution for the packed sand model ($Q_{inj} = 0.12$ mL/min).

The evolution of the averaged oil saturation as a function of time was calculated through the pore volume (PV) of the model and is presented in Figure 5.15.

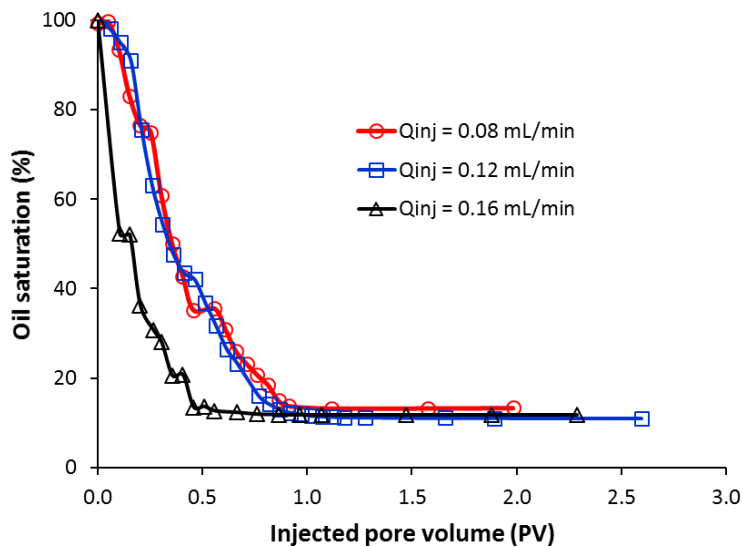


Figure 5.15. Averaged oil saturation vs injected PV for the packed sand model.

Most experiments with low injection rate show the stabilization of oil saturation up to S_{or} after 1 of PV injected, and for the rapid displacement one half of PV injected was enough to replace the mobile oil.

5.3 Relative phase permeability calculation

The experimental results of the displacement process gave us the possibility to determine the relative permeability (RP). Basing on the classical approach, that the relative permeability is the function of saturation only, we show the validity of $k_r(S)$ for our experimental model.

By definition, RP is a function which characterizes the reduction in flow capability of one phase due to the presence of other phases in the medium. The shape of this function depends mostly on the relative volume of fluid (phase saturation), but also on the rock wettability, geometry of the pore spaces and phase distribution.

The method of Johnson-Bossler-Naumann [81] for unsteady state displacement experiments was used. During the displacement of oil by water the measured saturation of oil was taken as the averaged value from the whole volume of area of interest studied by MRI. The saturation of oil obtained from the MR signal intensity is presented on the Figure 5.16.

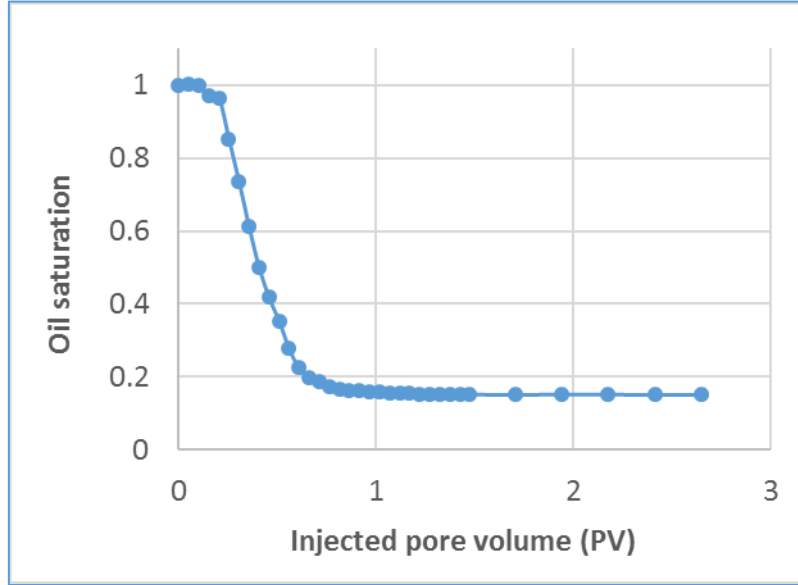


Figure 5.16. Averaged oil saturation vs injected PV for the model of packed sand for injected flow rate $Q_{inj} = 0.12$ mL/min.

The injection velocity can be fined from the injection flow rate as follows:

$$V_{tot} = \frac{Q_{inj}}{A} = \frac{Q_{inj}}{\pi r^2} \quad (5.1)$$

where Q_{inj} is the flow rate generated by the syringe pump, A is the cross-section area of the model, r is the inner radius of the model.

We have measured the oil saturation evaluation in the area of interest each 15 minutes. The difference ΔS_{oil} between the measurements represent the volume of oil moved and displaced in the vertical section of the model. Thus, the value of ΔS_{oil} is the variation of mobile oil volume in studied area, which does not take into account the volume of trapped oil. Therefore, the average velocity of oil phase can be evaluated as follows:

$$V_{oil} = \frac{\Delta S_{oil}}{\Delta t} \frac{PV}{A} = \frac{\Delta S_{oil}}{\Delta t} L\phi \quad (5.2)$$

where ΔS_{oil} is the variation of the oil saturation in the area of interest during the time period of Δt , PV and L are the pore volume and the length of the area of interest, ϕ is the porosity.

The total velocity for displacement process is taken as the injection velocity from the syringe pump. The Figure 5.17 below shows the evaluation of averaged oil velocity (blue curve) and the total velocity (red line) in respect to the pore volume injected. The oscillations of the

averaged oil velocity can be explained by the variation of the direction of flow from vertical movement to the radial spreading and local downwards flow caused by gravity.

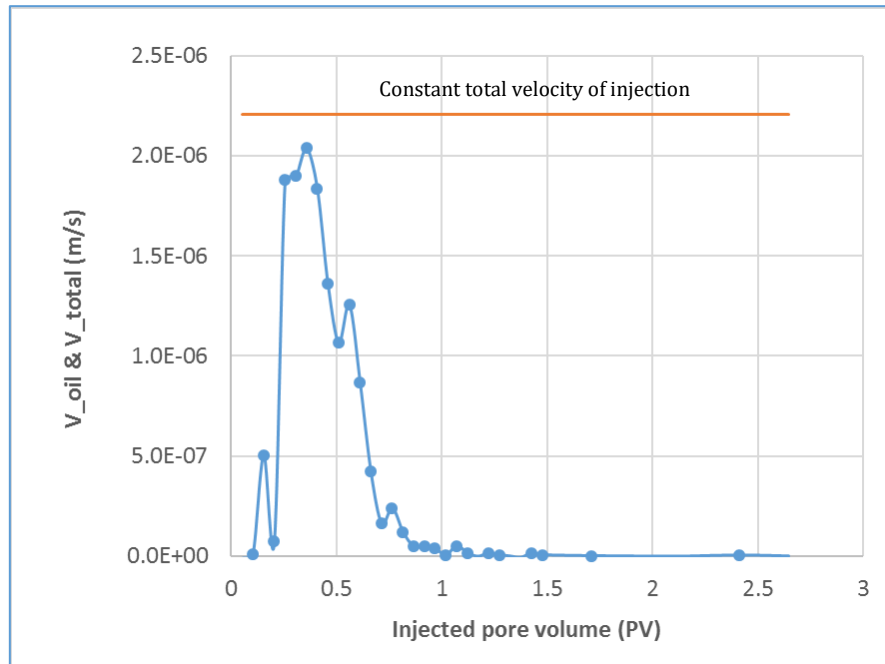


Figure 5.17. Averaged oil velocity and the constant total velocity of injection (2.2E-6 m/s) vs injected PV for the model of packed sand, $Q_{inj} = 0.12$ mL/min.

The general relation for phase permeability is given by Darcy's law:

$$K_{oil} = -\frac{\mu_{oil}}{grad P} |\vec{V}_{oil}| \quad (5.3)$$

Where K_{oil} is the phase permeability for oil, P is the pressure, μ_{oil} is the dynamic viscosity and \vec{V}_{oil} is Darcy's velocity of oil phase.

The relative phase permeability for oil phase can be calculated as the ratio between oil phase velocity and the total velocity:

$$k_{ro} = \frac{K_{oil}}{K} = \left(-\frac{\mu_{oil}}{grad P} V_{oil} \right) \times \left(-\frac{grad P}{\mu_{oil} V_{tot}} \right) = \frac{V_{oil}}{V_{tot}} \quad (5.4)$$

We suppose that the condition of constant inlet and outlet pressure are respected, because we have the constant flow rate and very slow variation of saturation in the model. Following the experimental setup, the outlet pressure was maintained by the constant level of output tank. The large diameter of the tank allows to keep the same level of oil in this recipient and to not be significantly perturbed by the very small volume of evacuated oil phase. The constant inlet pressure condition is maintained by the syringe pump.

The Figure 5.18 shows the relative permeability for oil phase for the experiment on the sand model with the injection flow rate of 0.12 mL/min.

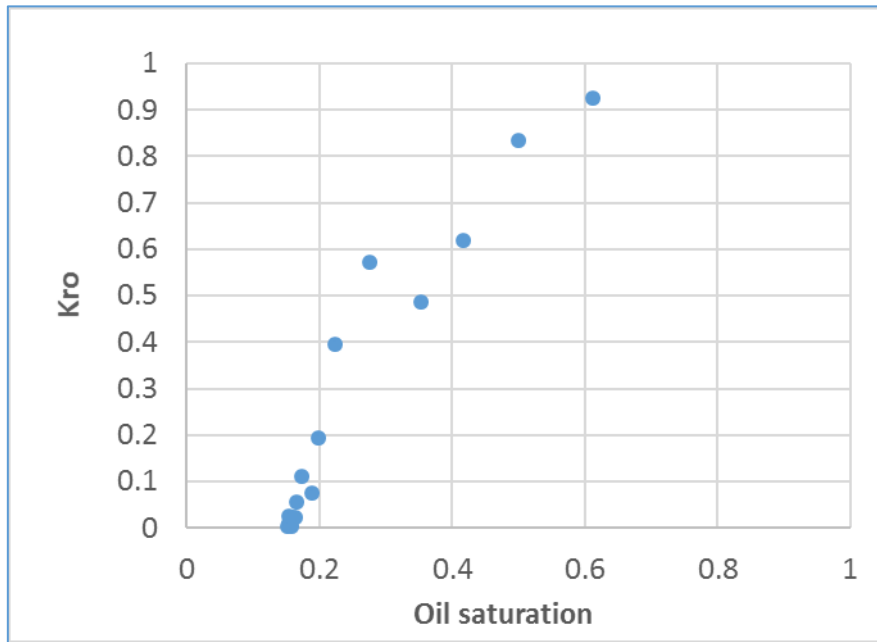
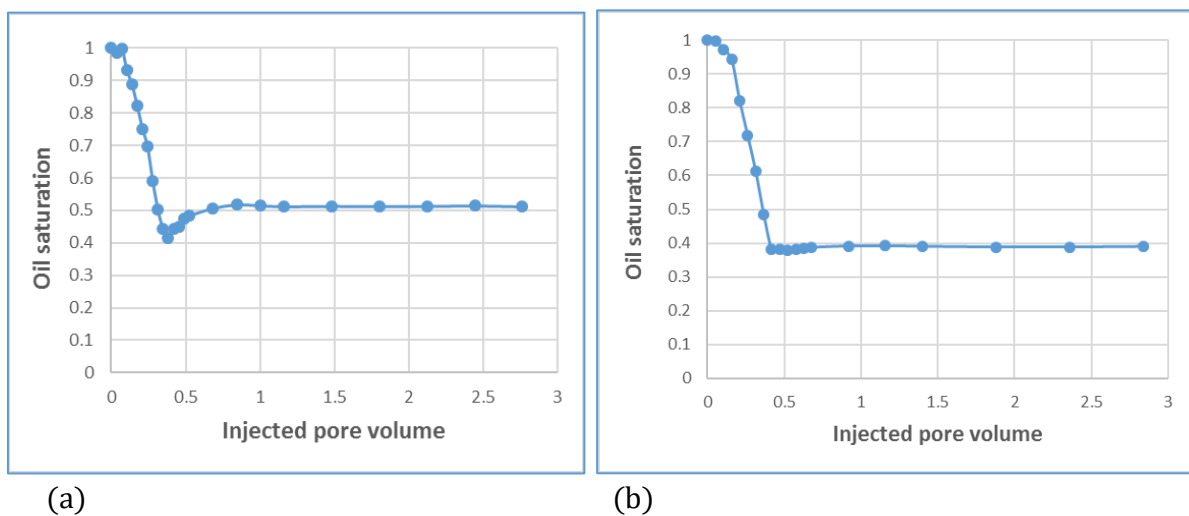


Figure 5.18. Relative permeability of non-wetting phase (oil) in the sand sample for injected flow rate $Q_{inj} = 0.12$ mL/min.

The points on the Figure 5.18 were plotted for the time interval from the appearance of the water in the inlet of FOV up to the water breakthrough to the outlet of the area of interest. The residual oil saturation, $S_{ro} = 0.15$, which was obtained from the experimental study, is clearly observed in the Figure 5.18 by the number of points corresponding for this value of oil saturation.

Polystyrene beads model

The Figure 5.19 shows the Averaged oil saturation vs injected PV for the model of polystyrene beads with the different injection flow rates.



(a)

(b)

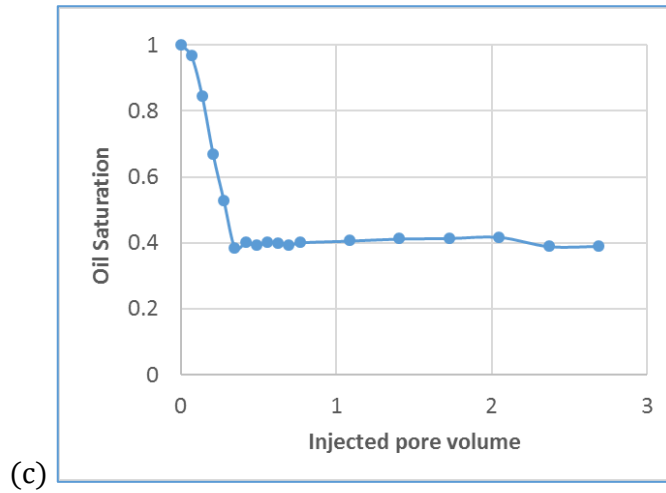


Figure 5.19. Averaged oil saturation vs injected PV for the model of polystyrene beads, (a) $Q_{inj} = 0.08$ mL/min; (b) $Q_{inj} = 0.12$ mL/min; (c) $Q_{inj} = 0.16$ mL/min.

Averaged oil velocity and the constant total velocity of injection vs injected PV for the model of polystyrene are shown in the figures below:

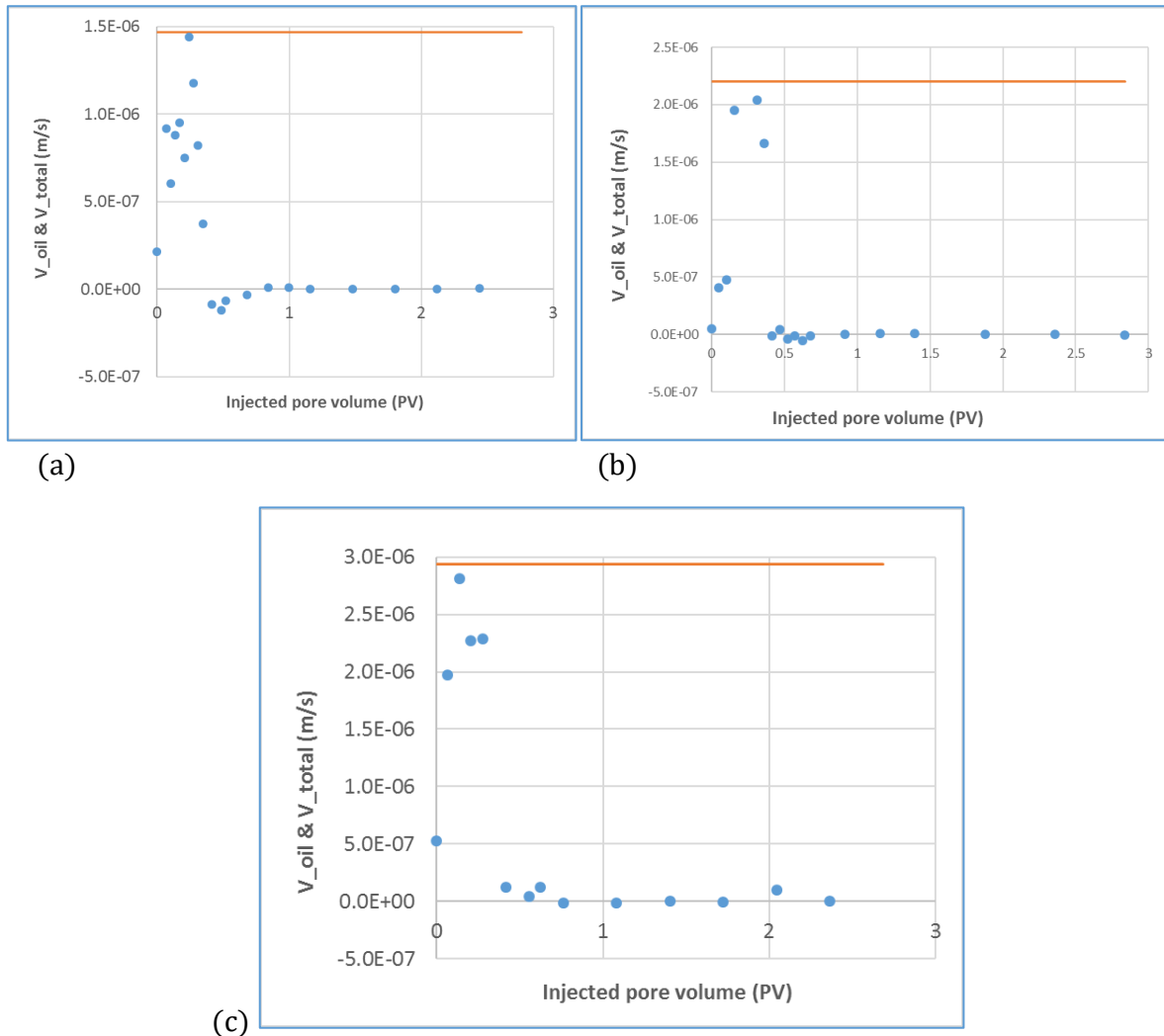


Figure 5.20 Averaged oil velocity and the constant total velocity of injection ($2.94E-6$ m/s) vs injected PV for the model of polystyrene beads, (a) $Q_{inj} = 0.08$ mL/min; (b) $Q_{inj} = 0.12$ mL/min; (c) $Q_{inj} = 0.16$ mL/min.

The Figure 5.21 shows the relative permeability for oil phase for the experiment on the polystyrene beads model with the different injection flow rates.

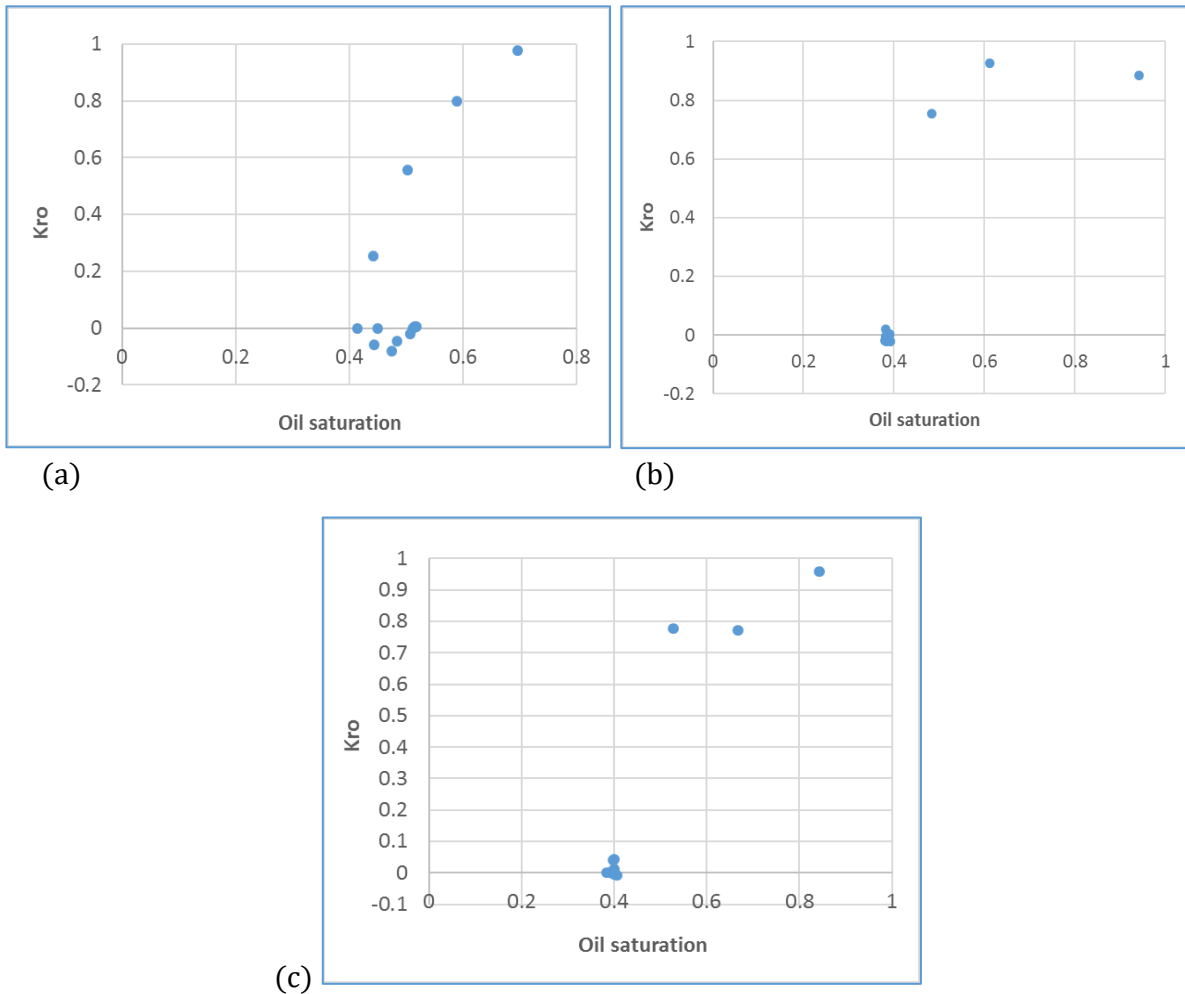


Figure 5.21. Relative permeability curve for nonwetting phase (oil) in the polystyrene beads model for different injected flow rates, (a) $Q_{inj} = 0.08$ mL/min; (b) $Q_{inj} = 0.12$ mL/min; (c) $Q_{inj} = 0.16$ mL/min.

The JBN method gives the generalized RP for the studied porous sample. In the displacement processes with mobile interfaces, the RP functions can be non-unique for the porous volumes containing these interfaces or not. Also, for the macroscopic flow in the direction of the pressure gradient, RP must be determined in each coordinate of the flow direction. With the proposed techniques, it is easily to obtain the RP for the chosen coordinate by the homogenization of saturation in the corresponding model volume because the MRI techniques allows to have the oil saturation for each pixel in area of interest for each acquisition time.

5.4 Discussion

The main purpose of the image processing was to visualize the dynamics of the oil displacement and also to highlight the influence of the different parameters governing the viscous digitisation mechanism on the residual oil saturation variation. The phenomenon of viscous digitation/fingering in porous media has been much discussed in the literature by several authors [82-89]. It is simply stated that the viscous fingering is governed by the forces

of gravity, viscosity and capillarity. These three forces can act as stabilizing forces or destabilizing forces of the displacement front, depending on the case conditions and material [90]. In the case of our study, the properties of the different fluids used remain constant, particularly with regard to fluids viscosity and density, the influence of the variation in these properties could not be analyzed. However, the viscosity contrast in the case of our study is not very consistent. It is therefore not absurd to postulate for a negligible influence of the viscosity forces. In addition, the gravity force has the opposite direction to the flow of displacement. Therefore, the gravity would reduce the growth of fingering.

In a porous medium, the capillarity forces are a function of the pore size, the surface tension between fluid and the wettability of the medium. It is recalled that according to the Young-Laplace law, the capillary pressure is given by the following equation:

$$\Delta p = p_c = p_o - p_w = \frac{2 \cdot \sigma_{ow} \cdot \cos \theta_{ow}}{r_c} \quad (5.5)$$

Where r_c is the tube radius, σ is the water-oil surface tension, θ is the contact angle and r_c is the pore radius.

Thus, the larger the pore size r_c , the lower the capillary pressure. Moreover, the orientation of these forces depends on the wettability of the medium. Depending on whether the medium is wetting or not to the displaced fluid, the capillarity forces tend to oppose or to be in the flow direction, and thus stabilizes or destabilizes the front movement (Wang, Feyen and Elrick, 1998).

In order to investigate the interaction of viscosity, gravity and capillary forces on oil displacement mechanism and residual oil saturation, the experimental results of sand model are analysed using proper dimensionless numbers.

5.4.1 Dimensionless groups

As discussed in section 2.3.4 of chapter 2, capillary number (Ca) and Bond number (Bo) are the main dimensional groups usually suggested to compute the relative magnitude of the prevailing forces in the water flood process:

$$Ca = \frac{d^2 v \mu_w}{K \sigma \cos \theta} \quad (5.6)$$

$$Bo = \frac{\Delta \rho g d^2}{\sigma \cos \theta} \quad (5.7)$$

The pore size d can be calculated as the hydraulic diameter deduced from the average grain diameter d_p and the porosity φ :

$$d = \frac{2\varphi}{3(1-\varphi)} d_p \quad (5.8)$$

In the following, the residual oil saturation from each sand experiment are analysed using the above-mentioned groups, taking into account different injection rates.

The capillary number is an important parameter to determine the stability of water displacement process. For low capillary number, less than $10E-5$, flow is dominated by

capillary forces [61]. The result at low flow rate has showed a slight increase of the residual oil (Table 5.6). Table 5.7 shows the relationship between the capillary number (Ca) and residual oil saturation (S_{or}) at different water injection rates. At low flow rate the capillary number decreases which can explain the increase of residual oil trapped in the porous medium because of capillary fingers growth.

| Q_{inj} (mL/min) | 0.08 | 0.12 | 0.16 |
|---------------------|----------|----------|----------|
| S_{or} (series 1) | 13.8 % | 11.3 % | 11.8 % |
| Ca | 6.41E-06 | 9.61E-06 | 1.28E-05 |

Table 5.7. Residual oil saturation at different injection rates for the packed sand model.

The experiments on sands with dominating capillary forces, $Q_{inj} = 0.08$ mL/min, have demonstrated a little lower “washing effect” for the displacement of oil. It confirms the contribution of the viscous forces on the displacement process at higher capillary numbers.

Fig. 5.22 shows a schematic capillary desaturation curves CDC [91] obtained from the experimental observation of residual saturation for non-wetting (red) and wetting (blue) phases.

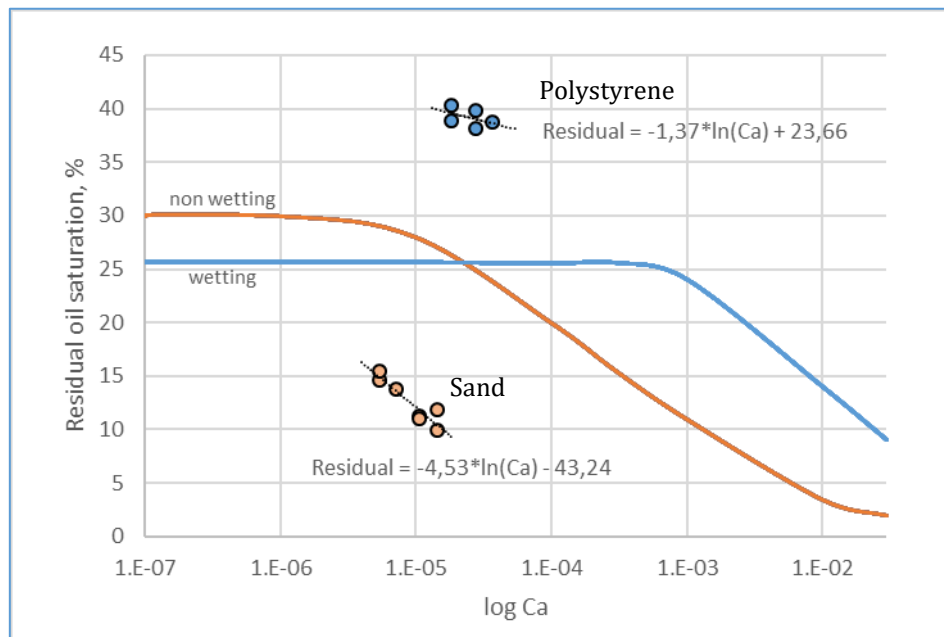


Figure 5.22. Comparison of capillary desaturation curves for wetting (blue) and non-wetting (red) media [91] and experimental results.

On the Fig. 5.22 the points correspond to the results obtained from our experimental studies. The blue points show the relation between the residual oil saturation and capillary numbers (Ca) for the model of polystyrene beads, which corresponds to the wetting medium for oil. Residual oil saturation was obtained for the experiments with the following injection rates: 0.08, 0.12 and 0.16 mL/min. The points have the slight tendency of S_{or} decreasing with increasing of Ca . The same tendency was observed for the CDC (Fig. 5.22) for the capillary number greater than the critical Ca . For our experiments we have obtained the decreasing of S_{or} for the low capillary numbers, it means that the critical Ca for the medium of polystyrene beads is different that observed by Lake and other authors.

From the observation of CDC it can be marked that the residual saturation for wetting system is higher than for non-wetting one for the capillary number greater than $\sim 2E-5$. From our experiments the residual saturation of non-wetting phase is greater than for the wetting phase for the capillary number of order $\sim 1E-5$, which is sufficiently coherent.

The red points on the Figure 5.22 show the residual oil saturation obtained from the model of the packed sand, where oil is considered as a non-wetting fluid. The trend of decreasing of oil saturation with respect to the greater capillary numbers is more evident for this kind of medium. The residual oil saturation corresponds to the rates of experiments as 0.06, 0.08, 0.12 and 0.16 mL/min.

In our experiments we could not go to the lower capillary numbers by variation of the injection flow rate because of the time of duration of our experiment and impossibility to tune it manually during the night. The experiments with the lower capillary number will be done in the fuser investigations by using the surfactants.

As for the Bond number, it becomes important when the buoyancy forces are noticeable. This condition requires a vertical direction of flow and a variation in fluid density between wetting and non-wetting phases, which is the case in our experiments.

The results show that in sand model experiments, the Bond number is equal to $Bo = 1.26E-04$. It is the same for all cases of sand models because there are no changes in fluid properties nor grain size. The gravitational forces are therefore relatively small compared to those of capillarity in our experiments.

Both Ca and Bo numbers confirm the important effect of the capillary phenomena. Therefore, the oil displacement largely depends on the capillary forces in the porous medium.

5.4.2 Displacement mechanism and the wettability effect

The three displacement forces of gravity, viscosity and capillarity can act as stabilizing or destabilizing forces of the displacement front depending on the case study. In our case, the properties of the different fluids used remain constant, especially with regards to the viscosity and the density. The viscosity contrast between the two fluids (2.9 cP for oil and 1 cP for water) is not very high, which makes it possible to suppose that initially the viscous effects are not dominant. Furthermore, the direction of the main flow is opposite to the gravity. Therefore, the gravity forces would tend to oppose the development of the fingerings along the model and to stabilize the displacement of the moving front. However, the MRI images of the experiments show that the flow is not in the form of a piston and generates fingerings of different scales.

If the capillarity effects are negligible (which is not the case here at all), it has long been known, C. Marle [92] that the displacement front is unstable when the injection velocity is greater than a critical value whose estimation is:

$$v_c = \frac{K g (\rho_w - \rho_o)}{\varphi(\mu_o - \mu_w)} \quad (5.9)$$

For experiments with sand, this critical velocity is about $0.040 \text{ mm}\cdot\text{s}^{-1}$ calculated from the data in Tables 4.1 and 4.2 (chapter 4). As for the injection rates, they lead to interstitial velocities

between 0.0038 and $0.0075 \text{ mm}\cdot\text{s}^{-1}$ below the critical value. However, the intrinsic permeability estimated here from the Kozeny-Carman formula (Eq. 4.1) has an uncertainty. Given the fairly large grain size distribution, it is likely that the intrinsic permeability is much lower than $K = 1.5\text{E-}11 \text{ m}^2$ estimated in Table 4.1. It is therefore likely that the displacement of the oil by the water in our experiments might result in viscous digitations.

In order to settling the question, one can refer to the phase diagram proposed by R. Lenormand et al. [93, 94] (Fig. 5.23) connecting the viscosity ratio to the capillary number. The values $\log(\mu_w/\mu_{nw}) = 0.47$ and $\log(Ca) \sim -5$ confirm that the experiments are located at the crossing between stable displacement and capillary fingering.

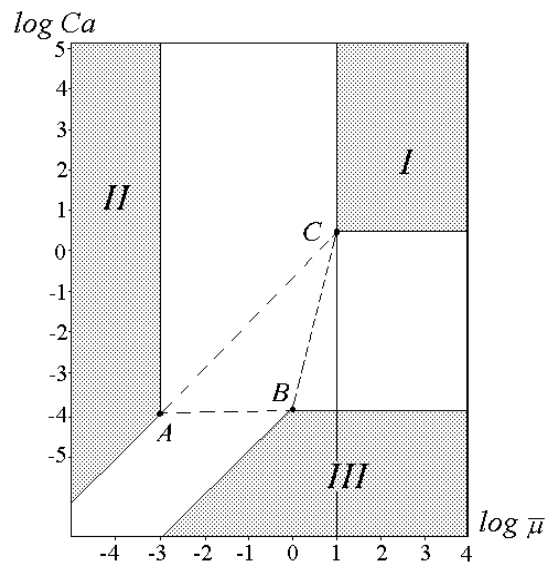


Figure 5.23. Diagram of flow regimes: I is stable displacement; II is viscous fingering; III is discontinuous capillary fingering [93].

Moreover, even if the porous medium was prepared in homogenous way, the local heterogeneities on micro-scale cause the appearance of fingers and non-symmetry in horizontal sections (Fig. 5.10). Nevertheless, the destabilizing effect of viscous difference cannot be compensated by gravity or capillarity forces. Finally, the forces that have a larger impact in the water flooding process and developing fingers are mainly the capillary forces, but to a lesser degree the viscosities difference between two fluids.

Oil-wetting and water-wetting porous media have been tested. In the oil-wetting pores (polystyrene beads), the polystyrene beads will prefer contact with the oil rather than water. In such a configuration, the capillary force acts as a resistance force that prevent oil movement and preserve it in contact with beads surface. The calculation gives $-4.7 < \log(Ca) < -4.4$ with $\log(\mu_w/\mu_o)$ unchanged, which proves that the situation is not fundamentally modified for the diagram of regimes of flow compared to that of the sand.

Conversely in water-wetting pores (packed sand), oil is the non-wetting phase, and the capillary force no longer acts as a resistance force, but as the positive contribution for the momentum balance. Consequently, in our experimental results we can observe that the remaining oil in the oil-wetting medium is approximately three times greater than in the

water-wetting medium, S_{or} is 38 % for polystyrene beads and 11% for sand at the same experimental conditions. Nevertheless, the oil displacement process in sand model is also impacted by the sample permeability and the capillary forces as the pore size is smaller than in polystyrene model, d is $2.36E-04$ m comparing with $4.03E-05$ m for sand model (Eq. 5.8).

5.4.3 Additional observations

Pore occupancy concept

The classic approach of phase distribution in pores was confirmed by the experimental studies on the sand models:

*The wetting phase occupies preferably small pores,
the non-wetting phase prefers to occupy the large pores.*

These observations were obtained from the “damaged tests” on the models of the packed sands. By accidental negligence we have formed a large transverse crack in the middle of the sand model while shaking the model with the objective to obtain the better compaction of sands. This thin fracture cannot be observed without displacement process, because of the homogeneous distribution of oil in the sand model. The fracture became visible only after the displacement was carried out, Figure 5.24.

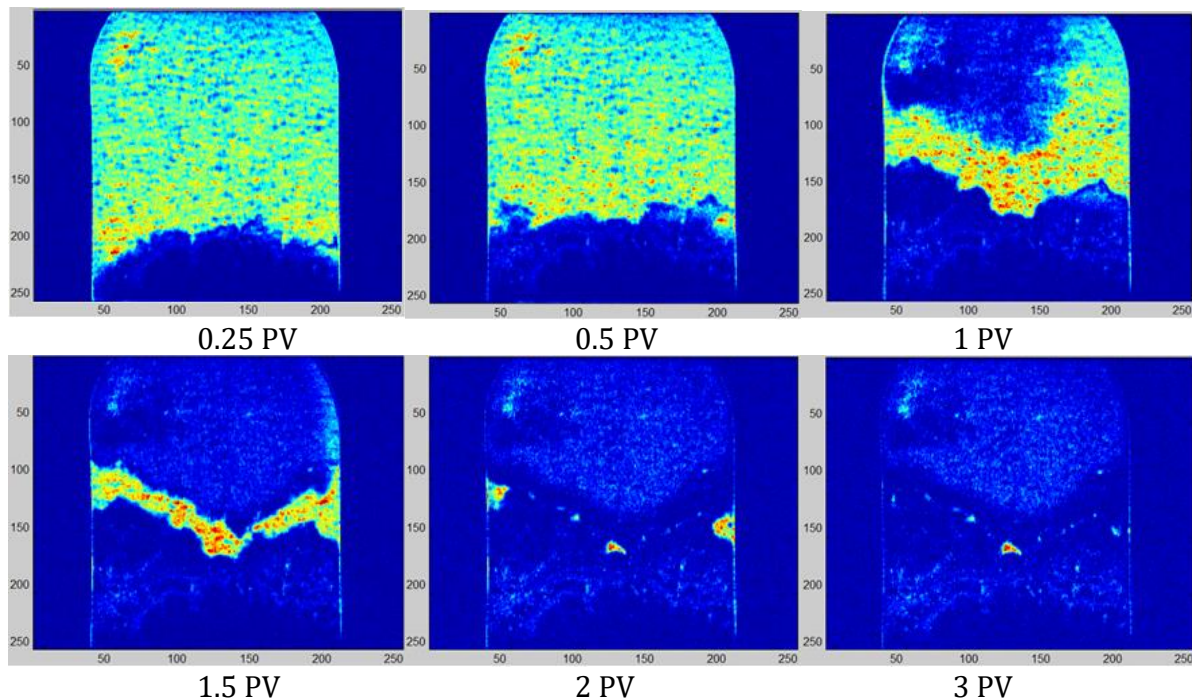


Figure 5.24. Series of consecutive images of oil displacement from the model with a thin fracture in respect of the injected pore volume.

The series of consecutive images from the Figure 5.24 shows the process of displacement from the model with a thin fracture in respect of the injected pore volume. It can be seen, that the oil from the fracture was evacuated at the latest stage. Also, oil couldn't be displaced completely, one part of oil phase remains trapped in the fracture forever.

Observing this test in detail, we can see that the displacement occurs from the bottom to the top of the model quasi uniformly until the moment when the front meets the fracture and stops. The movement of front continues at the locations where the medium is most uniform, i.e. locally the front bypasses the fracture and moves on. Then, due to the gravity, the front approaches the fracture from the other side, in the downward direction. The oil trapped in

the fracture is displaced last by continuous connection with some pores filled with the oil. Without this connection, the oil remains trapped. Therefore, large drops are trapped in the fracture region.

Because initially we couldn't find the clear explanation of the appearance of the fracture in the middle of the model, we have produced some number of experimental tests with the fractured medium before we have found the reason of its appearance and have changed the protocol of the model preparation. All of these tests have shown the similar behaviour of the non-wetting phase in respect to the largest pores.

The idea that in the small pore the hydraulic resistance is higher than in the large pores is true, but this resistance is neglected by the acting of the capillary forces, which are much higher in the small pore.

On the Figure 5.25 the evaluation of the oil saturation for the same test is presented as a function of the vertical length. The initial state corresponds to the saturation equals to 1. The last state corresponds to the saturation equals to residual oil, here the averaged value of residual oil is $S_{or} = 15\%$. The superposition of the number of saturation profiles in the middle of the model shows the local blockage of the displacement process near the fracture.

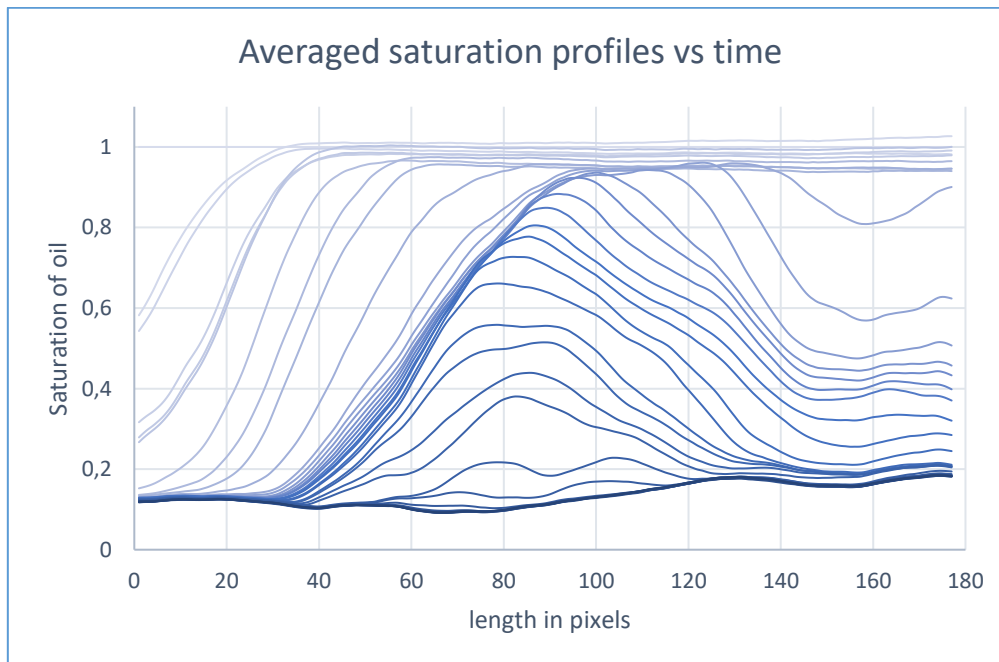


Figure 5.25. Oil saturation profiles, averaged in cross sections for the different moments of displacement, $Q_{inj} = 0.08$ mL/min.

For the medium of the polystyrene beads the thesis, that *the wetting phase occupies preferably small pores and the non-wetting phase occupies the largest pores*, is also true. The Figure 5.26 shows that the non-wetting water phase prefers to bypass the small pores occupied by oil than displaced it. As the result, the big trapped zones are rapidly created.

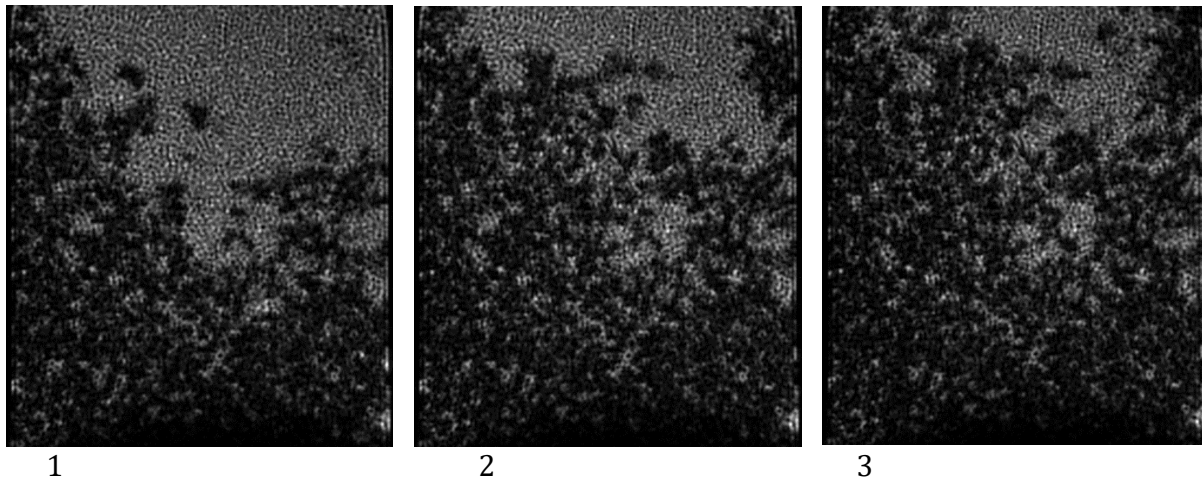


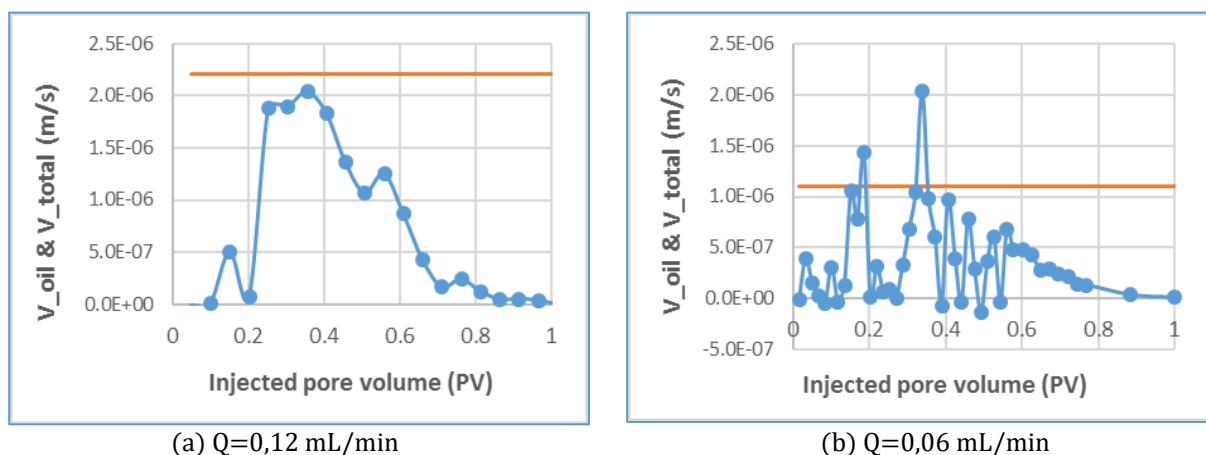
Figure 5.26. Consecutive images of the oil displaced by water in the model of polystyrene beads.

The Figure 5.26 also shows that the residual saturation of oil phase remains immobile once bypassed by water and disconnected from the oil cluster. Then, it cannot be displaced even with the big number of PV injected.

Averaged oil velocity in the vertical section

The averaged profile of saturation was constructed from the vertical sections of FOV. We should note that the vertical section represents only one part of the studied porous medium in form of the vertical slice with the thickness of 1mm. The variation of the oil saturation in this slice reflect qualitatively the displacement process in the area of interest (AOI), but does not match the exact change of the oil saturation in the whole model.

The averaged oil velocity, constructed from the saturation measurements in the vertical slice, are presented on the Figure 5.27. As mentioned above, in chapter 5.3, the average oil velocity was calculated from the variation of the oil saturation in AOI over the time. The value of ΔSoil was obtained as the change in the mobile oil volume in the vertical slice, it means the volume of oil displaced from this part of the model.



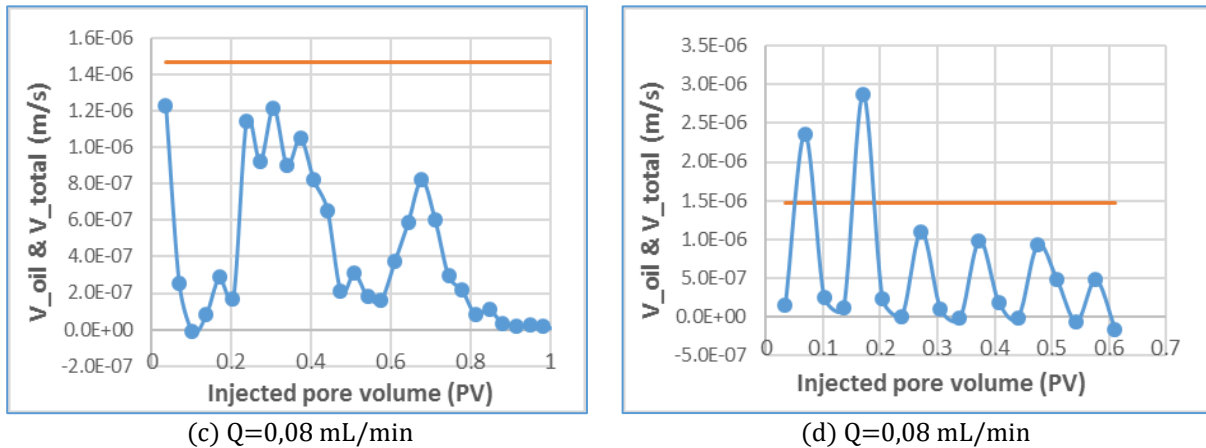


Figure 5.27. Averaged oil velocity for the low injection rates and constant total velocity of injection (orange line) versus injected pore volumes.

We can observe that the value of the averaged velocity oscillates in time. The greater values of oil velocity correspond to the displacement process, which mostly happens in the vertical direction, when the maximum of oil volume was displaced. This movement corresponds to the big growth of fingers or front advance in the AOI. The lower values of the oil velocity mean that the oil saturation variations in the AOI are insignificant. But knowing, that the injection was made continuously, we can consider that the oil saturation varies in the other parts of the model and mostly the water spreads in the radial direction, which cannot be captured by the MRI signal of oil in the vertical slice. This regime of flow corresponds to the radial movements of oil and water. Thus, the observed oscillations show the alternation in the movements in vertical direction and in the radial one. In other words, it can be explained as the alternation between the regime of finger growth in local areas and the regime of slow capillary penetration over all mobile interfaces. This analysis of the measured oil saturation corresponds exactly to the observed variation of oil distribution in the AOI from the MR images.

The comparison between the oil velocities for the different injection rates (Figure 5.27) shows that the variation in the injection rate influences on the alternation of the finger growth regime and capillary movement regime. Higher the injection rate, slow the observed oscillations between these regimes. For one special case, presented on the Figure 5.27 (d), the observed almost periodic oscillations in the oil velocity correspond well to the captured profiles of the saturation (Figure 6.11 in chapter 6) and to MRI registered images.

These periodic oscillations were observed for the model with minimum imperfections in the porous medium and slow injection rate. For the most cases the oscillations are random because of the local heterogeneities of the porous media.

5.5 Conclusions

High-resolution MRI technique was used to investigate two phase fluids flow of oil and water in porous media. The porous media was formed from packed polystyrene beads or sand. Two types of imaging methods have been investigated to obtained high quality MRI images (selective and non-selective methods). The importance of water channelling or fingering

phenomena was obviously found. Evidently, the size of the beads/grains and the value of porosity play an important role in the displacement front deformation.

Positive impact was observed by adding MnCl_2 to the injected water phase. It has shortened the T2 of water relaxation time to 0.7 ms instead of 2.35s without any effect on the T2 of the oil phase.

The relationship between the residual oil saturation and dimensionless numbers were also investigated. The water-oil displacement process and the amount of trapped oil mainly controlled by the wettability of matrix and capillary force.

In the polystyrene beads, oil is the wetting phase, so the pore channel walls preferred to contact with oil rather than water, which gives higher S_{or} comparing with water-wet material (sand packed column).

The water flooding in sand has shown that the advance of the displacement front happens in the form of occasional jumps and is controlled by the viscous and capillary forces but also by the heterogeneity of the medium.

6. Numerical simulation and comparison with experimental results

| | | |
|-------|--|-----|
| 6. | NUMERICAL SIMULATION AND COMPARISON WITH EXPERIMENTAL RESULTS..... | 120 |
| 6.1 | Introduction..... | 122 |
| 6.2 | Numerical modelling..... | 122 |
| 6.2.1 | Case 1 classical model, viscous force effect | 126 |
| 6.2.2 | Case 2 gravity and viscous forces effect..... | 127 |
| 6.2.3 | Case 3 gravity, capillary and viscous forces effect..... | 128 |
| 6.3 | Comparison of the influence of three main forces | 129 |
| 6.4 | Comparison of experimental results with the numerical model | 132 |
| 6.5 | Conclusions | 134 |

6.1 Introduction

In this chapter, the governing equations for two-phase flow in a porous media introduced in chapter two section 2.3.3 are analyzed using a numerical simulation model. Those equations were implemented in the Comsol Multiphysics interface. In the initial case we only simulate the viscous forces, then the gravity and the capillary forces were taken into account. Finally, the experimental results obtained by MRI such as displacement forces impact, oil saturation profile were verified with the numerical simulation model.

6.2 Numerical modelling

The numerical simulations were made for an axisymmetric 3D model. The geometrical parameters (Fig 6.1) and the properties of fluids were taken from the experimental investigation set for the packed sand. As it was introduced in the previous chapter, the model is a sand filled column where water is injected upward. For this medium the water is the more wetting fluid.

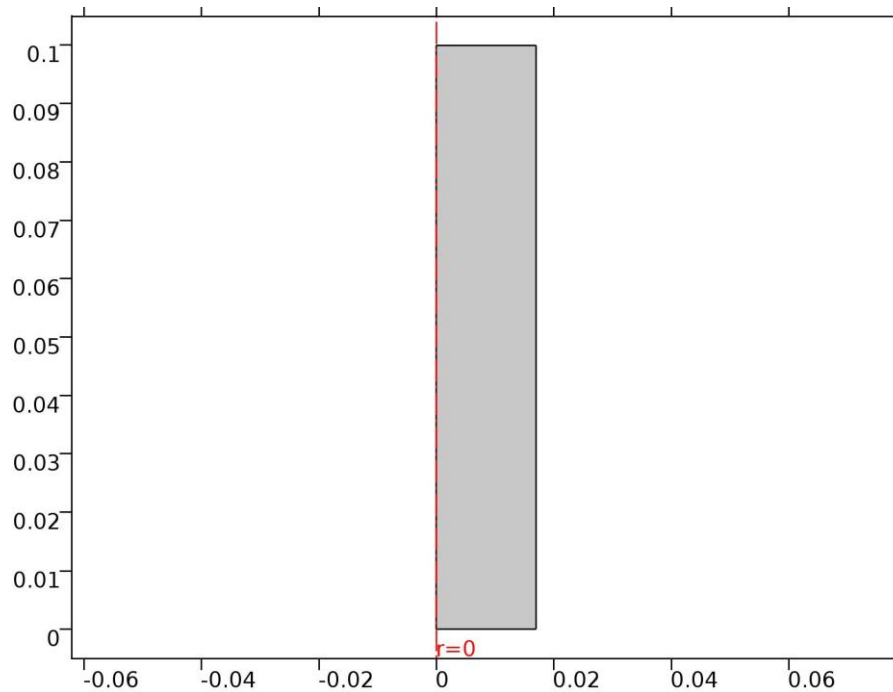


Figure 6.1. Axisymmetric vertical tube, 2D dimensions in meter.

Following the chapter 2, the two-phase immiscible flow can be written by one equation for water saturation S :

$$\varphi \frac{\partial S_w}{\partial t} - \nabla(F(S)V_{tot} - F(S) \lambda_o g (\rho_w - \rho_o) - F(S) \lambda_o \frac{dP_c}{dS} \frac{dS}{dz}) = 0 \quad (6.1)$$

The first term corresponds to the viscous forces (in red), while the second to the gravity forces (in green). The diffusive transport, related to the action of capillary forces, is represented by the third term in brackets (in blue).

The fractional flow function $F(S)$ has the following form:

$$F(S) = \frac{V_w}{V_{tot}} = \frac{V_w}{V_o + V_w} \quad (6.2)$$

$$V_w = V_{tot} * F(S) \quad (6.3)$$

$$\lambda_i = \frac{K k_{ri}(S_i)}{\mu_i}, i = w, o \quad (6.4)$$

The power-type relationships between the normalized saturation and the relative permeability was used to define the saturation functions $k_{ri}(S_i)$:

$$\begin{cases} S \leq S_{wr} : 0, & S > S_{wr} : k_{rw}(S) = \left(\frac{S - S_{wr}}{1 - S_{wr}} \right)^2 \\ S \leq S_{ro} : k_{ro}(S) = \left(\frac{1 - S - S_{or}}{1 - S_{or}} \right)^2, & S > S_{or} : 0 \end{cases} \quad (6.5)$$

where k_{rw} and k_{ro} are the relative permeability for water and oil phase respectively.

Initial and boundary conditions of the model

The system's initial condition can be described from the primary variables. The initial condition for two phase flow equations can be defined for pressure P_w and saturation S_w as (Szymkiewicz, 2013):

$$p_w(x, t = 0) = p_w^{init}(x) \quad (6.6)$$

$$S_w(x, t = 0) = S_w^{init}(x) \quad (6.7)$$

It is also possible to define the initial state in terms of the both pressures P_w and P_o :

$$p_w(x, t = 0) = p_w^{init}(x) \quad (6.8)$$

$$p_o(x, t = 0) = p_o^{init}(x) \quad (6.9)$$

The water saturation is then obtained as:

$$S_w^{init} = S_w(p_o^{init} - p_w^{init}) \quad (6.10)$$

In our model, the boundary and initial conditions are defined basing on the different stats of the experimental protocol. Therefore, the initial saturation of water in whole model equals to zero $S_w^{init} = 0$.

The initial pressure distribution corresponds to the state of equilibrium and follow the law of hydrostatics. Because the WOC contact is situated on the lower limit of the zone of FOV, the initial pressure distribution corresponds to $P = \rho_{oil}gh$.

The boundary conditions are:

Zero flux for the walls of tube and the constant flux for the top of the model.

The prescribed value of water saturation at the bottom of model equal to 1.

To complete the relations (Eq. 6.5) for the saturation functions, the residual saturations of phases were taken as follows: $S_{or} = 0.25$ and $S_{wr} = 0.15$. For further modeling, these values will be taken from the experimental results. The relationships between the normalized saturation and the relative permeability are shown in figure 6.2.

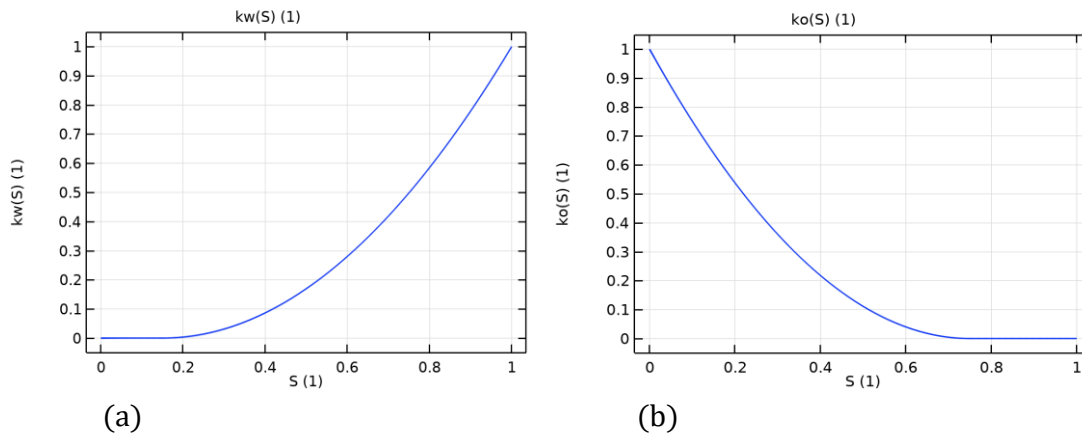


Figure 6.2. (a) water relative permeability vs. water saturation, and (b) oil relative permeability vs. water saturation

The figure 6.3 shows the first condition of the water and oil saturation along the vertical model.

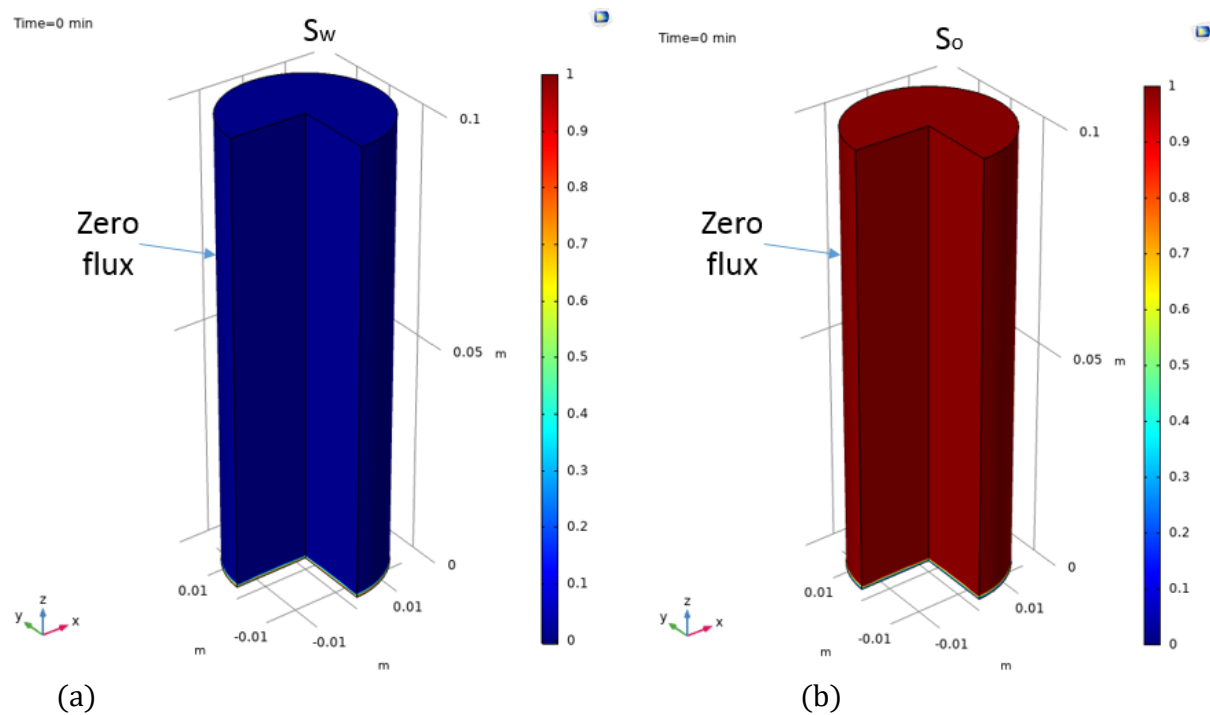


Figure 6.3. 3D view, (a) oil saturation distribution at the initial condition and (b) water saturation distribution at the initial condition.

Capillary pressure

The capillary pressure $P_c(s)$ was constructed basing on Leverett J-function for the unconsolidated porous materials, the data were taken from the Leverett's experiments. Figure 6.4 shows J-function values vs. water saturation for the unconsolidated sands.

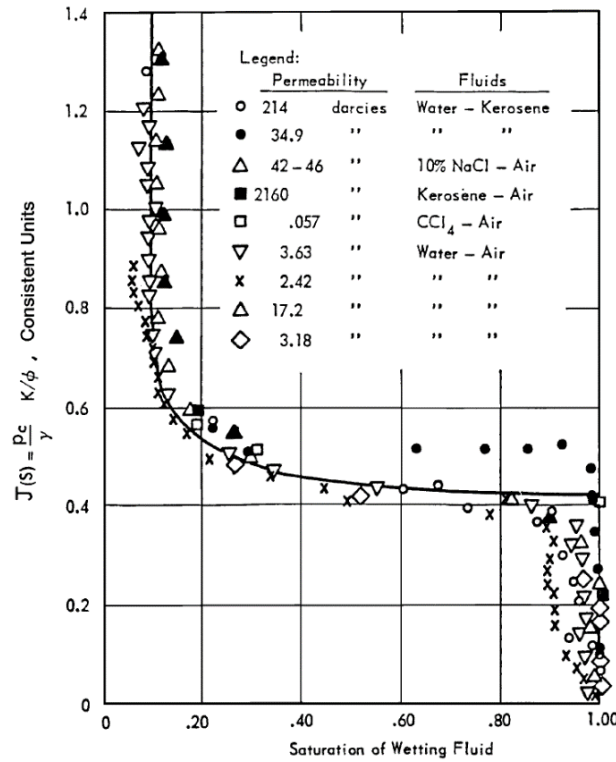


Figure 6.4. Leverett J-function for unconsolidated sands (after Leverett, 1941)

Then, the capillary pressure was obtained with the following equation:

$$P_{c \max} = J(S_*) \sigma \cos \theta \sqrt{\frac{\bar{\phi}}{K}} \quad (6.11)$$

Using the data for the porosity ϕ , the permeability K from the experimental study, and the data for the contact angle θ and the surface tension σ for chosen fluids, the value for maximum and averaged capillary pressures were calculated. The comparison with P_c calculated from the pore size distribution gives the correct match.

Model data:

The data used in this model refers to the sand experiments with a high injection rate as the front displacement was more stable. The main parameters of the simulation model are shown in Table 6.1.

| Name | Expression | Value | Description |
|------------------|----------------------------------|-----------------------------|----------------------------|
| gr | 9.81[m/s ²] | 9.81 m/s ² | Gravitational constant |
| rho _w | 1000[kg/m ³] | 1000 kg/m ³ | Density, water |
| rho _o | 800[kg/m ³] | 800 kg/m ³ | Density, oil |
| mu _w | 1[cP] | 0.001 Pa·s | Dynamic viscosity, water |
| mu _o | 2.9[cP] | 0.0029 Pa·s | Dynamic viscosity, oil |
| mu | mu _w /mu _o | 0.34483 | Viscosity ratio |
| r _t | 1.7e-2[m] | 0.017 m | Model radius |
| L | 10.e-2[m] | 0.1 m | Model length |
| poro | 0.39 | 0.39 | Porosity |
| Q | 0.16[ml/min] | 2.6667E-9 m ³ /s | Injection rate |
| A | pi*r _t ² | 9.0792E-4 m ² | Model cross sectional area |
| V _{tot} | Q/A | 2.9371E-6 m/s | Total fluid velocity |

Table 6.1. The main parameters used in the simulation model.

The computed time step for output was set for 15 minutes according to the experimental time steps.

6.2.1 Case 1 classical model, viscous force effect

For better understanding the effects of gravity, capillarity and viscosity's difference, we start from the simple two-phase flow which does not take on account on gravity and capillary effects.

In this model the reason of flow is the viscous forces, which appears due to water flux or water injection. If the capillary and gravity effects are neglected, the equation 6.1 reduces to the Buckley-Leverett equation (nonlinear advection equation), well known in petroleum reservoir engineering literature:

$$\phi \frac{\partial S_w}{\partial t} - \nabla(F(S)V_{tot}) = 0 \quad (6.12)$$

Figure 6.5 shows the solution of classical formulation, where the only viscous force is taken in consideration, the gravity and capillary forces are neglected (case 1).

From the simulation results, we observe the high residual oil saturation and reduced displacement front stability due to non-gravity and non-capillary effects (Fig 6.5.a).

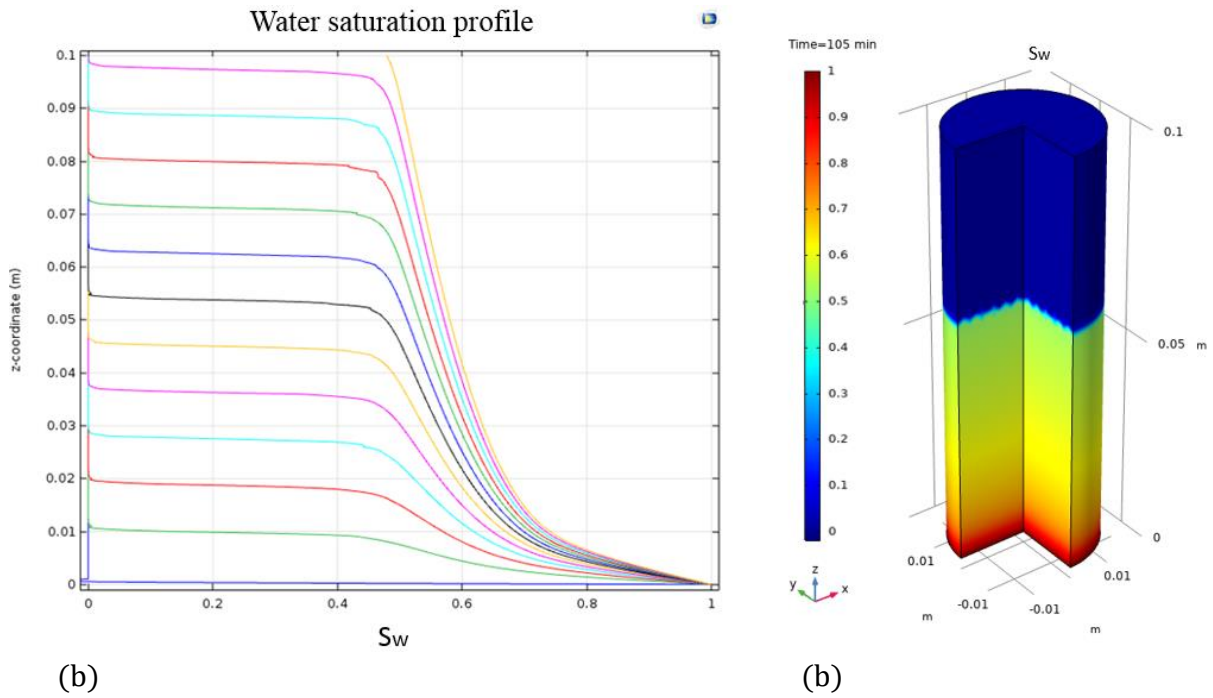


Figure 6.5. Case 1, (a) Oil saturation profile vs vertical position, and (b) saturation distribution in 3D view after 105 minutes.

6.2.2 Case 2 gravity and viscous forces effect

Considering of the effects of gravity and viscous forces (case 2), the equation 6.2 modified takes the following form:

$$\varphi \frac{\partial S_w}{\partial t} - \nabla(F(S)V_{tot} - F(S) \lambda_o g (\rho_w - \rho_o)) = 0 \quad (6.13)$$

The results in figure 6.6 show more stable displacement front and low value of residual oil saturation S_{or} compared to case 1. For the upward flow direction, the gravity plays a stabilizing role.

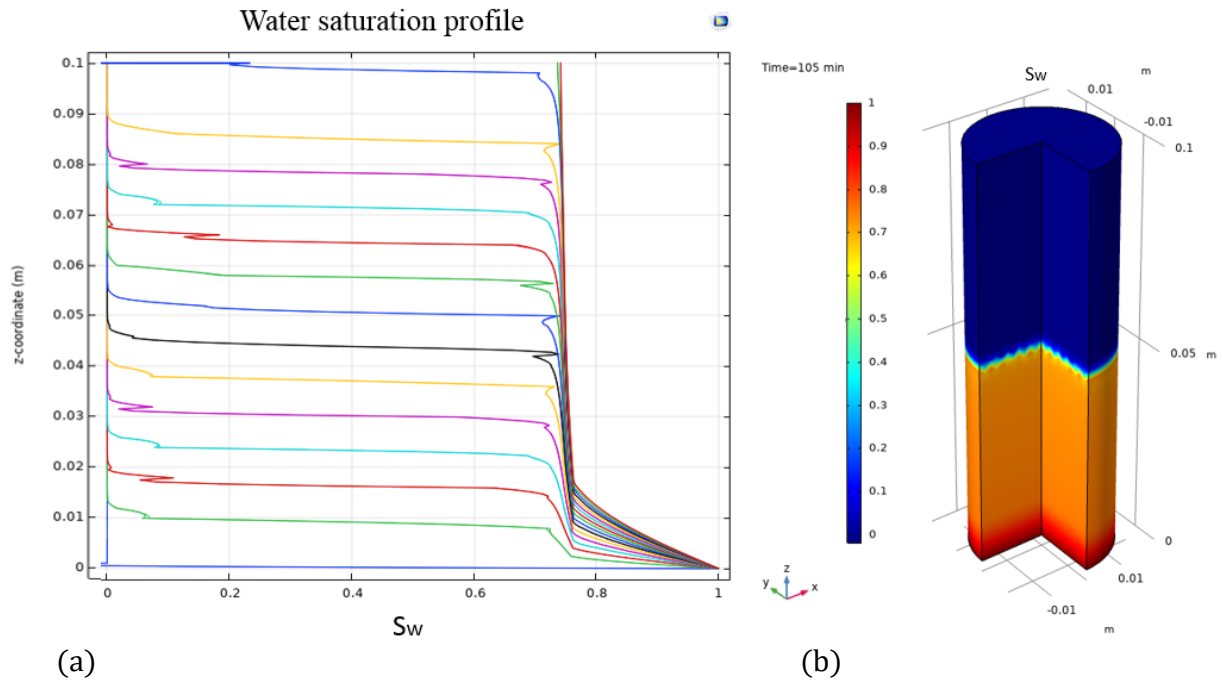


Figure 6.6. Case 2, (a) Oil saturation profile vs vertical position, and (b) saturation distribution in 3D view after 105 minutes.

6.2.3 Case 3 gravity, capillary and viscous forces effect

Figure 6.7 shows the solution for the formulation, where 3 forces are taken in consideration, namely the gravity, capillary and viscous forces (case3).

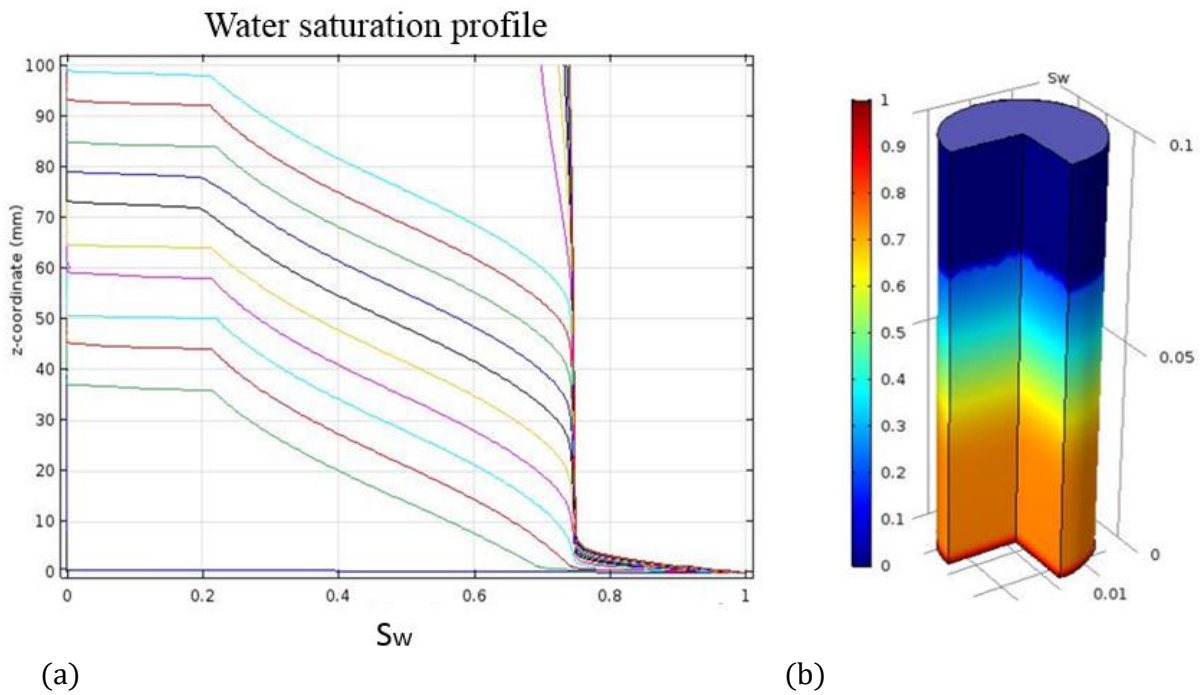


Figure 6.7. Case 3, (a) Oil saturation profile vs vertical position, and (b) saturation distribution in 3D view after 105 minutes.

The qualitative match of the experimental results with the numerical model results was done by the time of averaged front propagation: the time and height of front appearance in the experimental study corresponds well to the equivalent process in the numerical simulations.

The simulation results show that the oil saturation trapped in the model remains constant with time and equals to the micro trapped oil saturation S_{or} , Figure 6.7.a. This fact also matches well the experimental study: after multiple PV injected into the sand model the residual oil saturation becomes quasi constant in respect of the length of the model, see Figure 5.13. It means that for our case of sand model, the classical approach with the important influence of the gravity and capillary forces leads to the maximum recovery.

6.3 Comparison of the influence of three main forces

The comparison of the influence of three main forces was made in Figure 6.8. The oil saturation profile for the time of water injection about 1.5 hour was calculated for three cases: classical Buckley-Leverett model (case 1), model with gravity effects (case 2) and finally the Buckley-Leverett model with gravity and capillary phenomena (case 3). It is evident that the gravity forces slow down the front propagation in the model, but they also stabilize the displacement process in upward direction. The capillarity effects accelerate the front propagation mostly for the small water saturations, where the capillary pressure is maximum. Following these results, the gravity and capillary phenomena lead to a good sweep efficiency and does not take into account the macro oil trapping provoked by the viscous instability.

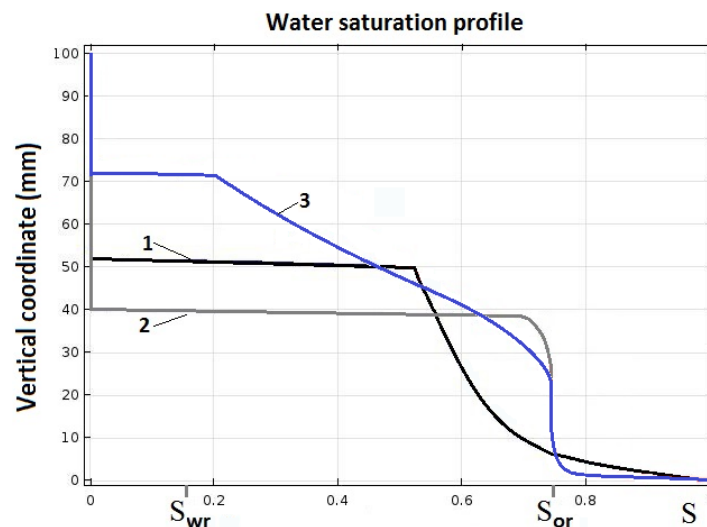


Figure 6.8. Water saturation profile vs vertical coordinate for 3 cases: (1) classical BL model, (2) BL model with gravity, (3) BL model with gravity and capillarity.

The numerical simulation with the vector model of capillary forces show qualitatively similar results (Fig. 6.9.a). But here, the sharp shock observed for the model of case 3 disappears for the vectoral model of capillary forces. The simulation for the equation 6.13 (see section 2.3.3 in chapter 2) used the specific parameter η_c as the meniscus concentration in space or volume fraction of mobile wetting phase in the area of interface. This parameter was obtained by the analysis of the experimental results and it is presented in figure 6.9.b. The zone of the residual oil saturation was removed because of the immobility of fronts in this area (figure 6.9.b). The

figure 6.9.c shows the mobile phase saturation, which was obtained by the calculation of the saturation differences from the MRI images.

$$\phi \frac{\partial S_w}{\partial t} + \nabla \left(F(S) V_{tot} - F(S) \lambda_o g (\rho_w - \rho_o) + F(S) \lambda_o \gamma \eta_c \frac{P_c}{l} \right) = 0 \quad (6.13)$$

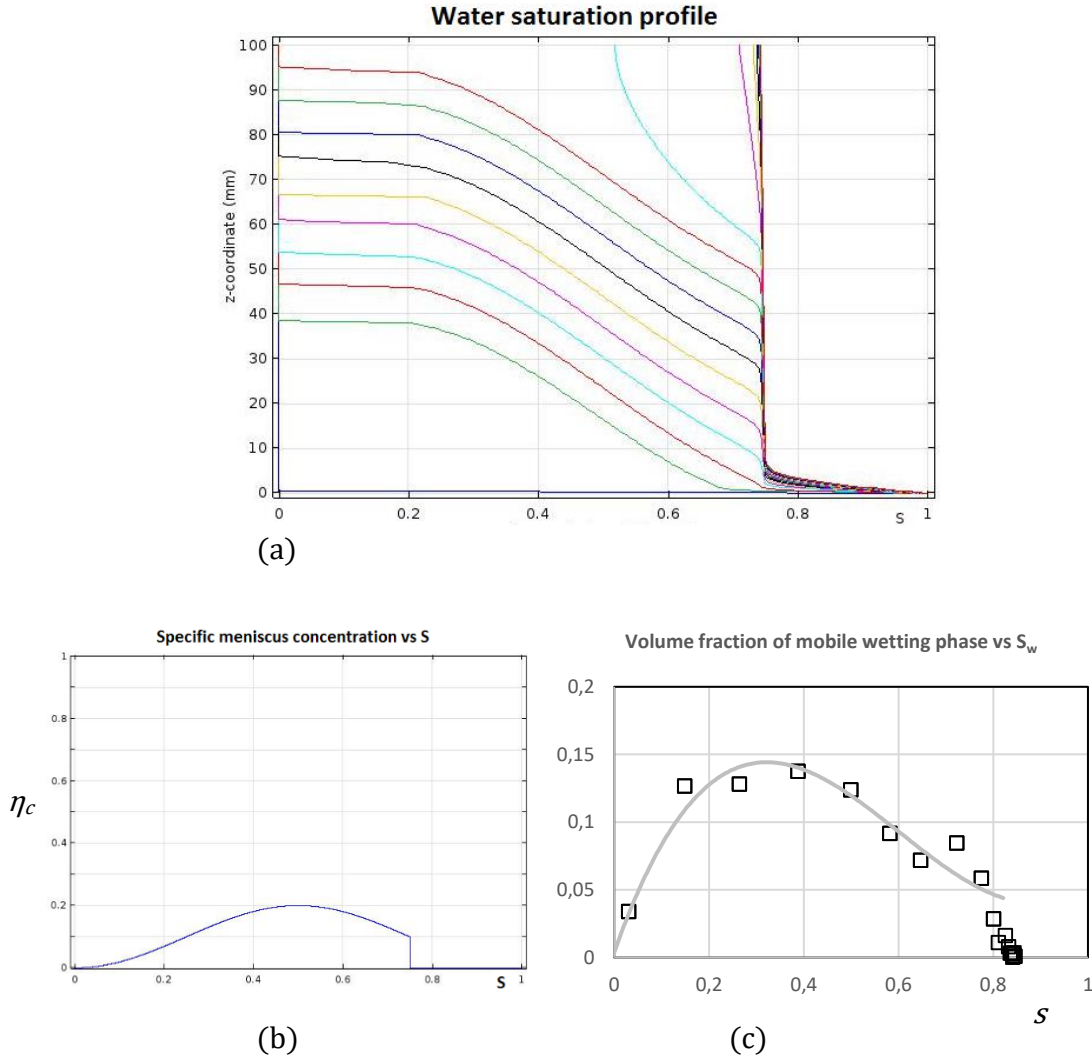


Figure 6.9. (a) Water saturation profile vs vertical position for vector capillary model and (b) specific meniscus concentration as a function of saturation, (c) volume fraction of mobile wetting phase as a function of water saturation obtained from experimental test.

Finally, the comparison between the fluxes caused by three main forces was made in Figure 6.10. In Figure 6.10.a, the fractional flow flux, the capillary flux and the gravity flux are shown separately to better understand the influence of each term.

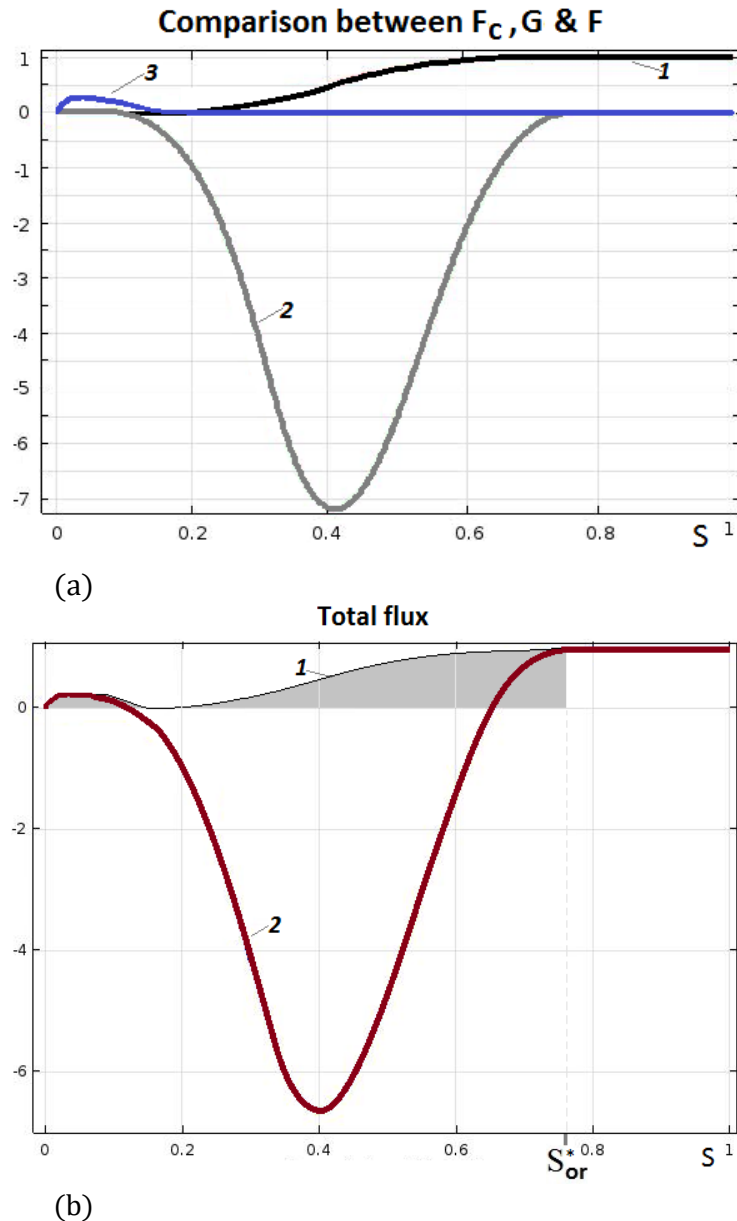


Figure 6.10. Comparison between the fractional flow flux "F", the capillary flux " F_c " and the gravity flux "G": (a) Fractional flow (1), gravitational (2) and capillary (3) fluxes for the equation 6.13; (b) Total flux (2), the sum of capillary and gravity flux (1), the grey color indicates the zone of the water saturation, where the front can move forward.

Figure 6.10 helps to explain some behavior observed during the experimental tests on the packed sand model. We have seen that the fingers have grown under the capillary and gravity forces, but at the same time the propagation of water was blocked locally, and some part of the displacement front did not move for hours. The experimentally measured profiles of oil saturation, averaged through the cross sections, are shown on Figure 6.11. The superposition of many saturation profiles shows that the oil saturation can be blocked locally from 30 minutes up to 1.5 hour. Then, the situation of local front immobility was changed. It happens by the collapse of the fingers, or by gravity segregation, or by slow capillary penetration.

This partial immobility can be explained by the following: when the gravity is compensated by the water pumping, only the saturation with non-zero mobility can move. In Figure 6.10.b

the area of mobile water saturation is marked in grey color. It means, that water can flow upwards only in area of grey color when the total flux is positive. For negative total flux, water can go downwards by gravity. There is some interval of small saturations, where the sum of capillary and gravity flux is closed to zero or equals to zero. For this interval of saturations, water can move in radial direction by the capillary forces. To move in vertical direction, the saturation of water should be increased to become mobile.

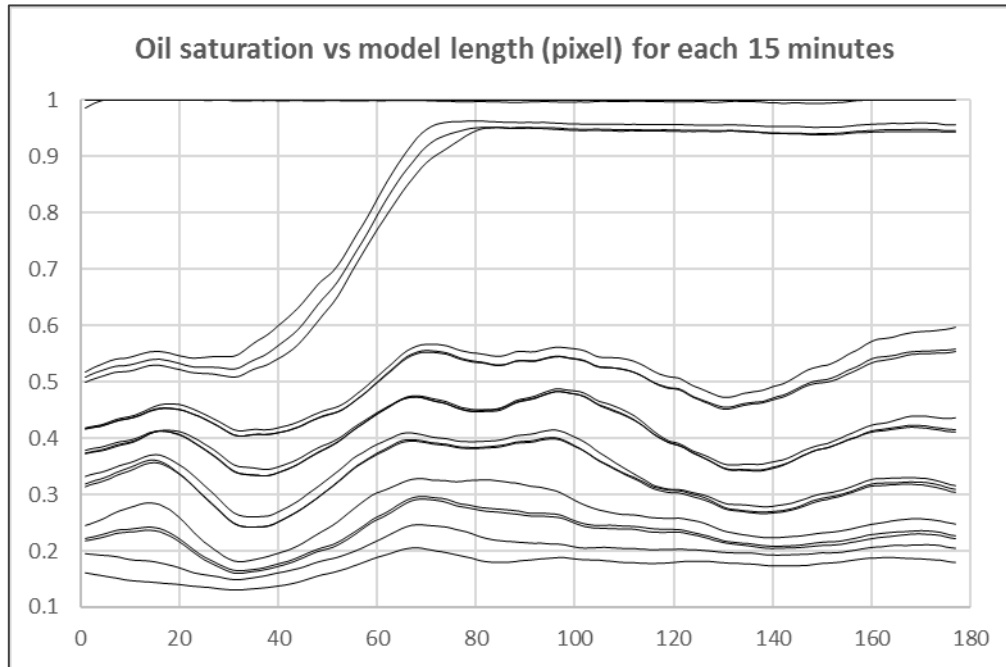


Figure 6.11. Saturation profile of oil phase during displacement in the sand model with injection flow rate of 0.08 mL/min.

Figure 6.10 also shows that the capillary effects are important only for the small water saturation; for the other values of saturation the capillary effects are negligible in comparison with gravity and viscous effects.

6.4 Comparison of experimental results with the numerical model

As stated in the previous section, the parameters for the numerical modeling have been selected according to the sand model. Therefore, the comparison between the experimental results and the predictive numerical model will be based on the outcomes of the sand model experiments.

Figure 6.12 illustrates the sand experimental results of the high injection rate (more stable front), which have been selected to be compared with the numerical model (case 3) where the three forces are taken in consideration, namely the gravity, capillary and viscous forces.

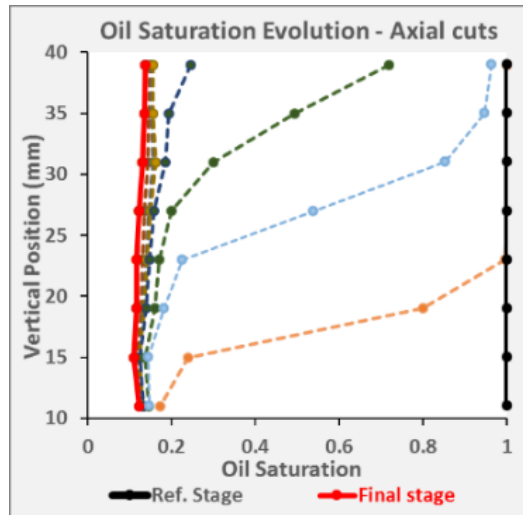


Figure 6.12. Oil saturation distribution in the packed sand model at the high injection flow rates of 0.16 mL/min.

The relative permeability of both fluids obtained by the correlations (6.5) considered to be the most uncertain parameters. Therefore, in order to obtain a good match of the numerical simulation with the experimental data, the relative permeability curves and the relative permeability end points have been adjusted. Figure 6.13 shows the adjusted relative permeability curves for both fluids.

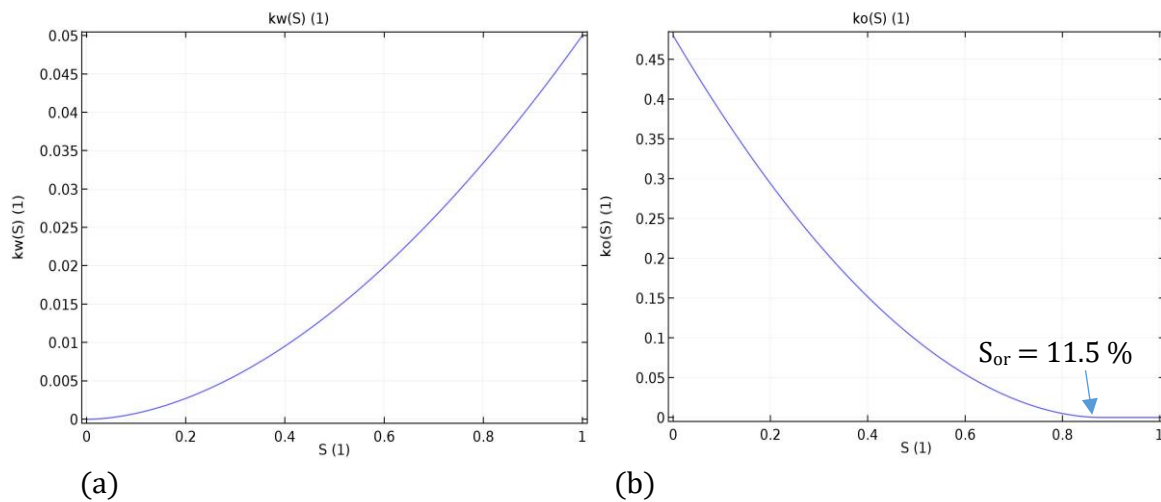


Figure 6.13 (a) adjusted water relative permeability vs. water saturation, and (b) adjusted oil relative permeability vs. water saturation. $S_{or} = 11.5\%$, obtained from experimental results.

The comparison of the oil saturation profile for both approaches (numerical and experimental) is shown in Figure 6.14. The curves on the graph are the numerical model results of the oil saturation profile and the star points are the MRI experimental results. Here we take the averaged oil saturation measured in the horizontal section for different times. The time step is 15 minutes for the numerical and experimental cases.

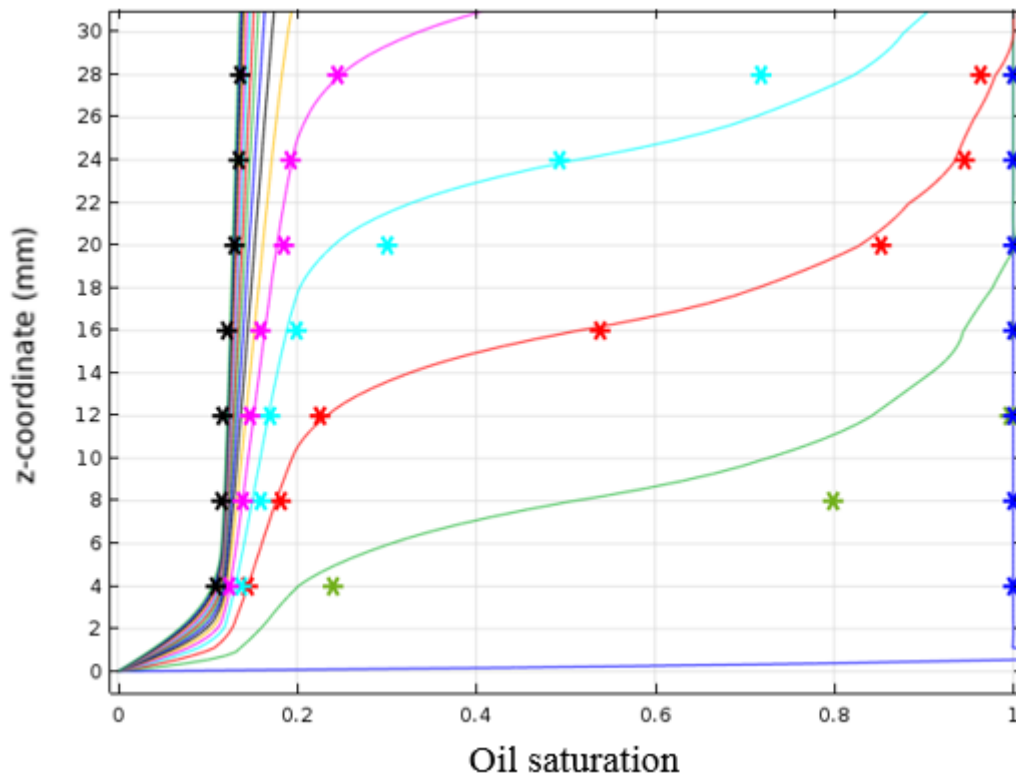


Figure 6.14 Simulation results for the Case 3, the three forces were taken into account, has proved to be in a good agreement with the experimental results of the sand model. The star points on the chart are the experimental data at each experimental step.

The experimental results of each step were shown to be well consistent with the numerical model prediction. For both methods the initial condition was 100 percent of oil saturation. The simulation predicts the same residual oil saturation values, ~ 12 %, as in the experimental results.

6.5 Conclusions

The numerical simulations, which take into consideration the phase distribution in porous medium, the displacing front deformation and the residual phase formation, were made. The simulations confirmed qualitatively the experimental results for the classical approach.

The closing relations for the two-phase capillary vector model were evaluated from the given experiments. The results of simulation with the vector model are not very different from the classical model, but they show more important role of the capillary effects.

The matching of the experimental results and the numerical model was obtained for one of the experiments on the sand model. A good match was obtained for the evaluation of saturation profile in time. The data used in the model are the same as for the experiment. The uncertain parameters, such as the K_r functions, were matched with the simulation model.

7. General conclusions and perspectives

| | |
|--|-----|
| GENERAL CONCLUSIONS AND PERSPECTIVES..... | 136 |
| CONCLUSIONS ET PERSPECTIVES (VERSION FRANÇAISE)..... | 138 |
| CONCLUSIONS AND PERSPECTIVES (ENGLISH VERSION)..... | 143 |
| BIBLIOGRAPHY..... | 147 |

Conclusions et perspectives (Version Française)

Il est essentiel de bien comprendre les forces motrices sous-jacentes qui contrôlent l'écoulement diphasique de deux fluides immiscibles dans un milieu poreux. En effet, il existe une large gamme d'applications des écoulements diphasiques, notamment pour les procédés d'ingénierie pétrolière et de récupération hydrogéologique. Elles impliquent généralement le déplacement d'un fluide non mouillant par un fluide mouillant, par exemple l'injection d'eau dans la technique de récupération secondaire d'huile (EOR). Cette technique n'est pas encore jugée satisfaisante en termes d'efficacité de récupération du pétrole, car le processus de déplacement des fluides dans la matrice poreuse n'est pas bien défini.

Une méthode de visualisation directe et de mesure de l'écoulement des fluides dans les milieux poreux, telle que la technique IRM, est un outil extrêmement utile pour une meilleure compréhension du processus de déplacement des fluides. L'efficacité de cette méthode dépend de la résolution des images, elle-même liée à la puissance et la qualité du système IRM.

Les recherches que nous avons réalisées ont consisté à effectuer différentes expériences de déplacement du pétrole par de l'eau dans des milieux poreux modèles : empilement de grains de sable ou de billes en polystyrène. Les objectifs étaient les suivants :

- Mesurer la saturation en huile dans le support poreux pendant toute la durée du processus de déplacement et obtenir au final la saturation résiduelle en huile.
- Capturer les images consécutives des structures formées lors du déplacement du front eau-huile ; ces images comprennent une tranche verticale suivant un diamètre de la colonne et huit sections horizontales régulièrement espacées dans la partie la plus homogène de la sonde d'imagerie.
- Traiter les résultats fournis par l'IRM à l'aide du code Matlab de façon à reconstruire les images et réaliser des traitements statistiques à partir des données enregistrées.
- Etudier le mécanisme de propagation des empreintes visqueuses obtenues à partir des images IRM
- Analyser les données afin d'obtenir les paramètres de processus cinétiques de la formation de la phase piégée et comprendre les mécanismes dominant du déplacement des fluides.

Au terme de cette étude, nous pouvons tirer quelques conclusions importantes :

- En comparant différents types de méthodes d'imagerie, y compris les rayons X ou l'imagerie optique, il a été montré que seule l'IRM est capable de visualiser la structure interne d'un système tridimensionnel avec une résolution spatiale des espèces présentes. La technique IRM est bien adaptée pour distinguer la distribution des fluides par rapport à d'autres modalités d'imagerie car elle ne fait que « voir » les protons (^1H) en phase liquide.
- La distribution des temps de relaxation T2 est l'information clé de la mesure par IRM. Ainsi, nous avons d'abord évalué la plage des temps de relaxation des fluides utilisés dans nos expériences et ensuite estimé l'ampleur de la modification de ce paramètre lors de la mise en place dans le support poreux. Différents échantillons ont été

préparés et nous avons utilisé un spectromètre à bas champ (Minispec Bruker mq20) pour mesurer ces distributions de T2 à l'aide d'une séquence CPMG. Les valeurs de T2 pour l'eau pure et l'huile à 20 MHz sont respectivement de 2,02 s et 0,88 s. Ces valeurs varient en fonction du type de support poreux et diminuent quand la taille de leurs pores décroît.

- Une technique d'IRM à haute résolution a été utilisée pour étudier l'écoulement diphasique d'huile et d'eau dans un milieu poreux. L'outil IRM utilisé s'appuie sur un aimant vertical de 14 T, pouvant fournir pour nos expériences une résolution de 190 μm par pixel.
- Deux types de méthodes d'imagerie ont été testés pour obtenir des cartes IRM de haute qualité. La première méthode est basée sur le phénomène de déplacement chimique (méthode sélective), et la deuxième est une méthode non sélective qui repose sur l'annulation du signal de l'eau par ajout d'ions Mn^{2+} lesquels font chuter le temps de relaxation de l'eau (T2). La seconde méthode a donné de très bons résultats et a été sélectionnée pour la suite de notre étude expérimentale en raison de sa simplicité de mise en œuvre. Un protocole d'imagerie IRM approprié, basé sur la méthode d'écho de spin (MSME : Multi Slice - Multi Echo) a été ensuite utilisé.
- Les expériences ont été menées sur une colonne poreuse verticale formée de billes de polystyrène ou de sable tassé, deux matériaux ayant des propriétés de mouillage différentes. L'impact positif sur la procédure d'imagerie a été observé en ajoutant du chlorure de manganèse (MnCl_2) à la phase aqueuse injectée. Il a raccourci le temps de relaxation de l'eau T2 à 0,7 ms au lieu de 2,35 s sans aucun effet sur le T2 de la phase huileuse. Compte tenu du déplacement relativement lent des phases impliquées (plus de 10 heures pour une expérience), la technique IRM nous a permis d'avoir une description temporelle et spatiale (presque 3D) très précise du mouvement de l'huile et par voie de conséquence, de l'eau.
- Nous sommes en mesure de visualiser par IRM des billes de petite taille jusqu'à 0,4 mm de diamètre qui constituent le milieu poreux. Il est par conséquent possible d'obtenir des valeurs locales de la saturation en eau et en huile (presque à l'échelle des pores), et sans difficulté d'en déduire les profils de saturation moyenne suivant la verticale. L'importance des phénomènes de chemins préférentiels de l'eau, ou de digitations, a été mise en évidence. Évidemment, la taille des billes/grains et la valeur de la porosité jouent un rôle important dans la déformation du front en mouvement. La relation entre la saturation résiduelle finale en huile et les nombres sans dimension a également été étudiée. Il en ressort que le processus de déplacement eau-huile et la quantité d'huile piégée sont principalement contrôlés par la mouillabilité de la matrice poreuse et par les forces de capillarité.
- Dans les pores hydrophobes (billes de polystyrène), l'huile est la phase mouillante, de sorte que les parois des canaux des pores préfèrent le contact avec l'huile plutôt que l'eau. Dans une telle configuration, la force capillaire agit comme une force de résistance qui empêche le mouvement de l'huile et la maintient en contact avec la surface des billes. Nous avons observé en fin d'essai une saturation résiduelle en huile d'environ 38% pour ce type de milieu. Les expériences ont été effectuées dans les conditions telles que $-4,7 < \log(\text{Ca}) < -4,4$ et avec $\log(\mu_w/\mu_o)$ inchangé, ce qui montre que ce type de processus de déplacement est situé dans le diagramme de régime d'écoulement (Lenormand et al. 1988) à l'intersection du déplacement stable et de la formation de digitations capillaires.

- Dans le matériau hydrophile (colonne de sable), l'huile est la phase non mouillante et la force capillaire n'agit plus comme une force de résistance, mais comme une contribution positive au mouvement des deux fluides. Par conséquent, la saturation résiduelle en huile à la fin des essais est bien inférieure à celle du modèle avec les billes en polystyrène. Chaque expérience a été répétée pour confirmer les résultats obtenus. Les saturations résiduelles en huile dans le modèle de sable allaient d'environ 10% à 14% à trois débits d'injection différents. La saturation résiduelle en huile pour les différents débits d'injection est tout à fait du même ordre de grandeur, avec une légère augmentation régulière dans les cas de déplacements plus lents. Ceci s'explique par la contribution des forces visqueuses à des nombres capillaires plus élevés. En général, le processus d'invasion donne les nombres sans dimension suivants : $6,4E-6 < Ca < 1,3E-5$ et $Bo = 1,26E-4$, ce qui confirme l'effet important de la capillarité.
- Davantage d'essais ont été menés sur l'expérience avec le sable en faisant varier le débit d'injection. Pour un essai représentatif, la vitesse moyenne du flux advectif est de l'ordre de $2,6E-6$ m/s en tenant compte du volume d'huile piégé. Sur la base d'une propagation du front eau-huile dans le modèle de sable, la vitesse moyenne du front a été estimée à $1,0E-6$ m/s. Dans les conditions $Ca \sim 1E-5$ et $Bo \sim 1E-4$, la redistribution radiale de l'eau est donc plus faible que l'advection verticale globale.
- L'invasion d'eau dans le sable a montré que l'avancée du front de déplacement se présente sous la forme de sauts occasionnels et est contrôlée par les forces visqueuses et capillaires, mais est aussi très sensible à l'hétérogénéité du milieu. La comparaison des résultats à partir des diagrammes de régime d'écoulement proposés par R. Lenormand (Lenormand et al. 1988) confirme que les expériences sont situées à l'intersection des régimes de déplacement visqueux stable et de digitations capillaires, ce qui explique que des doigts d'amplitude relativement faible sont observés.
- Une méthode est proposée pour le calcul des courbes de perméabilité relative à partir du signal IRM.
- La simulation numérique d'écoulement diphasique non miscible (eau-huile) dans un milieu poreux vertical est réalisée à l'aide du logiciel COMSOL. Les données d'entrée ont été extraites du jeu de données expérimentales pour le sable tassé. L'effet des différentes forces impliquées a été étudié. Le profil vertical de saturation en fluide a été vérifié avec le modèle de simulation numérique. Les simulations ont confirmé qualitativement les résultats expérimentaux. Un bon accord est obtenu sur la comparaison avec les résultats expérimentaux.

Grâce aux travaux de recherche menés dans ce travail, les perspectives suivantes et études futures peuvent être proposées :

- Des échantillons de roche (milieu réservoir réel) pourrait être utilisés afin d'étudier un type de support poreux consolidé plus proche de la réalité ; dans ce cas, la configuration expérimentale doit être modifiée afin de gérer une pression d'injection attendue beaucoup plus élevée.
- Les propriétés des fluides en phase huileuse ont été choisies de manière à être plus représentatives des propriétés du pétrole brut léger. Les différentes gammes de viscosité et de densité des fluides doivent être étudiées.
- L'étude de la récupération assistée par voie chimique (C-EOR), par utilisation de polymères ou de surfactants pourrait être étudiée de façon systématique en mettant à profit notre technique IRM et le montage expérimental que nous avons utilisé.

Quelques essais effectués en ce sens nous ont montré la possibilité et l'intérêt de tester les performances de ces techniques de récupération.

- Des courbes de perméabilité relative dynamique pourront être construites pour les résultats expérimentaux futurs.
- Nous n'avons pas été en mesure d'inclure des capteurs de pression dans la configuration expérimentale, car la plupart de ces instruments contiennent des éléments métalliques qui ne peuvent pas être installés dans le système IRM. La recherche de capteurs de pression travaillant dans les gammes d'intérêt, et compatibles avec les mesures IRM, permettraient d'apporter des renseignements précieux sur le déplacement des fluides dans nos structures poreuses. Nous aurions alors une information quasiment complète de la dynamique du système en accédant in-situ aux courbes de pression capillaires et aux perméabilités relatives.

Conclusions and perspectives (English Version)

It is essential to understand the underlying driving forces that control the two-phase flow of immiscible fluids in a porous medium. Indeed, there is a wide range of applications of two-phase flows in various areas, particularly for oil engineering and hydrogeological recovery processes. They usually involve the displacement of a non-wetting fluid by a wetting fluid, for instance the injection of water in the secondary oil recovery technique (EOR). This technique is not yet considered satisfactory in terms of oil recovery efficiency, because fluid displacement process in porous media is not well defined.

A direct visualization and measurement method of fluid flow in porous media, such as MRI technique can be a useful tool for a better understanding of the fluid displacement process. The effectiveness of this method depends on the image resolution, itself related to the strength and quality of the MRI system.

This research consisted to realize different experiments of displacement of oil by water in porous media models: stacking of sand grains or polystyrene beads. The objectives were:

- Measure the oil saturation and residual oil in the porous media, during the whole period of the displacement process.
- Capture the consecutive images of the structures formed by the deformed displacement of the water-oil front. These images include a vertical slice along a diameter of the column and eight horizontal sections evenly spaced in the most homogeneous part of the imaging probe.
- Treat the results provided by the MRI device with Matlab codes so as to rebuild the images and perform statistical processing from the recorded data.
- Study the mechanism of propagation of viscous fingering according to MRI data.
- Analyze the data to obtain the kinetic process parameters of the trapped phase formation and to understand the dominant mechanisms of fluid displacement.

At the end of this study, we can draw some important conclusions:

- By comparing different types of imaging methods, including X-rays or optical techniques, it has been shown that only MRI is able to visualize the internal structure of a three-dimensional system with a spatial resolution of the species present. The MRI technique is well adapted to distinguish the distribution of fluids in comparison with other imaging modalities because it only "sees" the protons (^1H) in the liquid phase.
- The distribution of T2 relaxation times is the key information in MRI measurement. Thus, we first evaluated the range of the relaxation times of the fluids used in our experiments and then we estimated the modification of this parameter once placed in a particular porous structure. Different samples were prepared and we used a low field spectrometer (Minispec Bruker mq20) to measure these T2 distributions using a CPMG sequence. The T2 values at 20 MHz for pure water and oil are 2.02 s and 0.88 s, respectively. These values vary according to the type of porous support and decrease as the pore size is reduced.

- A high-resolution MRI technique was used to investigate the two-phase flow of oil and water in a porous medium. The MRI tool used is based on a vertical magnet of 14 T, which can provide for our experiments a resolution of about 0.2 mm per pixel.
- Two types of imaging methods have been tested to obtain high quality MRI maps. The first method is based on the chemical shift phenomenon (selective method), and the second is a non-selective method based on the cancelling of the water signal by adding Mn^{2+} ions which reduce the relaxation time of water (T_2). The second method gave very good results and was selected for the rest of our experimental study because of its simplicity to be implemented. An appropriate MRI imaging protocol based on the spin echo method (MSME: Multi Slice - Multi Echo) was then used.
- Experiments were conducted on a vertical porous column formed from polystyrene beads or packed sand, two materials with different wetting properties. A positive impact on the imaging procedure was observed by adding manganese chloride ($MnCl_2$) to the injected aqueous phase. It shortened the T_2 water relaxation time to 0.7 ms instead of 2.35 s without any effect on the T_2 of the oil phase. Given the relatively slow displacement of the involved phases (more than 10 hours for an experiment), the MRI technique allowed us to have a very precise temporal and spatial (almost 3D) description of the movement of oil, and consequently of water.
- We are able to visualize by MRI small beads size, up to 0.4 mm in diameter that make up the porous medium. It is therefore possible to obtain local values of water and oil saturation (almost at the pore scale), and without difficulty to deduce the mean saturation profiles along the vertical. The importance of water channeling or fingering phenomena has been highlighted. Obviously, the size of the beads/grains and the value of the porosity plays an important role in the deformation of the moving front. The relationship between final residual oil saturation and dimensionless numbers was also studied. It shows that the water-oil displacement process and the amount of trapped oil are mainly controlled by the wettability of the porous matrix and the capillary force.
- In the oil-wet pores (polystyrene beads), oil is the wetting phase, so the pore channel walls prefer contact with oil rather than water. In such a configuration, the capillary force acts as a resistance force which prevents oil movement and keeps it in contact with beads surface. We have observed the residual oil saturation about 38% for the cases of this type of medium. The experiments were made under the conditions of $-4.7 < \log(Ca) < -4.4$ with $\log(\mu_w / \mu_o)$ unchanged, which proves that this type of displacement process is located (Lenormand et al. 1988) at the crossing between stable displacement and capillary fingering.
- In the water-wet material (sand packed column), oil is the non-wetting phase, and the capillary force no longer acts as a resistance force, but as a positive contribution to the movement of the two fluids. Consequently, the residual oil saturation at the end of the tests is much lower than that of the model with polystyrene beads. Each experiment was repeated to confirm the obtained results. Residual oil saturations in the sand model ranged from about 10% to 14% at three different injection rates. The residual saturation in oil for the various injection flow rates is quite of the same order of magnitude, with a regular slight increase in the case of slower displacements. This is explained by the contribution of viscous forces on the displacement process at higher capillary numbers. In general, the flooding process yields the following dimensionless numbers: $6.4E-6 < Ca < 1.3E-5$ and $Bo = 1.26E-4$, which confirms the important effect of capillarity.

- More tests were conducted on the sand experiment by varying the injection rate. For a representative test, average flow velocity is of the order of $2.6\text{E-}6$ m/s, taking into account the volume of trapped oil. Basing on the front propagation in the sand model, the average velocity of front diffusion was estimated as $1.0\text{E-}6$ m/s. It gives that under the conditions of $Ca \sim 1\text{E-}5$ and $Bo \sim 1\text{E-}4$ the radial redistribution of water is lower than the global vertical advection.
- The water flooding in sand has shown that the advance of the displacement front happens in the form of occasional jumps and is controlled by viscous and capillary forces, but is also very sensitive to the heterogeneity of the medium. The comparison of the results with the diagram of the flow regimes proposed by R. Lenormand (Lenormand et al. 1988) confirms that the experiments are located at the intersection of the stable viscous displacement and capillary fingering regimes, which explains why relatively small amplitude fingers are observed.
- A method is proposed for calculating the relative permeability curves from the MRI signal.
- The numerical simulation of immiscible two-phase flow (water-oil) in a vertical porous medium is achieved using COMSOL software. Input data were extracted from the experimental data set for packed sand. The effect of the different forces involved has been investigated. The vertical fluid saturation profile has been verified with the numerical simulation model. The simulations qualitatively confirmed the experimental results. A good agreement is obtained on the comparison with the experimental results.

Through the research conducted in this work, the following perspectives and future studies can be proposed:

- A real core sample (reservoir rock) could be used in order to investigate a consolidated porous medium, closer to reality. In this case, the experimental setup should be modified to handle a much higher expected injection pressure.
- Oil phase fluid properties were chosen to be more representative of light crude oil. The different ranges of viscosity and density of the fluids should be investigated.
- The study of chemically assisted recovery (C-EOR) using polymers or surfactants could be studied systematically using our MRI technique and the experimental setup we used. Some tests in this direction have shown the possibility and interest of testing the performance of these recovery techniques in this way.
- The dynamic relative permeability curves can be constructed for the future experimental results.

We have not been able to include pressure sensors in the experimental setup because most of these instruments contain metal elements that cannot be installed in the MRI system. The search for pressure sensors working in the ranges of interest, and compatible with MRI measurements, would provide valuable information on the movement of fluids in the porous structures. We would then have almost complete information about the dynamics of the system by having access to in situ capillary pressure curves and relative permeability.

Bibliography

- [1] Akin, S. and Kovscek, A.R., Computed tomography in petroleum engineering research, in Application of X-ray computed tomography in the geosciences, Geological Society, London, Special Publication, vol. 215, (2003), pp. 23-38.
- [2] F. Larachi, R. Hannaoui, P. Horgue, F. Augier, Y. Haroun, S. Youssef, E. Rosenberg, M. Prat, M. Quintard, X-ray micro-tomography and pore network modeling of single-phase fixed-bed reactors, Chemical Engineering Journal, vol. 240, (2014), pp. 290-306.
- [3] T. Pak, I.B. Butler, S. Geiger, M.I.J Van Dijke, K. S. Sabie, Droplet fragmentation: a new pore-scale process, Proceedings of the national Academy of Sciences, 112 (7), (2015), pp. 1947-1952.
- [4] D. Bernard, 3D Quantification of Pore Scale Geometrical Changes Using Synchrotron Computed microtomography, Oil & Gas Science and Technology, Vol. 60, (2005), pp. 747-762.
- [5] S. Chen, K-H. Kim, F. Qin, A.T. Watson, Quantitative NMR imaging of multiphase flow in porous media, Magnetic Resonance Imaging Vol. 10, (1992), pp. 815-826.
- [6] Y. Zhao, Y. Song, Y. Liu, H. Liang, B. Dou, Visualization and Measurement of CO₂ Flooding in Porous Media Using MRI, Industrial & Engineering Chemistry Research, Vol. 50, (2011), pp. 4707-4715.
- [7] Y. Zhao, Y. Song, Experimental investigation on spontaneous counter-current imbibition in water-wet natural reservoir sandstone core using MRI, Magnetic Resonance in Chemistry, Vol. 55, (2016), pp. 546-552.
- [8] J. Mitchell, T.C. Chandrasekera, D.J. Holland, L.F. Gladden, E.J. Fordham, Magnetic resonance imaging in laboratory petrophysical core analysis, Physics Reports, Vol. 526, (2013), pp. 165-225.
- [9] M. Li, L. Romero-Zerón, F. Marica, B. J. Balcom, Polymer Flooding Enhanced Oil Recovery Evaluated with Magnetic Resonance Imaging and Relaxation Time Measurements, Energy Fuels, Vol. 31, (2017), pp. 4904-4914.
- [10] Johns, M. L. and Gladden, L.F., Magnetic resonance imaging study of the dissolution kinetics of octanol in porous media, Colloid and Interface Science, 210, (1999), pp. 261-270.
- [11] Ersland, G., Fernø, M.A., A. Graue, Baldwin, B.A., Stevens, J., Complementary imaging of oil recovery mechanisms in fractured reservoirs, Chemical Engineering Journal, 158, (2010), 32-38.
- [12] W. Salameh, S. Leclerc, D. Stemmelen, J.M Escanye, NMR Imaging of Water Flow in Packed Beds, diffusion-fundamentals.org 14 (5), (2010), pp 1-5.
- [13] Panfilova, I. and Panfilov, M. (2005) Phenomenological meniscus model for two-phase flow through porous media. Transport in Porous Media, 58(1), (2005), 87-119.

- [14] Abdus Satter Ghulam M. Iqbal, Reservoir Engineering, The Fundamentals, Simulation, and Management of Conventional and Unconventional Recoveries, 1st Edition (2015).
- [15] L. N. Nwideo, S. Theophilus, A. Barifcani, M. Sarmadivaleh, S. Iglauer, EOR Processes, Opportunities and Technological Advancements, chapter In book of Chemical Enhanced Oil Recovery (cEOR) - a Practical Overview, DOI: 10.5772/64828 (2016).
- [16] Erle C. Donaldson and Waqi Alam, Wettability, book, chapter 3 - Wettability and Production, (2008).
- [17] Habermann B., The efficiencies of miscible displacement as a function of mobility ratio. Petroleum Transactions, AIME, 219, pp. 264-272; Miscible processes, reprint series, SPE Dallas, (1960) 8, 106-114.
- [18] Les principes de la RMN par Joseph P. Hornak, Ph.D. : <http://www.cis.rit.edu/htbooks/nmr/inside.htm>.
- [19] Sprawls P. , Magnetic Resonance Imaging; Principles Methods and Techniques, chapter 2: Magnetic Resonance Imaging System Components, pp. 13–23, Medical Physics Publishing Corporation (2000).
- [20] H. Haynes, W. Holmes, The Emergence of Magnetic Resonance Imaging (MRI) for 3D Analysis of Sediment Beds, book: Geomorphological Techniques, Chapter 1, Publisher: Wiley & Sons, Editors: British Society of Geomorphology, (2013).
- [21] Gladden LF, Hollewand MP, Alexander P. Characterization of structural inhomogeneities in porous media. AIChE J. 1995; 41: pp. 894–906.
- [22] Song YQ. Determining pore sizes using an internal magnetic field, 2000; 143(2): pp. 397– 401. [PubMed: 10729266]
- [23] Song YQ, Ryu SG, Sen PN. Determining multiple length scales in rocks, 2000; 406(6792), pp. 178–181. [PubMed: 10910355].
- [24] Gingras MK, MacMillan B, Balcom BJ. Visualizing the internal physical characteristics of carbonate sediments with magnetic resonance imaging and petrography. Bull. Canad. Petrol. Geol. 2002; 50(3): pp.363–369.
- [25] Quan Chen, Andrew E. Marble, Bruce G. Colpitts, Bruce J. Balcom. 2005; The internal magnetic field distribution, and single exponential magnetic resonance free induction decay, in rocks. Journal of Magnetic Resonance, Volume 175, Issue 2, August 2005, pp. 300-308.
- [26] Zhou Yu, Yan Zhang, Lizhi Xiao, Guangzhi Liao. Characterization of porous media by T2-T2 correlation beyond fast diffusion limit. Magnetic Resonance Imaging, Volume 56, February 2019, pp. 19-23.
- [27] Yoon HK, Zhang CY, Werth CJ, Valocchi AJ, Webb AG. Numerical simulation of water flow in three dimensional heterogeneous porous media observed in a magnetic resonance imaging experiment. Wat. Resour. Res. 2008; 44:W06405.

- [28] L. Jianga, Y. Songa, Y. Liua, M. Yanga, N. Zhua, T. Wang, Y. Zhao, Magnetic Resonance Imaging of CO₂/water two phase flow in Porous media, *Energy Procedia* 37 (2013), pp. 6839 – 6845.
- [29] Kuniyasu Ogawa, Takeshi Matsuka, Shuichiro Hirai and Ken Okazaki. Three-dimensional velocity measurement of complex interstitial flows through water-saturated porous media by the tagging method in the MRI technique. *Measurement Science and Technology*, 2001, Volume 12, Number 2.
- [30] Ai-xiang WU, Chao LIU, Sheng-hua YIN, Zhen-lin XUE, Xun CHEN. Pore structure and liquid flow velocity distribution in water-saturated porous media probed by MRI. *Transactions of Nonferrous Metals Society of China*, Volume 26, Issue 5, May 2016, pp. 1403-1409.
- [31] Ying Teng, Guohuan Lu, Yinting Fan, Yu Liu, Yongchen Song. Experimental Study of Density-driven Convection in Porous Media by Using MRI. *Energy Procedia*, Volume 105, May 2017, pp. 4210-4215.
- [32] Daan W. de Kort, Stefan A. Hertel, Matthias Appel, Hilko de Jong, Lynn F. Gladden. Under-sampling and compressed sensing of 3D spatially-resolved displacement propagators in porous media using APGSTE-RARE MRI. *Magnetic Resonance Imaging*, Volume 56, February 2019, pp. 24-31.
- [33] T. Bahar, Fabrice Golfier, C. Oltean, E. Lefevre, C. Lorgeoux. Comparison of theory and experiment for NAPL dissolution in porous media. *Journal of Contaminant Hydrology*, Elsevier, 211, pp.49-64 (2018).
- [34] J.P. Stokes, D.A. Weitz, J.P. Gollub, A. Dougherty, M.D. Robbins, P.M. Chaikin, H.M. Lindsay; *Physical Review Letters* 57,1718 (1986).
- [35] Corapcioglu, M. Yavuz; Fedirchuk, Paula, Glass bead micromodel study of solute transport, *Journal of Contaminant Hydrology*, Volume 36, Issue 3, pp. 209-230, (1999).
- [36] G. Blois, J. M. Barros, T. Christensen, PIV investigation of two-phase flow in a micro-pillar microfluidic device, 10th international symposium particle image velocimetry, 2013.
- [37] Tsakiroglou C., Vizika-Kavvadias O., Lenormand R., Use of micromodels to study multiphase flow in porous media, International Symposium of the Society of Core Analysts held in Napa Valley, California, USA, 16-19 September, (2013).
- [38] G. Lekmine, H. Auradou, M. Pessel, J.L. Rayner, Quantification of tracer plume transport parameters in 2D saturated porous media by cross-borehole ERT imaging, *Journal of Applied Geophysics* 139 (2017), pp. 291–305.
- [39] Charles J. Werth, C. Zhang, M. Brusseau, M. Oostrom, and T. Baumann, A review of non-invasive imaging methods and applications in contaminant hydrogeology research, *J. Contam Hydrol.* 2010 April 1; 113.
- [40] M. Beston, J. Barker, P. Barnes, T. Atkinson, D. Jupe, Porosity Imaging in Porous Media Using Synchrotron Tomographic Techniques, *Transport in Porous Media* 57: pp. 203–214, (2004).

- [41] Wang S., Ayra LS, Castellana FS, Gryte CC. Reconstruction of Oil Saturation Distribution Histories During Immiscible Liquid-Liquid Displacement by Computer-Assisted Tomography. *American Institute of Chemical Engineers J.* 1984; 30(4): pp. 642–646.
- [42] R. Moreno-Atanasio, R. A. Williams, X. Jia, Combining X-ray microtomography with computer simulation for analysis of granular and porous materials, *particuology journal* 8 (2010), pp. 81–99.
- [43] Hicks PJ Jr, Deans HA, Narayanan K. Distribution of Residual Oil in Heterogeneous Carbonate Cores Using X-Ray Computerized CT. *SPE Formation Evaluation.* 1992; 7(3): pp. 235–240.
- [44] Fagerlund F., Illangasekare THA, Niemi A. Nonaqueous-phase liquid infiltration and immobilization in heterogeneous media: 1. Experimental methods and two-layered reference case. *Vad. Zone J.* 2007; 6: pp. 471–482.
- [45] F. E. Alvarado, A. S. Grader, O. Karacan, P. M. Halleck, visualization of three phases in porous media using micro computed tomography, *International symposium society of core analysis*, Pau, France (2003).
- [46] K. Mikami, T. Mukunoki Study On Mechanism Of Two-phase Flow In Porous Media Using Micro Focused X-ray CT, *International Petroleum Technology Conference*, 19-22 January, Doha, (2014).
- [47] E. Guyon, Jean-Pierre Nadal, Y. Pomeau, *Disorder and Mixing Convection, Diffusion and Reaction in Random Materials and Processes*, Series E: Applied Sciences - Vol. 152, 1988.
- [48] B.C. Craft, M. Hawkins, revised by R. E. Terry, *Applied Petroleum Reservoir Engineering*, book (second edition), 1991, ISBN 0-13-039884-5.
- [49] B. Guo, k. Sun, A. Ghalambor, *Well Productivity Handbook*, chapter 3 - Properties of Petroleum Reservoirs, Gulf Publishing Company, 2008, pp. 45-62.
- [50] Coneybeare, C. E. B., 1967, Influence of compaction on stratigraphic analysis: *Canadian Petroleum Geology Bulletin*, v. 15, pp. 331–345.
- [51] Keelan, D. K., 1982, Core analysis for aid in reservoir description: *Journal of Petroleum Technology*, v. 34, p. 2483–2491, DOI: 10.2118/10011-PA.
- [52] Y. Nakayama, R. F. Boucher, *Introduction to Fluid Mechanics*, book, chapter 2, Butterworth-Heinemann, ISBN 0 340 67649 3, 1999.
- [53] https://en.wikipedia.org/wiki/Viscosity#/media/File:Laminar_shear.svg
- [54] John R. Fanchi, *Shared Earth Modeling*, chapter 7: Measures of Rock-Fluid Interactions, Pages 108-132, 2002, DOI: <https://doi.org/10.1016/B978-0-7506-7522-2.X5000-9>.
- [55] S. H. Raza, L. E. Treiber, and D. L. Archer, "Wettability of Reservoir Rocks and Its Evaluation," *Producers Monthly*, vol. 32, pp. 2-7, 1968.
- [56] S. Zeppieri, J. Rodriguez, and A. L. Lopez de Ramos, Interfacial Tension of Alkane + Water Sustems, *Chemical Engineering Journal*, 46, (2001), pp. 1086-1088.

-
- [57] W. Abdullah, J. Buckley, A. Carnegie, J. Edwards, B. Herold, E. Fordham, A. Graue, T. Habashy, N. Seleznev, C. Signer, H. Hussain, B. Montaron, M. Ziauddin, *Fundamentals of Wettability*, Oilfield Review, Schlumberger, 2007.
- [58] Leverett, M.C., 1941, *Capillary Behavior in Porous Solids*, Trans, AIME v. 142, pp. 341-358.
- [59] A. Szymkiewicz, *Modelling Water Flow in Unsaturated Porous Media* (2013), Chapter 2: Mathematical models of flow in porous media, pp. 9-44, GeoPlanet: Earth and planetary sciences book series, Springer, DOI 10.1007/978-3-642-23559-7.
- [60] G. Løvoll, Y. Meheust, K. Jørgen Maløy, E. Aker, J. Schmittbuhl, Competition of gravity, capillary and viscous forces during drainage in a two-dimensional porous medium, a pore scale study. *Energy* 30, (2005), pp. 861–872.
- [61] M. J. Blunt, *Multiphase flow in permeable media*, Cambridge University Press, 2017.
- [62] Bloch F., Nuclear induction. *American Physical Society*, Rev. 70: pp. 460-474, 1946.
- [63] Bloch F., Hansen W.W., Packard M.E., The nuclear induction experiment. *Phys Rev*: 70, pp. 474-485, 1946..
- [64] Purcell E., Torrey H.C., Pound R.V. Resonance Absorption by Nuclear Magnetic Moments in a solid. *Phys. Rev.* 69 : pp. 37-38, 1946.
- [65] Hahn E.L., An accurate nuclear magnetic resonance method for measuring spin-lattice relaxation times. *Phys. Rev.* 76: pp. 145-146, 1949.
- [66] Hahn E.L., Spin echoes. *Phys. Rev.* 80: pp. 580-594, 1950.
- [67] Torrey H.C., Transient nutations in nuclear magnetic resonance. *Phys Rev.* 76: pp. 1059-1068, 1949.
- [68] Ernst R.R., Anderson W.A., Application of Fourier transform spectroscopy to magnetic resonance. *Review of Scientific Instruments* 37 : pp. 93–102, 1966.
- [69] Lauterbur P.C., Image formation by induced local interactions: examples employing nuclear magnetic resonance. *Nature* 242: pp. 190-191, 1973.
- [70] Mansfield P., Grannell P.K., NMR diffraction in solids. *J. Phys. C Solid State* 6: L422-L426, 1973.
- [71] Mansfield P., Multi-planar image formation using NMR spin echoes. *J. Phys. C Solid State* 10: L55-L58, 1977.
- [72] Canet D., Boubel J.C., and Canet-Soulas E. *La RMN concepts, méthodes et applications*. Dunod 2ème édition, 2002, 235 pages.
- [73] Callaghan P.T. *Principles of nuclear magnetic resonance microscopy*. Oxford science publications. 1991, 516 pages.
- [74] XRayPhysics. *Interactive Radiology Physics*. MRI Physics: Pulse sequences Available from: <http://xrayphysics.com/sequences.html>.
- [75] Mariluce Gonçalves Fonseca (March 13th 2013). *Spin Echo Magnetic Resonance Imaging, Imaging and Radioanalytical Techniques in Interdisciplinary Research - Fundamentals and Cutting Edge Applications*, Faycal Kharfi, IntechOpen, DOI:

- 10.5772/53693.
- [76] Liang Z, Lauterbur PC., Principles of Magnetic Resonance Imaging: A Signal Processing Perspective. Wiley-IEEE Press; 1999.
- [77] M. Bernstein, K. King, X. Zhou, Handbook of MRI pulse sequences (2004), Chapter 4: spectral radiofrequency pulses, pp. 96 - 124, Elsevier Academic Press - UK, ISBN-13: 978- 0-12-092861-3.
- [78] e-MRI, The-Physics, K-space <https://www.imaios.com/es/e-Cursos/e-MRI/The-Physics-behind-it-all/K-space>.
- [79] J. Yan, X. Luo, W. Wang, F. Chen, R. Toussaint, J. Schmittbuhl, G. Vasseur, L. Zhang, Testing oil saturation distribution in migration paths using MRI, Journal of petroleum Science and Engineering 86-87, (2012), pp. 237-245.
- [80] N. Bloembergen, Proton relaxation times in paramagnetic solutions. Journal of Chemical Physics, (1957), 27, 572-573.
- [81] Johnson, E.F., Bossler, D.P. and Naumann, V.O., Calculation of relative permeability from displacement experiments, Trans. AIME 216 (1959), 370.
- [82] S. Hill and P. F. I. (1952) 'Channeling in packed columns', Chemical Engineering Science. Pergamon, 1 (6) , pp. 247–253. doi: 10.1016/0009-2509(52)87017-4.
- [83] Saffman, P. G. and Taylor, G. (1958) 'The Penetration of a Fluid into a Porous Medium or Hele-Shaw Cell Containing a More Viscous Liquid', Proceedings of the Royal Society A: Mathematical, Physical and Engineering Sciences. The Royal Society, 245(1242), pp. 312–329. doi: 10.1098/rspa.1958.0085.
- [84] Chuoke, R. L., van Meurs, P. and van der Poel, C. (1959) 'The Instability of Slow, Immiscible, Viscous Liquid-Liquid Displacements in Permeable Media'. Society of Petroleum Engineers. Available at: <https://www.onepetro.org/general/SPE-1141-G> (Accessed: 4 January 2018).
- [85] Saffman, P. G. (1986) 'Viscous fingering in Héle-Shaw cells', Journal Fluid Mechanics, volume 173, pp. 73-94.
- [86] Homsy, G. M. (1987) 'Viscous Fingering in Porous Media', Annu. Rev. Fluid Mech., 19, pp. 271–311. doi: 10.1146/annurev.fl.19.010187.001415.
- [87] Homsy, G. M. (1988) 'Chapter XIV THE EFFECT OF DISPERSION ON FINGERING IN MISCIBLE DISPLACEMENTS', pp. 237–251.
- [88] Wang, Z., Feyen, J. and Elrick, D. E. (1998) 'Prediction of fingering in porous media', 34(9), pp. 2183–2190.
- [89] H. E. L. Rose, M. M. Britton (2013) 'Magnetic resonance imaging of reaction-driven viscous fingering in a packed bed, University of Birmingham, Microporous and Mesoporous Materials 178, pp. 64–68.
- [90] P. Daripa and G. Paşa, 'On capillary slowdown of viscous fingering in immiscible displacement in porous media', Transport in Porous Media, (2008) 75 (1), pp. 1–16. doi: 10.1007/s11242-008-9211-2.
- [91] Larry W. Lake, Enhanced oil recovery, book, Prentice Hall, Englewood Cliffs, New

- Jersey (1989) pp. 195-197.
- [92] C. Marle, Cours de production, Les écoulements polyphasiques en milieu poreux, tome 4, Technip (1972).
- [93] R. Lenormand, E. Touboul, C. Zarcone, Numerical models and experiments on immiscible displacements in porous media, *Journal Fluid Mechanics*, 189 (1988), pp; 165-187.
- [94] R. Lenormand, Liquids in porous media, *Journal of Physics: Condensed Matter*, Vol. 2 (1990), pp. 79-88.
- [95] Fleury M., Bossler, Measurement of interfacial area from NMR time dependent diffusion and relaxation measurements, *IFP Energies Nouvelles, Journal of Colloid and Interface Science* 509 (2018), pp. 495–501.
- [96] Carr HY, Purcell EM (1954) Effects of Diffusion on Free Precession in Nuclear Magnetic Resonance Experiments. *Physical Review* 94: p. 630.
- [97] Meiboom S, Gill D (1958) Modified Spin-Echo Method for Measuring Nuclear Relaxation Times. *Review of Scientific Instruments* 29: pp. 688-691.

A. Annexes

| | | |
|------|--|-----|
| I. | Details of the experimental installation..... | 157 |
| II. | Sample preparation | 160 |
| III. | Determination of porous media porosity | 162 |
| IV. | NMR relaxation time measurements T2 (CPMG): | 162 |
| V. | MRI Experimental results for some experiments: | 171 |
| VI. | PTX2000 data sheet | 178 |

I. Details of the experimental installation

The following images are for the MRI instruments and sample components used in our experimental work.

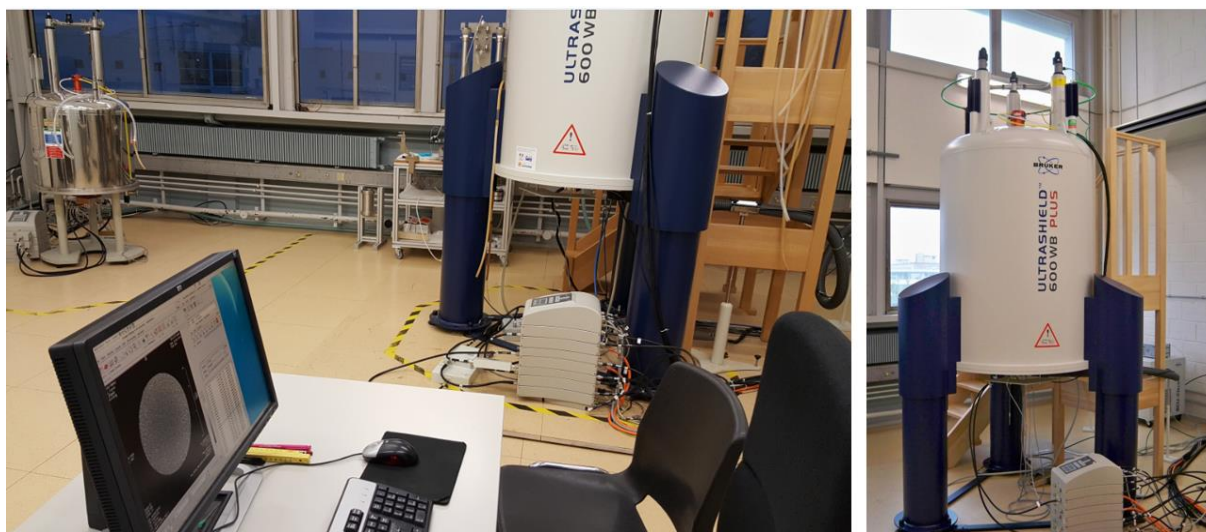


Figure A.1. LEMTA MR imaging platform (14,1 T, 600 MHz)

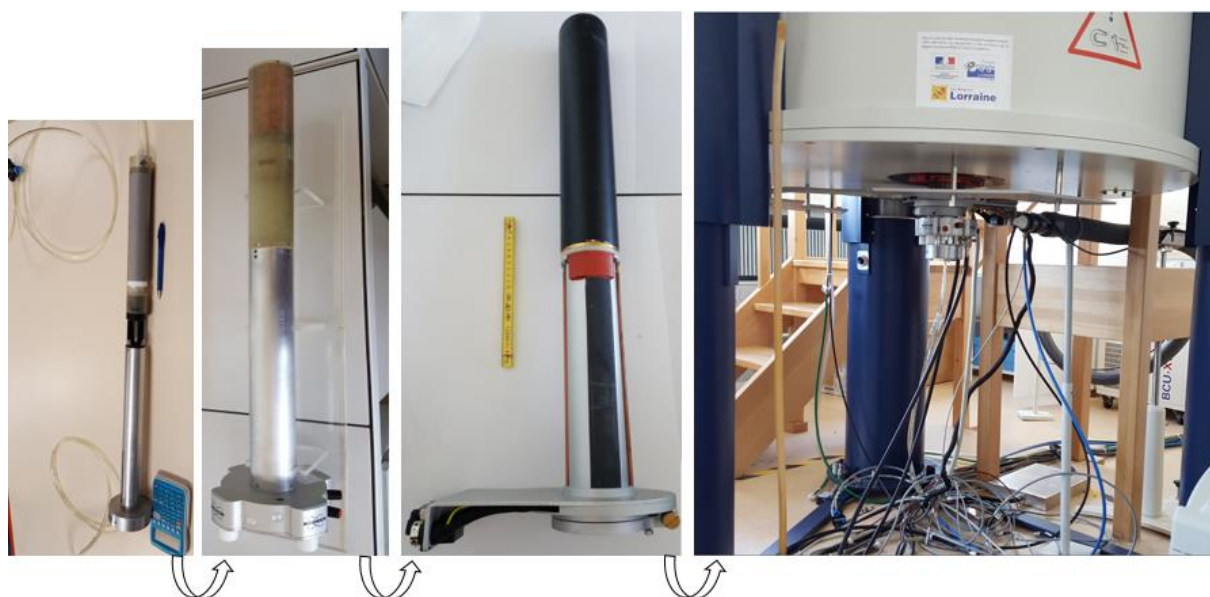


Figure A.2. MRI probe in combination with the Gradient System and the holder with PVC tube sample

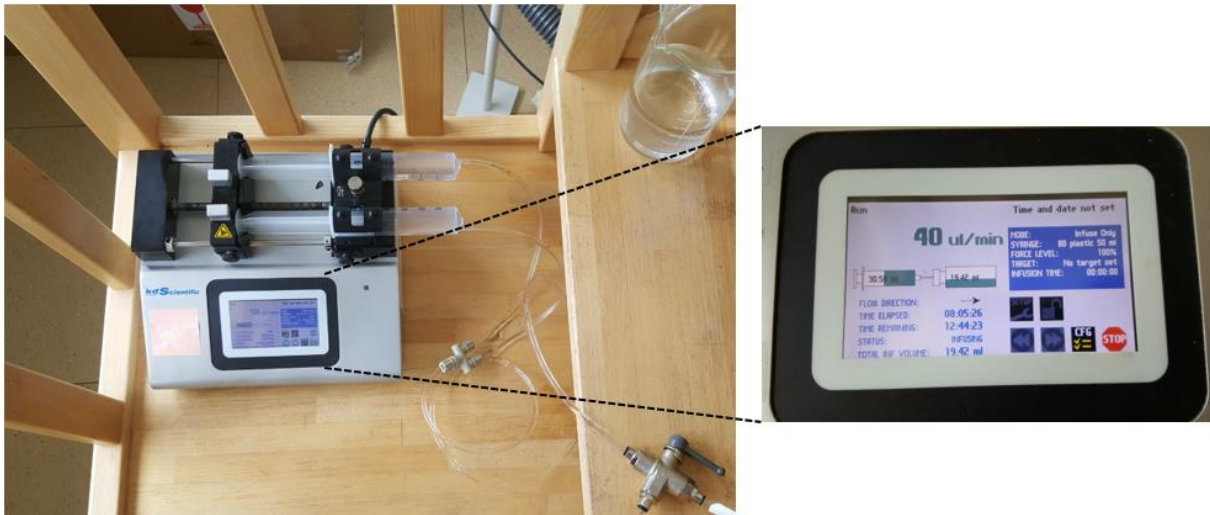


Figure A.3. Syringe injection pump that used in our experiments to inject water, it can inject at a very low rate with an accuracy of $\pm 0.5\%$.

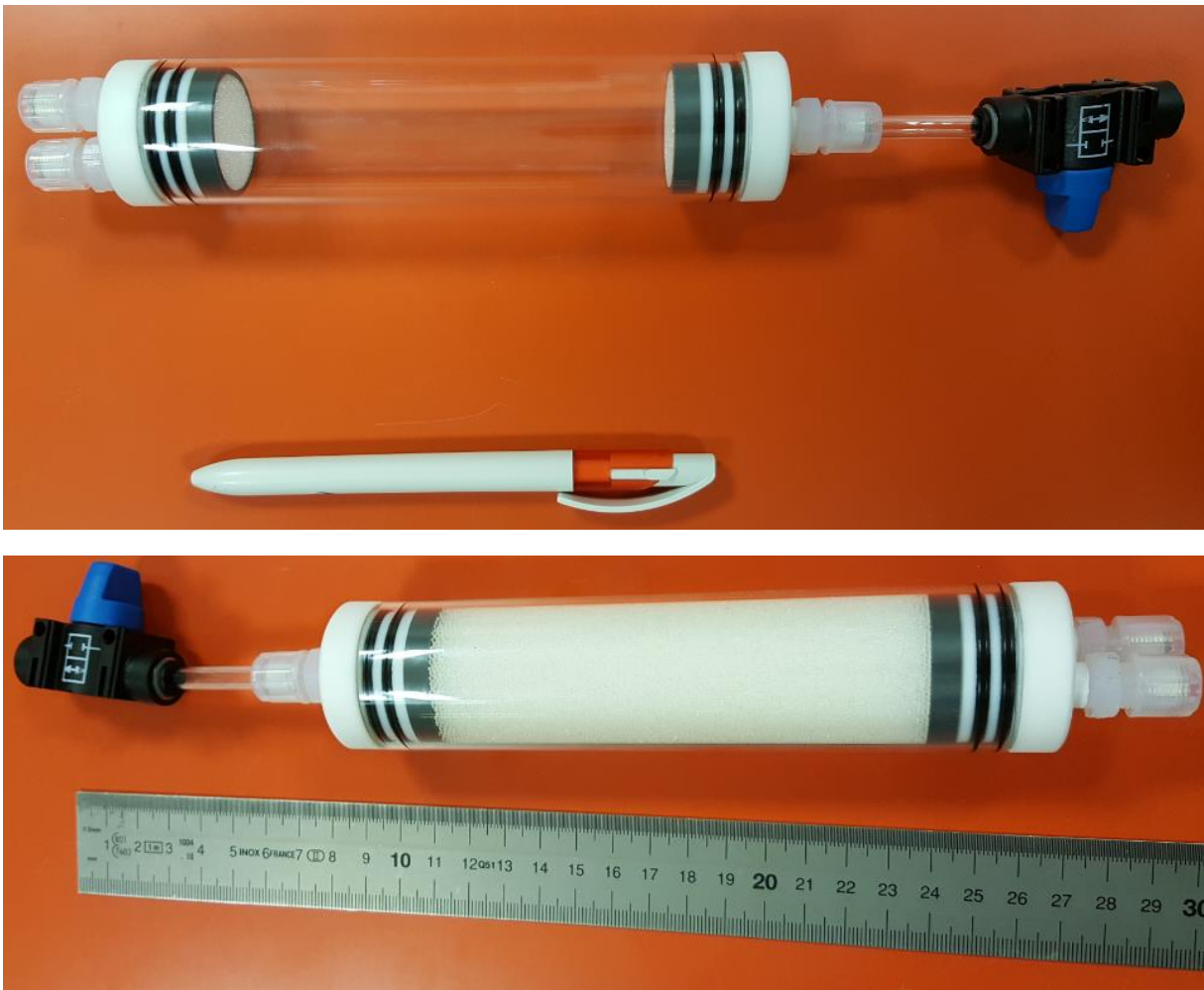


Figure A.4. Glass tube sample with and without beads (10 cm of the final net length).



Figure A.5. Sample components, filters and caps.



Figure A.6. PVC sample and its components (10 cm of the final net length), the weight with and without sand.

Different types of material were used as porous media in this study, starting with glass beads, then polystyrene beads and ending with sands that is more representative for real porous media.

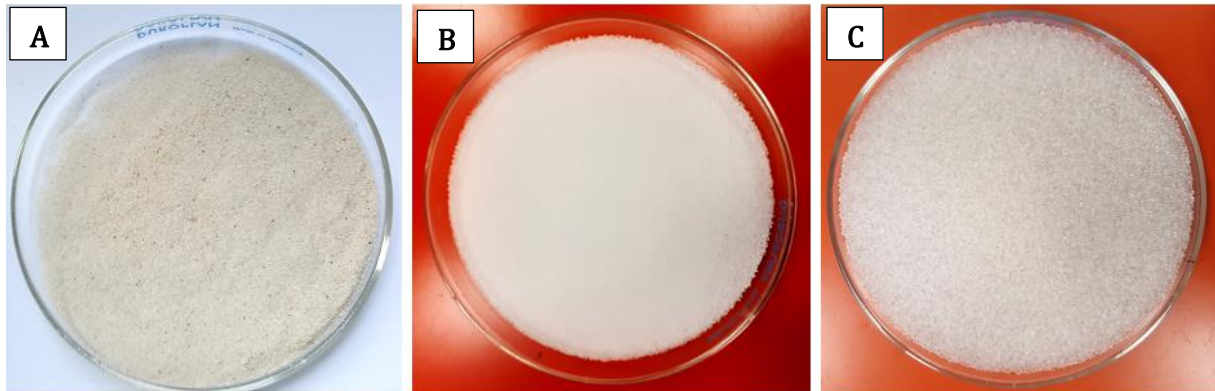


Figure A.7. Various types of materials used as porous medium, (a) sand with a diameter of approximately 0.13 mm, (b) polystyrene beads with a diameter of 0.4 to 0.6, (c) glass beads with a diameter of 1 mm.

II. Sample preparation

The following diagram illustrates the main steps we used to prepare and saturate the samples with the oil phase.

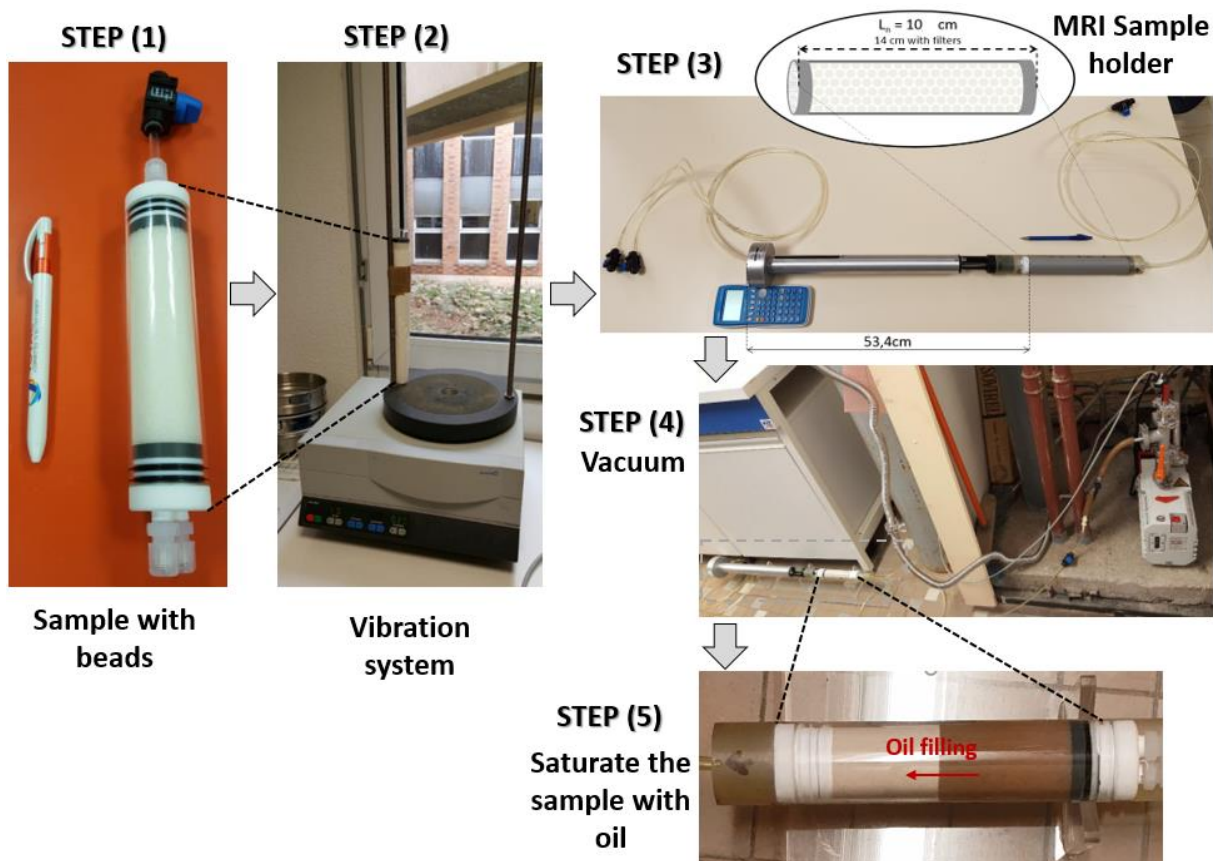


Figure A.8. Five steps of sample preparation.

The figure below shows the first experimental setup preparation and testing prior to the first MRI installation.

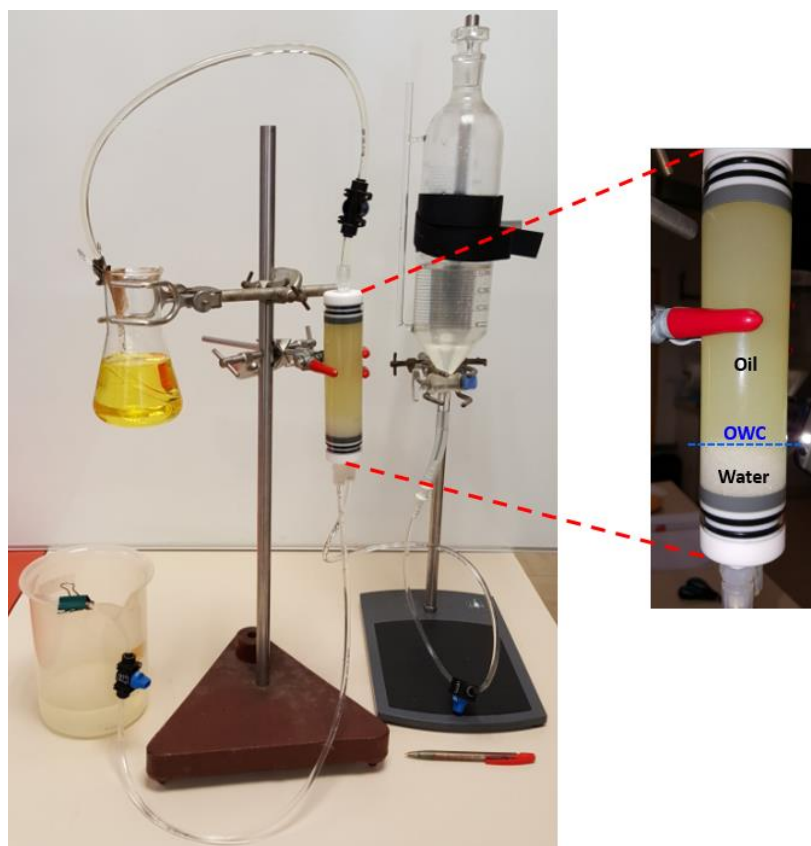


Figure A.9. First try in the lab, to test the model installation and OWC determination.

III. Determination of porous media porosity and PV

As part of this study, the porosity is calculated from the dimensions of the tube and the material used (sand or polystyrene beads):

Volume of tube (V_{tube}) is:

$$V_{tube} = r_c^2 \pi L_{net} \quad (A.1)$$

where:

V_{tube} : volume of tube [m^3]

r_c : tube radius [m]

L_{net} : net length of tube [m]

Volume of the material used (Sands or Polystyrene Beads ($V_{sand \text{ or } beads}$)) is:

$$V_{sand \text{ or } beads} = \frac{M_{sand \text{ or } beads}}{\rho_{sand \text{ or } beads}} \quad (A.2)$$

where:

$V_{sand \text{ or } beads}$: volume of Sands or Beads [m^3]

$M_{sand \text{ or } beads}$: mass of sands or beads [kg]

$\rho_{sand \text{ or } beads}$: density of sands or Beads [kg/m^3]

The porosity of media with a sands or Beads ($\varphi_{sands \text{ or } beads}$) is:

$$\varphi_{sand \text{ or } beads} = \frac{V_{tube} - V_{sand \text{ or } beads}}{V_{tube}} \quad (A.3)$$

Porosity of the experimental models

According to the equation A.1, and with the characteristics of borosilicate glass tube radius of 1.7 cm and length of tube L_{net} is 10.1 cm, the volume of tube = 91.96 cm^3 .

a. Porosity of polystyrene packed beads sample:

The density of the polystyrene beads is $\rho_b = 1.04 \text{ gm/cm}^3$. The mass of polystyrene beads that fills the 10.1 cm of the tube is $M_b = 57.82 \text{ gm}$. Thus, according to the equations A.2 & A.3 the volume of the beads (V_{beads}) is 55.6 cm^3 , and the porosity of media with the polystyrene beads is 38 %.

b. Porosity of sand column sample:

The same procedure was applied to the sand model; sand grain density is approximately ρ_{sands} is 2.638 gm/cm^3 . The porosity determined in the sand is therefore 39 %.

Pore volume of model (PV)

$$PV = \varphi V_{tube} \quad (A.4)$$

For example, for the model of packed sand: $PV = 0.39 \times (1.7)^2 \times \pi \times 10.1 = 35.76 \text{ mL}$

IV. NMR relaxation time measurements T2 (CPMG):

The T2 relaxation time distribution is the key information for the MRI measurement. Therefore, as a first step, it is important to know the range of the relaxation time of the fluids used in our experiments, and the extent of the change in this parameter when placing these fluids in porous media, the principle is similar the use in M. Fleury [95].

The MRI signal from T2 relaxation decays as an exponential curve given by formula (3.5) (see chapter 3). T2 represents the time needed for M_x or M_y to decline to approximately 37% of their initial peak values.

$$M_{XY}(t) = M_{XY \max} \left(e^{\left(-\frac{t}{T2}\right)} \right)$$

This curve is shown in Figure A.10.a. Further analysis, with the with the inverse Laplace transformation (ILT), will provide a T2 relaxation time distribution based on the decay curve, Figure A.10.b.

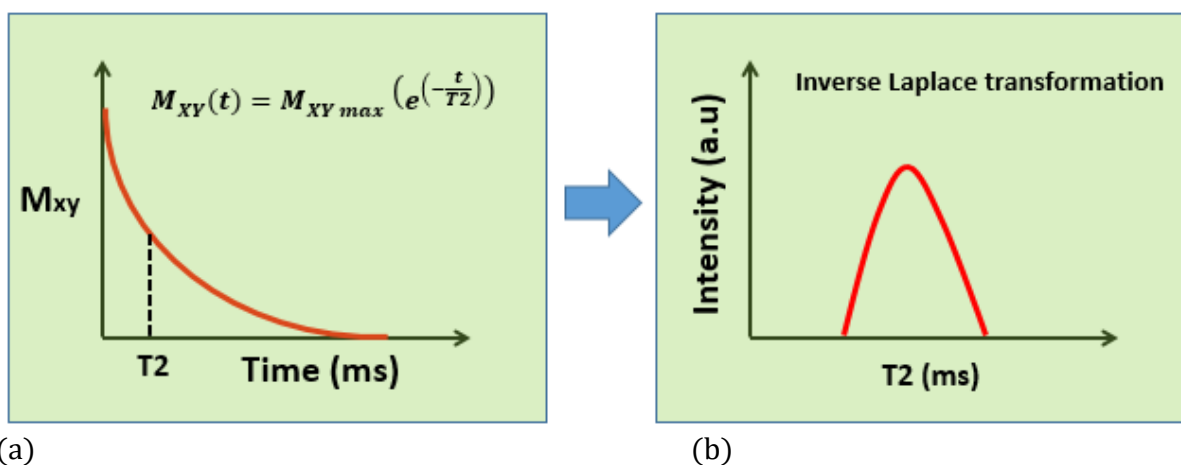


Figure A.10. (a) The decay curve for T2 relaxation time, (b) T2 relaxation time distribution obtained from an inverse Laplace transformation.

The known protocol of CPMG (Carr and Purcell [96], and Meiboom and Gill [97]) will both provide the resulting information with exponential decay curves. The CPMG protocol measures the T2 relaxation process and provides an average value for the total sample under investigation. The inverse Laplace transformation can then be used to find the distribution of T2 relaxation time.

CPMG scan is based on the cycle of RF pulses to produce echoes according to T2 relaxation develops. In this protocol, T2 mapping initiates with a 90° RF pulse, the nucleus then will flip 90 degrees to the XY plane, as indicated in Chapter 3.3. After applying the 90° pulse, the transverse magnetization decays, and this decay signal is called free induction decay (FID). This phenomenon occurs so rapidly that it is difficult to record signals. The solution to refocus the net magnetization is to apply a series of 180° RF pulses creating a series of signals called echoes, see figure A.11.

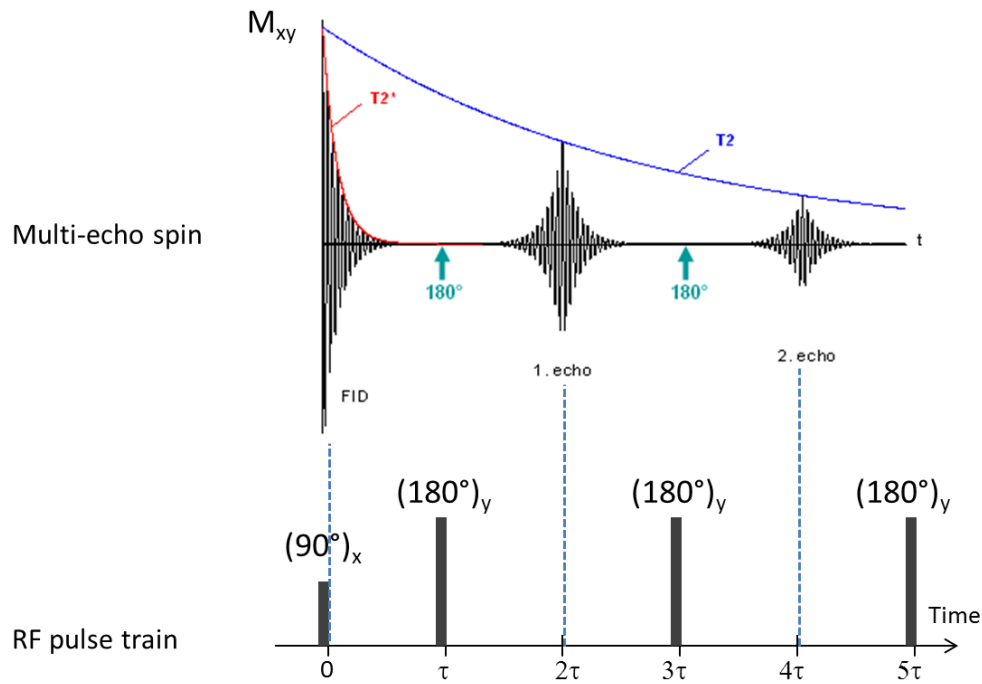


Figure A.11. CPMG pluses sequence to measure $T2$ relaxation time, a series of 180° RF pulses applied to refocus the signal.

The CPMG sequences were performed using a NMR Bruker Minispec mq20 (Fig. A.12) to measure $T2$ for both fluids (water and oil), then for both porous media containing fluids (polystyrene packed beads and sand packed column with fluids). Figure A.13 shows the samples used; pure water, pure oil (PTX2000/Kerosene), sand with water/oil and polystyrene with water/oil. The sample tube internal diameter is 0.878 cm and the height of substances is around 12 mm.

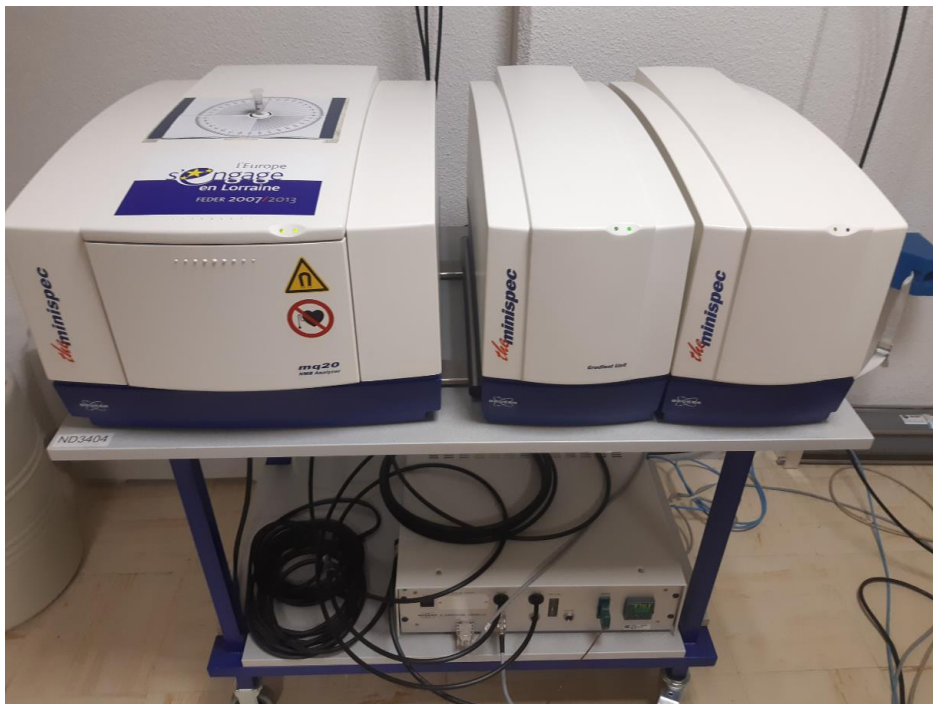


Figure A.12. NMR Bruker Minispec mq20 (equipped with magnetic field gradient of 0.47 T/m) used to measure $T2$ of each sample using CPMG protocol.



Figure A.13. Samples used to measure T2 relaxation time; pure water, pure oil (PTX2000/Kerosene), sand with water/oil and polystyrene with water/oil. The sample tube internal diameter is 0.878 cm and the height of substances is around 12 mm, the total tube height is 12 cm.

The following parameters should be set to perform CPMG scan:

- Echo spacing (2τ), the time delay between the RF pulse and its echo, or between two consecutive echoes.
- Repetition time TR: the required time before the sequence is repeated.
- Determine the number of refocusing pulses.
- The measurements should be repeated many times and the average value of these measurements is estimated.

Note: The CPMG scan does not create an image, but generate a (multi-)exponential relaxation curve, that could be used for further analysis.

We then use the UPENWIN software to obtain, from the CPMG relaxation curve, the average value of the T2 relaxation time (mono-exponential decay) for pure fluid, or the T2 relaxation time distribution (multi-exponential decay) for fluid in porous media.

T2 experimental results:

1. Sample of pure water:

Figure A.14 shows the relaxation time T2 distribution for the pure water in the NMR testing tube.

| | | | |
|-----------|----------------|--------------|---------------------|
| TR = 15 s | $\tau = 10$ ms | T2 = 2129 ms | Amplitude = 80.99 % |
|-----------|----------------|--------------|---------------------|

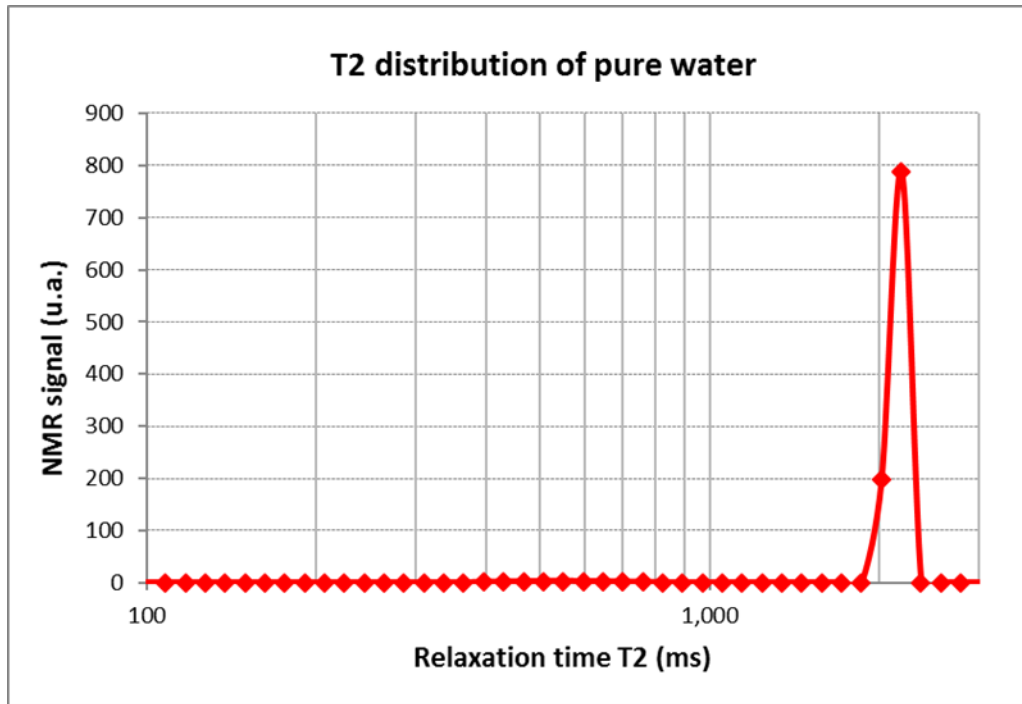


Figure A.14. T2 relaxation time distribution for pure water from CPMG scan. Only one peak point observed at 2129 ms.

2. Sample of pure oil (PTX2000/Kerosene):

Figure A.15 shows the relaxation time T2 distribution for the oil (PTX2000) obtained from CPMG scan in the NMR testing tube.

| | | | |
|-----------|---------------|---------------|---------------------|
| TR = 10 s | $\tau = 2$ ms | T2 = 884.8 ms | Amplitude = 87.77 % |
|-----------|---------------|---------------|---------------------|

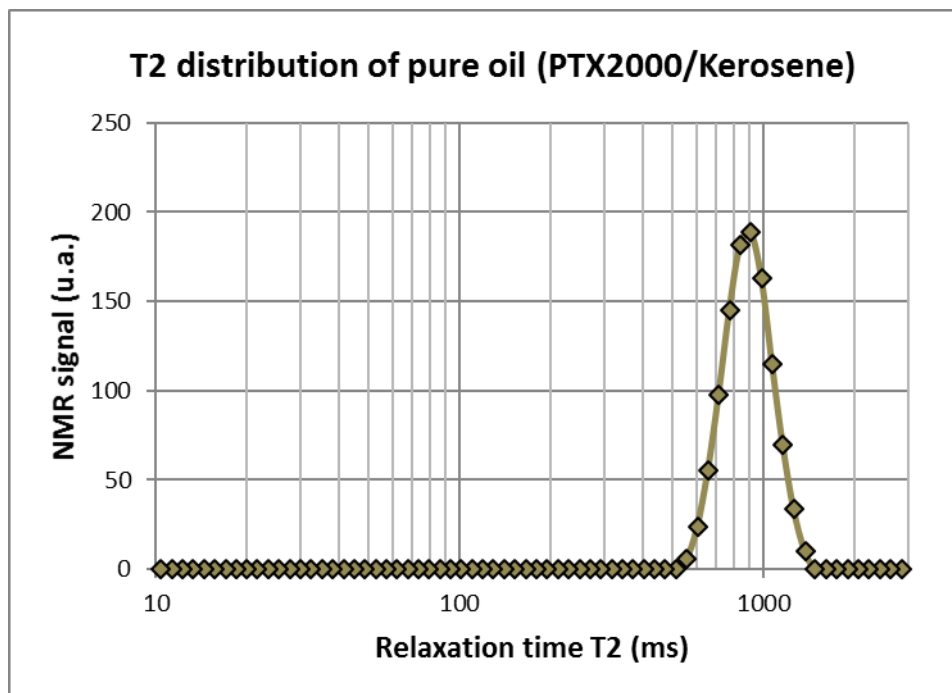


Figure A.15. T2 relaxation time distribution for pure oil (PTX 2000) from CPMG scan. Only one peak point observed at 884.8 ms.

1. Sample of polystyrene containing water (oil-wet porous media):

Figure A.16 below shows the results of T2 relaxation time distribution for the sample of oil-wet polystyrene containing water from CPMG scans, and the results comparison with pure water sample.

| | | | |
|-----------|----------------|--------------|----------------------|
| TR = 10 s | $\tau = 10$ ms | T2 = 1640 ms | Amplitude = 11.747 % |
|-----------|----------------|--------------|----------------------|

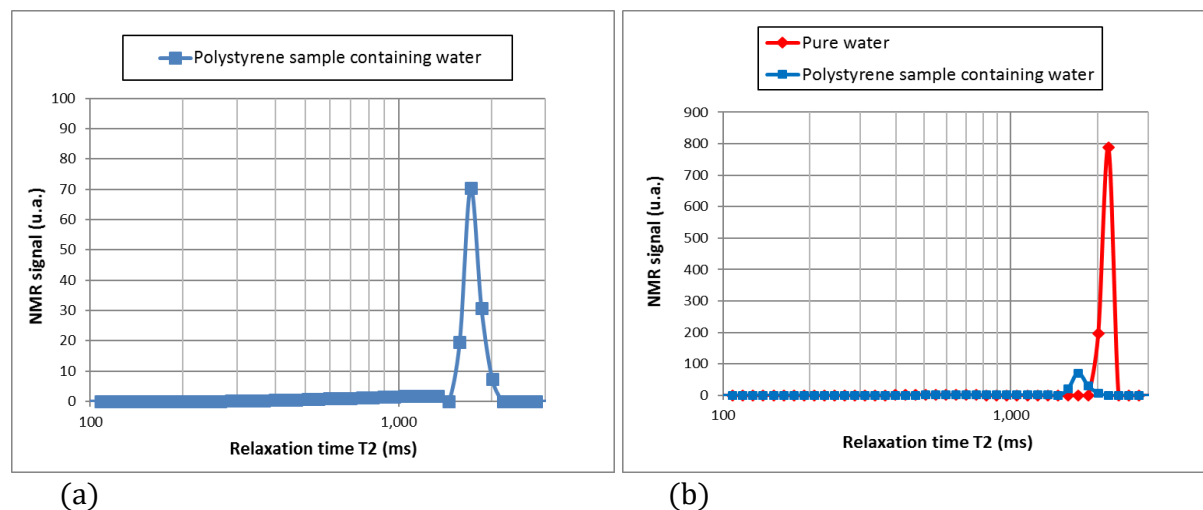


Figure A.16. (a) T2 relaxation time distribution for oil-wet polystyrene sample containing water, (b) T2 comparison between pure water sample and the sample of oil-wet polystyrene containing water.

The presence of water in polystyrene beads resulted in a small shift in the T2 relaxation time distribution comparing with the pure water sample, and the signal intensity value is reduced as well.

2. Sample of polystyrene containing oil (oil-wet porous media):

Figure A.17 below shows the CPMG scan results of T2 relaxation time distribution for the sample of oil-wet polystyrene containing oil (PTX2000/Kerosene), and the results comparison with pure oil sample.

| | | | |
|-----------|---------------|-------------|--------------------|
| TR = 10 s | $\tau = 4$ ms | T2 = 809 ms | Amplitude = 32.1 % |
|-----------|---------------|-------------|--------------------|

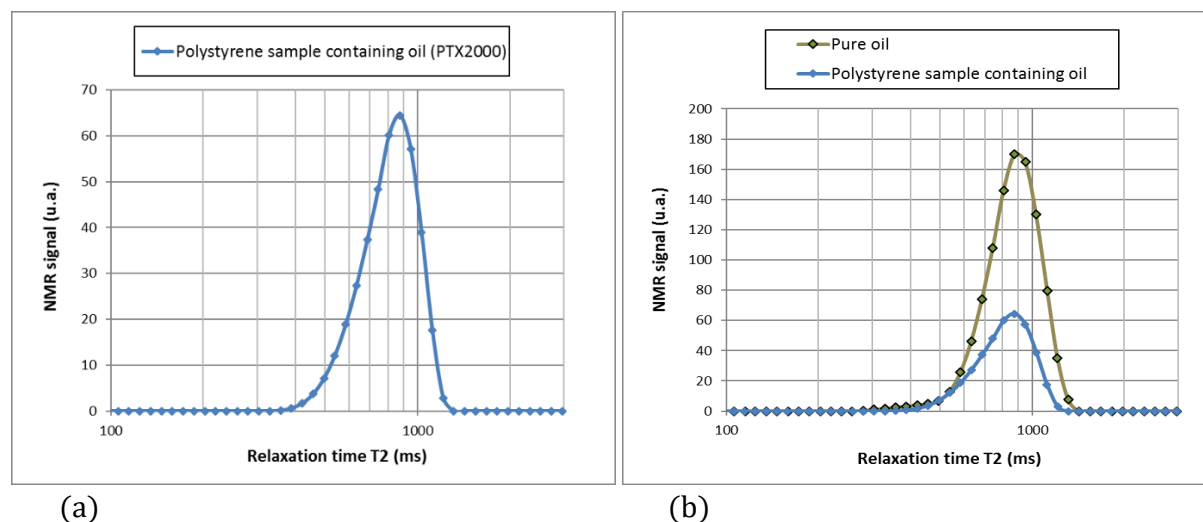


Figure A.17. (a) T2 relaxation time distribution for oil-wet polystyrene sample containing oil, (b) T2 comparison between pure oil sample (PTX2000) and the sample of oil-wet polystyrene containing oil.

In this case, the presence of oil in polystyrene beads gives almost the same peak values for the T2 relaxation time. This could be as a result of the wettability preference effect. The T2 relaxation time is slower in this case comparing with the polystyrene beads containing water.

3. Sample of water-wet sand containing water:

Figures below show the results of T2 relaxation time distribution for the sample of water-wet sand containing water from CPMG scans, the measurements were repeated several times to confirm the results.

Test 1:

| | | | |
|----------|---------------|---------------|---------------------|
| TR = 5 s | $\tau = 2$ ms | T2 = 273.7 ms | Amplitude = 34.99 % |
|----------|---------------|---------------|---------------------|

Test 2:

| | | | |
|----------|---------------|------------|---------------------|
| TR = 5 s | $\tau = 2$ ms | T2 = 280 s | Amplitude = 34.72 % |
|----------|---------------|------------|---------------------|

Test 3:

| | | | |
|----------|---------------|--------------|---------------------|
| TR = 5 s | $\tau = 2$ ms | T2 = 274.2 s | Amplitude = 35.08 % |
|----------|---------------|--------------|---------------------|

Test 4:

| | | | |
|----------|---------------|--------------|---------------------|
| TR = 5 s | $\tau = 2$ ms | T2 = 276.2 s | Amplitude = 35.10 % |
|----------|---------------|--------------|---------------------|

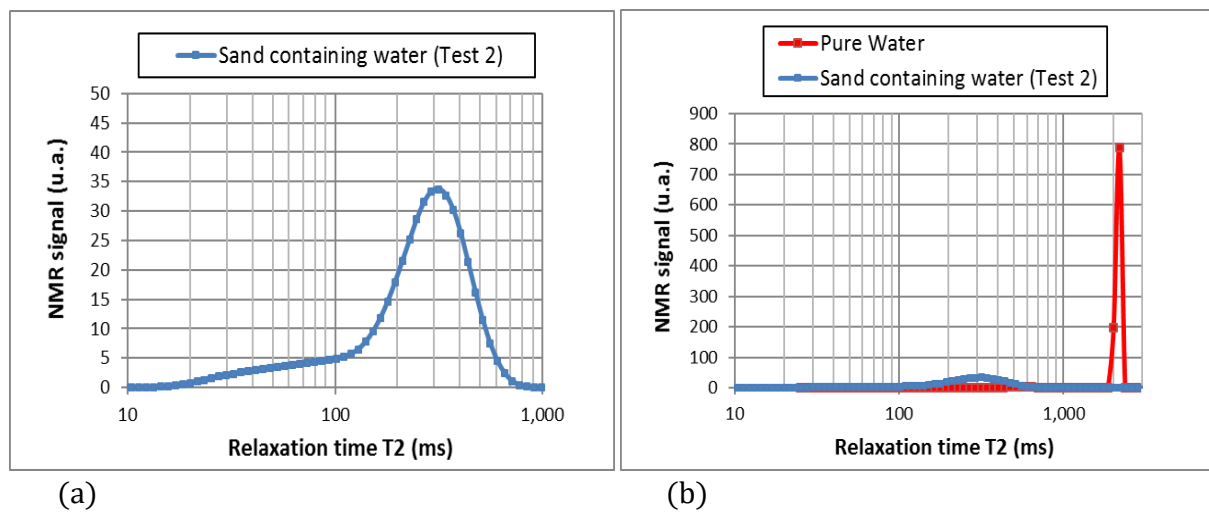


Figure A.18. Test 2 results (a) T2 relaxation time distribution for water-wet sand containing water, (b) T2 comparison between pure water sample and the sample of water-wet sand containing water.

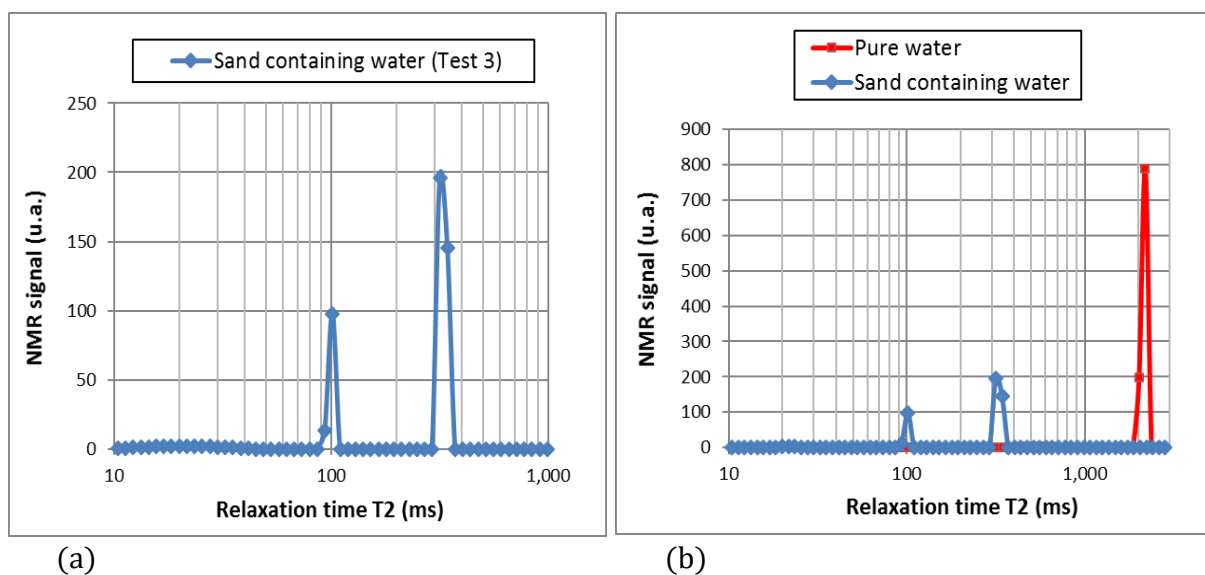


Figure A.19. Test 3 results (a) T2 relaxation time distribution for water-wet sand containing water, (b) T2 comparison between pure water sample and the sample of water-wet sand containing water.

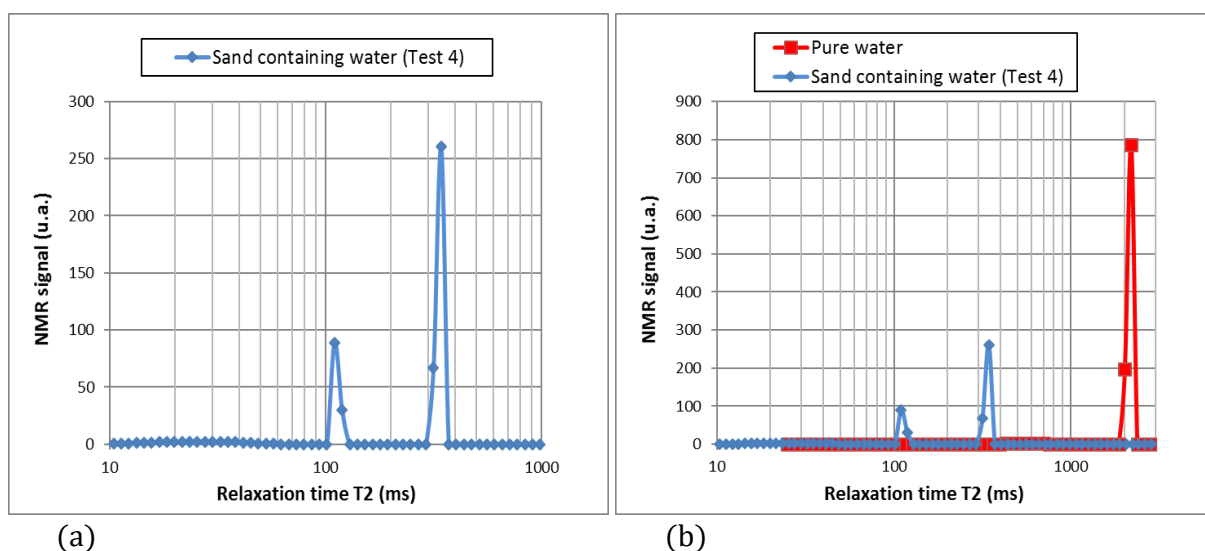


Figure A.20. Test 4 results (a) T2 relaxation time distribution for water-wet sand containing water, (b) T2 comparison between pure water sample and the sample of water-wet sand containing water.

The presence of water in sand media resulted in a clear shift in the T2 relaxation time distribution comparing with the pure water sample, and the signal intensity value is reduced as well.

1. Sample of water-wet sand containing oil:

Figure A.20 below shows the results of T2 relaxation time distribution for the sample of water-wet sand containing oil, and the results comparison with pure oil sample.

| | | | |
|-----------|---------------|-------------|---------------------|
| TR = 10 s | $\tau = 2$ ms | T2 = 355 ms | Amplitude = 29.95 % |
|-----------|---------------|-------------|---------------------|

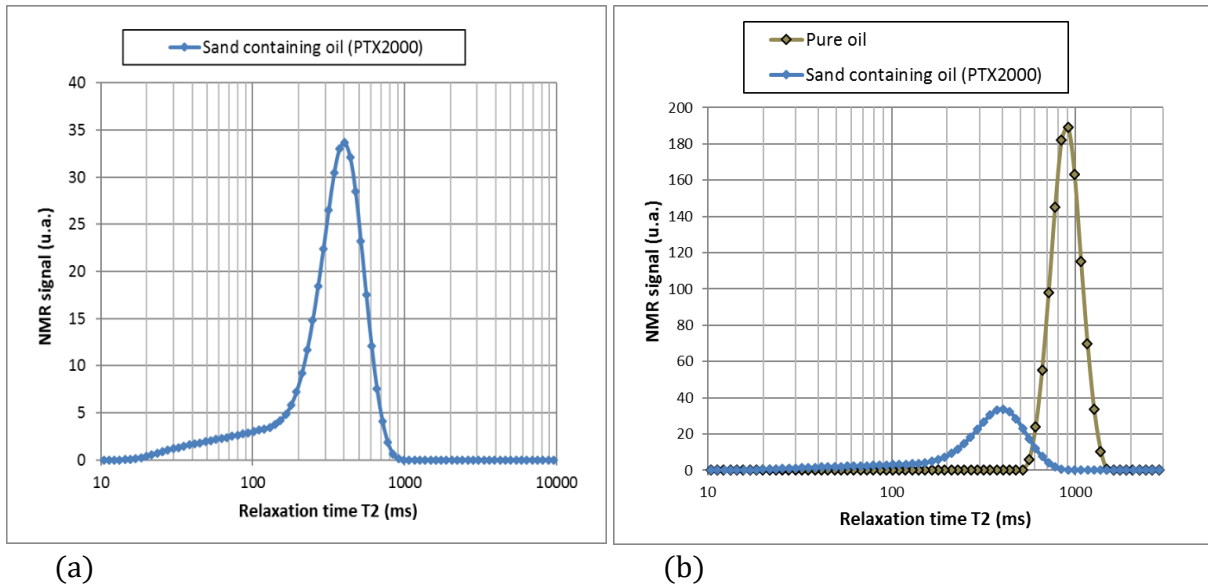


Figure A.21. (a) T2 relaxation time distribution for water-wet sand sample containing oil, (b) T2 comparison between pure oil sample (PTX2000) and the sample of water-wet sand containing oil.

The presence of oil in sand column resulted in a small shift in the T2 relaxation time distribution comparing with the pure oil sample, and the signal intensity value is reduced as well.

V. MRI Experimental results for some experiments:

Experiments with packed sand column:

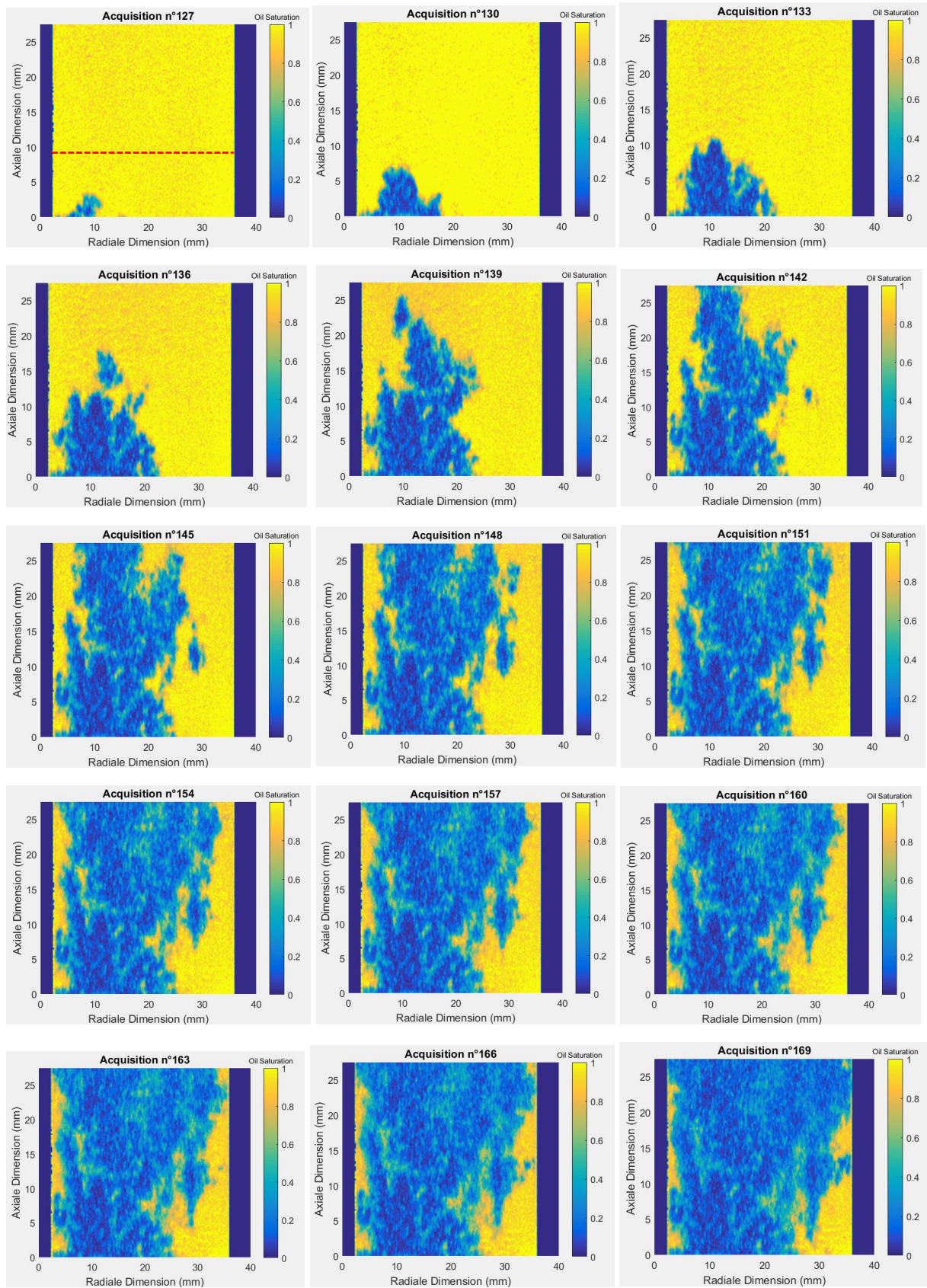
Flow rate 0.08 mL/min

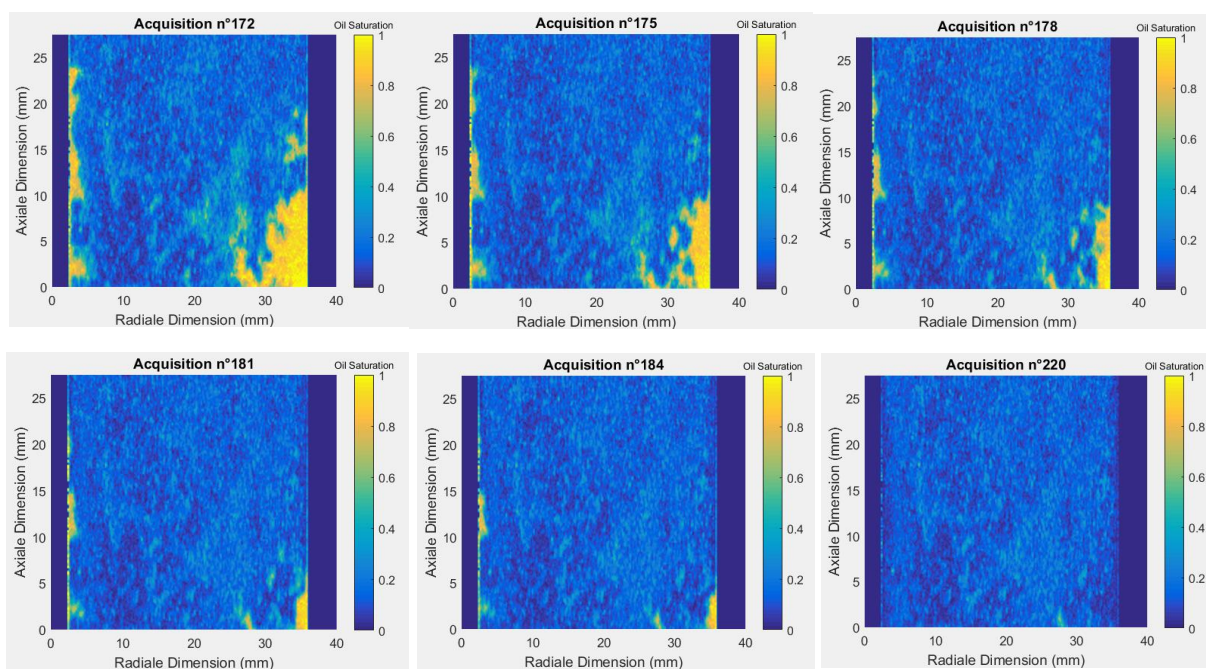
| | |
|-------------------------|--|
| Porous | Packed sand of particle size ~0.13 mm diameter |
| Tube | Plastic tube of 10 cm net length |
| Injection rate | 0.08 mL/min |
| Estimated porosity | 39% |
| Permeability | 1.5E-11 m ² |
| Injected fluid | Pure water + MnCl ₂ (C = 0.02 mole/l) |
| Oil phase (kerosene) | PTX2000 $\rho = 800 \text{ kg/m}^3$, $\mu = 2.96 \text{ mPa s}$ at 20°C |
| MRI Field of view | 5 cm (256 x 256 pixels) |
| TR (time of repetition) | 1 s |
| TE (time of echo) | 5 ms |

Table A.1. The experiment parameters of packed sand model, non-selective method.

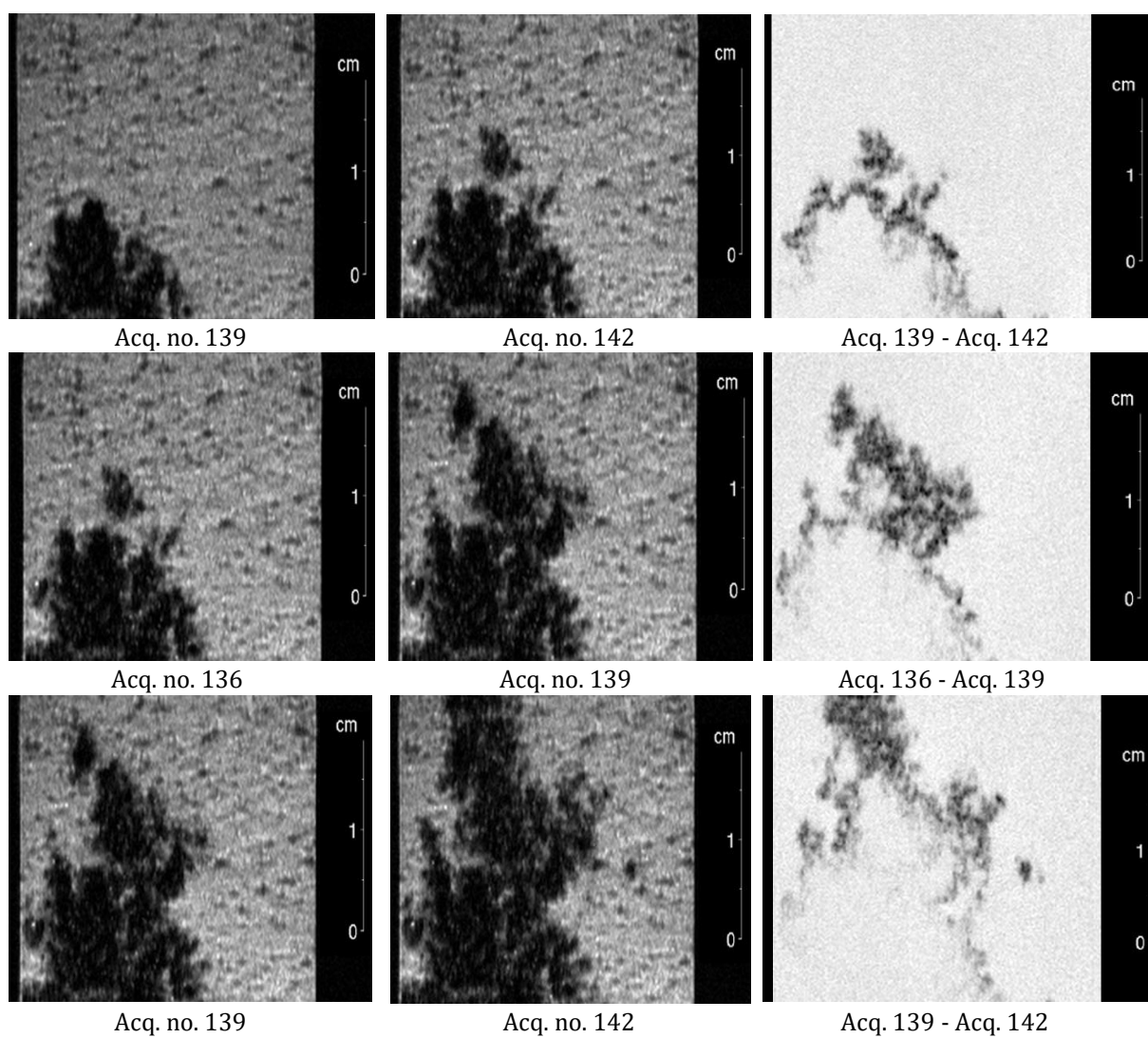
| | MRI acquisition no. | | Time of acquisition | | Cumulative time | Average oil saturation of the sample | |
|------------|---------------------|------------|---------------------|------------|-----------------|--------------------------------------|---------------------|
| | Vertical | Horizontal | Vertical | Horizontal | | Vertical image | Horizontal sections |
| Reference: | 115 V | 116 H | 11:15 | 11:19 | 0:00 | 1.0000 | 1.0000 |
| | 118 V | 119 H | 11:30 | 11:34 | 0:15 | 0.9728 | 0.9825 |
| | 121 V | 122 H | 11:45 | 11:49 | 0:30 | 0.9853 | 0.9890 |
| | 124 V | 125 H | 12:00 | 12:04 | 0:45 | 0.9801 | 0.9791 |
| | 127 V | 128 H | 12:15 | 12:19 | 1:00 | 0.9714 | 0.9526 |
| | 130 V | 131 H | 12:30 | 12:34 | 1:15 | 0.9644 | 0.8938 |
| | 133 V | 134 H | 12:45 | 12:49 | 1:30 | 0.8749 | 0.7776 |
| | 136 V | 137 H | 13:00 | 13:04 | 1:45 | 0.8009 | 0.6611 |
| | 139 V | 140 H | 13:15 | 13:19 | 2:00 | 0.6972 | 0.5613 |
| | 142 V | 143 H | 13:30 | 13:34 | 2:15 | 0.6302 | 0.5117 |
| | 145 V | 146 H | 13:45 | 13:49 | 2:30 | 0.5490 | 0.4632 |
| | 148 V | 149 H | 14:00 | 14:04 | 2:45 | 0.4887 | 0.4281 |
| | 151 V | 152 H | 14:15 | 14:19 | 3:00 | 0.4436 | 0.4070 |
| | 154 V | 155 H | 14:30 | 14:34 | 3:15 | 0.4321 | 0.3989 |
| | 157 V | 158 H | 14:45 | 14:49 | 3:30 | 0.4117 | 0.3825 |
| | 160 V | 161 H | 15:00 | 15:04 | 3:45 | 0.3983 | 0.3728 |
| | 163 V | 164 H | 15:15 | 15:19 | 4:00 | 0.3866 | 0.3569 |
| | 166 V | 167 H | 15:30 | 15:34 | 4:15 | 0.3592 | 0.3303 |
| | 169 V | 170 H | 15:45 | 15:49 | 4:30 | 0.3121 | 0.2851 |
| | 172 V | 173 H | 16:00 | 16:04 | 4:45 | 0.2470 | 0.2315 |
| | 175 V | 176 H | 16:15 | 16:19 | 5:00 | 0.2008 | 0.1925 |
| | 178 V | 179 H | 16:30 | 16:34 | 5:15 | 0.1778 | 0.1751 |
| | 181 V | 182 H | 16:45 | 16:49 | 5:30 | 0.1617 | 0.1625 |
| | 184 V | 185 H | 17:00 | 17:04 | 5:45 | 0.1557 | 0.1571 |
| | 187 V | 188 H | 17:15 | 17:19 | 6:00 | 0.1481 | 0.1496 |
| | 190 V | 191 H | 17:30 | 17:34 | 6:15 | 0.1458 | 0.1464 |
| | 193 V | 194 H | 17:45 | 17:49 | 6:30 | 0.1441 | 0.1440 |
| | 196 V | 197 H | 18:00 | 18:04 | 6:45 | 0.1422 | 0.1425 |
| | 199 V | 200 H | 19:00 | 19:04 | 7:45 | 0.1403 | 0.1407 |
| | 202 V | 203 H | 20:00 | 20:04 | 8:45 | 0.1397 | 0.1402 |
| | 208 V | 209 H | 0:00 | 00:04 | 12:45 | 0.1409 | 0.1397 |
| | 214 V | 215 H | 4:00 | 04:04 | 16:45 | 0.1391 | 0.1397 |
| | 217 V | 218 H | 6:00 | 06:04 | 18:45 | 0.1395 | 0.1395 |
| Final: Sor | 220 V | 221 H | 9:00 | 09:04 | 21:45 | 0.1385 | 0.1385 |

Table A.2. Sample's average oil saturation along the model, calculated using Matlab codes.

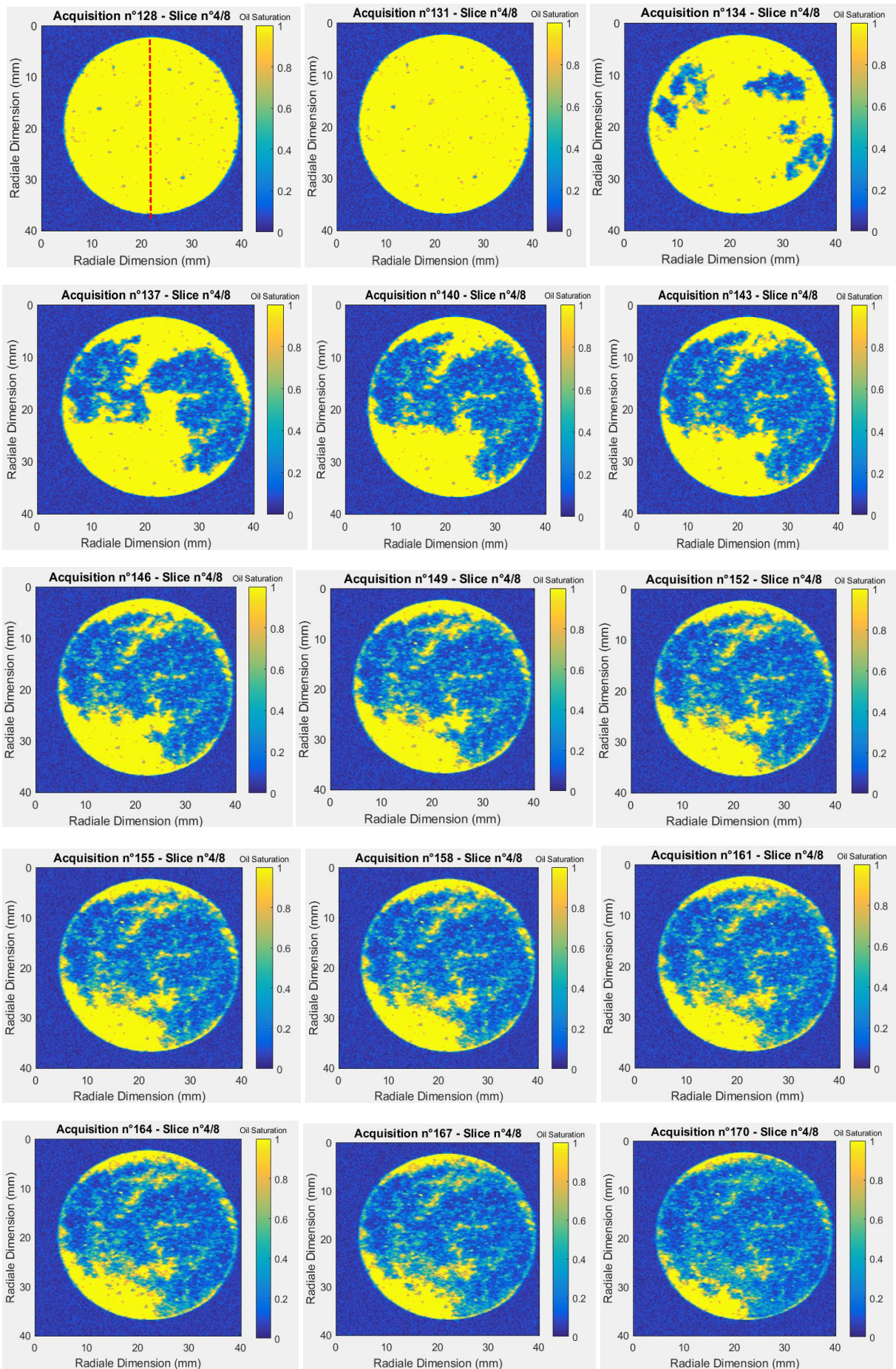


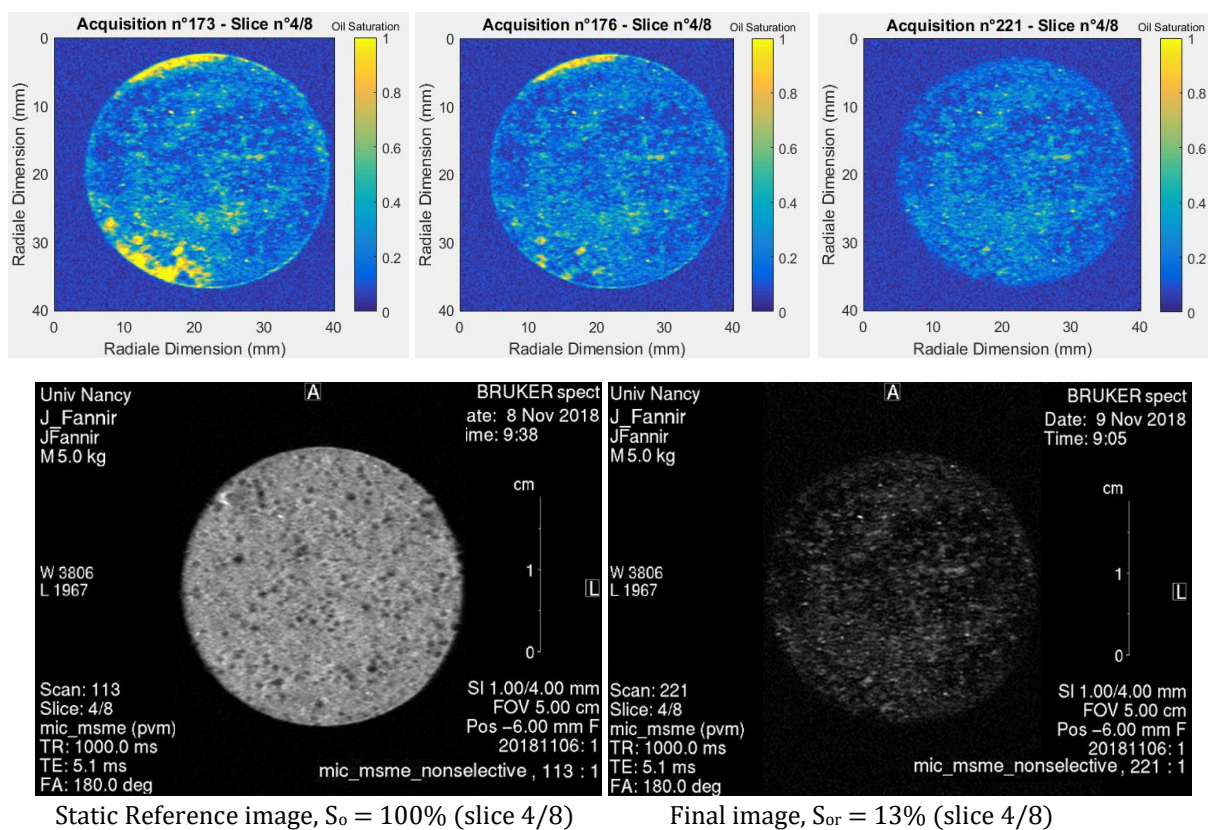


(a)



(b)

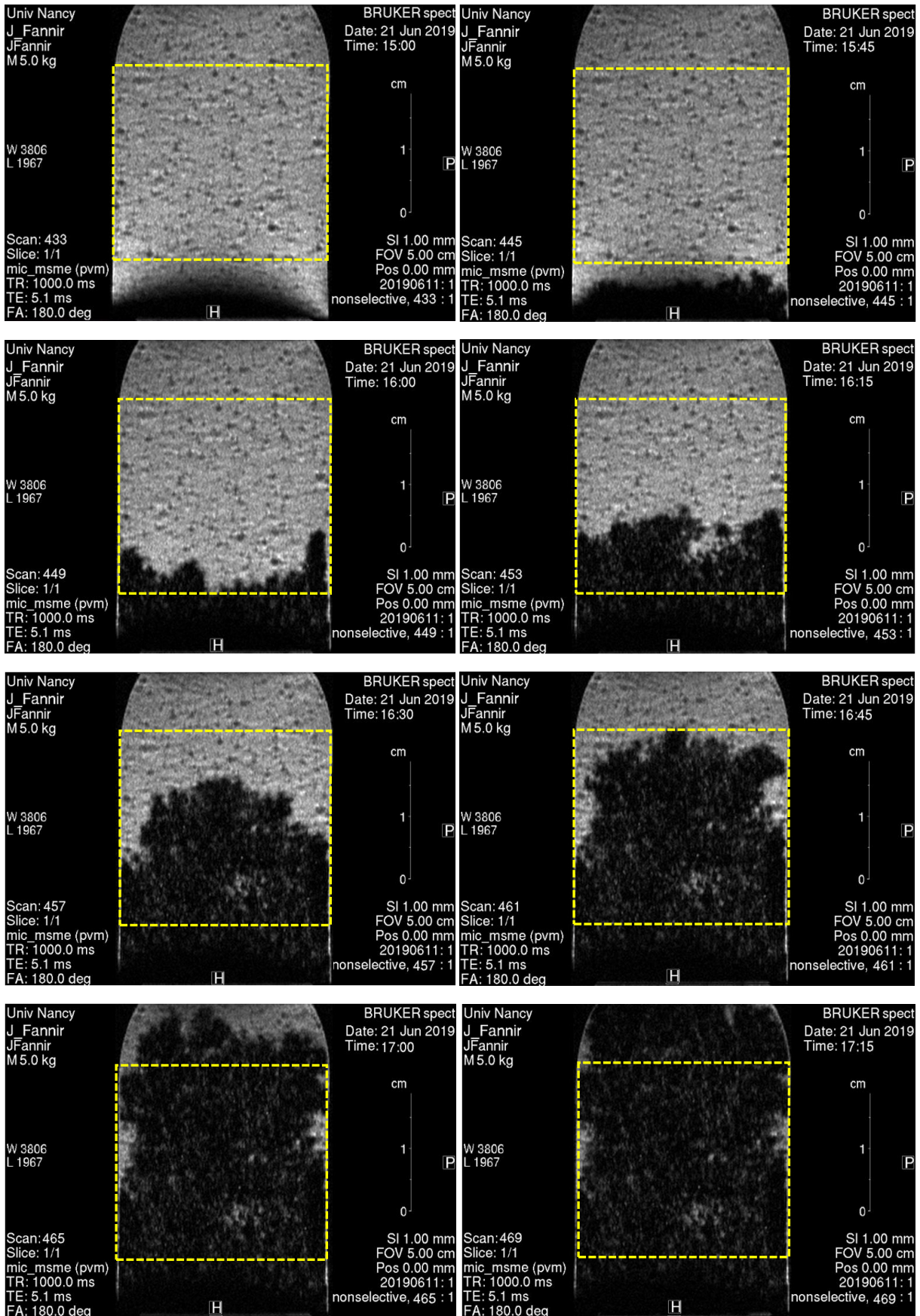




(c)

Figure A.22. (a) & (c) Consecutive MRI images of the water–oil displacement in the model of packed sand column with the low injection flow rate of 0.08 mL/min. The oil is yellow and the water is blue. The time interval between each image equals 15 minutes from the first water appearance in FOV. The dotted line on the first vertical section indicates the position of the horizontal sections (and vice-versa for the horizontal section below). (b) The difference between vertical images to show the local area where the displacement happens.

Flow rate 0.16 mL/min



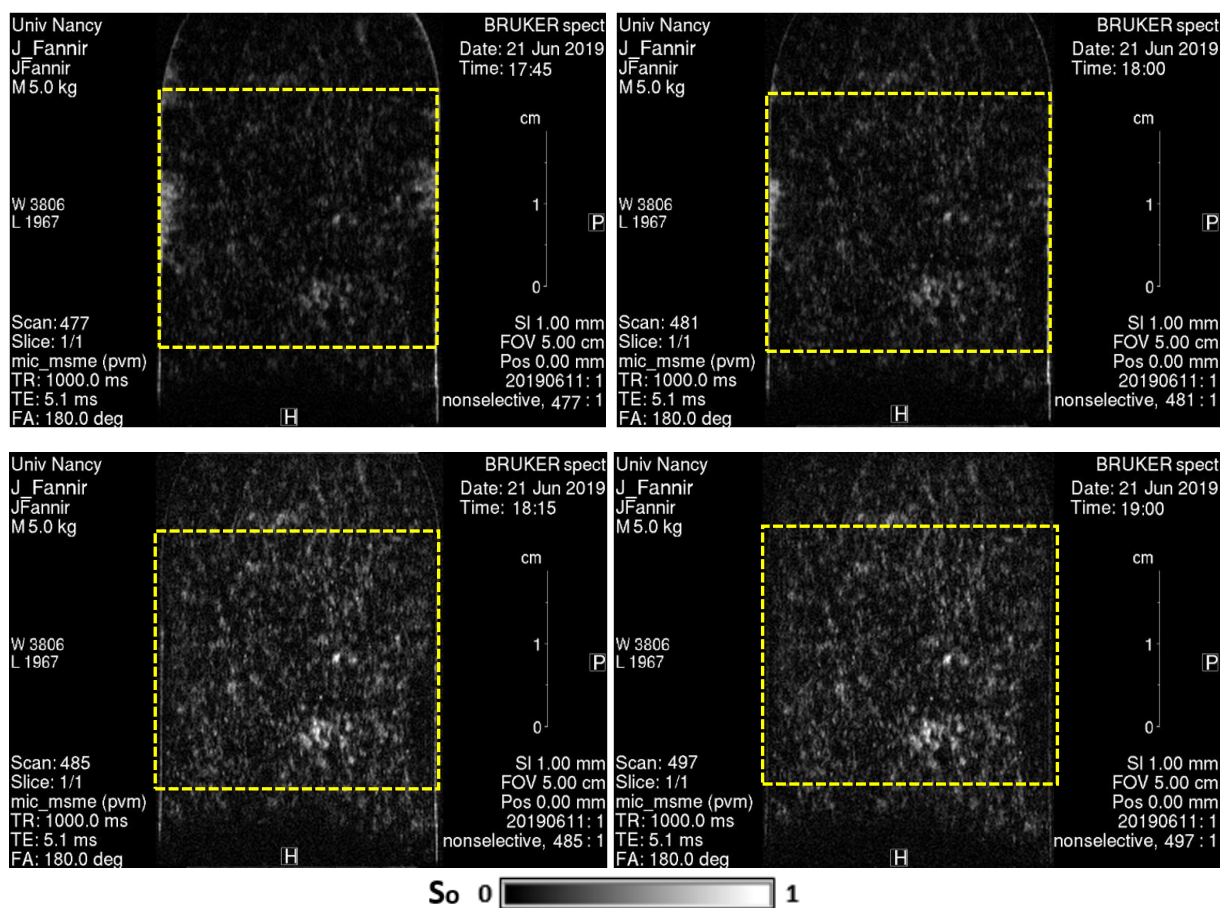



Figure A.23. Vertical consecutive MRI images of the water–oil displacement in the model of packed sand column with the high injection flow rate of 0.16 mL/min. The oil is grey and darker areas where a lower or no signal was recorded. The yellow dotted line indicates the area of interest.

VI. PTX2000 data sheet

Oil phase fluid properties (PTX 2000) used in our experiments, according to the product owner data.

|  FICHE DE DONNÉES DE SÉCURITÉ Basée sur Règlement (CE) n° 1907/2006, comme modifié par Règlement (CE) n° 453/2010 | | | | | | |
|--|--|---|---------------------------------|--------------------------|---------|----------|
| PTX 2000 | | | | | | |
| SECTION 1: Identification de la substance/du mélange et de la société/l'entreprise | | | | | | |
| 1.1 Identificateur de produit: | | | | | | |
| Nom de produit | : | PTX 2000 | | | | |
| Numéro d'enregistrement REACH | : | 01-2119456620-43 | | | | |
| Type de produit REACH | : | Substance/UVCB (Organique) | | | | |
| Numéro CAS | : | 64742-47-8 | | | | |
| Numéro CE | : | 265-149-8 | | | | |
| 1.2 Utilisations identifiées pertinentes de la substance ou du mélange et utilisations déconseillées: | | | | | | |
| 1.2.1 Utilisations identifiées pertinentes | | | | | | |
| Combustible liquide pour appareils mobiles de chauffage | | | | | | |
| 1.2.2 Utilisations déconseillées | | | | | | |
| Aucune utilisation déconseillée | | | | | | |
| 1.3 Renseignements concernant le fournisseur de la fiche de données de sécurité: | | | | | | |
| <u>Fournisseur de la fiche de données de sécurité</u> | | | | | | |
| PVG LIQUIDS NV Belgicastraat 1C - Haven 2290 B-9042 Gent Tel: +32 9 250 90 80 Fax: +32 9 250 90 89 reach@pvg.eu | | | | | | |
| 1.4 Numéro d'appel d'urgence: | | | | | | |
| 24h/24h (Consultation téléphonique: anglais, français, allemand, néerlandais): +32 14 58 45 45 (BIG) | | | | | | |
| P301 + P310 | EN CAS D'INGESTION: | appeler immédiatement un CENTRE ANTIPOISON ou un médecin. | | | | |
| P331 | NE PAS faire vomir. | | | | | |
| P405 | Garder sous clef. | | | | | |
| P501 | Éliminer le contenu/réceptacle dans un centre de collecte des déchets dangereux ou spéciaux. | | | | | |
| Informations supplémentaires | | | | | | |
| EUH066 | L'exposition répétée peut provoquer dessèchement ou gerçures de la peau. | | | | | |
| 2.3 Autres dangers: | | | | | | |
| CLP | | | | | | |
| Matière présentant un risque d'incendie | | | | | | |
| Légèrement irritant pour les yeux | | | | | | |
| SECTION 3: Composition/informations sur les composants | | | | | | |
| 3.1 Substances: | | | | | | |
| Nom (REACH n° d'enregistrement) | N° CAS N° CE | Conc. (C) | Classification selon DSD/DPD | Classification selon CLP | Note | Remarque |
| hydrocarbures, C11-C14, n-alcanes, iso-alcanes, cycliques, <2% aromatiques (01-2119456620-43) | 64742-47-8 265-149-8 | C≤100% | R66 Xn; R65 | Asp. Tox. 1; H304 | (1)(10) | UVCB |
| aromatiques (-) | -- | C≤1% | | | | |
| (1) Texte intégral des phrases R et H: voir point 16 | | | | | | |
| (10) Soumis aux restrictions de l'Annexe XVII du Règlement (CE) n° 1907/2006 | | | | | | |
| 3.2 Mélanges: | | | | | | |
| Ne s'applique pas | | | | | | |

8.1.2 Méthodes de prélèvement

| Nom de produit | Essai | Numéro |
|---------------------|-------|--------|
| Kerosene (Naphthas) | NIOSH | 1550 |

8.1.3 Valeurs limites applicables lorsqu'on utilise la substance ou le mélange aux fins prévues

Les valeurs limites sont reprises ci-dessous, si celles-ci sont disponibles et applicables.

8.1.4 Valeurs DNEL/PNEC**Travailleurs**

PTX 2000

| Seuil (DNEL/DMEL) | Type | Valeur | Remarque |
|-------------------|------|--------|--------------------------------|
| | | | Aucun renseignement disponible |

Grand public

PTX 2000

| Seuil (DNEL/DMEL) | Type | Valeur | Remarque |
|-------------------|------|--------|--------------------------------|
| | | | Aucun renseignement disponible |

8.1.5 Control banding

Cela est repris ci-dessous, s'il est disponible et applicable.

8.2 Contrôles de l'exposition:

Les informations dans cette section sont une description générale. Les scénarios d'exposition figurent en annexe, si ceux-ci sont disponibles et applicables. Utiliser toujours les scénarios d'exposition appropriés correspondant à votre utilisation identifiée.

8.2.1 Contrôles techniques appropriés

Mettre les appareils à la terre. Tenir à l'écart de flammes nues/la chaleur. Température > point d'éclair: appareils/éclairage pour atmosphère explosive. Fines particules: appareillage/éclairage pour atmosphère explosive. Finement divisé: à l'écart de sources d'ignition/étincelles. Faire les travaux en plein air/sous aspiration locale/ventilation ou protection respiratoire.

8.2.2 Mesures de protection individuelle, telles que les équipements de protection individuelle

Éviter le contact prolongé et répété avec la peau. Tenir l'emballage bien fermé. Ne pas manger, ni boire ni fumer pendant le travail.

a) Protection respiratoire:

Concentration élevée de gaz/vapeurs: masque à gaz, type de filtre A.

b) Protection des mains:

Gants.

- matériau approprié pour vêtements (bonne résistance)

Caoutchouc nitrile.

c) Protection des yeux:

Écran facial.

d) Protection de la peau:

Vêtements de protection.

8.2.3 Contrôles d'exposition liés à la protection de l'environnement:

Voir points 6.2, 6.3 et 13

SECTION 9: Propriétés physiques et chimiques**9.1 Informations sur les propriétés physiques et chimiques essentielles:**

| | |
|--------------------------|--|
| Aspect physique | Liquide |
| Odeur | Odeur faible Odeur de type pétrole |
| Seuil d'odeur | Aucun renseignement disponible |
| Couleur | Couleurs varient en fonction de la législation fiscale nationale |
| Taille des particules | Sans objet (liquide) |
| Limites d'inflammabilité | 0.6 - 7 vol % |
| Inflammabilité | Matière présentant un risque d'incendie |
| Log Kow | > 3 ; Littérature |
| Viscosité dynamique | 2.96 mPa.s ; 20 °C |
| Viscosité cinématique | 2.4 mm ² /s ; 20 °C |
| Point de fusion | -45 °C |
| Point d'ébullition | 203-238 °C |
| Point d'éclair | 77 °C |
| Taux d'évaporation | Aucun renseignement disponible |
| Pression de vapeur | Aucun renseignement disponible |

| | |
|------------------------------|--|
| Densité de vapeur relative | Aucun renseignement disponible |
| Solubilité | Aucun renseignement disponible |
| Densité relative | 0.81 ; 15 °C |
| Température de décomposition | Aucun renseignement disponible |
| Température d'auto-ignition | >200 °C |
| Propriétés explosives | Aucun groupement chimique associé à des propriétés explosives |
| Propriétés comburantes | Aucun groupement chimique associé à des propriétés comburantes |
| pH | Aucun renseignement disponible |

Dangers physiques

Aucune classe de danger physique

9.2 Autres informations:

| | |
|-----------------|-------------------------------|
| Densité absolue | 810 kg/m ³ ; 15 °C |
|-----------------|-------------------------------|

SECTION 10: Stabilité et réactivité**10.1 Réactivité:**

À température > point d'éclair: risque d'incendie/explosion accru.

10.2 Stabilité chimique:

Stable dans les conditions normales.

10.3 Possibilité de réactions dangereuses:

Aucun renseignement disponible.

10.4 Conditions à éviter:

Mettre les appareils à la terre. Tenir à l'écart de flammes nues/la chaleur. Température > point d'éclair: appareils/éclairage pour atmosphère explosive. Fines particules: appareillage/éclairage pour atmosphère explosive. Finement divisé: à l'écart de sources d'ignition/étincelles.

10.5 Matières incompatibles:

Agents d'oxydation.

10.6 Produits de décomposition dangereux:Formation de CO et de CO₂ en cas de combustion.**SECTION 11: Informations toxicologiques****11.1 Informations sur les effets toxicologiques:****11.1.1 Résultats d'essais****Toxicité aiguë**PTX 2000

| Voie d'exposition | Paramètre | Méthode | Valeur | Durée d'exposition | Espèce | Genre | Détermination de la valeur |
|----------------------|-----------|-----------------------|-----------------------------|--------------------|--------|------------------|----------------------------|
| Oral | DL50 | OCDE 401 | > 5000 mg/kg bw | | Rat | Masculin/féminin | Read-across |
| Oral | DL50 | Équivalent à OCDE 401 | >15000 mg/kg bw | | Rat | Masculin/féminin | Read-across |
| Dermal | DL50 | Équivalent à OCDE 402 | >3160 mg/kg bw | | Lapin | Masculin/féminin | Read-across |
| Dermal | DL50 | Équivalent à OCDE 402 | >5000 mg/kg bw | | Lapin | Masculin/féminin | Read-across |
| Inhalation (aérosol) | CL50 | Équivalent à OCDE 403 | >5000 mg/m ³ air | 8 h | Rat | Mâle | Read-across |
| Inhalation (vapeurs) | CL50 | Équivalent à OCDE 403 | 4467 ppm | 8 h | Rat | Mâle | Read-across |

Conclusion

Faible toxicité aiguë par voie cutanée

Faible toxicité aiguë par voie orale

Faible toxicité aiguë par inhalation

Corrosion/irritation cutanéePTX 2000

| Voie d'exposition | Résultat | Méthode | Durée d'exposition | Point de temps | Espèce | Détermination de la valeur |
|-------------------|--------------|-----------------------|--------------------|-------------------|--------|----------------------------|
| Oeil | Non irritant | Équivalent à OCDE 405 | | 24; 48; 72 heures | Lapin | Read-across |

Stabilité des écoulements diphasiques dans un milieu poreux étudié par des techniques d'IRM

Il est important de comprendre les forces motrices qui contrôlent l'écoulement de deux fluides immiscibles dans un milieu poreux. En effet, il existe une large gamme d'applications des écoulements diphasiques en milieux poreux, notamment ceux qui concernent la récupération assistée du pétrole (EOR). Le développement des techniques quantitatives d'imagerie par résonance magnétique (IRM) ouvre de nouvelles possibilités pour étudier et caractériser les flux multiphasiques en milieu poreux. Ce travail s'intéresse précisément à décrire le déplacement de deux fluides immiscibles (eau-huile) au sein d'un milieu poreux en utilisant les techniques d'IRM. Le milieu poreux est initialement saturé d'huile qu'on vient déplacer en injectant de l'eau par le bas, l'huile et l'eau pouvant s'évacuer par le haut. L'objectif général de l'étude est de déterminer le déplacement et la déformation du front (eau-huile) au cours du temps, et de préciser les mécanismes de piégeage des phases. Des expériences sont menées sur deux modèles poreux. L'un mouillant à l'huile consiste en un empilement de petites billes en polystyrène ($0,4 \text{ mm} < dp < 0,6 \text{ mm}$), l'autre mouillant à l'eau est un sable légèrement compacté ($0,02 \text{ mm} < dp < 0,50 \text{ mm}$). Nous avons utilisé un dispositif de micro-imagerie RMN fonctionnant à 14 T (résonance ^1H à 600 MHz) pour acquérir des images à haute résolution (0.2 mm) à l'intérieur des milieux poreux au cours du déplacement des deux fluides. Les résultats obtenus ont montré que le profil de saturation en huile est fortement influencé par les propriétés du matériau poreux, telles que la porosité et la perméabilité de l'échantillon, le mouillage des phases, le débit d'injection de l'eau ou encore l'hétérogénéité de la matrice solide. L'influence du débit d'injection d'eau sur la saturation résiduelle en huile a été plus particulièrement étudiée. Les résultats expérimentaux permettent une compréhension fine du déplacement de deux fluides non miscibles pour deux types de milieux poreux, qui se différencient principalement par les effets de la mouillabilité. Dans le même temps, une simulation numérique du déplacement vertical ascendant de l'huile poussée par de l'eau dans une colonne poreuse a été réalisée et les résultats ont été comparés à nos expériences sous IRM.

Mots-clefs : IRM, écoulement diphasique, milieu poreux, déplacement huile-eau, digitations visqueuses, saturation résiduelle en huile.

Stability of the two-phase displacement in porous media studied by MRI techniques

It is important to understand the driving forces that control the flow of two immiscible fluids in a porous medium. Indeed, there is a wide range of applications of two-phase flows in porous media, especially those relating to enhanced oil recovery (EOR). The development of quantitative magnetic resonance imaging (MRI) techniques opens up new possibilities for studying and characterizing multiphase flows in porous media. This work is specifically concerned with describing the displacement of two immiscible fluids (water-oil) in a porous medium using MRI techniques. The porous medium is initially saturated with oil which is displaced by injecting water from below, oil and water can be evacuated from above. The general objective of the study is to determine the displacement and the deformation of the front (water-oil) over time, and to specify the trapping mechanisms of the phases. Experiments are conducted on two porous models. One oil wetting consists of a stack of small polystyrene beads ($0.4 \text{ mm} < dp < 0.6 \text{ mm}$), the other wetting with water is a slightly compacted sand ($0.02 \text{ mm} < dp < 0.50 \text{ mm}$). We used a 14 T NMR micro-imaging device (^1H resonance at 600 MHz) to acquire high resolution images (0.2 mm) inside the porous media during the movement of the two fluids. The results obtained showed that the oil saturation profile is strongly influenced by the properties of the porous material, such as the porosity and the permeability of the sample, the wetting of the phases, the injection rate of the water or even the heterogeneity of the solid matrix. The influence of the water injection flow rate on the residual saturation of oil has been studied more particularly. The experimental results allow a fine understanding of the displacement of two immiscible fluids for two types of porous media, which mainly differ by the effects of wettability. At the same time, a numerical simulation of the upward vertical displacement of oil pushed by water in a porous column was performed and the results compared to our MRI experiments.

Keywords: MRI, two-phase flow, porous media, oil-water displacement, viscous fingering, residual oil saturation.